Design, operation and dynamic performance of a brushless DC tubular drive system

Akmese, Recep

Award date:
1989

Awarding institution:
University of Bath

DESIGN, OPERATION AND DYNAMIC PERFORMANCE OF A BRUSHLESS DC TUBULAR DRIVE SYSTEM

Submitted by

Recep Akmeşe

for the degree of Doctor of Philosophy

of the University of Bath

1989

ProQuest LLC
789 East Eisenhower Parkway
P.O. Box 1346
Ann Arbor, MI 48106-1346

ACKNOWLEDGEMENTS

The author wishes to express his sincere gratitude to Professor J. F. Eastham for his invaluable guidance, keen interest and continuous encouragement throughout the course of this project.

The author also wishes to thank the academic, research and technical University staff who have helped in any way.

Finally, the author is grateful to his parents and to the members of his family for all their patience, endurance and encouragement which provided the strength and drive to see this work to its successful conclusion.

ABSTRACT

This thesis presents the principle of operation, design and dynamic performance of an oscillatory tubular linear machine system with permanent magnet excitation. Based on the brushless dc machine principle, the system is driven by a power integrated circuit designed especially for rotary machines and achieves oscillatory motion with minimum additional hardware.

A novel skew scheme applied to the excitation permanentic magnet poles is used to eliminate the unwanted tooth-cogging forces. This skew also minimizes the other unwanted cogging force due to the finite length of the armature and has a smoothing effect on the electromagnetic force.

Finite element methods are used to find both the standstill forces and the machine parameters as the first part of a Computer Aided Design (CAD) process. These parameters are used in the system equations which describe the system both electrically and mechanically. The system equations are solved numerically as the second part of the CAD process and the results are compared with experimental data obtained from a practical model. The good agreement between the two sets of results shows that a complete modelling of these machines can be achieved using computer aided analysis techniques.

A design optimization procedure based on analytical formulae is also given. This can be used to estimate the size of the machine required for a proposed duty prior to the use of the relatively expensive CAD tools.

TABLE OF CONTENTS

LIST OF SYMBOLS

Where a symbol has been used to represent more than one quantity it is listed in the order of most frequent usage.

A_{arm}	Total cross-sectional area of the armature back-iron
A_{Cu}	Net copper area of an armature slot
$A_{slot\text{-}net}$	Net area of an armature slot
A_w	Cross-Sectional area of the armature winding wire
A_t	Radial cross-sectional area of an armature tooth (circumferential)
a	Excitation acceleration
a_n	Cosine coefficients of the phase flux linkage
B	Flux density
B_c	Saturation flux density of the armature core
B_g	Air-Gap flux density
B_m	Permanent magnet working-point flux density
B_n	Normal component of flux density
B_r	Remanence of the permanent magnets
B_t	Saturation flux density of the armature tooth
b_n	Sine coefficients of the phase flux linkage
C1,..,C6	Armature coils
D1,..,D6	Inverter diodes
DS	Direction signal
d_1	Excitation core diameter
d_{out}	Armature outer diameter
E	Line to line (loop) emf of the circuit models
E_1, E_2	Loop emfs of the direction transients, two-loop circuit model
E_{on} , E_{off}	On and off-loop emfs of the one-way operation, two-loop circuit model
$[E]$	Loop emf column vector of the two-loop circuit models

e_a , e_b , e_c	Machine phase to neutral back emfs
e_{ab} , e_{bc} , e_{ca}	Machine line to line emfs
e_1 , e_2	Phase emfs of the one-way operation, one-loop circuit model
$[e]$	Column vector of phase to neutral emfs
ESleft	Left travel-end sensor
ESright	Right travel-end sensor
F_{em}	Electromagnetic force
F_{end}	End-Effect force
F_{pp}	Standstill electromagnetic force per armature pole
$F_{per\text{-}Vol}$	Standstill electromagnetic force per unit of machine volume
g	Air-Gap Length
g_{eff}	Effective air-gap length
H	Magnetising force
H1, H2, H3	Excitation position (Hall) signals
H_m	Permanent magnet working point magnetising force
h_b	Armature back-iron height
h_s	Armature slot height
I, i	Current
I_{max}	Magnitude limit for the dc link current
I_{ph}	Phase current magnitude limit
I_s	Total slot current
i_1, i_2	Loop currents of the direction transients, two-loop circuit model
i_a , i_b , i_c	Machine phase currents
i_{on} , i_{off}	On and off-loop currents of the one-way operation two-loop circuit model
$[i]$	Column vector of phase currents
J_s	Slot current density
L	Self inductance
L	Average effective phase self inductance
L_a , L_b , L_c	Machine phase self inductances

L-M	Effective phase inductance of the decoupled machine model
[L-M]	Inductance matrix of the decoupled machine model
l	Length
l_m	Permanent magnet length
M	Mutual inductance
M	Average effective phase to phase mutual inductance
M_{ab}, M_{bc}, M_{ca}	Machine phase to phase mutual inductances
m	Mass of the moving parts
N_c	Number of turns in an armature coil
N_s	Number of armature slots in a pole
n	Harmonic order of phase flux linkages and emfs
n_h	Number of flux linkage and emf harmonics
p	Number of armature pole-pairs
R	Resistance
R	Average effective machine phase resistance
R_a, R_b, R_c	Machine phase to neutral resistances
R_{ext}	Resistance of the wire which connects the supply battery to the driver
R_{ph}	Machine phase resistance per pole-pair
R_s	Sense resistor used for current magnitude control
[R]	Phase resistance matrix
r	Radius
SI1,..,SI6	Inverter switching intervals
T	Period of an excitation oscillation
T1,..,T6	Inverter transistors
T1,..,T6	Inverter transistor switching signals
t	Time
t_{ins}	Thickness of the armature slot wall insulation
t_{off}	Turn-off time of the inverter bottom transistors
t_p	Pole pitch

t_s	Slot pitch
t_t	Tooth width
V	Voltage
V_a , V_b , V_c	Machine phase to neutral voltages
V_{ab} , V_{bc} , V_{ca}	Machine line to line voltages
V_{DC}	Supply battery voltage
V_{pp}	Maximum required dc input voltage per phase
V_{res}	Phase voltage drop due to phase resistances
$[V]$	Column vector of phase to neutral voltages
v	Excitation velocity
Vol_{pp}	Machine volume per pole
W	Magnetic stored energy in a field
w_m	Permanent magnet width
w_s	Slot width
x	Excitation displacement
α	Tooth width to slot pitch ratio
β	Magnet width to pole pitch ratio
Δ	Finite perturbation
δ	Force angle
δt	Time-step length
θ	Phase shift in the flux linkage waveform
λ	Flux linkage
λ_a , λ_b , λ_c	Machine phase flux linkages due to permanent magnet fields
λ_{coil}	Armature coil flux linkage
$[\lambda]$	Column vector of phase flux linkages
μ_0	Permeability of free space
ρ	Resistivity of copper
ϕ	Flux
ϕ	Flux linking an armature coil-turn

ϕ_t	Armature tooth flux

Subscripts

a, b, c	Armature phases
(a)	Armature
j, k, n	Coils
n	Harmonic order
(ch)	Variable subject to chopping action

Superscripts

inc	Incremental
$'$	Variable value at the beginning of a time-step
$''$	Variable value at the end of a time-step
T	Transpose

CHAPTER 1

INTRODUCTION

1.1 Linear Machine Topologies

As well as being employed to produce torque in rotary machines, electromagnetic forces may be employed to produce linear motion resulting in linear machines. Linear machines have been in existence since the turn of the century. These machines have, however, found favour only after the 1960s.

A linear machine, when motion in a straight line is required, eliminates gears and rotary to linear converters. It therefore makes a quieter, cheaper and more reliable alternative to its rotary counterpart. Linear machines also offer possibilities for new design ideas such as magnetic levitation used in ground transportation applications **[1.1]**. In many applications, in contrast to rotary machines, linear machines are special purpose devices and it is this feature that broadens their range of uses.

Topologically, linear machines can be divided into two classes: flat machines and tubular machines [please see Fig. 1.1(a) and (b)]. These machines can be obtained from a rotary machine by a transformation process as will be described in Chapter 2.

A further topological division of linear machines can be made which applies to both flat and tubular machines. Once the moving member is displaced, a part of each member is no longer covered by the other, shortening the active part of the machine. However, since there is no reason why both members should be the same length, one member may be shorter than the other, leading to two main classes of linear machines,

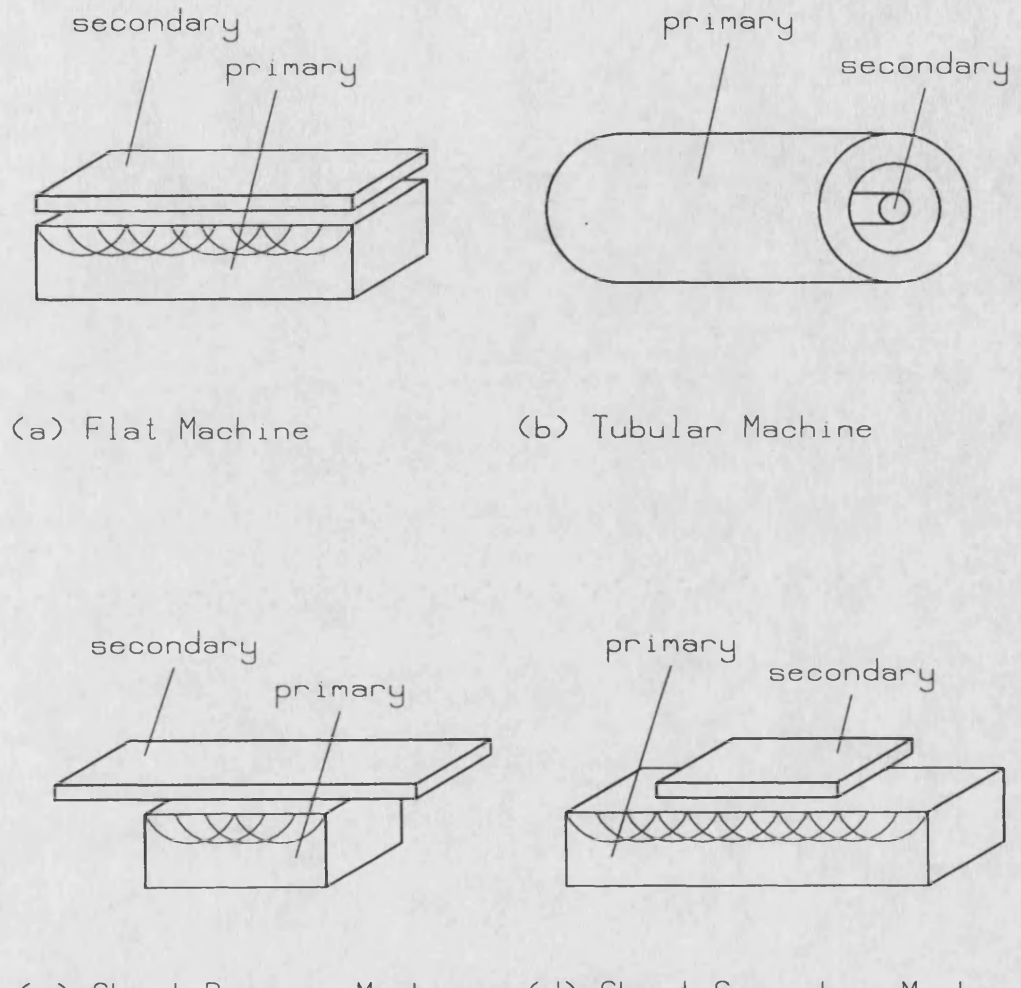

Figure 1.1 Topology of Linear Machines

namely short primary and short secondary, as drawn in Figs. 1.1(c) and (d). Unlike rotary machines, the short member now has a "beginning" and an "end" with respect to the longer one producing the phenomena known as "end-effects".

1.2 A New Machine

It is possible to make a linear version of any rotating electrical machine. To date linear machines which use the induction principle have been the most popular. They have been constructed in all the above topologies. Their popularity is due to two main factors:

- the moving secondary is supplied with current without an electrical or physical contact

- a variable frequency supply is unnecessary if the system efficiency is unimportant.

However linear synchronous and linear dc machines are beginning to be of interest despite the more complex supply conditioning required. They operate on a similar principle to rotary versions and have so far been mainly considered as an alternative to the linear induction machine in propulsion applications for high-speed ground transportation **[1.1]**. As shown in Fig. 1.2(a), the machine has a polyphase armature winding which produces the moving field and a dc excitation on the moving secondary. The excitation may also be supplied by superconducting magnets or permanent magnets installed on the moving vehicle. In order to produce time-average force, the moving field from the armature must stay in exact synchronism with the moving secondary. Hence a variable frequency supply -often provided by an inverter- is necessary.

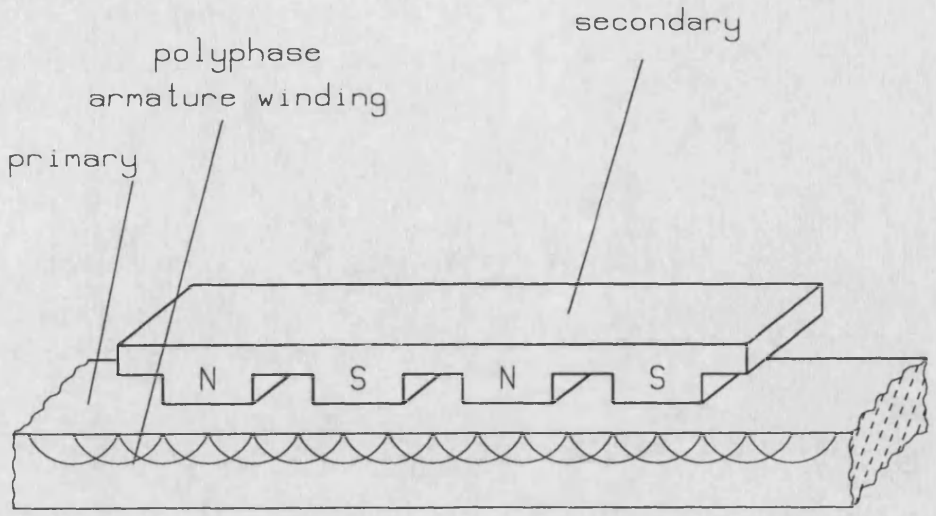

(a)

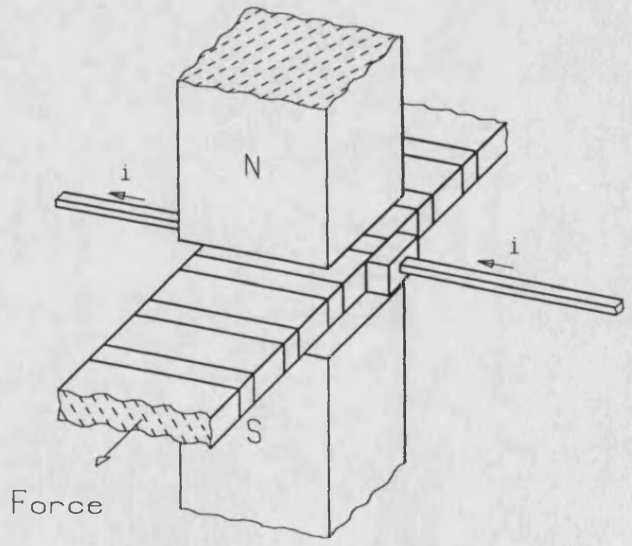

(b)

Figure 1.2 (a) Linear Synchronous Machine
(b) Linear DC Machine

The new uses for linear synchronous machines which are beginning to emerge are "long stroke actuator" applications. Their viability as a product has been enhanced by the advent of single chip inverters which can be used for their supply.

This thesis presents one new version of these machines in tubular form, which is electronically commutated using a three-phase brushless dc driver designed for rotary machines and achieves oscillatory operation with minimum additional hardware. This machine can be thought of as an alternative to the induction machine where easy control of position, velocity and stroke-rate at low supply voltage is necessary.

Chapter 2 shows the development of the prototype machine configuration. A novel skew scheme applied on the excitation magnet poles is used to eliminate the magnetic forces between the slotted armature and the excitation. This technique proves extremely useful in totally eliminating the tooth cogging forces and reducing the other unwanted cogging force, end-effect force.

Chapter 3 presents the standstill force and parameter determination of the machine using finite element (FE) techniques to be used in the system simulation. The 2D FE used was found to be adequate for the conditions investigated and particularly suitable in the analysis of the effect of step-skew. A progressive skew, however, may require a 3D field solution.

The operation of the oscillatory drive system is given in Chapter 4. Ferrite type magnet material used for the prototype machine provides an economic means of obtaining the permanent magnet excitation. For an improved machine, however, it is desirable to use a better magnet material.

The parameters gained from Chapter 3 are used in Chapter 5, in the system electrical equations which describe both the machine and the inverter supply. The system equations are simplified by a decoupling procedure which leads to a decoupled

abc machine model based on phase variables. These equations are solved by a step by step numerical method to find the dynamic performance of the drive system in an oscillatory mode. The work is verified by experimental results obtained from the practical system.

Chapter 6 presents a first order optimization process for the design of the machine.

Finally, Chapter 7 gives the conclusions drawn from the work and suggestions for further design and analysis.

CHAPTER 2

THE DESIGN AND CONSTRUCTION OF THE TUBULAR PERMANENT MAGNET MACHINE

2.1 Introduction

Most of the tubular machines which have been constructed to date have used the induction principle. However, because of the increase in magnetising current with size, the performance of small induction machines is limited. This is because the magnetising current which gives the excitation is inversely proportional to (pole-pitch)^2 and hence the force producing rotor current becomes a smaller fraction of the input current as the size of an induction machine is reduced. The limitation can be overcome by using machines with permanent magnet excitation. These must be electronically commutated in the brushless form.

Permanent magnets are used in an increasing range of electromechanical applications. This is mainly because of the rapidly improving magnetic characteristics of new permanent magnet materials and their increased availability and cost-effectiveness. They are used in a variety of magnetic configurations. Most of these configurations have been of the rotary type in the form of synchronous and brushless dc machines and are supplied by power electronic converters. These machines offer several advantages over their conventional counterparts, such as no need for brushes and a commutator, no excitation power losses and greater overall simplicity. These advantages lead to high efficiency machines.

Relatively few applications involving linear machines with permanent magnet excitation have appeared in the literature. The majority of these designs fall into two categories: synchronous and pulse machines. Most of the synchronous machine work is devoted to ground transportation applications where the flat type is of interest

[2.1-2.7]. These machines have permanent magnets in place of coils as excitation and apply either self-synchronism with self-starting capabilities or use variable frequency supplies. The pulse type of machines, on the other hand, have one or more coils which are switched on alternately and are power electronically operated [2.8-2.12]. These machines are being considered for actuator, artificial heart pump drives and automatic transfer system applications. The brushless dc form has also been applied [2.13].

Three tubular machines with permanent magnets are known. Two of these act as electromechanical solenoids [2.14-2.15]. The third is in the form of a brushless dc machine and was described recently [2.16-2.17]. This has a different magnetic circuit arrangement to the one used for the practical model described in this thesis and the work is concerned only with measurements.

2.2 Tubular Machine Construction

Tubular machine geometry can be best explained by subjecting rotary machine geometry to topological changes, following Laithwaite on induction machines [2.18]. The usual form of rotary brushless machine is shown in Figure 2.1. This has a permanent magnet rotor and a three phase stationary armature winding. Commonly, Hall effect sensors are used to detect rotor position and thus control a 3-phase inverter which in turn supplies the armature winding.

If the rotor and the stator of the machine shown in Figure 2.1 is cut along a radial line, AB, and unrolled, a flat linear machine is obtained. This is shown in end view in Figure 2.2 and in developed form in Figure 2.3. If this flat linear machine is now rolled up so that lines AB and CD join, the tubular form emerges as shown in Figure 2.4. The magnets become radially magnetised cylindrical shells and the armature coils simple circles without end-turns.

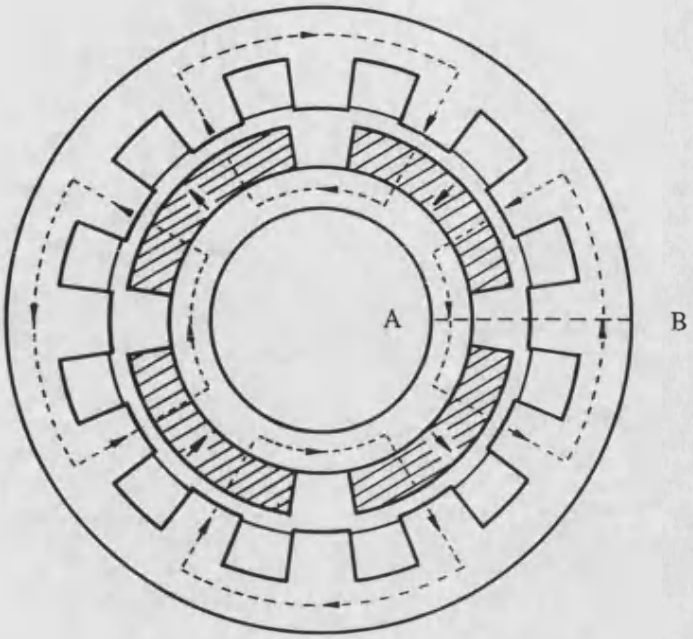

Figure 2.1 A Rotary Brushless Permanent Magnet Machine

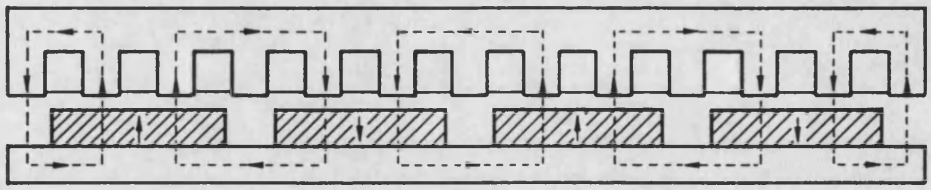

Figure 2.2 Flat Linear Permanent Magnet Machine

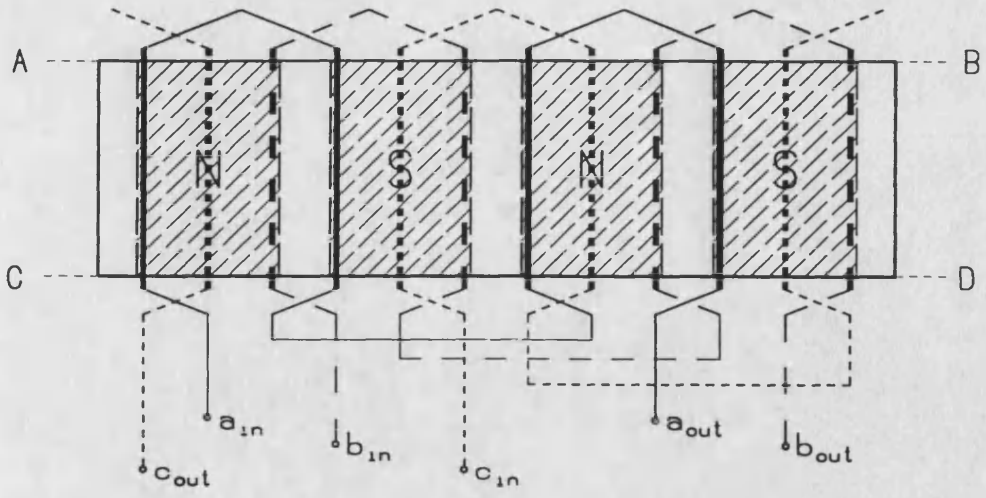

Figure 2.3 Developed Form of Flat Permanent Magnet Machine

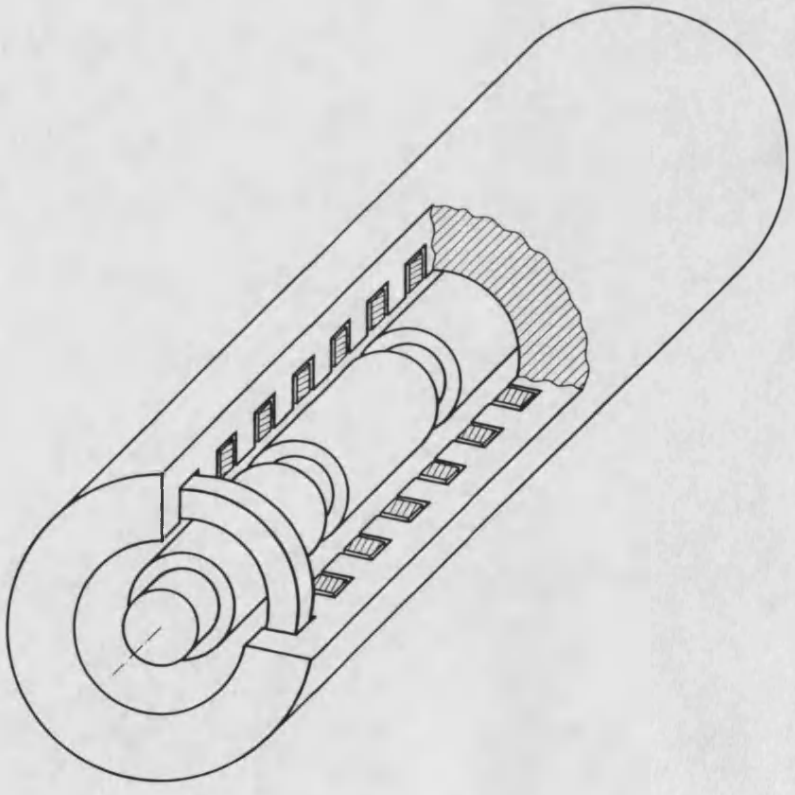

Figure 2.4 Tubular Permanent Magnet Machine

2.3 Practical Design Considerations

The above transformation, however, is not quite enough to construct a practical machine. There are two difficulties that must be overcome. First, a lamination system must be devised which will allow for both axial and radial flux paths and prevent any circumferential flux in the machine. Secondly, a method for armature coil insertion must be conceived. One solution to these two limitations is shown in Figure 2.5. Here the machine is transformed into a four blocked structure, each block of which is formed from an axially laminated stack transversely shaped into an arc of a cylinder. The laminations have open slots so that the armature coils can be pre-positioned on a mandrel and the blocks pushed over them.

Although this modification means that the circumferential continuity of the actual tubular structure is abandoned, it will be shown later, in terms of magnetic modelling, that it does not introduce any appreciable difference in the magnetic circuit. The only flux in the armature lies in axial planes and this is unrestricted by the geometrical adaptation.

The excitation of the machine is also modified in order to eliminate unwanted tooth cogging forces due to the armature teeth and permanent magnet field. As will be shown later, the period of this force is one slot-pitch and it can be eliminated by either an armature slot skew of one slot-pitch for the whole circumference or by using a corresponding skew on the permanent magnet rings of the machine of Figure 2.4.

Magnet skew is the best of these two options so as not to affect the stator coil insertion explained above. The excitation permanent magnet poles are step skewed by using three 120 ° span magnet segments as shown in Figure 2.5 and in Figure 2.6 in developed form. This is a good approximation to the ideal progressive skew and was made necessary by the lack of skewed magnet rings.

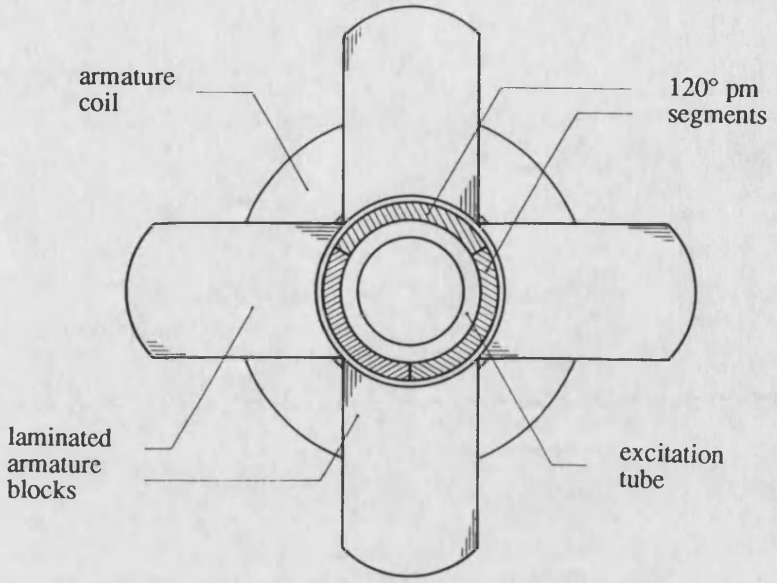

Figure 2.5 End View of the Practical Machine

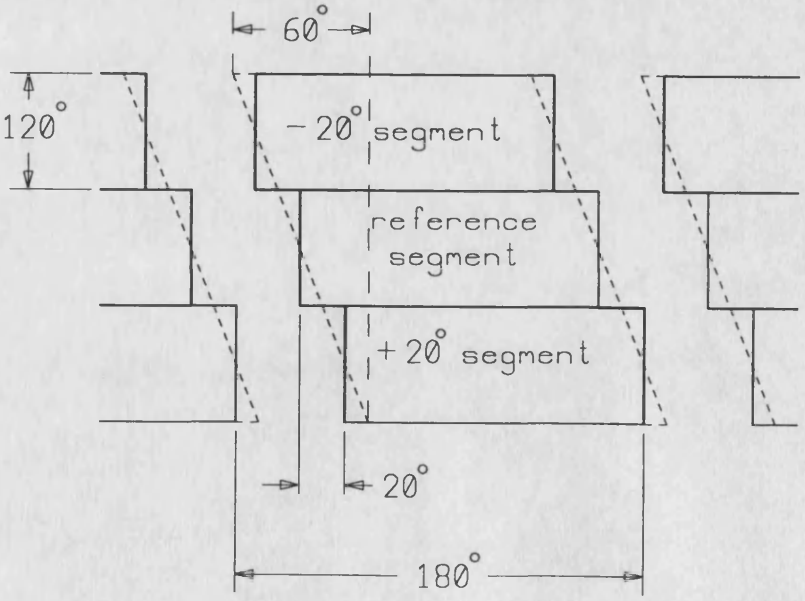

Figure 2.6 Developed View of Permanent Magnet Placement

It will be shown later that one-slot skew not only eliminates the tooth cogging forces but also has a harmonic reduction effect for the other two standstill forces that exist between the excitation and the armature. These are the electromagnetic force and the end-effect force. This latter force being due to the finite length of the primary. Skew also has a smoothing effect on the flux linkages of the armature phases and thus on the phase back emfs.

2.3.1 The Choice of Permanent Magnet Material

The need for better permanent magnets for use in electromechanical devices has given rise to developing new materials and improvements in the magnetic characteristics of the existing ones. As a result, *Samarium-Cobalt* and, more recently, *Neodymium-Iron-Boron* alloy materials have been developed. These new materials have influenced the design and performance of permanent magnet machines substantially, reducing their size and improving their performance. Figure 2.7 illustrates the historical development of the maximum energy product of commercial permanent magnets **[2.19]**. The impact of both samarium-cobalt and neodymium-iron-boron materials has been effected by their high price due to their using rare-earth type materials. In addition they both have thermal limitations with samarium cobalt being better than neodymium-iron-boron. Figure 2.8 shows the characteristics of the most popular magnet materials.

Ferrite material, due to its easy availability, was chosen for the practical model built for this project despite the reduced flux density that it provides. Philips made strontium ferrite type material was used **[2.20]**. The demagnetisation curve of this material, Ferroxdure 330, and its physical and magnetic properties are given in Appendix A.

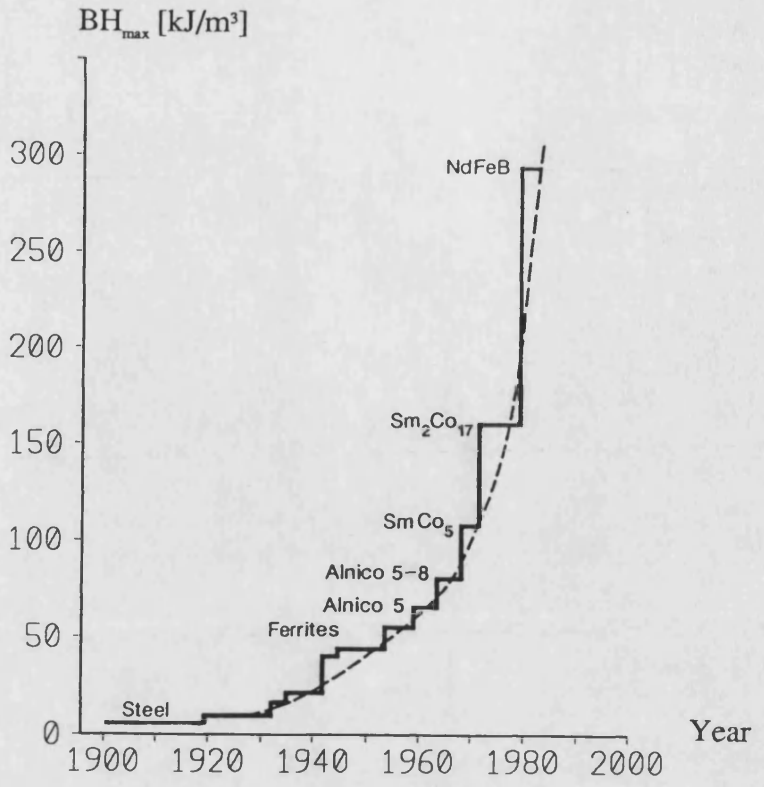

Figure 2.7 Development of the Permanent Magnet Materials

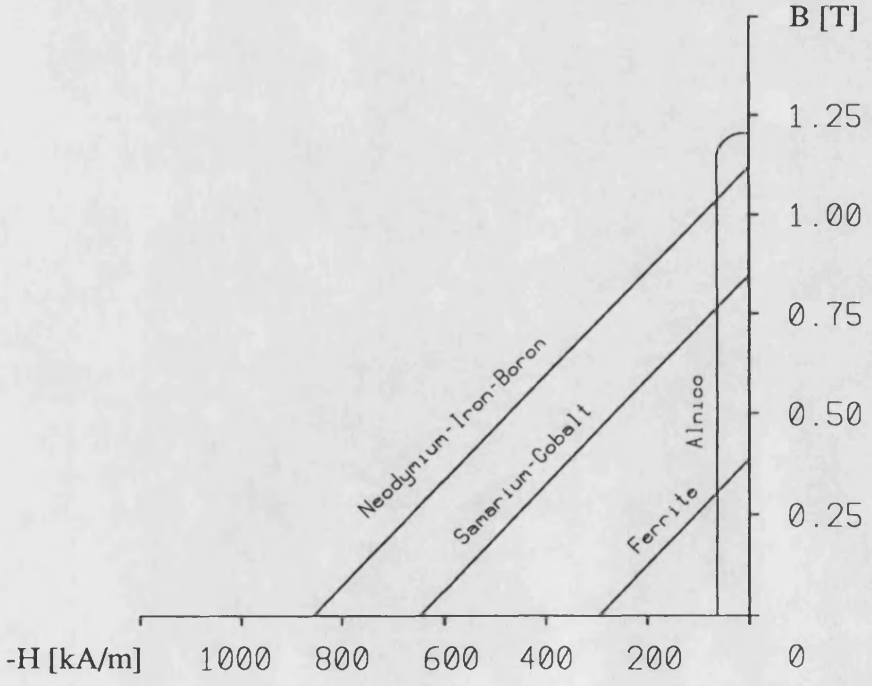

Figure 2.8 Demagnetisation Curves of the Permanent Magnet Materials

2.4 A Practical Model

Using the above considerations a short primary prototype machine has been constructed in order to have an insight into the end-effects as well as other characteristics [Figure 2.9]. It has a two-pole winding on the stationary armature and four poles on the moving excitation. The armature winding has one coil per pole and phase for simplicity [Figure 2.10]. Ready-made laminations were used to construct the armature blocks.

The permanent magnet segments were magnetised after assembly, i.e. after they were placed on the excitation. This was done by using a specially built two-pole electromagnet [please see Appendix B]. One pair of unlike segments of adjacent poles were magnetised at a time. The action was, therefore, repeated six times to magnetise all four armature poles. Sufficient mmf was provided to saturate the magnets fully.

Table 2.1 gives the specifications of the prototype machine. Figure 2.11 shows three views of the complete machine with dimensions. It also shows the Hall effect position sensor placements.

2.5 Conclusions

The construction of a prototype design of the tubular permanent magnet machine has been described. A skew scheme which can be applied to other permanent magnet machines has been given. This is more practical compared to the more familiar slot skew in terms of both construction and analysis.

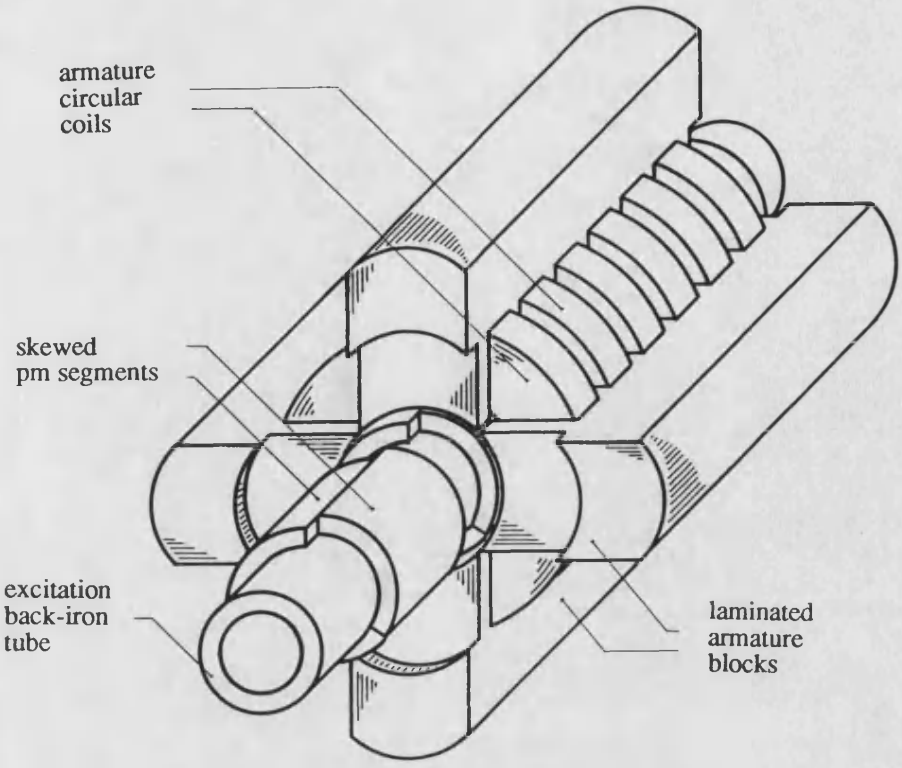

Figure 2.9 Construction of the Practical Tubular Machine

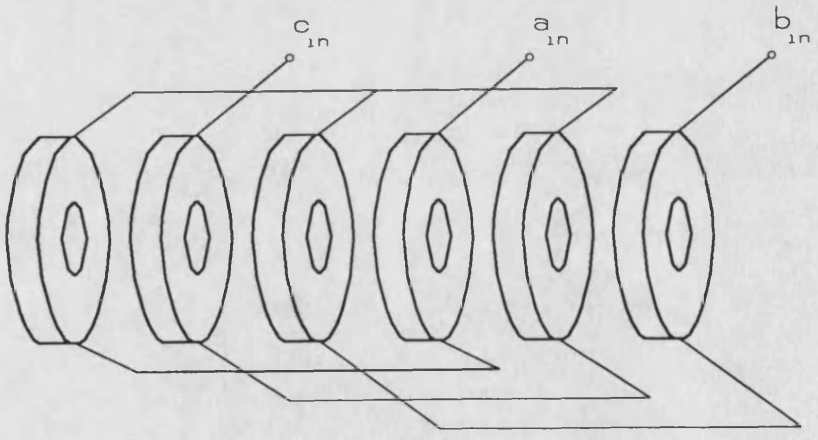

Figure 2.10 Armature Winding Connection Diagram

Table 2.1

Prototype machine specifications

Armature	
Pole-pitch	: 56.7 mm
Slot-pitch	: 18.9 mm
Slot-width	: 12.8 mm
Tooth-width	: 6.1 mm
Material	: laminated steel
Number of poles	: 2
Winding	: 3-phase, star-connected
Number of coils per pole and phase	: 1
Number of turns in a coil	: 150
Wire diameter of the winding	: 1.25 mm
Air-gap	
Length	: 1.5 mm
Effective length	: 2.6 mm
Effective flux density	: 0.22 T
Excitation	
Tube material	: bright-mild steel
Number of poles	: 4
Travel length	: 114 mm
Total weight	: 7.662 kg
Excitation permanent magnet poles	
Material	: Philips Ferroxdure 330
Remanence	: 0.37 T
Coercivity	: -240 kA/m
Radial thickness	: 7.1 mm
Axial length	: 39.3 mm
Inside diameter	: 58 mm

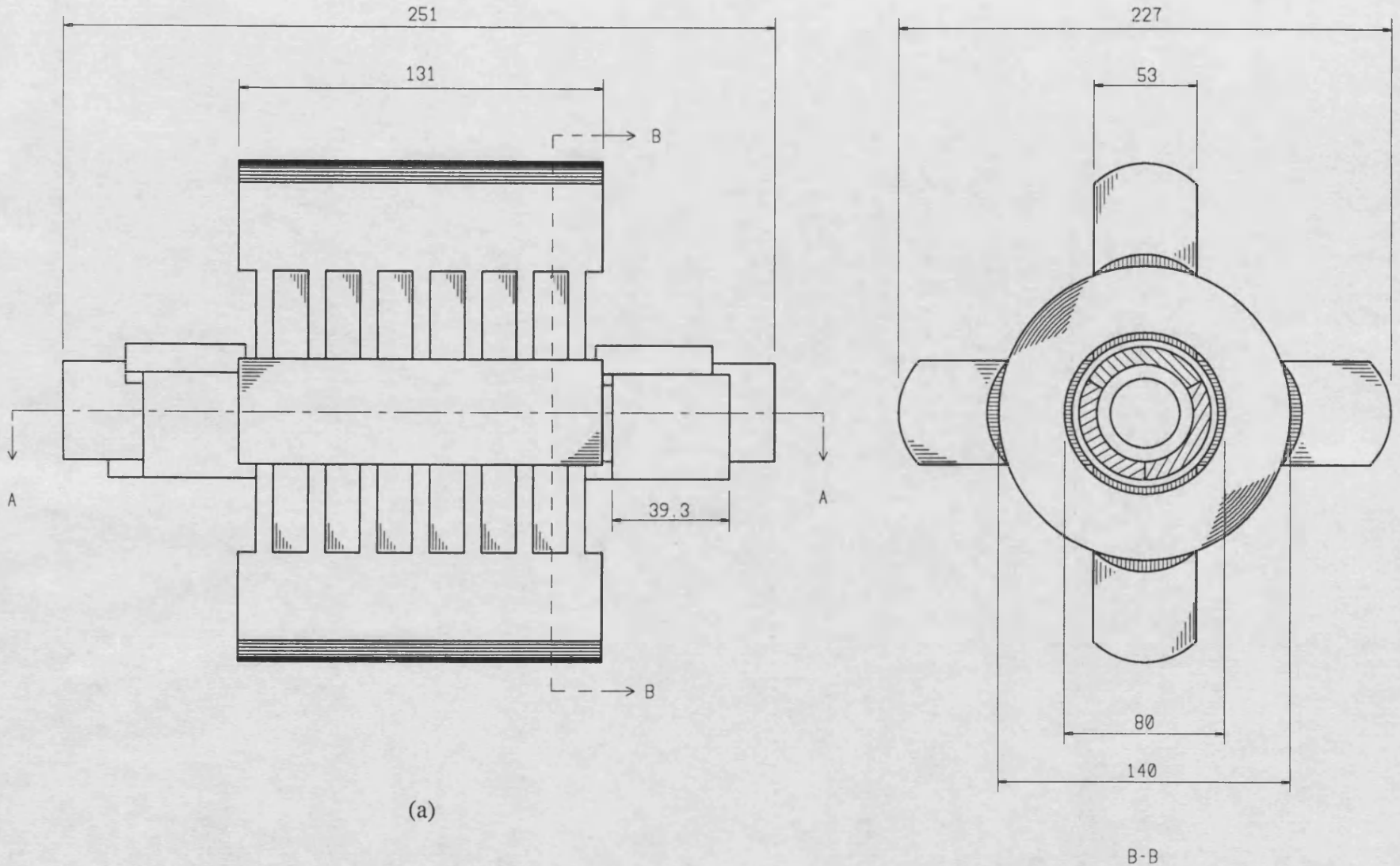

Figure 2.11 Three Views of the Prototype Tubular Machine (Dimensions in mm)

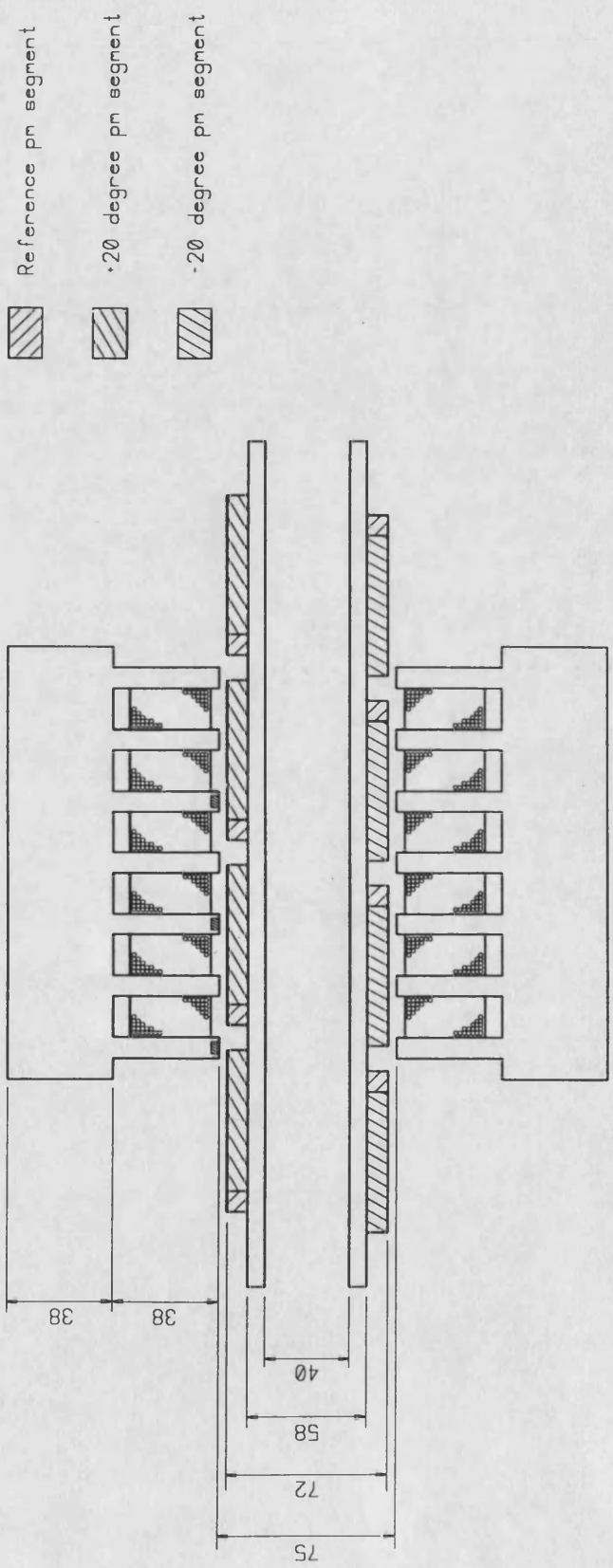
Reference pm segment
+20 degree pm segment
-20 degree pm segment
38
38
40
58
72
75
A-A

(c)

CHAPTER 3
CALCULATION OF MACHINE PARAMETERS AND STANDSTILL FORCES BY MEANS OF FINITE ELEMENT METHODS

3.1 Introduction

The brushless tubular motor operates by means of an electromechanical energy conversion process which takes place in the electromagnetic fields of the machine. The variables that define this process are important in terms of design and performance of the machine.

Moreover, as will be shown later the machine can electrically be represented by a classical three phase synchronous machine model. In this model the interaction between the armature and the excitation is represented by means of phase emfs which are induced in the fixed armature winding by the moving permanent magnets of the excitation. The other components in this model comprise inductances and resistances. The electrical system matrix equation is given below:

$$[V] = [R][i] + \frac{d}{dt}\{[L][i]\} + \frac{d}{dx}[\lambda] \cdot v \qquad \ldots(3.1)$$

where x is the excitation displacement, λ phase flux linkages and v the excitation velocity. The last term of the equation in effect represents the back emf of the phases.

Finite Element (FE) methods were used to calculate the parameters of the above equation using a two dimensional (2D) FE package. This equation was later used in a dynamic simulation program to compute the system electrical and mechanical performances.

The 2D-FE package used is introduced in the next section.

3.2 The 2D-FE Package

The program is a computer based FE package for solving electromagnetic problems which can be described by the two dimensional equations of Laplace or Poisson.

It consists of two parts. The first part is the pre- and post-processor which is used to define problem geometry and data and to evaluate results. The second part consists of analysis programs for solving steady-state, ac and transient problems. The package has both cartesian and axisymmetric options. The problem is broken into regions each of which is of one type of material. Inside these regions mesh generation is automatic.

3.3 Finite Element Models

Three axisymmetrical FE models were used. The first used one pole and was employed to calculate parameters in the case of an infinite machine by appropriate choice of boundary conditions. The second and the third models had the actual geometry of the machine and were used to calculate the effects of the finite length of the machine.

In all of the three models the armature of the machine was modelled as a complete shell which assumed no leakage flux out of the armature for the armature length. The armature material was defined magnetically nonlinear using the magnetisation curve given in Appendix C. However, because of the low current loadings magnetic saturation was not encountered.

The excitation cannot be modelled strictly by a 2D method because of the skew. However in each of the models permanent magnets were first modelled with a ring representing the reference magnet and an approximation to the skewed results was obtained by adding together suitably phase shifted versions. The *BH* curve of the permanent magnet material was defined nonlinearly using the second and the third quadrant of the curve and is given in Appendix A.

The models were created in a special manner in order to easily obtain results at different positions of the excitation with respect to the armature over about two pole pitches of travel. This made it possible to easily modify the permanent magnet regions for new displacement values.

The FE models are outlined in the following sections.

3.3.1 1-Pole FE Model

This model has one pole as shown in Figure 3.1 and uses periodicity boundary conditions on the boundaries that are at right angles to the axis of symmetry thus assuming an infinitely long machine. It was used to calculate:

- the magnetic tooth cogging forces due to the permanent magnet, fields and armature teeth
- the electromagnetic thrust force due to armature currents,
- armature phase flux linkages without end-effects due to the permanent magnet fields.

The 1-pole model has about 2700 triangular elements.

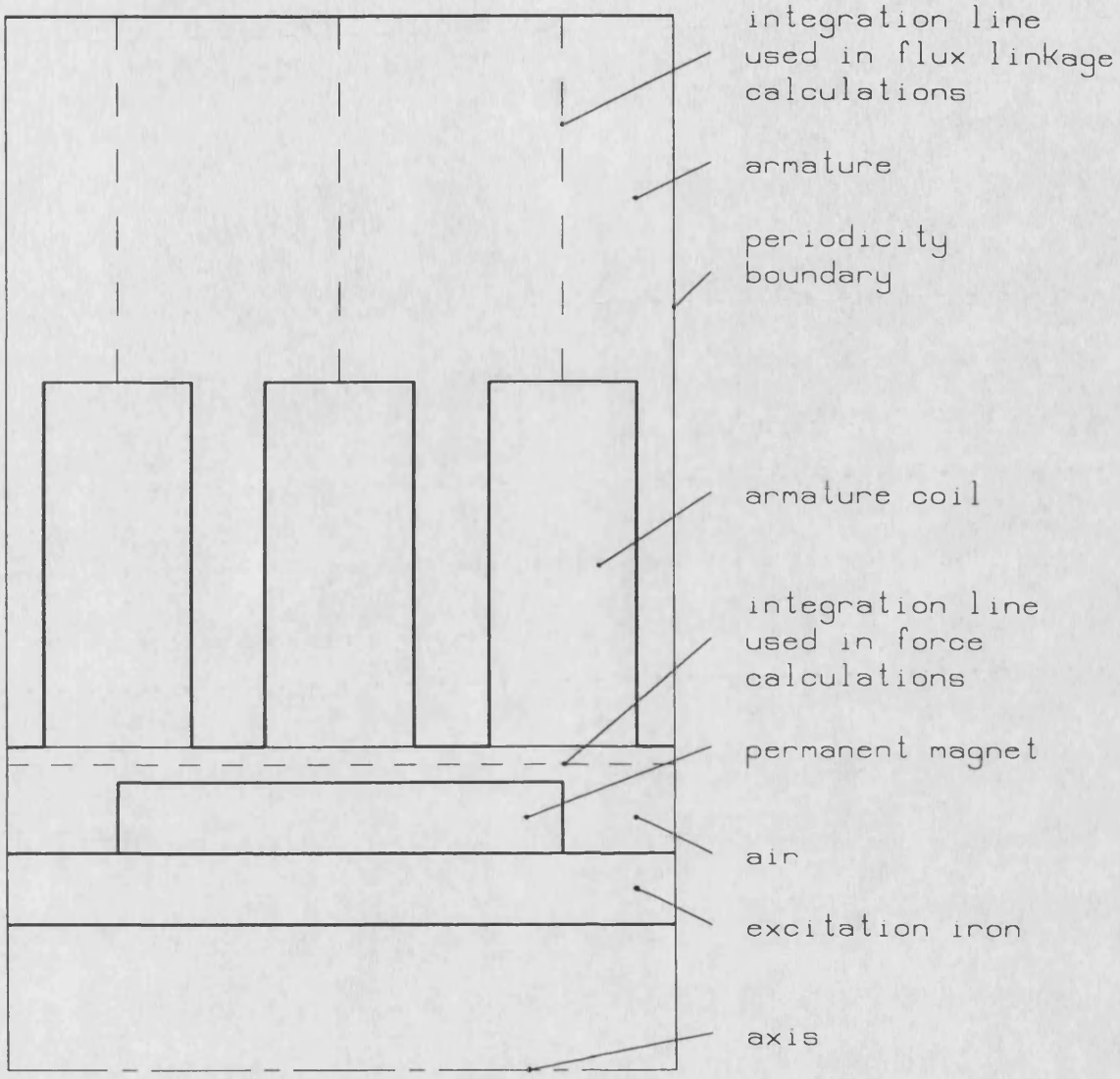

Figure 3.1 1-Pole Finite Element Model

3.3.2 Full FE Model

This is the actual model of the machine having two poles on the armature and four on the excitation and is given in Figure 3.2. It was used to calculate:

- the end-effect force due to the finite length of the armature,
- armature coil and phase flux linkages due to the permanent magnet fields taking into account the end-effects.

5500 elements were used in this model.

3.3.3 Full FE Model Without Permanent Magnets

This model also has the actual 2-pole armature but has no permanent magnets on the excitation [Fig. 3.3]. It was used to calculate the armature field for different sets of excited coils and hence the armature coil and phase self and mutual inductances. Elimination of permanent magnets from the excitation does not affect the armature field due to the near unity permeability of the permanent magnet material. However it usefully reduces the number of models to calculate each inductance as will be explained later. It also reduces the computer run time.

3.4 Standstill Forces

As most applications for actuators involve very low speeds the standstill force performance of the system is of most interest. All the forces were calculated using Maxwell stresses. The line integral was taken along the mid air-gap for the full length of the models [Fig. 3.1]. The calculations were performed nonlinearly in order to take into account the armature reaction effects.

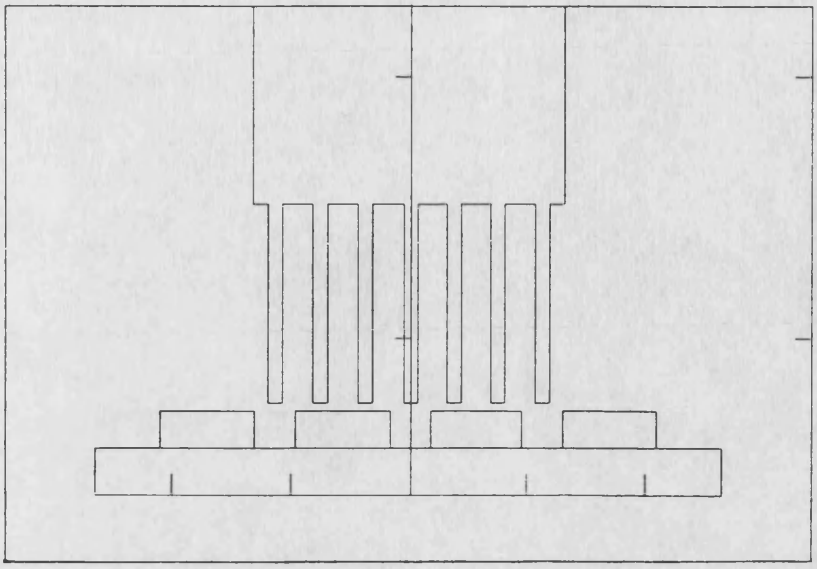

Figure 3.2 Full Finite Element Model

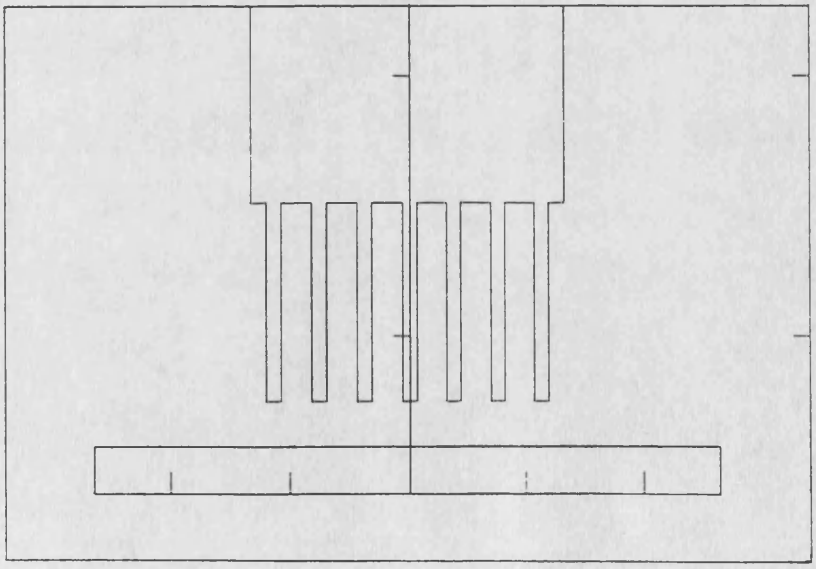

Figure 3.3 Full Finite Element Model Without Permanent Magnets

The results of an investigation are presented in the following sections. Since normal forces are cancelled automatically in tubular machines only axial thrust forces were studied [3.1].

3.4.1 Tooth Cogging Forces

An undesired force exists in most electrical machines namely tooth cogging force. It is a result of the magnetic attraction between teeth of one member and the field (or teeth) of the other. Tooth cogging force exists in permanent magnet machines when there is no current in any of the coils of the machine windings. Figure 3.4 shows a typical mesh used for 1-pole models. Fig. 3.5 illustrates the permanent magnet field distribution on no-load of one of the 1-pole models used to calculate the tooth cogging force. This corresponds to 10 ° displacement of the reference permanent magnet segment. It will be observed that the excitation is forced by the permanent magnet field to move to the right (or armature to the left) so that the field aligns itself symmetrically with respect to the armature teeth [please see Appendix D for displacement values].

The FE results for the three displaced permanent magnet segments are shown in Figure 3.6 along with the experimental results. It can be observed that the space period of the force from the reference segment is 60 ° or one slot pitch. Hence adding in the forces due to the other two segments, +20 ° and -20 °, a virtual one slot skew, gives a practically zero resultant. This predicted lack of cogging force is confirmed by the practical model and is also plotted on the graph.

It will be shown later that one slot skew also eliminates the harmonics of the coil and phase flux linkages; and also harmonics of the electromagnetic thrust and magnetic end-effect forces.

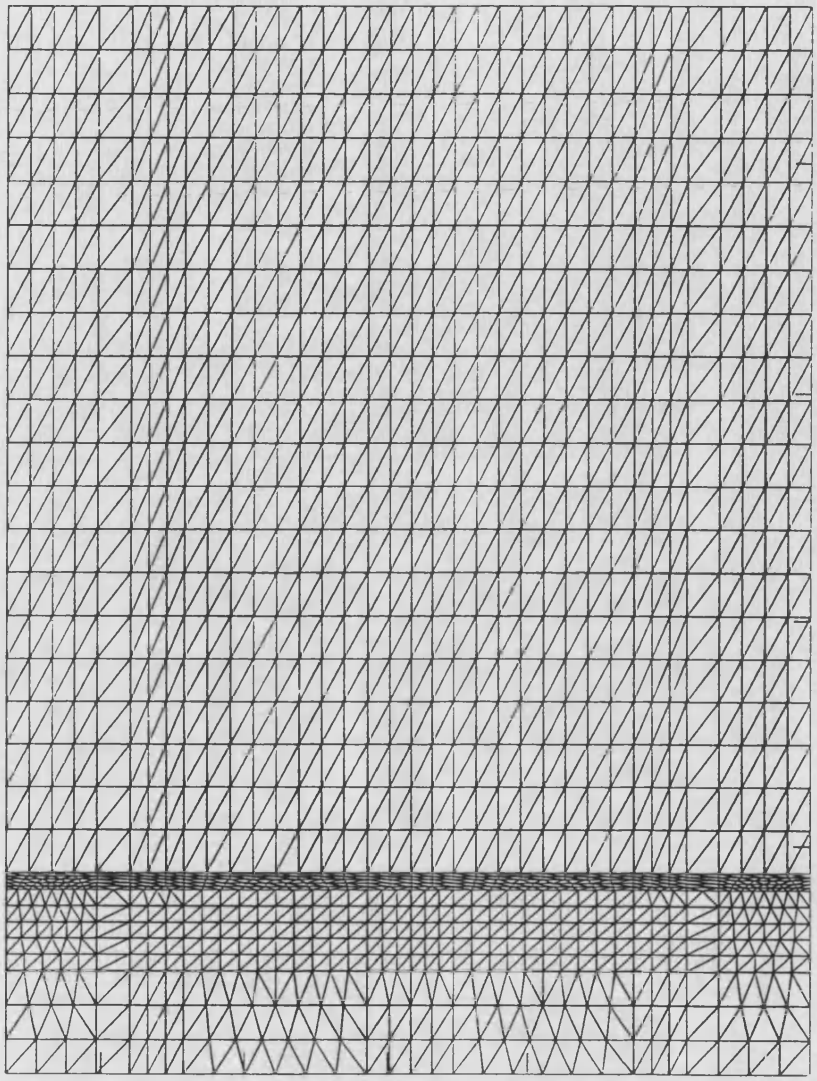

Figure 3.4 Typical Mesh Used for 1-Pole FE Model

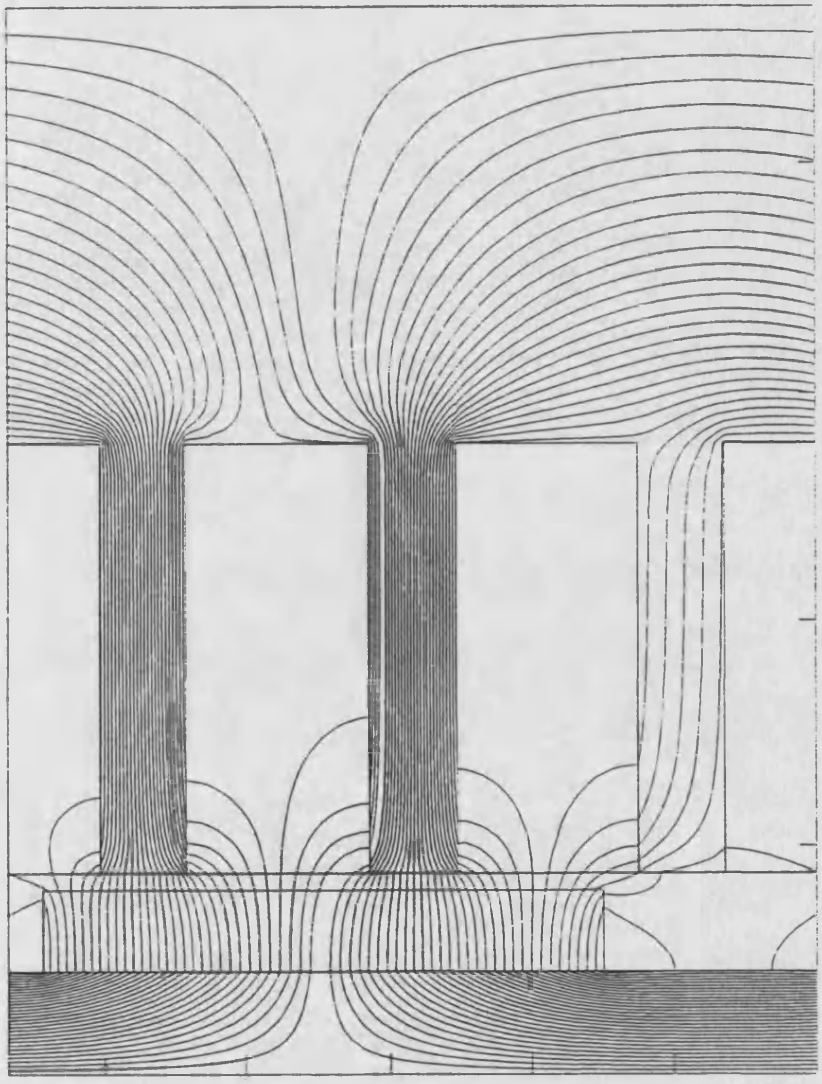

Figure 3.5 Field Distribution on No-Load in a 1-Pole Model

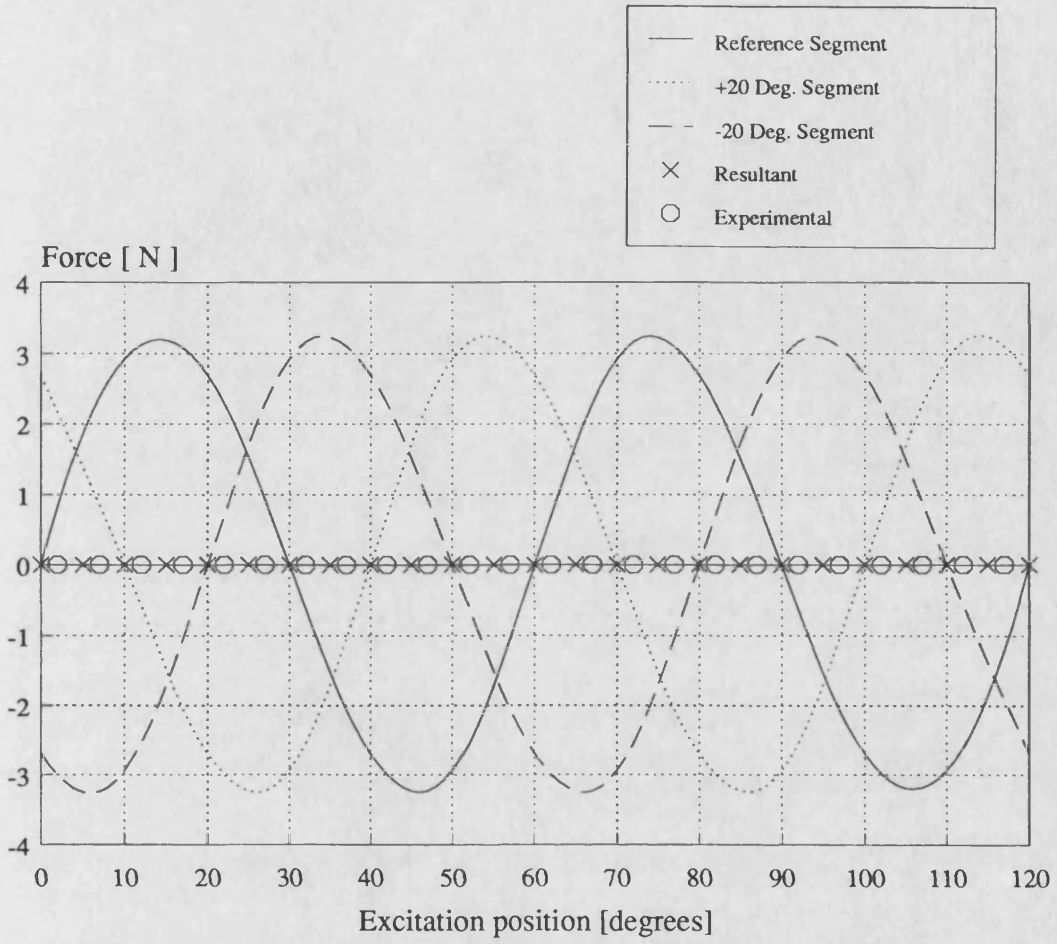

Figure 3.6 FE Calculated Tooth-Cogging Forces due to Three Permanent Magnet Segments and Resultant Calculated and Experimental Force for One-Slot Skew

3.4.2 End Effect Force

Using full FE model the magnetic force was calculated at zero armature currents as shown in Figure 3.7. This force is due to the finite length of the armature and includes the tooth cogging force i.e. the end-effect force which would exist in the case of no skew. When, however, one-slot skew (20 ° shift between permanent magnet segments) is applied to this force the solid curve of Figure 3.8 is obtained which represents the end-effect force only. A comparison of Figs. 3.7 and 3.8 will reveal the reduction effect of the skew on this undesired force. The magnetic force which was measured with zero armature current is also shown on Fig. 3.8. The correlation is good between the calculated and measured results confirming that this force can be predicted using the full FE model. The space period of the force is about 180 ° or one pole-pitch. It will be shown later in this chapter that the end-effect force can be reduced further by applying the right amount of skew while retaining the zero resultant tooth-cogging force.

This calculated end-effect force will be used as a forcing function in the system dynamic equations later in Chapter 5.

Zero displacement is defined as the position when the excitation and the armature symmetry lines coincide. Increasing displacement is taken to be as the excitation moves in right hand direction [please see Appendix D].

3.4.3 Electromagnetic Thrust Force

The electromagnetic thrust force was calculated at an instant in time of the supply cycle. As will be explained later (Chapter 4) two phases of the three-phase star connected armature winding are on at a time. The currents of these two phases are of equal magnitude and of opposite sign. Using the 1-pole model for an instant

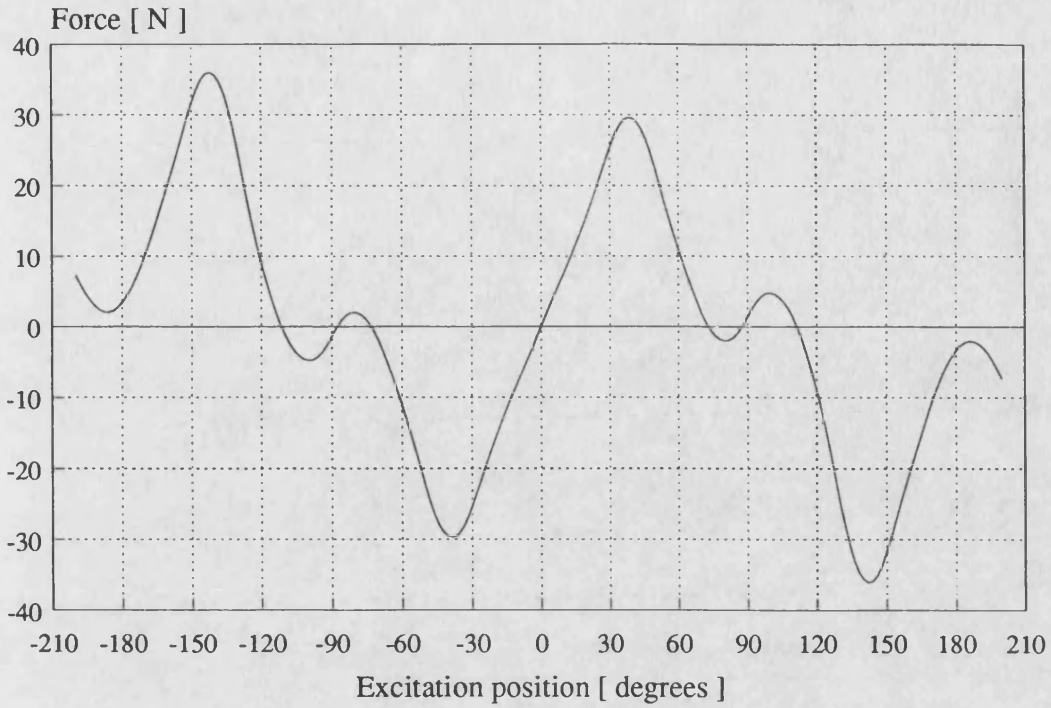

Figure 3.7 FE Calculated End-Effect Force with No Skew

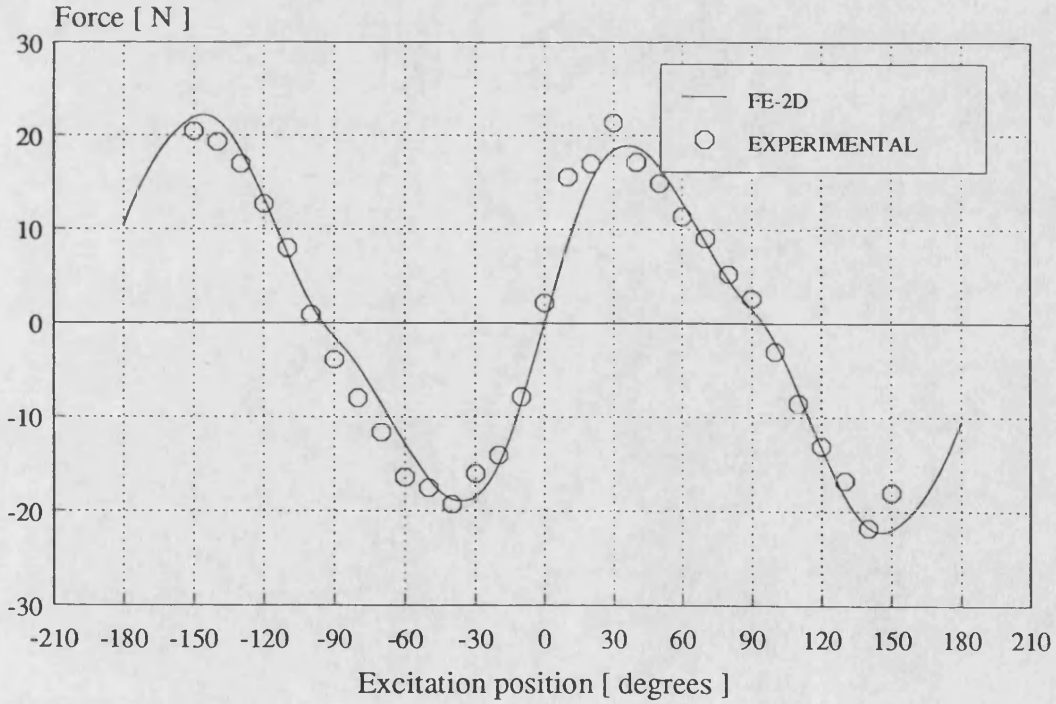

Figure 3.8 End-Effect Force with One-Slot Skew

($i_a=I$, $i_b=-I$, $i_c=0$) at a number of current magnitudes and for different displacements, space profiles of force were calculated [please see Appendix D for positive force and displacement and the instant taken for currents]. Figure 3.9 shows one of them for 1 A phase currents. These force profiles include the tooth cogging force which is explained in Section 3.4.1 and would exist in a machine with no skew. The force at three fixed excitation positions is also shown plotted against armature current magnitude in Figure 3.10.

The electromagnetic thrust force for the skewed case can be calculated by adding together forces from three displaced permanent magnet segments. The calculated resultant electromagnetic force with a half-slot skew (10 ° shift between permanent magnet segments) is given in Figure 3.11. Resultant force for a one-slot skew (20 ° between segments) is shown by a solid line in Figures 3.12 and 3.13. Inspection of Figures 3.9, 3.11 and 3.12 shows the harmonic elimination effect produced by skewing.

Measured values at the same instant of time are also shown on the same figures. These values have been corrected for end-effect force by subtracting it from the total measured value.

Figure 3.12 reveals that maximum electromagnetic force exists at 90 ° displacement which corresponds to 90 ° phase shift between excitation and armature mmfs. This quantity is known as the *torque angle* , δ , in rotary machine terminology and may be named the *force angle* for linear machines. The average machine thrust force can therefore be maximised by keeping the force angle around 90 °. This will be dealt with in Chapter 4.

The measured and calculated electromagnetic forces are in close agreement. This confirms that magnetic and electromagnetic forces can be calculated using 1-pole and full FE models taking these forces separately.

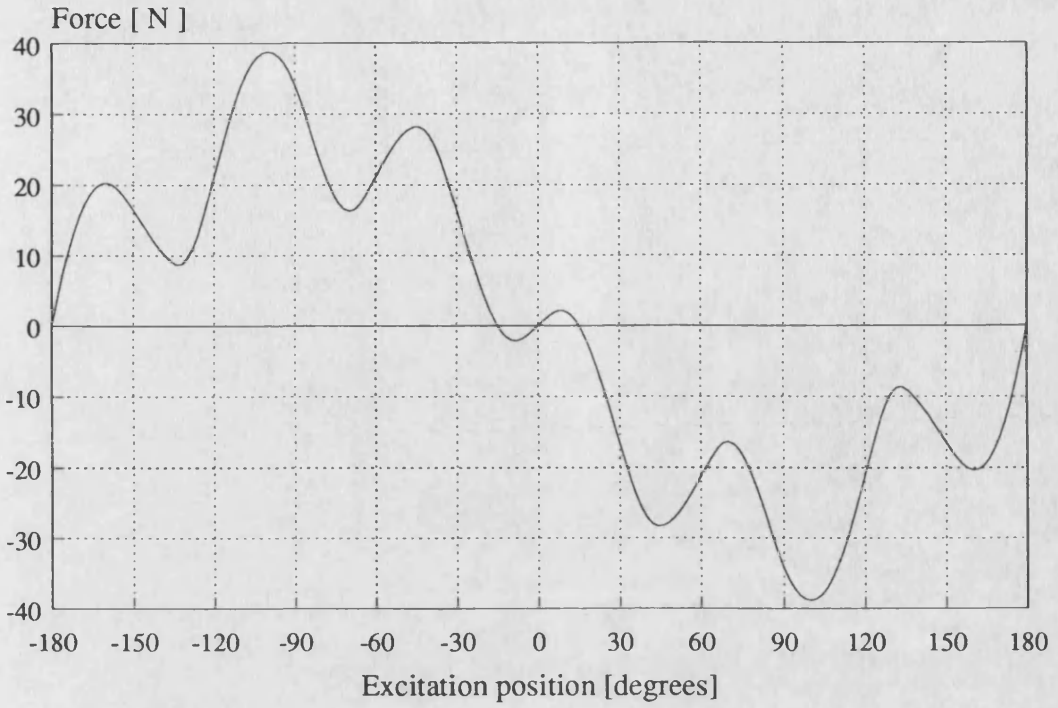

Figure 3.9 FE Calculated Electromagnetic Force at 1 A Phase Currents with No Skew

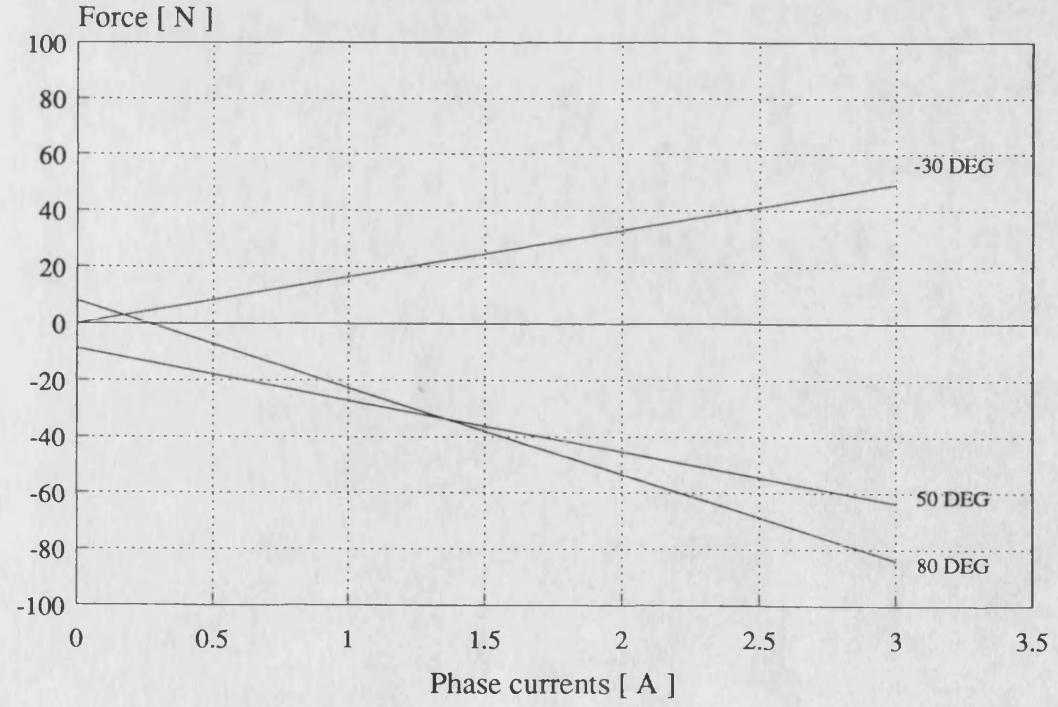

Figure 3.10 FE Calculated Electromagnetic Force at Fixed Excitation Positions with No Skew

Figure 3.11 FE Calculated Electromagnetic Force at 1 A Phase Currents with Half-Slot Skew

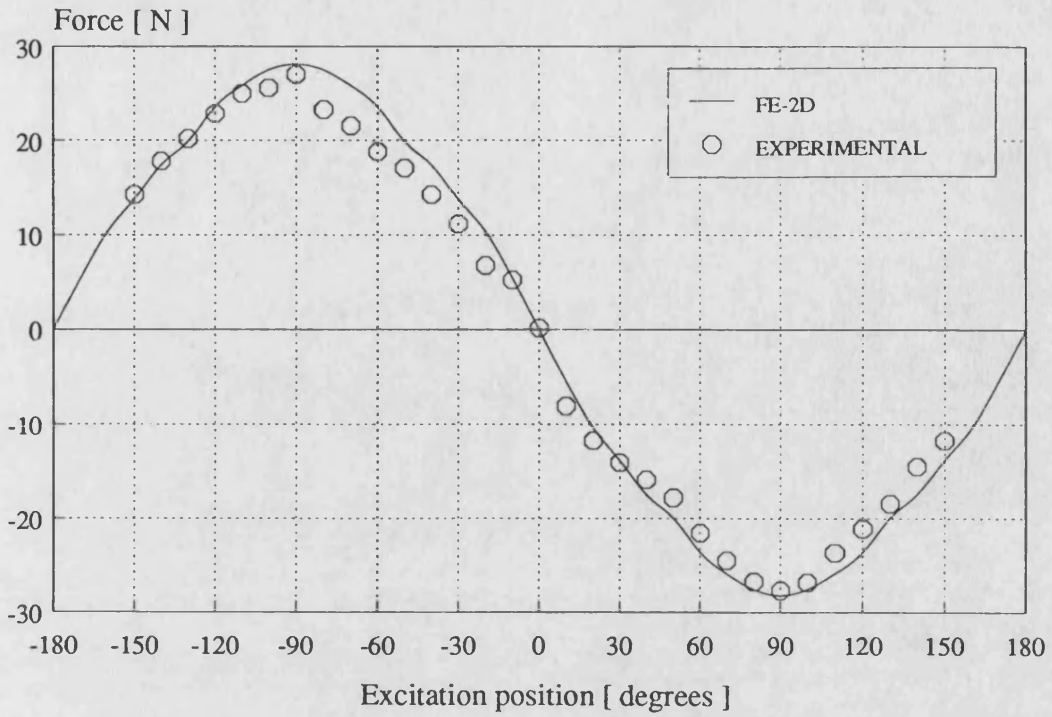

Figure 3.12 Electromagnetic Force at 1 A Phase Currents with One-Slot Skew

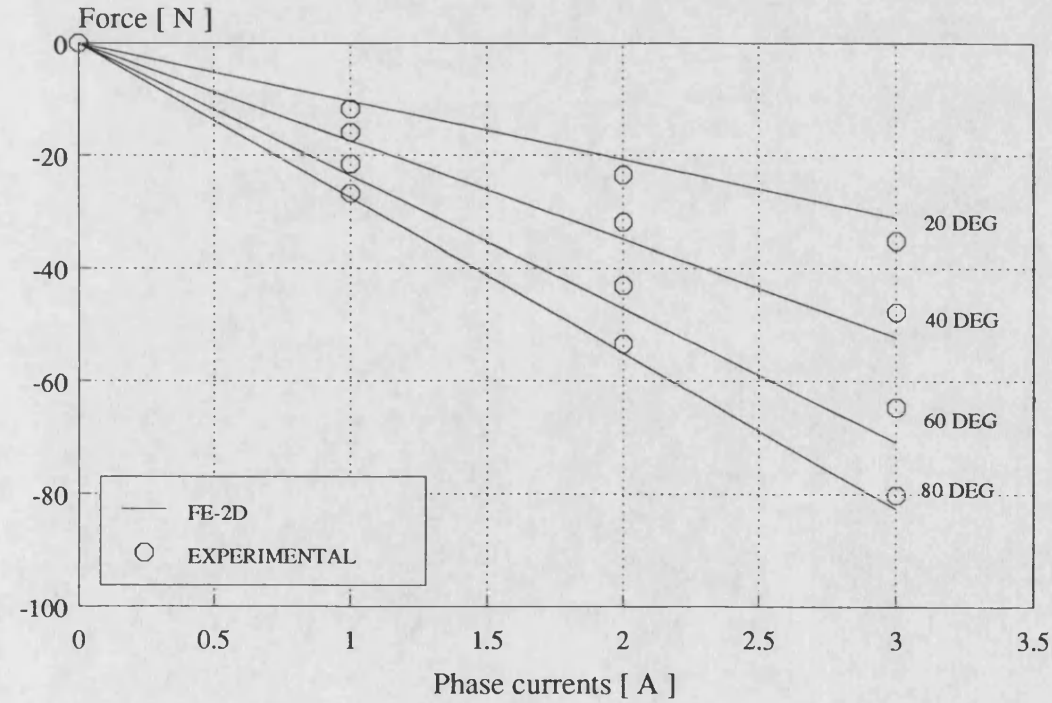

Figure 3.13 Electromagnetic Force at Fixed Excitation Positions with One-Slot Skew

3.4.4 The Effect of Magnet Skewing on Standstill Forces

It was shown earlier that magnet skewing can successfully eliminate the tooth-cogging forces given that the right amount of skew is applied. One-slot skew (1/3 slot-pitch i.e. 20 ° shift between permanent magnet segments) applied on the prototype machine eliminated this force completely.

Magnet skewing may also be used to minimise the other unwanted magnetic force, end-effect force, while keeping the tooth-cogging force zero. It may be observed from Fig. 3.6 that zero resultant tooth cogging can also be achieved with two-slot skew (2/3 slot-pitch i.e. 40 ° shift), four-slot skew (4/3 slot-pitch i.e. 80 ° shift) etc. 2D calculated resultant end-effect forces are given in Fig. 3.14 with no, one-slot, two-slot and four-slot skew cases for the positive excitation displacement. It may be seen that up to two-slot skew the maximum value of the force is reduced by about 10 N as the skew amount is increased. However, for four-slot skew there is no improvement and the waveform is distorted. Therefore two-slot skew gives the minimum resultant end-effect force while eliminating the tooth-cogging force.

As skewing has an impact on the wanted electromagnetic force as well as the above end-effect force it has also to be considered in order that a constructive conclusion can be drawn. It was shown in Figs. 3.9, 3.11 and 3.12 that skewing has a smoothing effect on the electromagnetic force as well as the other forces. With one-slot skew the electromagnetic force profile is nearly a sine-wave. Fig. 3.15 gives the calculated electromagnetic force for no-skew and when the amount of skew is one, two and four slots. It will be observed that in the one-slot and two-slot cases the force profiles are good but that the maximum force is reduced by about 20 % in the two-slot skew case. This is of course because of the lower forces contributed from the + and - shifted permanent magnet segments. The electromagnetic force is further reduced and distorted with four-slot skew.

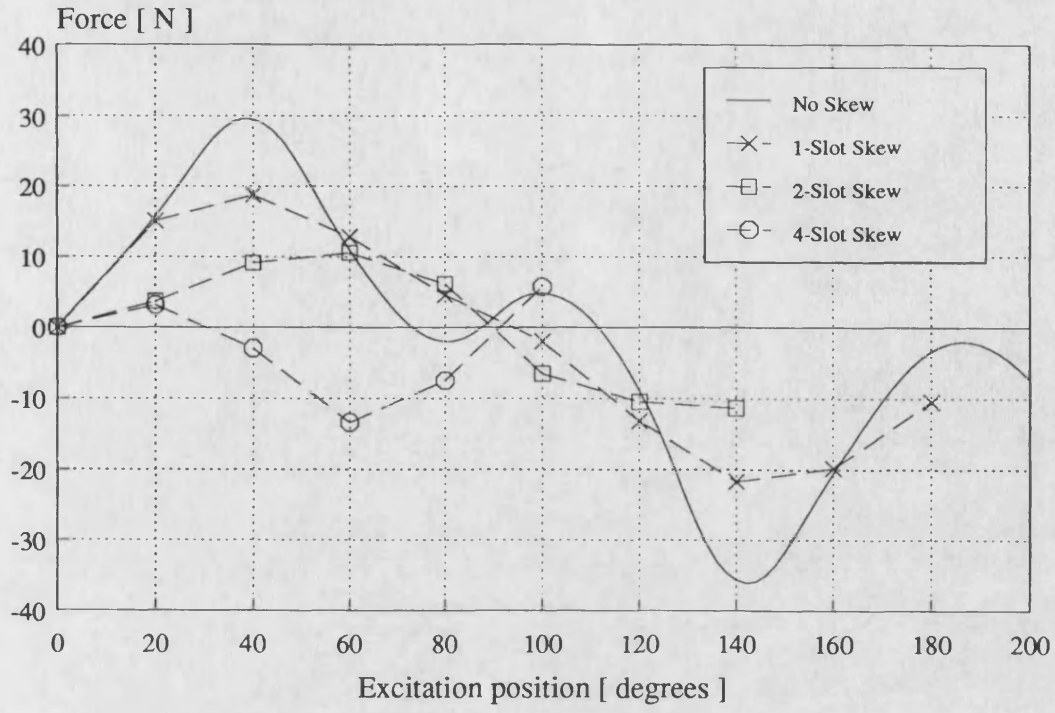

Figure 3.14 Calculated End-Effect Force for Different Skew Cases

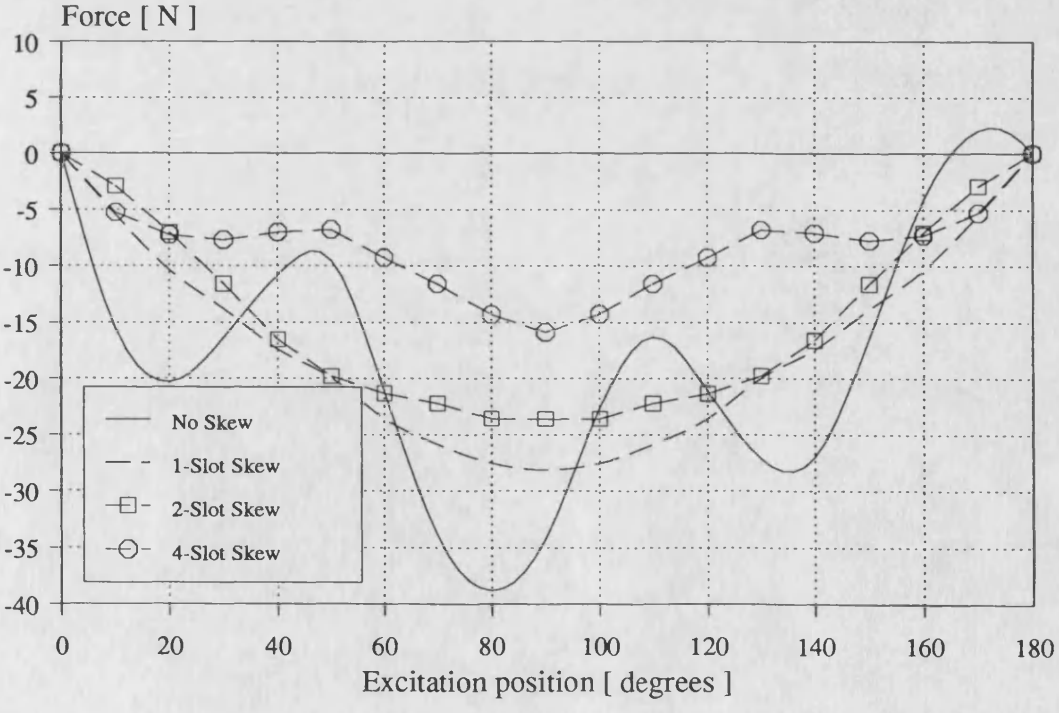

Figure 3.15 Calculated Electromagnetic Force at 1 A Phase Currents for Different Skew Cases

These calculations, however, are based on 2D results and there are limitations to the amount of skew that can safely be applied. This can be explained with Fig. 3.16 which illustrates the developed view of permanent magnet placement for (a) one-slot and (b) for two-slot skew. In the latter case two segments of opposite polarity are adjacent and establish overlapping poles. This may give rise to an appreciable increase in the amount of interpolar leakage flux which can only be analysed by 3D finite elements. The 2D method therefore may not be reliable when the skew is greater than one slot-pitch. Pending further work using 3D finite elements even though there are indications that a two-slot skew would be better one-slot skew must be recommended at the present time.

3.5 Calculation of the Armature Phase Flux Linkages on No-load for Back Emf Calculations

When the permanent magnet tubular machine operates emfs are induced in the armature phases as a result of the movement of the excitation permanent magnets with respect to the fixed armature. These emfs interact with the DC supply voltage to determine the phase currents and hence the electromagnetic forces and machine performance. It is therefore necessary to calculate these emfs for the simulation of the system. This is done by calculating the phase flux linkages for the excitation stroke length at different excitation positions with respect to the armature. Once the spacial distribution of phase flux linkages is known the phase emfs can be calculated using

$$e = \frac{d\lambda}{dx} \cdot \frac{dx}{dt} \qquad \ldots(3.2)$$

where λ is the phase flux linkage and x the excitation displacement.

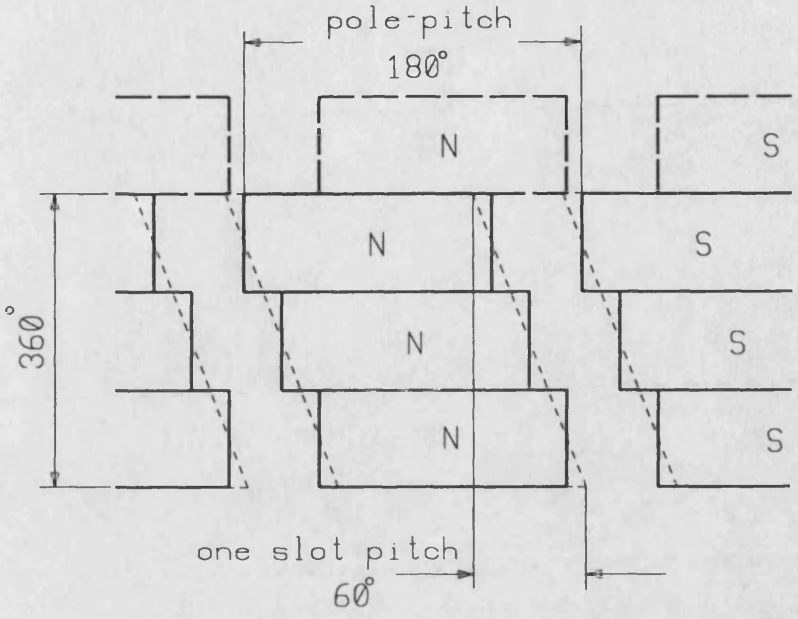

(a)

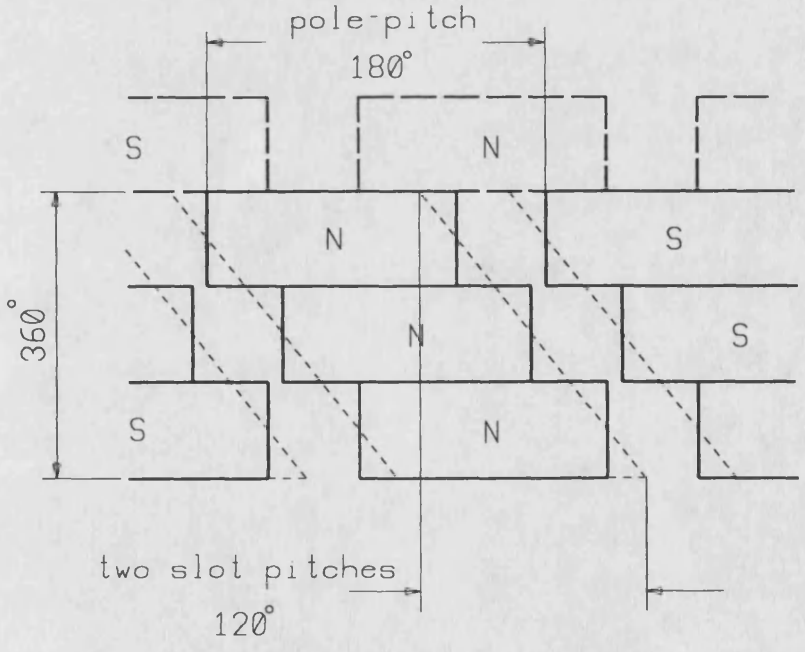

(b)

Figure 3.16 Developed View of Permanent Magnet Placement
(a) One-Slot Skew
(b) Two-Slot Skew

In order to calculate the phase flux linkages the flux linking the separate armature coils was first calculated. The surface integral that needs to be computed reduces to a line integral because of the 2D representation. This line integral was taken along the slot centre line in the radial direction in the armature back iron region as shown in Fig. 3.1 using

$$\phi = \int 2\pi r B_n dl \qquad \ldots(3.3)$$

to give the quantity of normal flux linking the coil in the respective slot. This flux does not include the leakage flux that partially encircles the coil. The amount of this leakage flux however is about 1 % of the useful flux and is therefore negligible. Coil flux linkages were then calculated by

$$\lambda_{coil} = N_c \phi$$

where N_c is the number of turns in a coil. Phase flux linkages were consequently calculated using coil linkages and armature winding connection.

Figure 3.17 gives the coil numbering used in the calculations and the phase connection arrangement of the winding. It also shows the positive displacement and flux linkage conventions used in both 1-pole and full FE models. Positive flux linkage direction is taken such that a positively increasing flux linkage, when the excitation moves in the positive direction, induces an emf in the coil such that the IN terminal of the coil is at positive potential with respect to the OUT terminal. This convention is used both for the experimental model and in the dynamic analysis program (Chapter 5).

Coil and phase flux linkages were calculated both for an infinitely long machine and for the actual machine. The results are presented in the following sections.

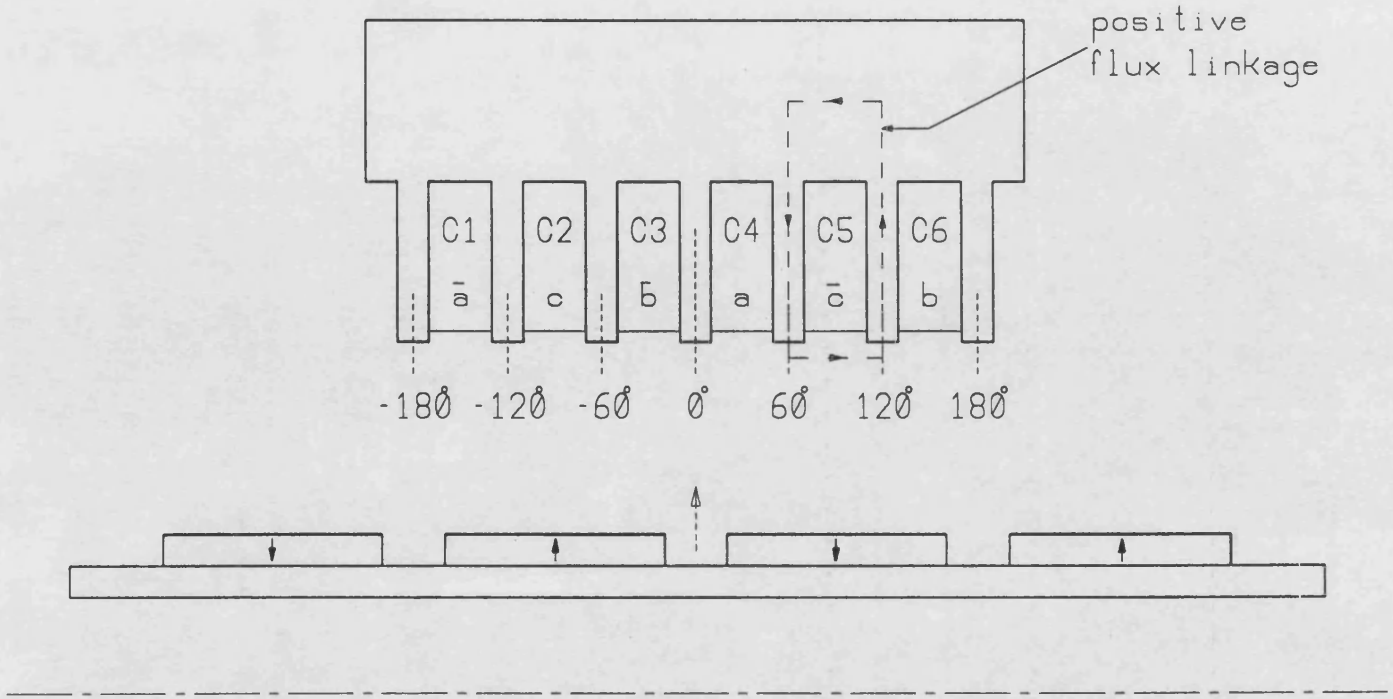

Figure 3.17 Armature Winding Coil Numbering and Positive Displacement and Flux Linkage Directions Used in Flux Linkage Calculations (Only Upper Section Shown and Air-Gap Exaggerated for Clarity)

3.5.1 Flux Linkages of Armature Coils Without End-effects

Armature coil and phase flux linkages were first calculated using the 1-pole model for an infinitely long machine. Figure 3.18 shows the field distribution in one of the models used in the calculations. This corresponds to -120 °, -60 °, 0 °, +60 ° etc. excitation positions with the appropriate permanent magnet pole sign due to symmetry and the infinite length of the model. The normal component of the mid-air-gap flux density with the excitation at standstill is plotted on Fig. 3.19. Calculated flux linkages of the coils at different excitation positions with no skew are given in Figure 3.20. It will be observed that there is 60 ° (one slot-pitch) space shift between consecutive coils' linkages as expected. There is also symmetry about the y axis between the linkages of C1 and C6, C2 and C5, and C3 and C4 as there is in their placements.

Results with skew can be obtained by adding together the linkages from three displaced permanent magnet segments. This is shown in Figure 3.21 which compares one-slot skew with no skew for C2. Comparing the two waveforms will reveal that the skewed flux linkage profile is smoother than in the unskewed case. This can also be seen from Table 3.1 which gives the harmonic content of both profiles as a percentage of their respective fundamental component. Sinusoidal phase flux linkage and emf would be best for a machine with sinusoidal applied currents. For a square-wave current/voltage system however, such as the one at hand, it is better to have a trapezoidal phase emf profile in order to obtain constant torque or force.

The phase flux linkages were calculated using individual coil linkages as will be shown later in this chapter. It will also be shown in Section 3.5.5 that the phase emf profiles produced by the skewed flux linkages have a trapezoidal waveform.

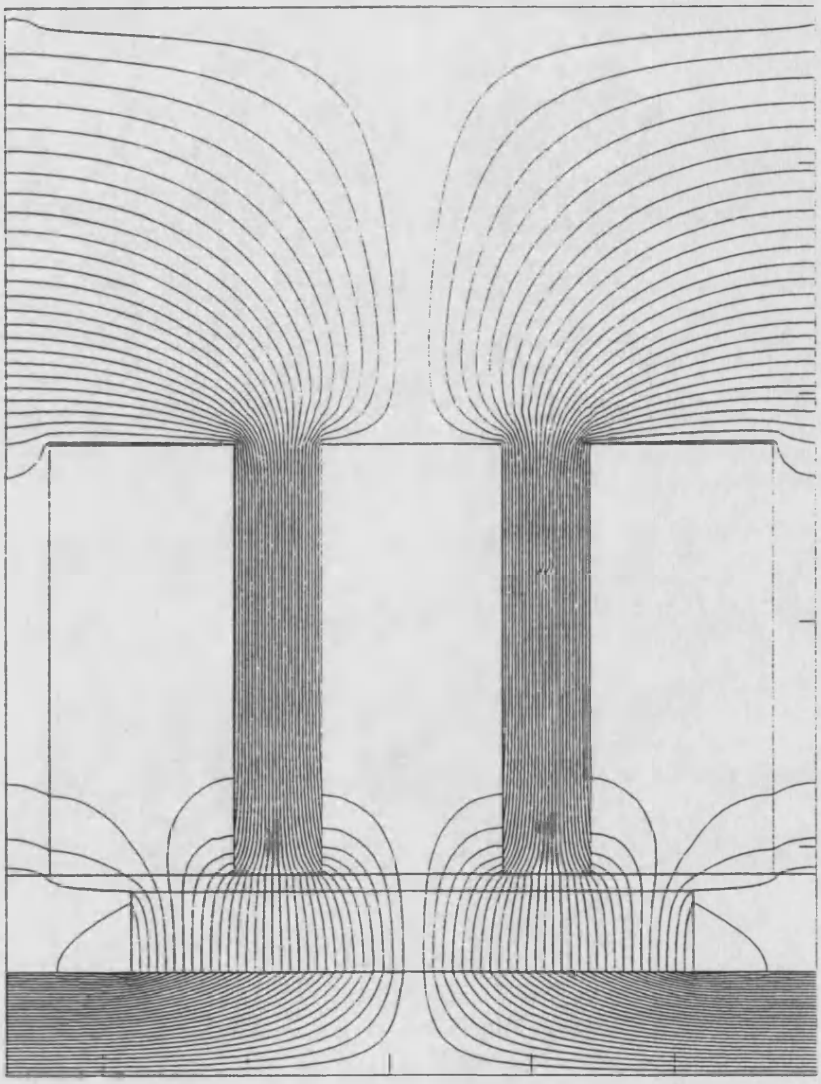

Figure 3.18 Excitation Field Distribution of a 1-Pole Model

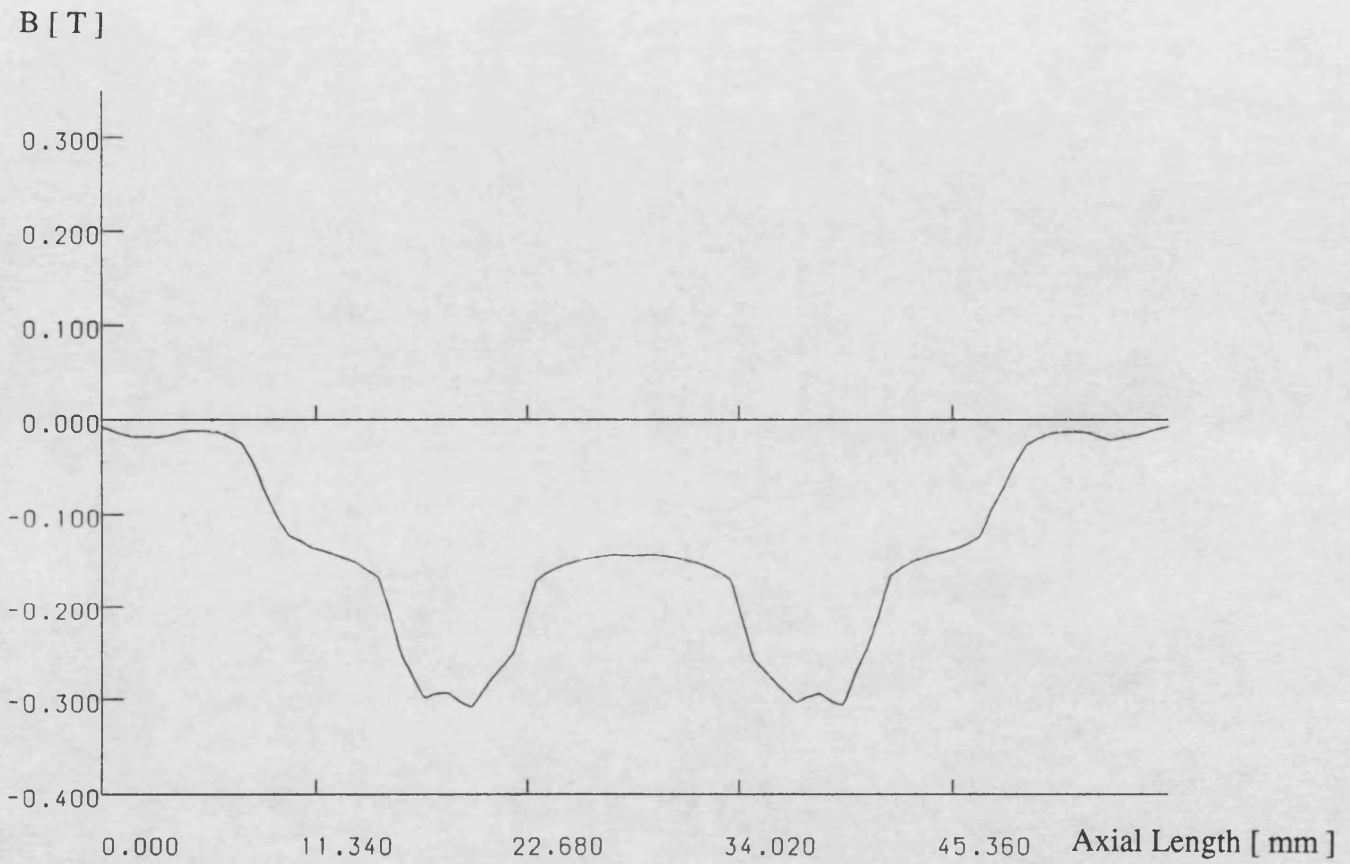

Figure 3.19 Calculated Radial Component of the Mid-Gap Flux Density on No Load in an Infinitely Long Machine with Excitation at Standstill

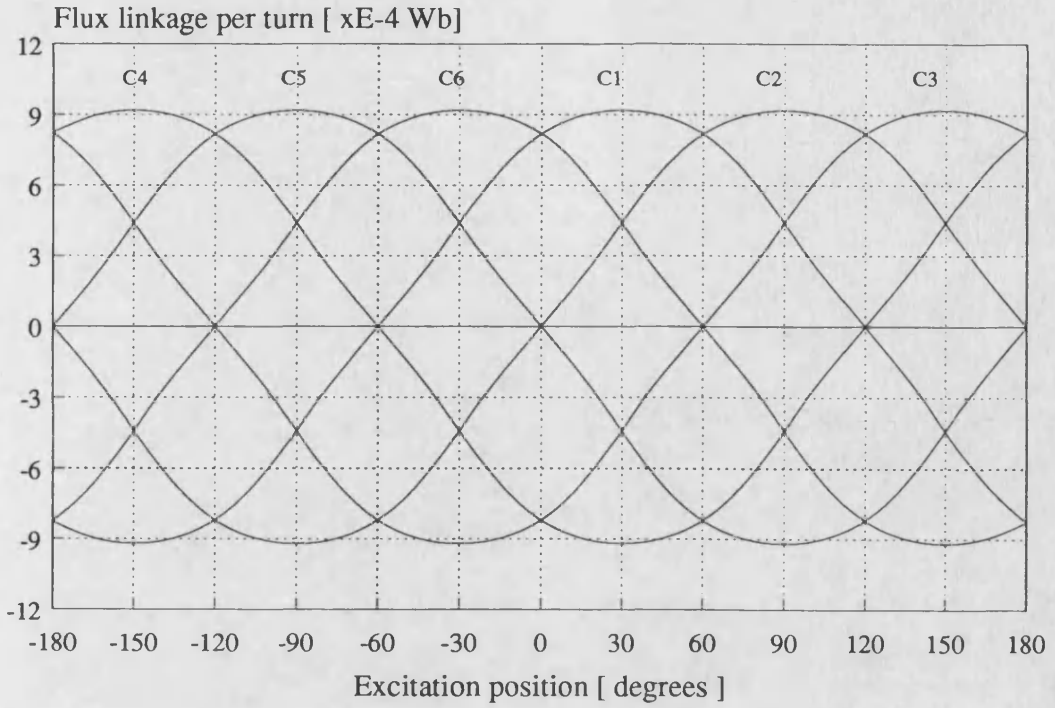

Figure 3.20 Calculated Coil Flux Linkages for an Infinitely Long Machine with No Skew

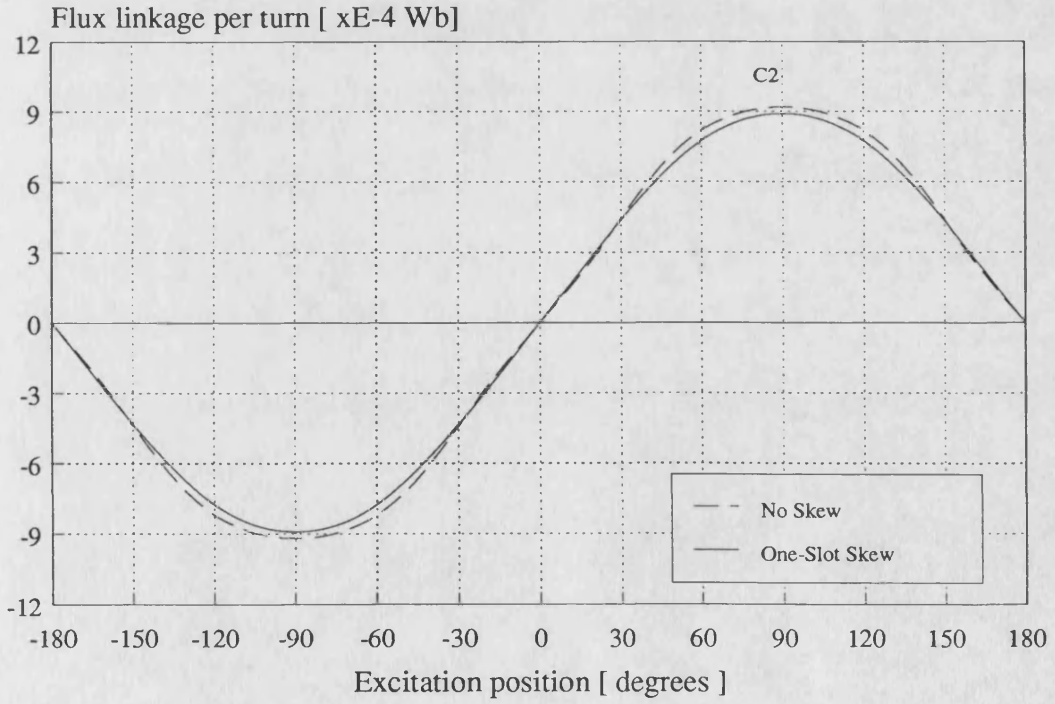

Figure 3.21 Calculated Flux Linkage of Coil2 for an Infinitely Long Machine

Table 3.1

Harmonic Content of Coil Flux Linkage For an Infinitely Long Machine as a Percentage of the Fundamental Component

Order	No Skew	1-Slot Skew
1	100	100
3	-1.31	-0.94
5	-2.66	-0.77
7	-0.47	-0.18

3.5.2 Flux Linkages of Armature Coils with End-Effects

It was assumed in the previous section that both the armature and the excitation of the machine were infinitely long. However, whilst this gives an approximation to the actual machine the effects of having one member shorter (armature) and having the other moving (excitation) are important and require investigation.

The full FE model was used for this purpose. The field distribution of one of the models corresponding to 0 ° displacement is shown in Figure 3.22. Comparison between this and Figure 3.18 of the previous section will reveal the effect of having a finite length machine: in the full model solution the first coil on the left, C1, has less linkage compared with the 1-pole model solution of Figure 3.18, C2 a small quantity instead of zero, and C3 more than previously. Fig. 3.23 illustrates the air-gap distribution of the normal component of the flux density, with the excitation at standstill, calculated along the mid-air-gap. A comparison of this profile with that of an infinite machine given in Fig. 3.19 for one pole also demonstrates the finite machine-length effect.

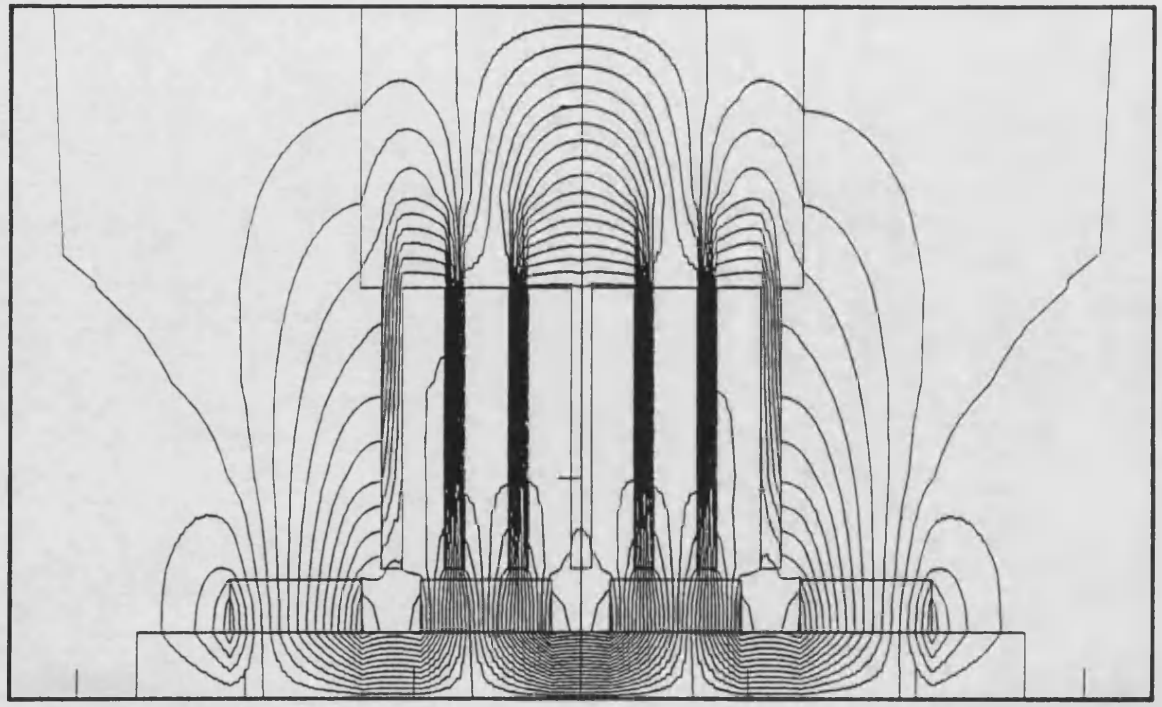

Figure 3.22 Excitation Field Distribution of a Full FE Model Corresponding to 0 ° Excitation Displacement

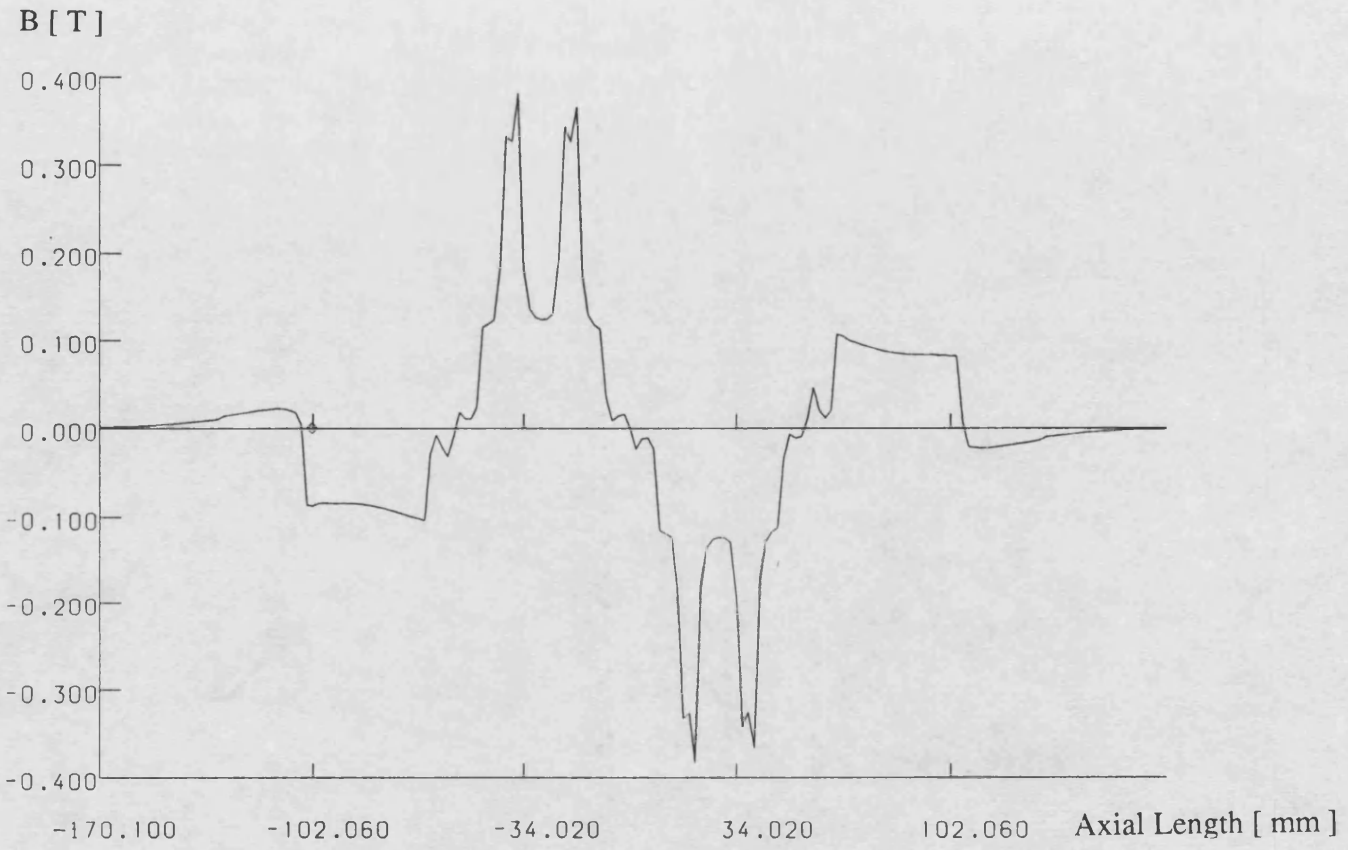

Figure 3.23 Calculated Radial Component of the Mid-Gap Flux Density on No Load in the Actual Machine with Excitation at Standstill

The flux linkages of all six coils were calculated and are given in Figure 3.24. As before the linkages of coils C4, C5 and C6 correspond to those of coils C3, C2 and C1 respectively. It can also be observed from Fig. 3.24 that C3 linkage is higher than that of C2 which in turn is higher than that of C1 i.e. the nearer a coil is to the centre of the armature the more linkage it has. This is what would be expected from this kind of magnetic structure.

Flux linkages due to the skewed excitation can be calculated in the same fashion as in the previous calculations: flux linkages from three shifted segments are added together. The resultant coil flux linkages with end-effects for one slot skew are given in Figure 3.25. When these skewed flux linkages are compared with those of Figure 3.24 it will again be seen that they are smoother than in the unskewed case. It can also be seen that there is no half wave symmetry in any linkage waveform unlike the case without end-effects.

Another useful comparison can be made between skewed linkages with and without end-effects by taking C2 flux linkage of Figure 3.25 contrasted with Figure 3.21 of the previous section. This clearly shows the effect of finite machine length on coil linkages. However when phase flux linkages are calculated this effect and the lack of half wave symmetry in coil linkage waveforms are greatly reduced as will be shown in the next section.

3.5.3 Armature Phase Flux Linkages

Phase emfs can be calculated directly using phase flux linkages. Phase flux linkages can in turn be calculated using the armature winding configuration and coil flux linkages. This method is flexible and can be used to calculate phase flux linkages and thus emfs for any armature winding however complex it may be.

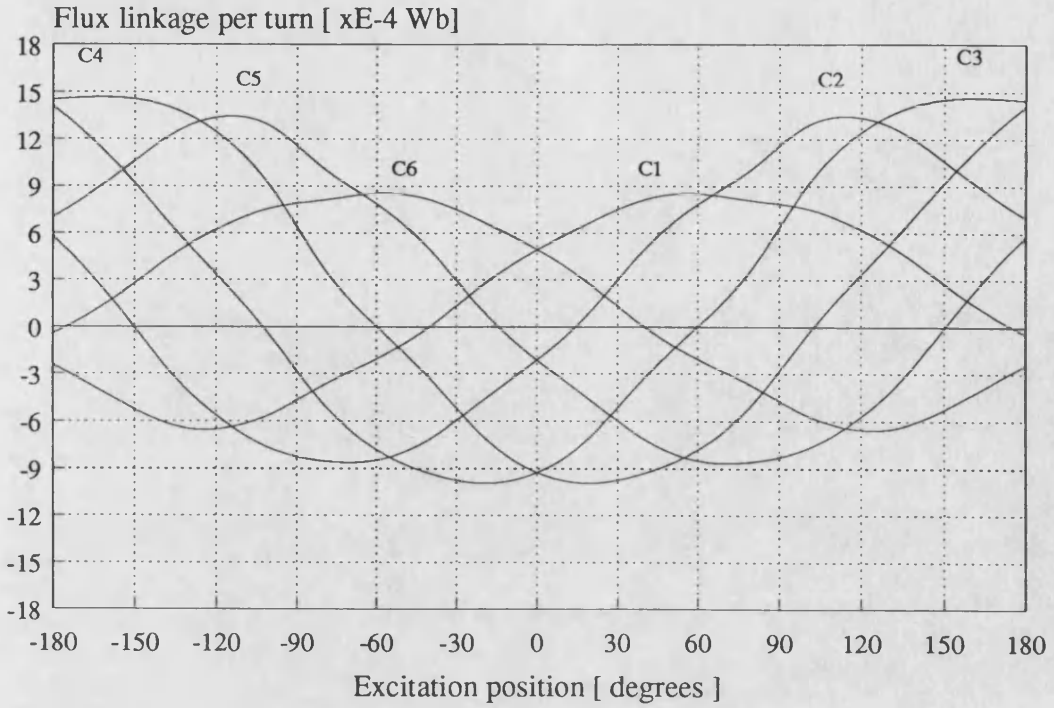

Figure 3.24 Calculated Coil Flux Linkages of the Actual Machine with No Skew

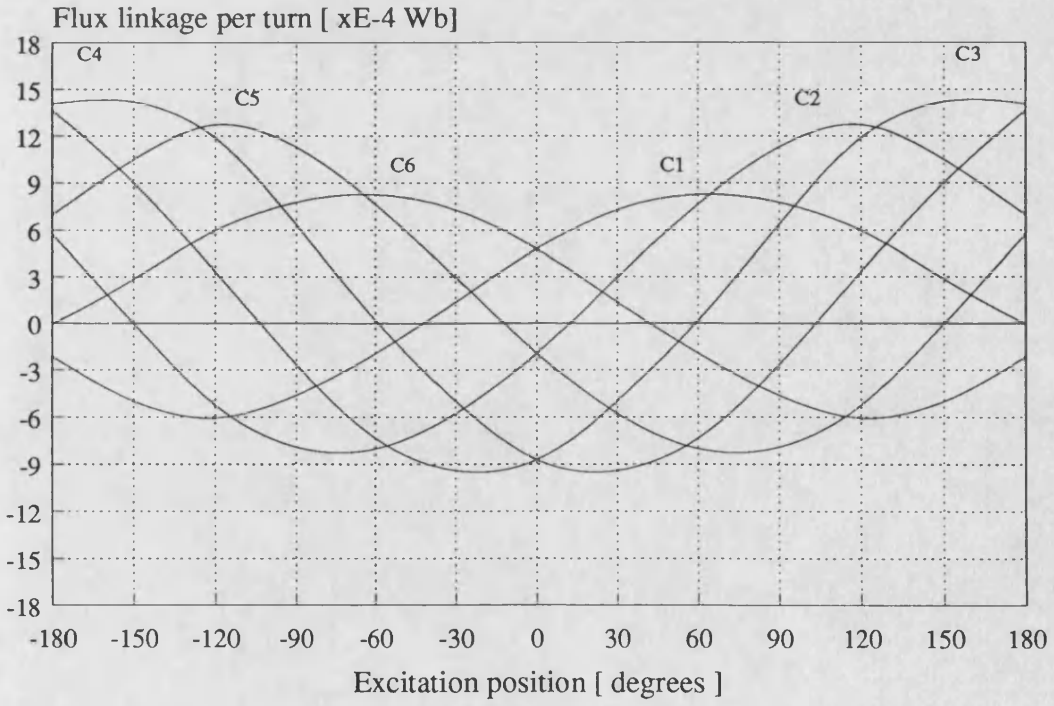

Figure 3.25 Calculated Coil Flux Linkages of the Actual Machine with One-Slot Skew

For the simple winding used, shown in Figure 3.17, phase flux linkages can be expressed in terms of coil linkages as below:

$$\lambda_a = \lambda_4 - \lambda_1 \qquad \ldots(3.4)$$

$$\lambda_b = \lambda_6 - \lambda_3 \qquad \ldots(3.5)$$

$$\lambda_c = \lambda_2 - \lambda_5 \qquad \ldots(3.6)$$

where " - " sign simply represents the winding direction of the coil. Using these equations the phase flux linkages both with and without end-effects were calculated and are given in Figure 3.26. It can be observed that end-effects cause a space shift of about 10 ° for most of the period of the excitation travel length and distort the amplitude beyond about ±80 ° displacement where end-effects become more pronounced.

3.5.4 Calculation of No-Load Phase Emfs

Phase emfs are functions of two variables as expressed by Eqn. 3.2: phase flux linkage and the speed at which the flux linkage changes i.e. the excitation speed. The amount of phase flux linkage due to permanent magnet fields is constant at each excitation position with respect to the armature and has a sinusoidal space profile as shown in the previous sections. The reason for this is that armature phases see alternate permanent magnet poles. The space rate of change of phase flux linkages is also fixed at each excitation position. Phase emfs can therefore be calculated by multiplying the space rate of change of phase flux linkages by the excitation speed.

This is done by representing the space profile of the phase linkages in terms of a *Fourier* series which takes the form

$$\lambda(x) = \sum_{n=1}^{n_h} \left\{ a_n \cos n\left(\frac{x}{t_p}\cdot\pi - \theta\right) + b_n \sin n\left(\frac{x}{t_p}\cdot\pi - \theta\right) \right\} \qquad \ldots(3.7)$$

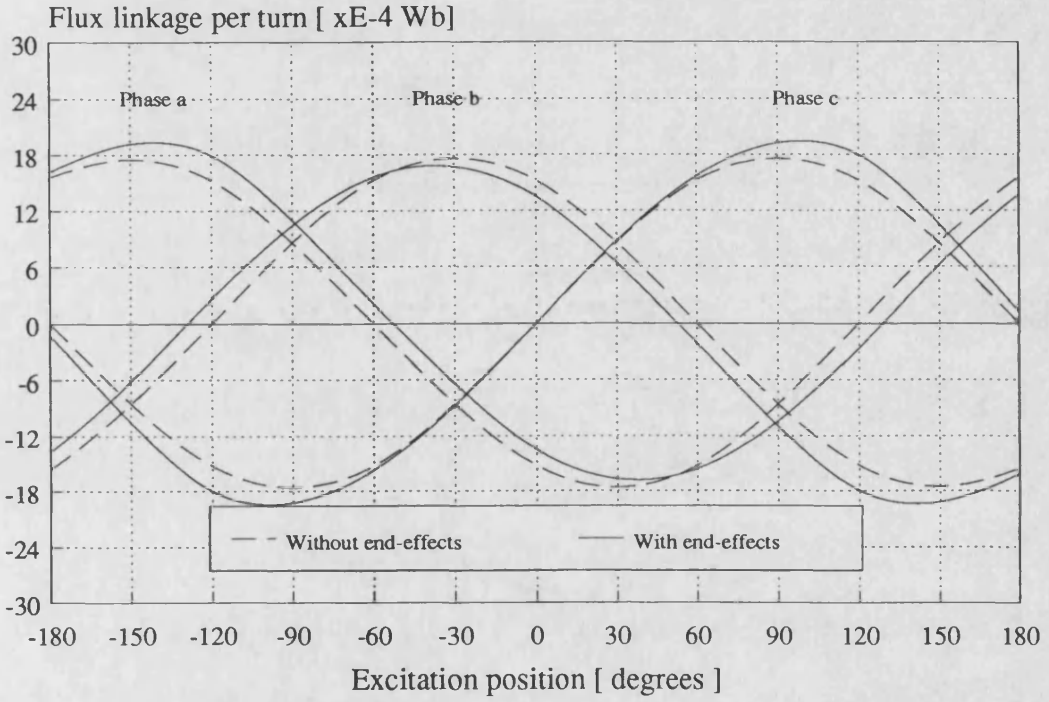

Figure 3.26 Calculated Flux Linkages of the Armature Phases with One-Slot Skew

where n is the harmonic order

n_h is the maximum order of harmonics

t_p is the pole pitch [m]

x is the axial excitation displacement [m]

θ is the phase shift [rad]

Phase emfs can then be calculated using Eqn. 3.2.

This method was used both in the dynamic simulation program and in emf coefficient calculations which will be detailed in the next section.

3.5.5 Verification of Flux Linkage and Emf Calculations

The results given in the previous sections were calculated using FE techniques. However, because of the difficulties involved in using search coils in devices with moving permanent magnet parts no flux linkage measurements were made. Instead two tests were performed to verify the calculations. The first compares calculated and measured air-gap flux densities as the excitation moves. The second uses calculated and measured phase emf coefficients.

Tooth-tip flux densities along the mid-air-gap for different excitation positions were calculated for the reference permanent magnet segment using the 1-pole model solutions used in flux linkage calculations. The calculated radial component of the tooth-tip flux density for the middle armature teeth is given by the solid curve in Figure 3.27. Measured flux densities are also given in the figure. Measurements were made by *Hall effect* sensors placed at the tooth-tips. They were calibrated for the ambient temperature conditions using electromagnets and a Hall-effect meter before installation in the armature. It can be seen that the measured excitation flux

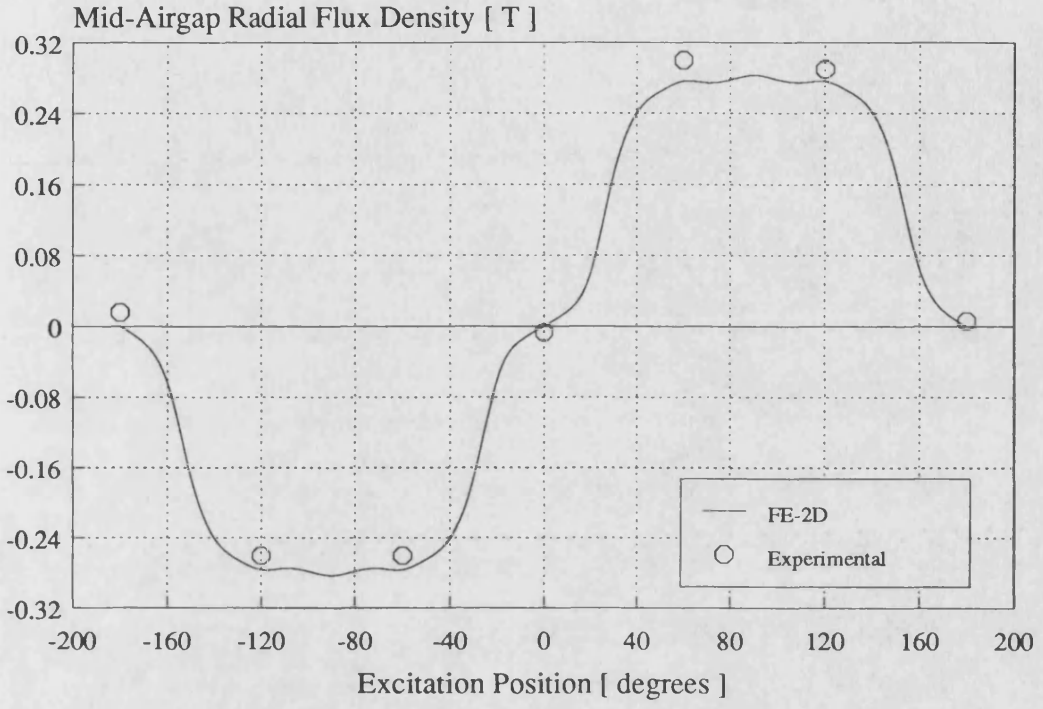

Figure 3.27 Radial Component of the Mid-Air-Gap Flux Density From the Reference Segment at the Central Tooth

from the permanent magnets is in close agreement with the FE calculated flux. This confirms that the technique used to magnetise the permanent magnet poles outlined in Appendix B is adequate.

It was shown that in order to calculate the phase emfs, the space rate of change of flux linkage must be multiplied by the excitation speed which is the speed at which the flux linkage changes. However, the space rate of change of the flux linkage can be used as an emf coefficient i.e. emf per unit speed to provide a comparison between calculations and experiment. This method was considered as an alternative to the actual phase emf comparison due to the difficulties in running the experimental excitation at a fixed speed.

Theoretical calculations were performed for both with and without end-effects. Experimental emf coefficients, on the other hand, were obtained by moving the excitation and dividing the recorded emf by the recorded excitation speed throughout the excitation stroke length. Emf coefficients can be found at any excitation position by this means. The results of this theoretical and experimental investigation are presented in Figures 3.28(a), (b) and (c). The generally consistent correlation shows that flux linkage and emf calculations that have been performed can be said to be reliable.

3.6 Armature Winding Self and Mutual Inductances

A detailed knowledge of the armature self and mutual inductances is important in order to complete the parameter determination of the machine.

Two calculation techniques were compared for a system of two coils. It was found that they give the same self and mutual inductance values. The simpler one

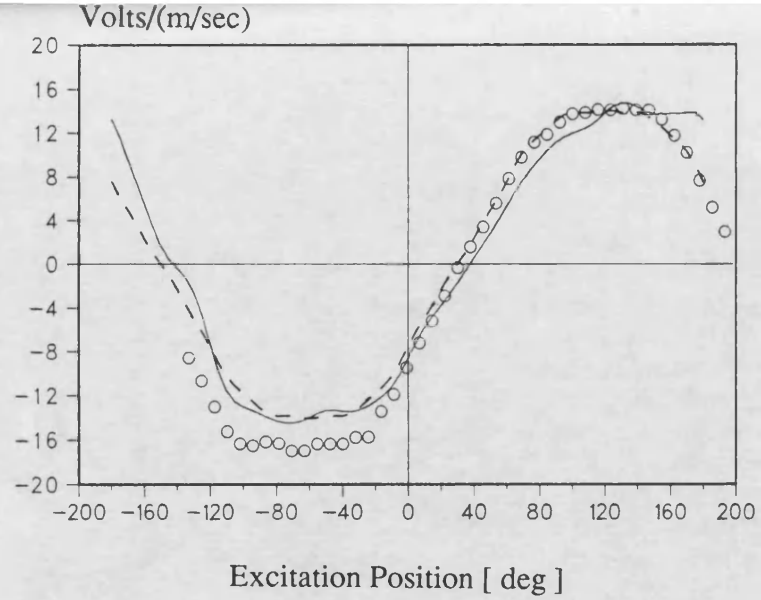

(a)

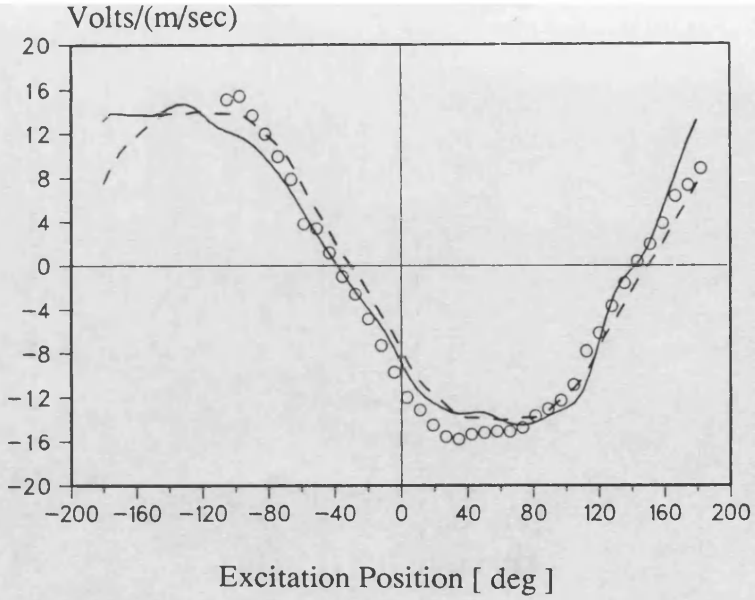

(b)

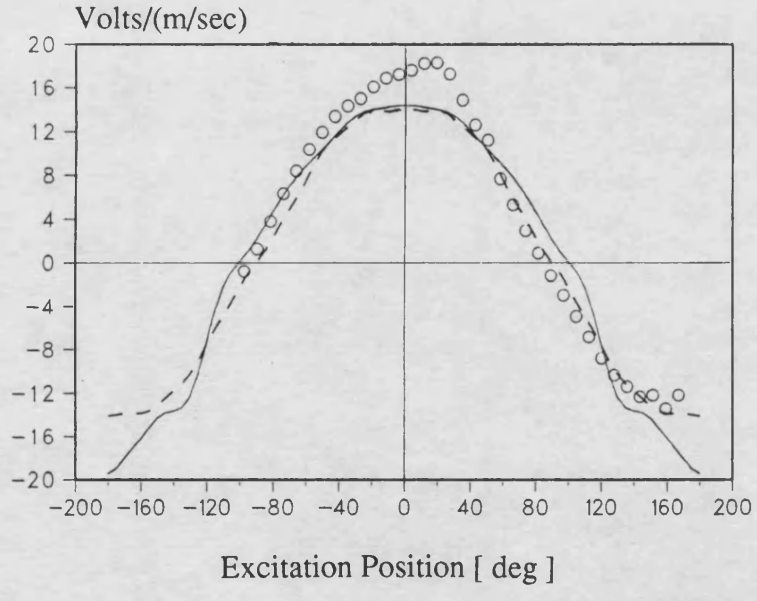

(c)

— — — Without End-Effects
——— With End-Effects
o Experimental

Figure 3.28 Phase Emf Coefficients
(a) Phase a
(b) Phase b
(c) Phase c

was chosen for the system inductance calculations. Similarly two measurement techniques were compared and after obtaining similar results the simpler one was chosen.

The air-gap distance between the excitation and the armature does not change as the excitation moves. This, combined with the near unity permeability of the permanent magnet material makes the inductances independent of the excitation position. This was confirmed both theoretically and experimentally. It was also confirmed theoretically that the presence of the permanent magnets does not affect the armature field distribution and therefore the armature inductances if saturation is neglected. This is a direct result of the permanent magnet material's near unity permeability. As a consequence permanent magnets were eliminated from the FE models used in the calculations to reduce the data preparation and CPU times.

The results of the work is presented below.

3.6.1 Calculation of Self and Mutual Inductances by Two Methods

Using the 1-pole model, the self and mutual inductances of two adjacent coils were calculated using two numerical electromagnetic techniques. The first one is based on an energy method and called the *energy perturbation method* **[3.2]**. The second one is also based on the magnetic energy stored in the system fields but uses a simpler approach **[3.3]**.

3.6.1.1 Energy Perturbation Method

This is a general technique that can be employed for both *apparent* and *incremental* inductance calculations taking into account saturation effects. It is based on the perturbations of the machine winding currents and calculating the associated

change of the stored energy in the magnetic fields of an n winding system. This method will be briefly outlined here quoting Reference [3.2] for the sake of completeness.

The energy perturbation method is based on the total energy stored in the field of a magnetic circuit with n coils. Consider the voltage at the terminals of the *jth* coil, it can be written that

$$V_j = R_j i_j + \frac{\partial \lambda_j}{\partial i_1}\frac{di_1}{dt} + \frac{\partial \lambda_j}{\partial i_2}\frac{di_2}{dt} + \cdots + \frac{\partial \lambda_j}{\partial i_j}\frac{di_j}{dt} + \cdots + \frac{\partial \lambda_j}{\partial i_n}\frac{di_n}{dt} \qquad \ldots(3.8)$$

In this equation the partial derivative of the flux linkage, λ_j with respect to a coil current i_k , $(k=1, 2,.., j,.., n)$ is the incremental inductance, L_{jk}^{inc} . Therefore the total stored energy, W, associated with the system of n coils can be written as:

$$W = \sum_{j=1}^{n} W_j = \sum_{j=1}^{n}\left\{\sum_{k=1}^{n}\int_{i_k(0)}^{i_k(t)} (L_{jk}^{inc} \cdot i_j) di_k\right\} \qquad \ldots(3.9)$$

Self and mutual inductances of the various n coils can be expressed as the partial derivatives of the total stored energy, W, with respect to various coil current perturbations, Δi_j . These derivatives can, in turn, be expanded around a *quiescent* magnetic field solution that are obtained for a set of coil currents, in terms of various current perturbations $\pm \Delta i_j$ and $\pm \Delta i_k$ in the *jth* and *kth* coils, and the resultant change in the total stored magnetic energy. For the system under investigation where $L_{jk}=L_{kj}$, this process results in for the self and mutual inductances the following:

$$L_{jj} = \frac{\partial^2 W}{\partial(\Delta i_j)^2} \cong [W(i_j - \Delta i_j) - 2W + W(i_j + \Delta i_j)]/(\Delta i_j)^2 \qquad \ldots(3.10)$$

and

$$L_{jk} = \frac{\partial^2 W}{\partial(\Delta i_j)\partial(\Delta i_k)} \cong [W(i_j + \Delta i_j, i_k + \Delta i_k) - W(i_j - \Delta i_j, i_k + \Delta i_k) - W(i_j + \Delta i_j, i_k - \Delta i_k) + W(i_j - \Delta i_j, i_k - \Delta i_k)]/(4 \cdot \Delta i_j \cdot \Delta i_k) \quad \ldots(3.11)$$

Here, the total energy W at the quiescent point is calculated from a magnetic field solution whose excitation current set in the n coils is $(i_1, i_2, \ldots, i_j, \ldots, i_k, \ldots, i_n)$. Also, the total energy $W(i_j \pm \Delta i_j)$ is the energy calculated from a magnetic field solution whose excitation currents in the n coils are $(i_1, i_2, \ldots, (i_j \pm \Delta i_j), \ldots, i_n)$ and the total energy $W(i_j \pm \Delta i_j, i_k \pm \Delta i_k)$ is the energy calculated from a magnetic field solution whose excitation currents in the coils are $(i_1, i_2, \ldots, (i_j \pm \Delta i_j), \ldots, (i_k \pm \Delta i_k), \ldots, i_n)$.

The perturbed field solutions can either be obtained using the incremental or apparent reluctivities of the various parts of the magnetic circuit, thus yielding the incremental or apparent coil self and mutual inductances.

3.6.1.2 Direct Energy Method

This technique utilises the equality of two expressions which are used to calculate the magnetic energy stored in a magnetic field. The first equation is the expression in terms of field quantities

$$W = \frac{1}{2}\int \vec{B} \cdot \vec{H} dv \quad \ldots(3.12)$$

which can be implemented with FE techniques. The second expression is the stored energy in terms of inductance for a linear magnetic circuit and is expressed by

$$W = \frac{1}{2} L \cdot i^2 \qquad \ldots(3.13)$$

for a one-coil system and

$$W = \frac{1}{2} [i_1 \quad i_2] \cdot \begin{bmatrix} L_{11} & L_{12} \\ L_{21} & L_{22} \end{bmatrix} \cdot \begin{bmatrix} i_1 \\ i_2 \end{bmatrix} \qquad \ldots(3.14)$$

for a two-coil system. Taking $L_{12} = L_{21} = M$ as all coils have equal number of turns and $i_1 = i_2 = i$ these equations yield

$$L = \frac{2 \cdot W}{i^2} \qquad \ldots(3.15)$$

for the self inductance of a one-coil excited system and

$$M = \frac{(2 \cdot W/i^2) - L_{11} - L_{22}}{2} \qquad \ldots(3.16)$$

for the mutual inductances of the two-coil system. It will be shown later that coil self inductance depends on position along the armature due to end-effects. Therefore when mutual inductances between two coils are calculated respective coil self inductances are used.

As mentioned above, this technique assumes a linear magnetic circuit in which there is no saturation effect. This does not introduce an appreciable error since, due to the large effective air-gap in this class of machine, magnetic saturation occurs at currents well above the normal load conditions. This was confirmed using the FE model by applying 20 A as armature phase current and solving the problem nonlinearly. The maximum flux density was found to be 0.8 T in the armature teeth. This value is within the linear region of the *BH* curve of the material used and the

inductance value obtained for this current was the same as the lower current case. The flux density level would be higher in the experimental model for the same current loading because of the four blocks used in the armature. However the difference is small and therefore negligible.

3.6.1.3 Inductances Calculated From the Two Methods

The 1-pole model shown in Figure 3.29 was used for inductance calculations by the two methods outlined above. For the energy perturbation method the model was taken including the permanent magnet. However for the simple energy method the permanent magnet region was taken as air for the reason given above. The two self and one mutual inductances of the system are given in Table 3.2. These calculations were performed for a few sets of current levels and found to give the same answer for normal load conditions. It can be seen that the results both methods give are approximately equal. The number of solutions required for each method are given in Table 3.3. As can be seen, to calculate the inductances of a given system the number of solutions required for the direct energy method is about half of the energy perturbation method. Therefore the direct energy method was adapted for the actual system inductance calculations.

Table 3.2

Inductance [mH]

	Energy Perturbation Method	Direct Energy Method
L_{11}	16.363	16.026
L_{12}	2.72	2.68
L_{22}	16.363	16.026

Table 3.3

Number of Solutions Required for a System of 2 Coils

	Energy Perturbation Method	Direct Energy Method
Self Inductance	3	1
Mutual Inductance	4	3

3.6.2 Measurements of a Phase Self and Mutual Inductance By Two Methods

Two methods were initially used for inductance measurements. The first one of these used the circuit shown in Figure 3.30. A step voltage was applied to the coil and the transient current build-up was recorded. Using the first section of the current waveform and assuming that there is negligible resistive voltage drop, the inductance was calculated using $L=V/(di/dt)$. A commercially available instrument, *Hewlett Packard Impedance Analyser,* was used as the second method.

Line to line, line to neutral self and the mutual inductances between two phases of the star connected three-phase winding were measured. The values are given in Table 3.4. It will be observed that the two methods give the same results. Hence the impedance analyser was chosen for the rest of the measurements because of its convenience for direct and quick measurements.

Mutual inductances can be measured directly. They are contained in the values of the line to line inductance readings of a two-coil (or two sets of coils) system. For example, suppose that two coils are connected in series and total line to line inductance is $L_{(Line1\text{-}Line2)}$. The mutual inductance is contained in this inductance value and can be obtained using

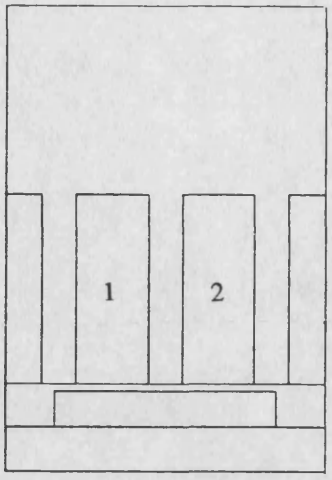

Figure 3.29 FE Model Used for the Two Inductance Calculation Techniques

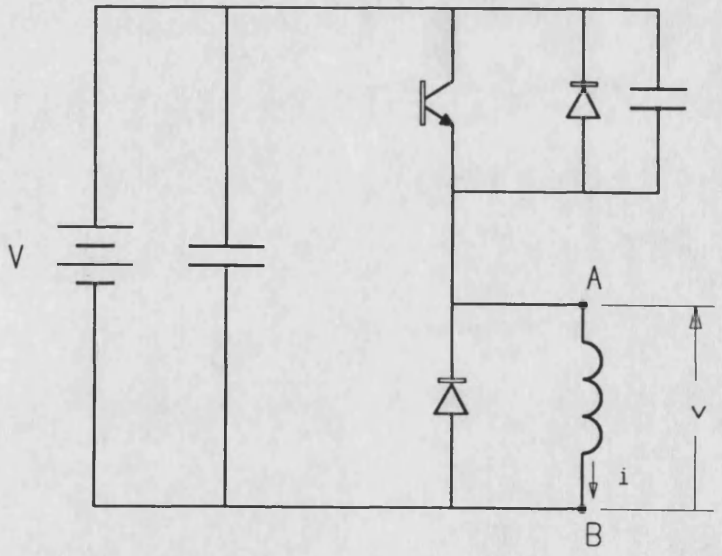

Figure 3.30 Circuit Used in Inductance Measurements by *di/dt*

$$L_{(Line1-Line2)} = L_{11} + L_{22} + 2M_{12} \qquad \ldots(3.17)$$

Table 3.4

Measured Inductances [mH]

	Measured by *di/dt*	Measured by Impedance Analyser
Line to Line Self	88.16	87.5
Line to Neutral Self	33.126	32.67
Phase to Phase Mutual	10.954	11.08

3.6.3 Armature Coil Self and Mutual Inductances

As was mentioned previously the armature phases are star connected and have one coil per pole (2 coils for the 2-pole armature prototype machine). The phase connection and coil numbering used are shown in Figure 3.31. Armature self and mutual inductances were first calculated on a coil by coil basis. That is individual coil self and mutual inductances between all possible combinations of two coils were calculated and measured. This is a good way as one can obtain the resultant phase inductances, both self and mutual, for any winding connection.

All inductance calculations were performed using the direct energy method as was explained in Section 3.6.1.2. The full FE model without permanent magnets was taken as the source model. The flux plot of the model with which Coil 1 and Coil 6 self inductances were calculated is given in Figure 3.32. Measured values with impedance analyser and calculated values of coil self inductances are given in Table 3.5. The general tendency of both theoretical and experimental results reveals that the inductance of a coil is maximum in the centre slots and decreases towards the armature edges. This is naturally due to the increase in leakage flux for the fields of the outer coils and can be attributed to the end-effects.

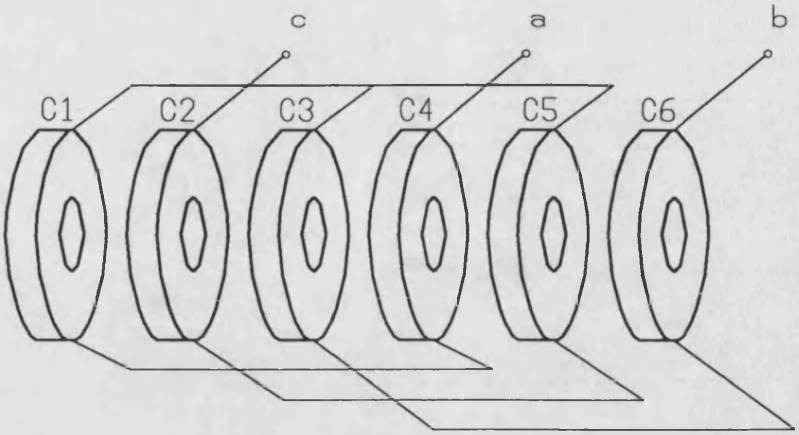

(a)

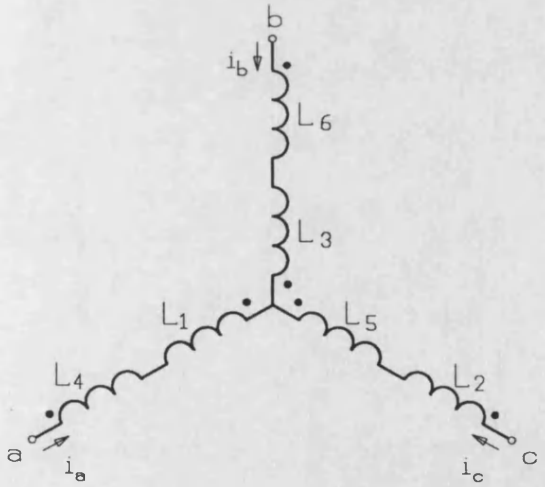

(b)

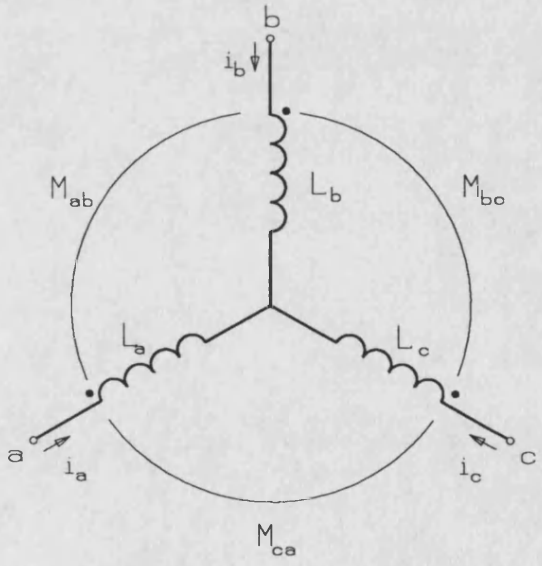

(c)

Figure 3.31 (a) Coil Numbering and Connection Used in the System Inductance Calculations
(b) Symbolic Diagram
(c) Classical Three Phase Armature Winding(Inductances shown only)

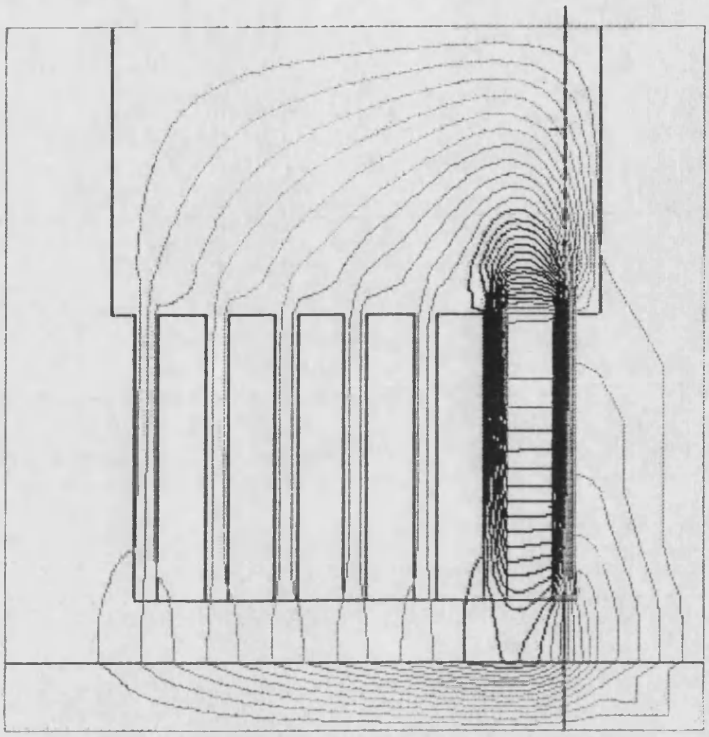

Figure 3.32 Armature Field Distribution Inside the Model Used To Calculate Coil1 and Coil6 Inductances (Coil6 excited only)

Table 3.5

Calculated and Measured Coil Self Inductances [mH]

	Calculated	Measured
L_1	21.20	20.7
L_2	26.24	22.9
L_3	28.93	24.5
L_4	28.93	25.3
L_5	26.24	23.6
L_6	21.20	21.6

Calculated and measured mutual inductances between any pair of armature coils are given in Table 3.6. It will be shown later that these inductances are necessary when phase mutual inductances are calculated. For the reason mentioned above, the mutual inductance between two adjacent coils also increases towards the armature centre. Since all coils have the same number of turns $M_{xy} = M_{yx}$ e.g. $M_{36} = M_{63}$ and because of the symmetry in the magnetic circuit $M_{xy} = M_{(7-x)\,(7-y)}$ e.g. $M_{12} = M_{65}$, $M_{46} = M_{31}$ etc. This can be seen in Table 3.6.

All mutual inductances shown are positive i.e. coil fields support each other. However, when phase inductances are calculated some of these mutual inductances will have a negative sign as a result of the phase connection forming the three-phase winding. This is presented next.

Table 3.6

Calculated and Measured Mutual Inductances

Between Armature Coils [mH]

	Calculated	Measured
M_{12}	11.18	11.6
M_{13}	9.09	8.35
M_{14}	7.06	6.25
M_{15}	5.06	4.89
M_{16}	2.91	3.40
M_{23}	15.01	13.9
M_{24}	11.58	9.69
M_{25}	8.31	7.18
M_{26}	5.06	4.97
M_{34}	16.25	13.95
M_{35}	11.58	9.96
M_{36}	7.06	6.65
M_{45}	15.01	13.75
M_{46}	9.09	8.95
M_{56}	11.18	12.50

3.6.4 Armature Phase Self and Mutual Inductances

Calculated coil self and mutual inductances can be used to find phase self and mutual inductances. This is done by using the coil and phase connections which form the three-phase winding and can be applied to any winding arrangement whose coil inductances are known.

The phase to neutral self inductances for the winding of the machine at hand can be formulated using the symbolic winding diagram and current directions shown in Figure 3.31(a) and (b) as below:

$$L_a = L_4 + L_1 - 2M_{14} \qquad \ldots(3.18)$$

$$L_b = L_6 + L_3 - 2M_{36} \qquad \ldots(3.19)$$

$$L_c = L_2 + L_5 - 2M_{25} \qquad \ldots(3.20)$$

Calculated phase to neutral inductances are given in Table 3.7 together with the measured values. These experimental values were measured directly i.e. on a phase by phase basis. However, the equations given above can also be applied to the measured coil inductances to obtain phase to neutral inductances which yield the same results. A comparison between calculated and measured phase to neutral inductances reveals that they are in good agreement and that the calculated results are slightly higher than the measured ones. The reason for this is that the armature was modelled as a complete shell whereas the prototype has four blocks with air regions between them. This results in more leakage flux and thus less useful flux for the experimental model which in turn means lower inductance. This effect corresponds to the winding-end effects in rotary machines. Another comparison between inductances of three phases, on the other hand, will reveal that L_a and L_b are equal due to the symmetry and L_c is slightly less in value. This is again a result of the finite length of the armature.

Table 3.7

Calculated and Measured Phase to Neutral Inductances [mH]

	Calculated	Measured
L_a	36.00	33.5
L_b	36.00	32.9
L_c	35.86	32.3

Phase to phase mutual inductances can be calculated in the same way using the current directions shown on the diagram of Fig. 3.31(b)

$$M_{ab} = -M_{34} + M_{46} + M_{13} - M_{16} \quad \ldots(3.21)$$

$$M_{bc} = -M_{56} + M_{26} + M_{35} - M_{23} \quad \ldots(3.22)$$

$$M_{ca} = -M_{12} + M_{24} + M_{15} - M_{45} \quad \ldots(3.23)$$

The current directions in Figure 3.31(b) are taken in order to maintain compatibility with the classical schematic representation of a three phase wye connected synchronous machine model. This will be used in Chapter 5 to obtain the mathematical equations of the system. This machine model is shown in Fig. 3.31(c) for the phase inductances.

Calculated and measured mutual inductances between phases are given in Table 3.8. As in the case of coil mutual inductances, phase mutual inductances were measured indirectly using measured values of line to line and phase to neutral total inductances and were found using

$$L_{(linea-lineb)} = L_a + L_b + 2M_{ab} \quad \ldots(3.24)$$

$$L_{(lineb-linec)} = L_b + L_c + 2M_{bc} \quad \ldots(3.25)$$

$$L_{(linec-linea)} = L_c + L_a + 2M_{ca} \quad \ldots(3.26)$$

It may be observed by comparing the mutual inductances that two are equal and the third is somewhat smaller than the other two. The equality is a result of having symmetry in the winding and in the magnetic circuit.

Table 3.8

Calculated and Measured Phase Mutual Inductances [mH]

	Calculated	Measured
M_{ab}	-0.98	-0.40
M_{bc}	-9.55	-10.70
M_{ca}	-9.55	-10.95

3.7 Armature Reaction Effect

Electromagnetic force and flux linkage calculations were performed under no-load conditions. That is, it was assumed that magnetic field set up by the armature currents had no effect on the permanent magnet excitation fields. This is, however, only true when there is no saturation in any part of the magnetic circuit.

This was investigated using the 1-pole model. The excitation position and armature current loading were taken to correspond to the case where there is 90 ° displacement between the excitation and the armature mmfs [Fig. 3.33]. The radial component of the mid-gap flux density at standstill for no-load and 1 A and 2 A phase currents along a pole pitch are given in Figure 3.34. It will be seen that the magnet field is equally distorted around the centre of the pole. No saturation effects were encountered in any parts of the magnetic circuit at current loadings well above normal operation conditions (up to 10 A). This is mainly because of the large air-gap due to the near unity permeability of the permanent magnet material.

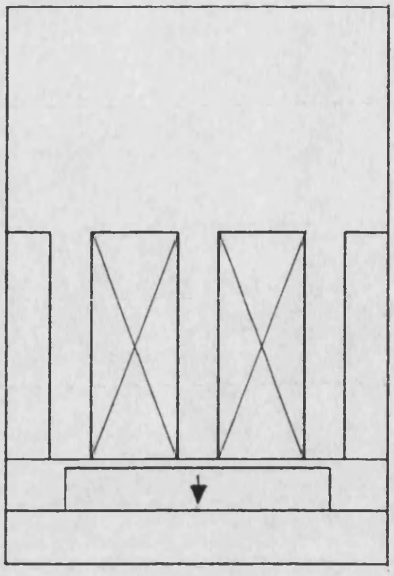

Figure 3.33 1-Pole Model Used in the Calculations of the Armature Reaction Effects on the Excitation Field

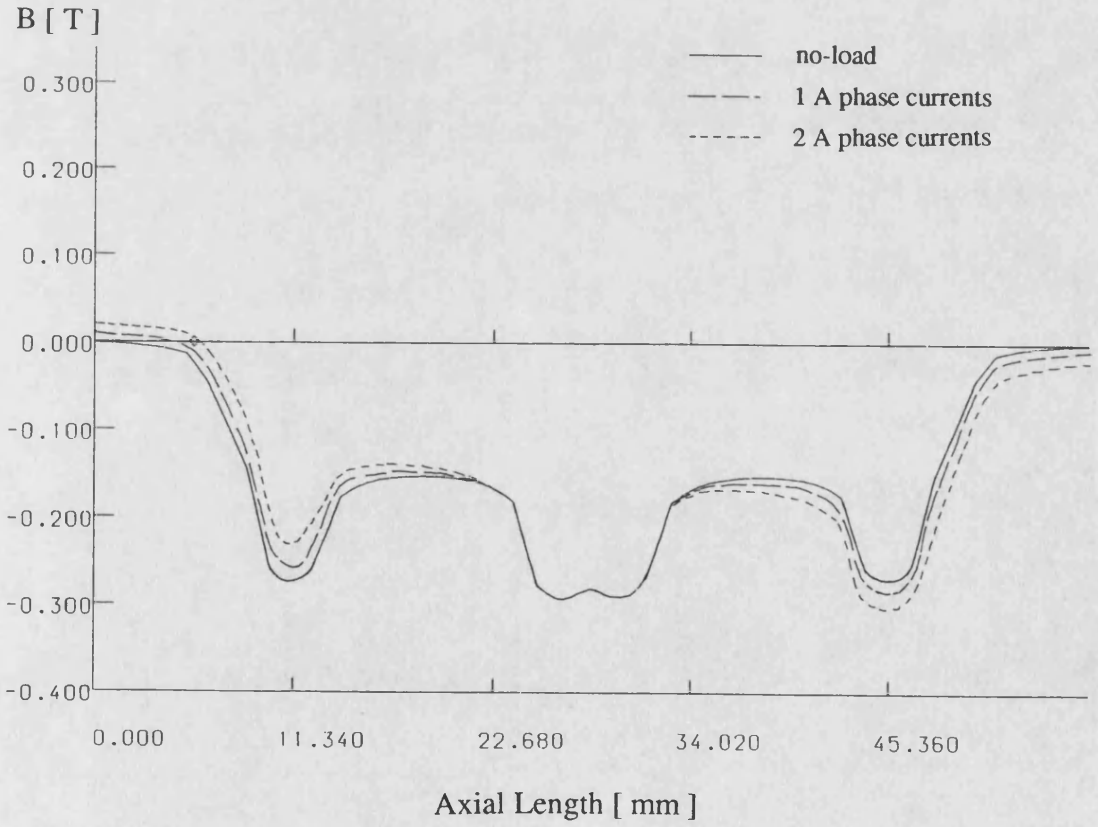

Figure 3.34 Mid-Air-Gap Radial Flux Density with Excitation at Standstill

Armature reaction therefore does not have an appreciable effect on the flux of the machine under normal operation. The machine does not saturate nor is the total permanent magnet flux reduced (an increase on one side of the pole is accompanied by a reduction on the other). However in more extreme conditions the armature reaction would need to be accounted for. An analysis is given in Appendix E where one of the magnetic circuits taken is that used here.

3.8 Conclusions

2D FE modelling of the machine gives satisfactory results in spite of the 3D nature of the magnetic structure involved. The machine has two main 3D features which cannot be directly modelled with a 2D code. One is the armature having four blocks of laminated iron instead of a tube and the other having skewed permanent magnet segments rather than a tubelike shell. The latter effect is more important in terms of design considerations and was incorporated into the FE models by summing suitably space-phase shifted versions. This made it possible to obtain near 3D results and showed how skewing changes machine parameters and standstill forces.

The optimum amount of skew was also investigated. It was found, within the limitations of 2D, that a skew of one slot-pitch gives zero resultant tooth-cogging force as well as reducing the end-effect force. Further skew can only be modelled using 3D FE in order to take into account the circumferential effects that may be important.

It is shown that for the conditions investigated it is possible to superpose the separate calculated forces to produce a composite force that agrees with practice. This is of course only possible if saturation effects are not important. However this is often the case in this form of machine because of the large effective magnetic gap due to the near unity permeability of the permanent magnet material.

Having symmetry in the geometry of the magnetic circuit and in the winding is important in having a near-balanced system where system inductances have close values and phases have a balanced emf distribution. It also makes it possible to model all aspects of the system with fewer displacement values and thus fewer models.

CHAPTER 4

OSCILLATORY OPERATION OF THE BRUSHLESS DC TUBULAR MACHINE

4.1 Introduction

This chapter details the principles of the brushless tubular machine operation concentrating first on the general brushless machine operation for one-way motion. This is then extended to include the requirements of a linear machine to produce a reciprocating motion.

The main feature of brushless dc machines, as their name suggests, is their ability to work without the need for brushes and a commutator. The task of these devices is performed by electronically sensing the excitation (rotor or secondary) position and making the necessary switching changes (commutation) automatically. Since the armature (stator or primary) coil currents are switched at fixed excitation (pole system) positions relative to the excitation field, the electromagnetic effect of a dc machine is produced.

These machines can be thought of as either a synchronous machine supplied at variable frequency or a dc machine. The essential difference between the two is that in one case, the dc machine system, the armature current loading is phase locked in quadrature to the poles as it is in a dc machine. Whereas in the other case whilst sychronism is maintained the phase angle between the rotor current pattern and the stator poles varies according to load.

4.2 The Principle of the Brushless Machine Operation

Hall effect devices are used for field poles position sensing. These unilateral devices are placed on the armature teeth of the top block at 120 ° intervals and detect the reference segment position [Figs. 4.1(a) and 2.11(c)]. Reading 0 when they see a south pole and 1 a north pole or no field they produce the digital signals shown as H1, H2 and H3 on Fig. 4.2(b). These signals are then used to produce the waveforms shown at T1 to T6 on Fig. 4.2(b) by means of a Hall signal decoder. These are in turn used to control the transistor switches of the inverter of Fig. 4.2(a) which produces the three phase currents of the armature winding. These are also shown on the figure in idealised form.

The Hall signal decoding and the production of the three-phase currents are accomplished by using a smart power chip as the driver. This power IC, Unitrode 3620, is a brushless dc motor driver capable of driving all three phases of a brushless dc motor **[4.1]**. It comprises of a Hall signal decoder, a three phase transistor inverter with free-wheeling diodes for transient current suppression and a current magnitude limiter. Appendix F gives the specifications of this driver.

The electromagnetic thrust force production of the machine and power conditioning system can be explained by examining the relationship between the distribution of the permanent magnet mmf and the armature mmf produced by the injected phase currents **[4.2]**. As previously discussed in order to obtain maximum thrust force from the machine the force angle δ, between excitation and armature mmfs, must be kept as close to 90 ° as possible throughout the machine operation. However, as can be observed from the current waveforms of Fig. 4.2(b), the phase currents stay fixed in space for 60 °, which is the switching interval length, while the pole system moves. One practical approach to this is to make the switching interval take place while the force angle changes between 120 ° and 60 ° thus covering the

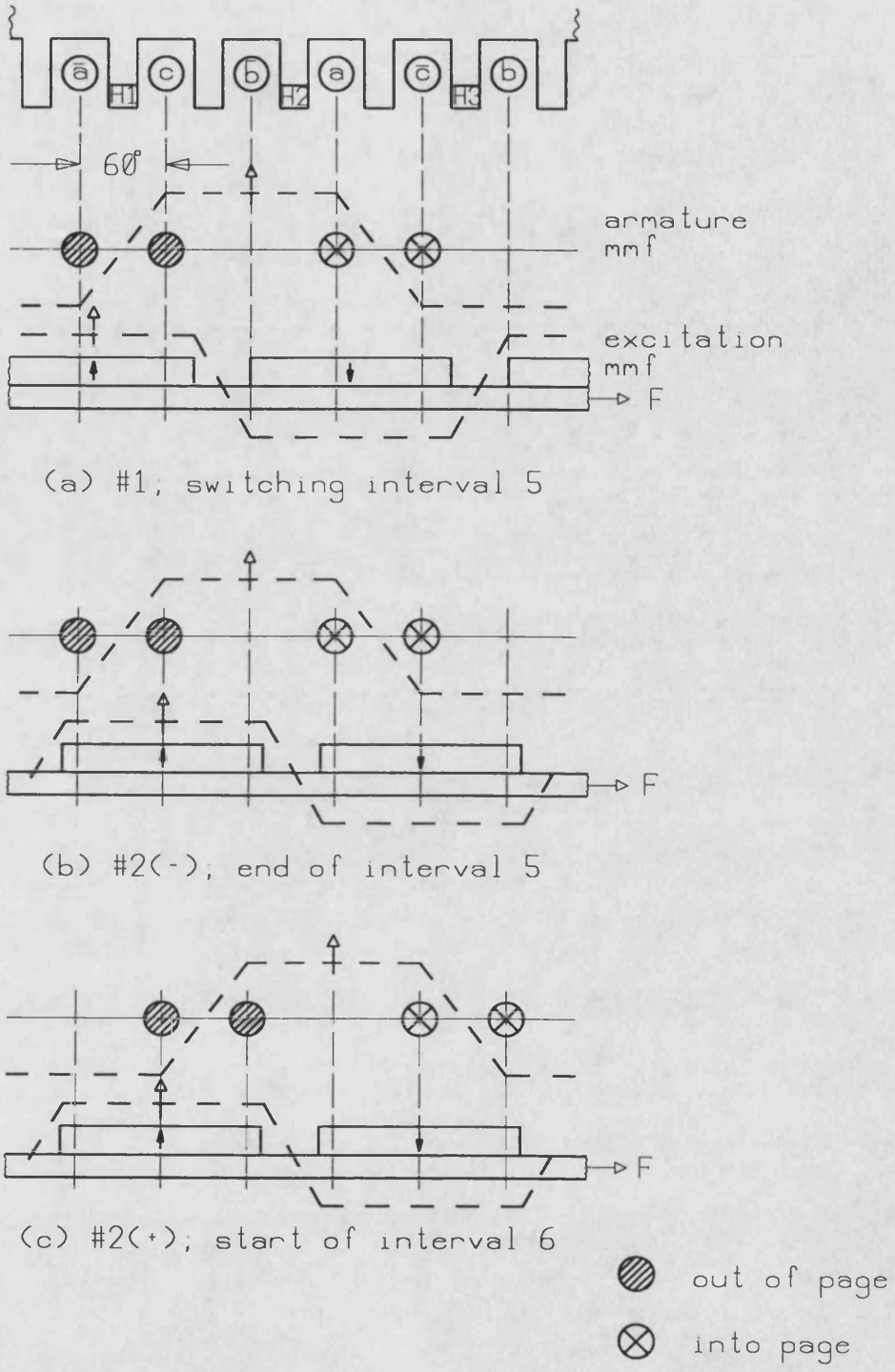

Figure 4.1 Force (Torque) Production of the Brushless DC Machine

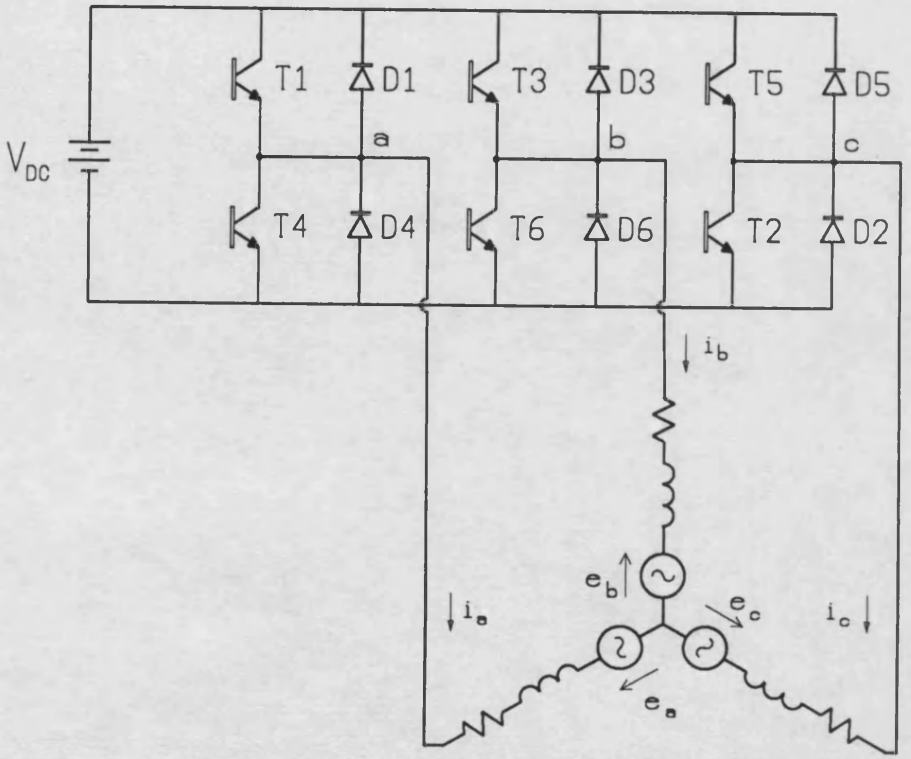

(a)

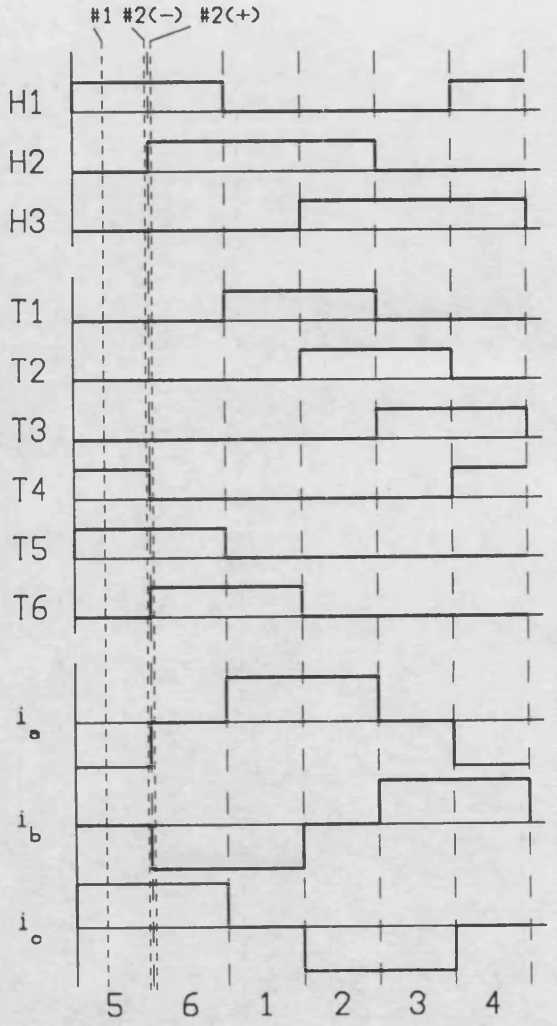

(b)

Figure 4.2 (a) Basic Inverter and Brushless DC Machine
(b) Excitation Position and Transistor Switching Signals and Idealized Phase Currents

maximum part of the electromagnetic force profile as given in Chapter 3. This is done by placing the Hall effect sensors with respect to the armature phases in the correct position.

The operation of the basic brushless dc machine can be explained by the interaction between armature currents and permanent magnets. For the pole system position shown in Fig. 4.1(a), Hall sensors H1, H2 and H3 will read 1, 0 and 0 respectively from the spacial distribution of the reference permanent magnet mmf. This Hall signal combination corresponds to switching period 5 as shown in Fig. 4.2(b). The instant is marked as #1 on the figure and makes the inverter switches T4 and T5 switch on for the direction of motion of interest. This produces three phase currents i_a , i_b and i_c with signs -, 0 and + respectively causing the armature current and mmf distribution shown in Fig. 4.1(a). As a result of armature and pole system mmfs' interaction, the pole system is moved to the right. These currents stay fixed in time and space, while the pole system moves, until the end of switching interval 5 which is marked as #2(-) on Fig. 4.2(b). The force angle between field poles and armature axes at this instant is 60 ° [Fig. 4.1(b)]. At position #2(+) the Hall signal combination changes to 1, 1 and 0 as a result of sensor H2 being under the field of a north pole magnet, giving rise to a switching interval change and making i_a , i_b and i_c 0, -1 and 1 respectively and to a new current distribution as shown on Fig. 4.1 (c). At this moment armature mmf suddenly "jumps" 60 ° forward in space changing the force angle from 60 ° to 120 °. In this new switching interval and fixed armature current and mmf placement the field poles continue to move on, reducing the force angle from 120 ° down to 60 ° where it again becomes 120 ° due to another switching change. This results in an armature mmf which takes 60 ° discrete jumps.

The magnitude of the force exerted on the moving pole system are proportional to the product of the pole system and armature mmfs and the sine of the angle δ between their axes. Pole system mmf is constant due to the permanent magnet poles

and armature mmf is proportional to the magnitude of the current flowing in its winding. Therefore the electromagnetic thrust force is a function of the armature currents and force angle δ.

The armature field set up by the phase currents has a demagnetising and remagnetising effect on the permanent magnet poles **[4.3]**. This effect may cause permanent demagnetisation in parts of the poles and is therefore important in terms of both design and operation of the machine. Appendix E gives, to a first approximation, an analysis for different pole system positions and calculates the maximum allowable phase currents to prevent any permanent change in the permanent magnet magnetisation.

4.2.1 Circuit Modes for One-Way Operation

During the normal force production process of the brushless dc machine, different circuit configurations are formed. These configurations include the transient circuits that are produced when a switching interval change takes place. They are formed because of the inductive nature of the machine winding and the necessity to provide a path for the transient currents involved. This can be explained in detail by taking the same example used in the previous section. Figure 4.3(a) gives the circuit formed when the switching interval is 5. The current directions are -, 0 and + for phases *a, b* and *c* respectively and the emfs oppose the currents. As soon as the switching interval changes and becomes 6, T4 switches off and T6 switches on. While the current in the newly formed *bc* loop increases, the inductive current of the outgoing phase *a* flows through D1 and T5 and decays [Figure 4.3(b)]. This continues until the associated energy of phase *a* current is completely dissipated in the phase resistances leaving the circuit as shown in Figure 4.3(c). The current commutation is now complete and only two phases carry current.

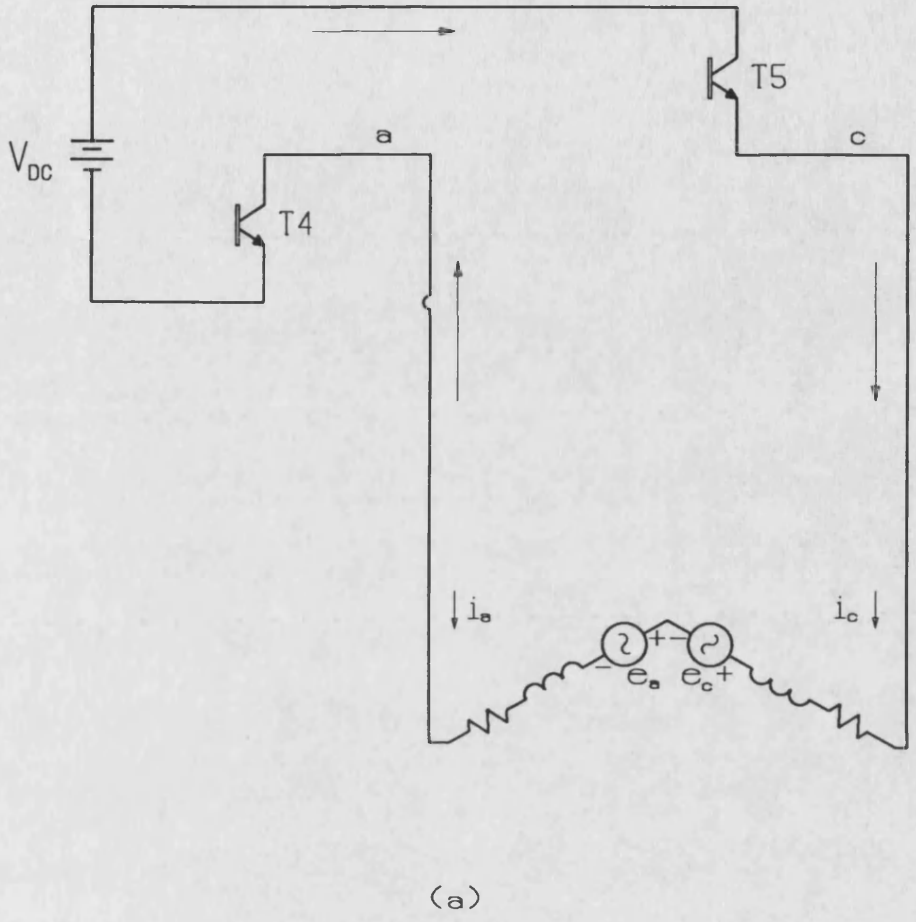

Figure 4.3 Circuits Formed During:
(a) Switching Interval 5
(b) Commutation from 5 to 6
(c) Switching Interval 6

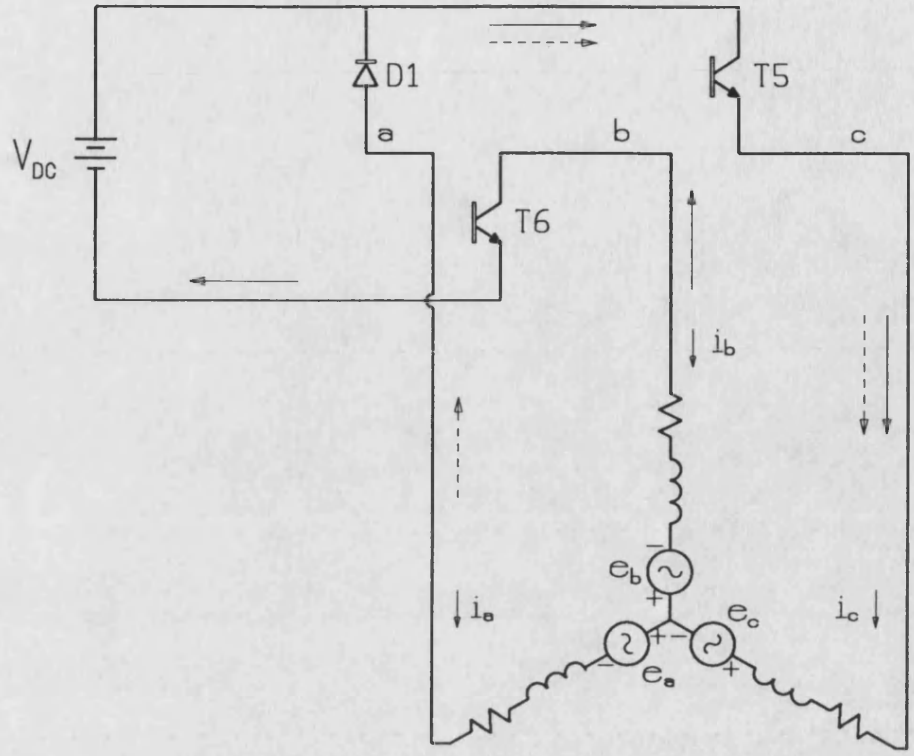
D1
T5
T6
a
b
c
V_{DC}
i_b
i_a
i_c
e_b
e_c
e_a

(b)

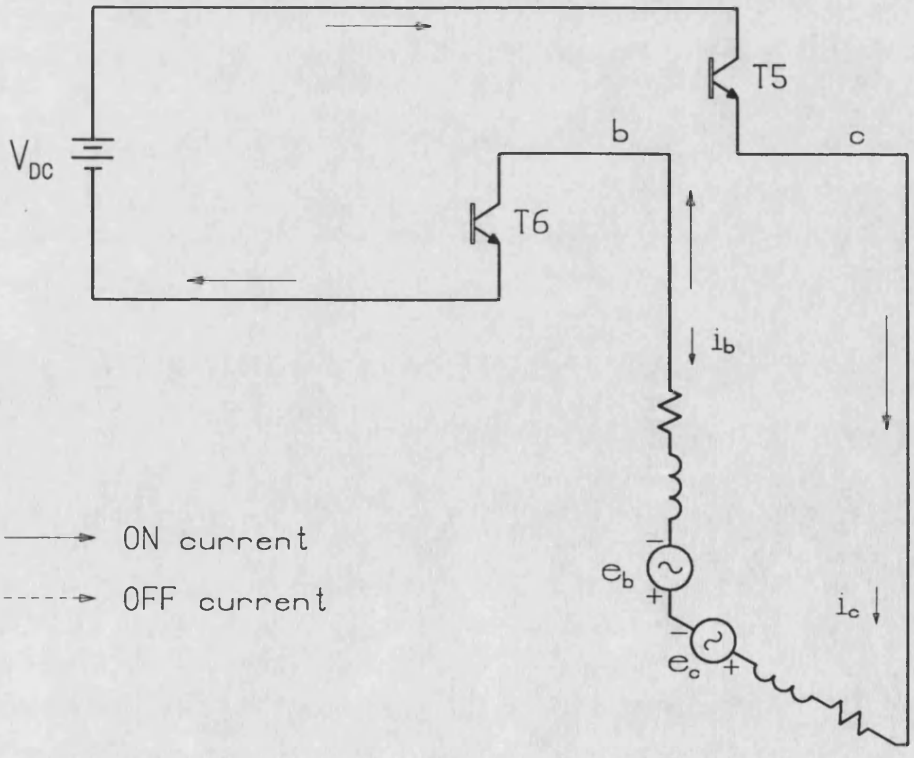
T5
T6
b
c
V_{DC}
i_b
i_c
e_b
e_c
ON current
OFF current

(c)

4.3 Oscillatory Operation of the Brushless Tubular Machine

The previous section detailed the basic principles on which the brushless dc machine operation is based. This, although being applicable to the tubular motor, involves only unidirectional motion. For some applications, however, the machine needs to be arranged to perform in a repetitive fashion. Reverse direction for this oscillatory operation can be obtained by applying reverse currents, at an excitation position, to those shown in the previous section.

A simplified block diagram of the oscillatory operation of the drive system is given in Figure 4.4. In addition to the driver chip and the tubular motor with Hall sensors for excitation position sensing, it has two additional sensors, ESright and ESleft, for travel end sensing and a sense resistor (R_s) for current magnitude limiting.

The current magnitude control is accomplished by sensing the voltage drop across the sense resistor, R_s , and feeding it to the voltage comparator of the chip which compares this voltage with a predetermined reference voltage. The output of the comparator is fed into a monostable multivibrator, which controls the on-off states of the bottom transistors of the three inverter legs. When the voltage signal from the sense resistor exceeds the reference voltage, the bottom transistors are switched off and the inductive phase currents circulate through the conducting upper transistor and a free-wheeling diode. The off-time of the monostable is determined by appropriately choosing a timing capacitor and a resistor which are connected to the timing input of the chip. Current magnitude can consequently be controlled by the proper selection of R_s [please see Appendix F].

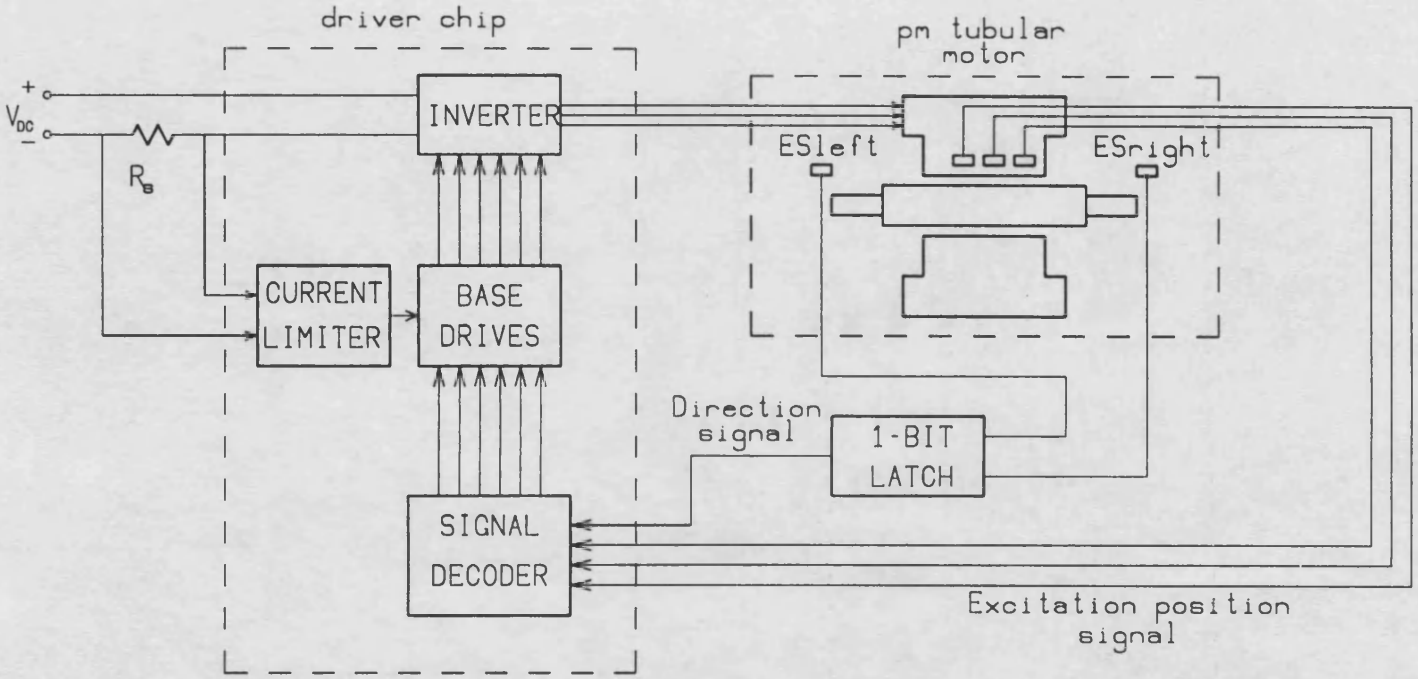

Figure 4.4 Block Diagram of the Oscillatory Drive System

Table 4.1 shows the 60 ° Hall decoding used for the oscillatory operation of the system. Here, *abc* phase sequence is taken to be when the pole system moves from left to right and direction signal is 0. Phase sequence *bac* is then the reverse direction for which direction signal is 1.

Table 4.1

Function Table for the Oscillatory Operation

Direction Signal (DS)	H1	H2	H3	Switching Interval	i_a	i_b	i_c
1	1	0	1	1	+	-	0
1	1	0	0	2	+	0	-
1	1	1	0	3	0	+	-
1	0	1	0	4	-	+	0
1	0	1	1	5	-	0	+
1	0	0	1	6	0	-	+
0	1	0	1	4	-	+	0
0	1	0	0	5	-	0	+
0	1	1	0	6	0	-	+
0	0	1	0	1	+	-	0
0	0	1	1	2	+	0	-
0	0	0	1	3	0	+	-
DS=1; Phase Sequence=bac; Excitation Direction=left DS=0; Phase Sequence=abc; Excitation Direction=right							

4.3.1 Direction Control for the Oscillatory Operation

The digital Forward/Reverse input of the driver chip is used for direction control by combining it with the other three Hall effect signals to determine the switching interval, i.e. the phase current directions of the inverter. The direction signal (DS) is obtained by using two additional Hall effect sensors, end sensors (ES) as a basis of end-stops. These sensors, one on the left of the armature and one on the right, are placed on the extensions of the armature frame which holds the four armature blocks together and are on the line of the reference permanent magnet segment [Figure 4.4]. They detect the existence of permanent magnets in the same way as the other Hall sensors do, reading 0 when their marked side sees a south pole and 1 a north pole or no field. They read the fields of the left and rightmost segments. Since the leftmost segment is a south pole and the rightmost a north pole, the marked side of ESleft faces the field poles and the unmarked side of ESright. This is done in order to get the same response from the sensors.

The outputs of these sensors are fed into a 1-bit memory latch as shown in Figure 4.5 as inputs. This memory uses two TTL NAND logic gates and is made necessary by the requirement for a memory device which can hold the last reading of the sensor-pair after the pole system has reached an end and reversed. The way the direction control works can be explained by the help of Tables 4.1 and 4.2. Suppose that the end-sensors do not see any magnet when the system is switched on (the pole system is in the middle of its travel), then both sensors will be high (1). The Q output of the latch will also be 1. Taking the pole system position to be the same as that of Figure 4.1(a) where one-way motion is explained, position sensors H1, H2 and H3 will be 1, 0 and 0 respectively. According to Table 4.1, these direction and position signals will give rise to phase currents with the direction +, 0, - for i_a , i_b and i_c respectively. This will move the pole system to the left, that is in the reverse direction to that of Figure 4.1(a). The pole system continues to move in this direction with

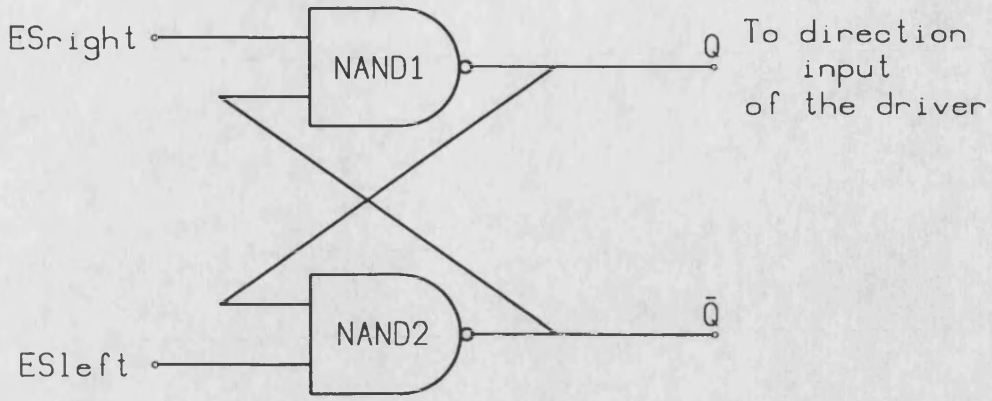

Figure 4.5 The Direction Control Latch

Table 4.2

Operation of the Direction Control Latch

Excitation Position	ESleft	ESright	Q(DS)	Excitation Direction Command
middle	1	1	1	left
left	0	1	0	right
left	1	1	0	right
right	1	0	1	left
right	1	1	1	left
left	0	1	0	right

phase sequence *bac* in the way explained in Section 4.2, until the left end-sensor detects the left-hand-end south pole. At this point it becomes 0, making the latch output 0 as shown in Table 4.2. This change in the direction signal demands reversed phase currents to those just before the direction signal change, exerting a right-hand directed force on the field poles. When it moves in this direction, the left end-sensor becomes 1 again as the magnet pole at the left-hand-end of the pole system moves away from the sensor. But the latch output stays the same; thus the pole system carries on in the right-hand direction. This goes on until the right end-sensor detects the right-hand-end pole and direction signal becomes 1 when the pole system is first decelerated by the reversed electromagnetic forces and then accelerated in the left-hand direction.

This simple technique, however, should be used with care as, in the case of high excitation speeds, the transient currents which are driven by the phase back emfs can be very high. Since these currents circulate through diodes and phases, they cannot be limited by the chip's protection circuitry and can be dangerous for the switching devices. These transients are discussed next.

4.3.2 Circuit Modes For the Oscillatory Operation

The transient circuit for one-way operation is taken care of by the antiparallel diodes and upper transistors. These components of the inverter carry the transient inductive phase currents during commutation. This was explained in Section 4.2.1. For oscillatory operation, however, there is an additional transient period during which, along with the above inverter components, phase emfs also play an important role. This "direction transients" period starts with the change of direction signal and ends when the excitation stops at one end of its travel.

How this happens can be explained by the help of Figures 4.6 and 4.7. Figure 4.6 shows transient plots of the direction signal, the timing-pin voltage of the driver chip and the three phase currents for the period when direction signal changes from 0 to 1 (pole system at the right-hand-end). When the timing voltage of the driver is high, the bottom transistors of the inverter are enabled and when it is low they are disabled. Figure 4.7 shows the circuits formed by the conducting transistors and/or diodes of the inverter-machine diagram of Figure 4.2(a). Until the moment when the direction signal change takes place, $t<t_1$, the system is in its normal mode of operation. With direction signal 0, H1 = 0, H2 = 1 and H3 = 1, the switching interval is 2 and the operating circuit is as shown in Figure 4.7(a) and the pole system moves to the right. Here, T1 and T2 are conducting and the phase currents are i_a = +, i_b = 0 and i_c = - (please see Table 4.1). When direction signal becomes 1 at t_1 the new switching interval 5 demands reversed currents by switching off T1 and T2 and switching on T4 and T5. Transistors T1 and T2 switch off instantly. However, T4 and T5 cannot switch on immediately because of the inductive phase currents in the circuit. These currents now flow through D4 and D5 as shown in Figure 4.7(b). This very short transient period lasts until the current is reversed by the sum of the supply voltage and the induced emfs which act in the same direction. The magnetic energy of the phases and the kinetic energy of the moving pole system are fed into the supply battery during this period. The pole system moves to the right with a right-hand directed electromagnetic force. When the current reverses at t_2 , T4 and T5 are switched on and take over this current. Phase currents i_a , i_b and i_c have now become -, 0 and + respectively and the circuit is as shown in Figure 4.7(c). The pole system still moves to the right but as the electromagnetic force has also reversed, it is now decelerated. In the new circuit shown in Figure 4.7(c), the supply voltage and induced emfs continue to support each other. It will be observed that for the periods $t_1<t<t_2$ and $t_2<t<t_3$ the components *(V, e, R, L)* of the circuit stay the same, i.e. there is no switching action. This can also be seen from the current waveforms in Figure 4.6 from t_1 to t_3. At t_3 as the magnitude of current reaches the maximum allowed current

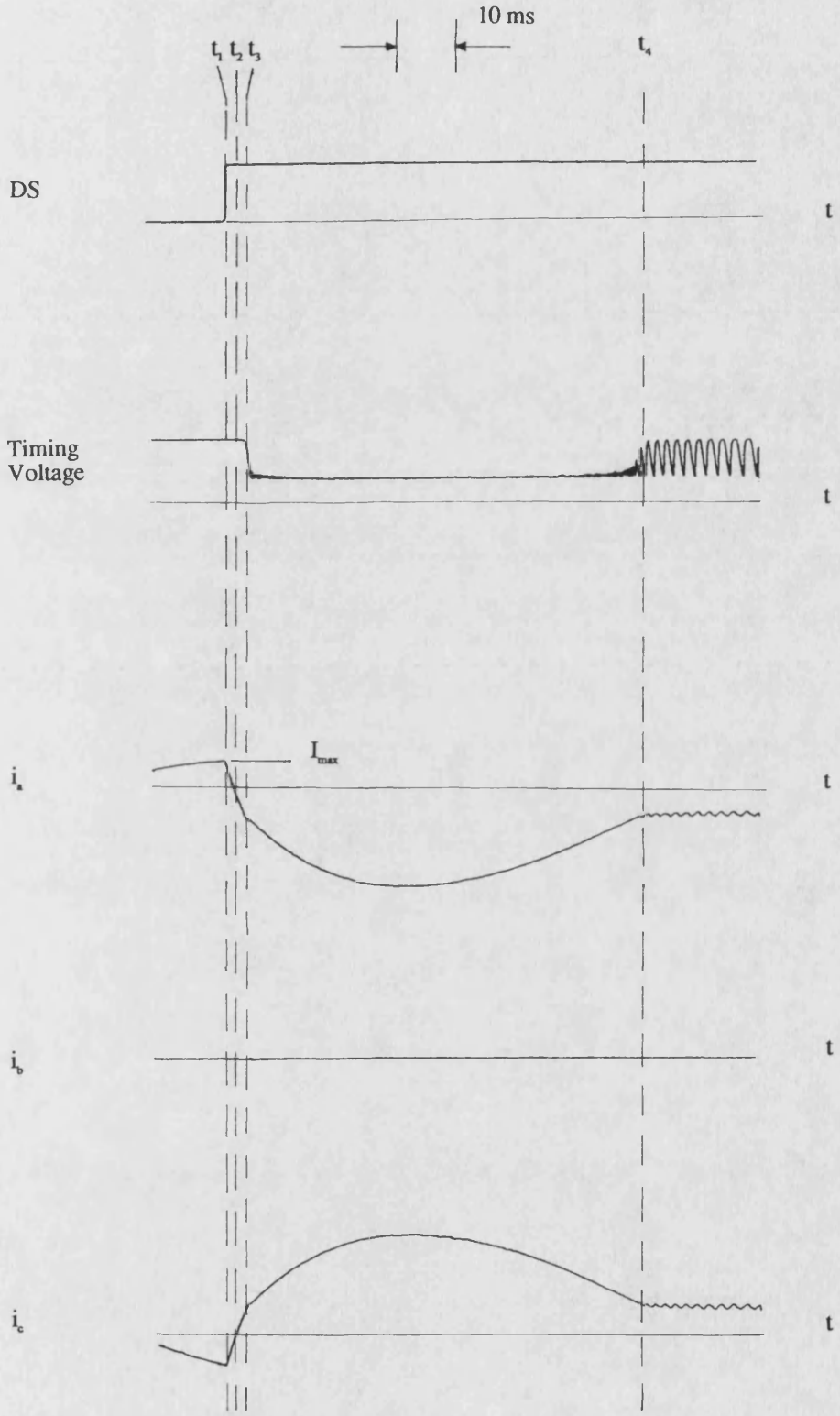

Figure 4.6 Circuit Transients When the Excitation is at the Right-Hand-End (Right-Hand-End Direction Transients)

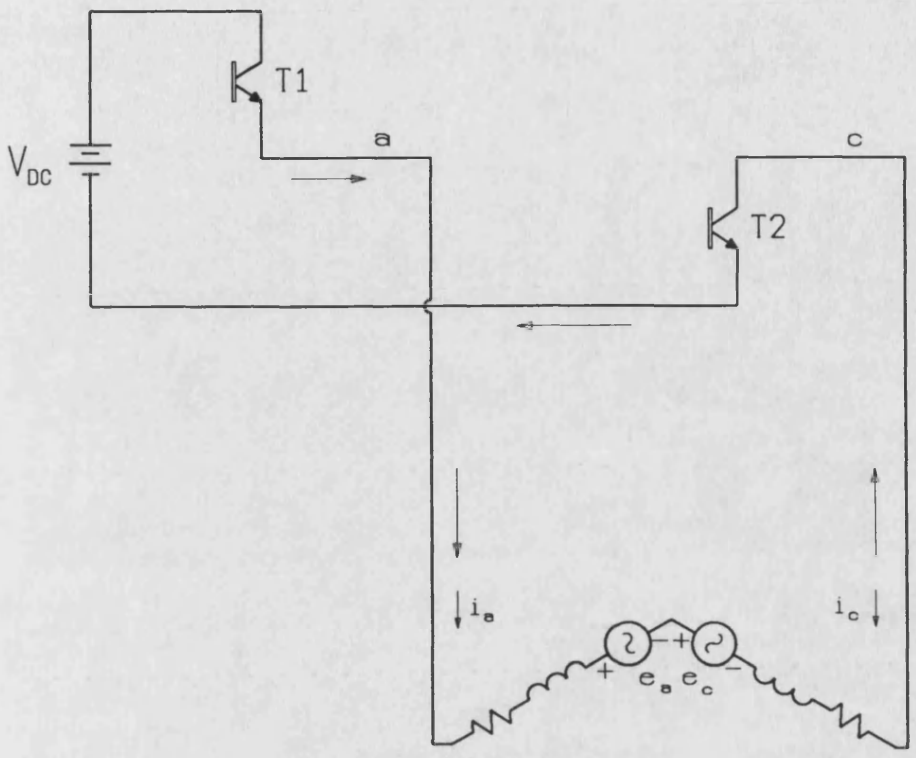

(a) $t<t_1$

Figure 4.7 Circuits Formed During Right-Hand-End Direction Transients

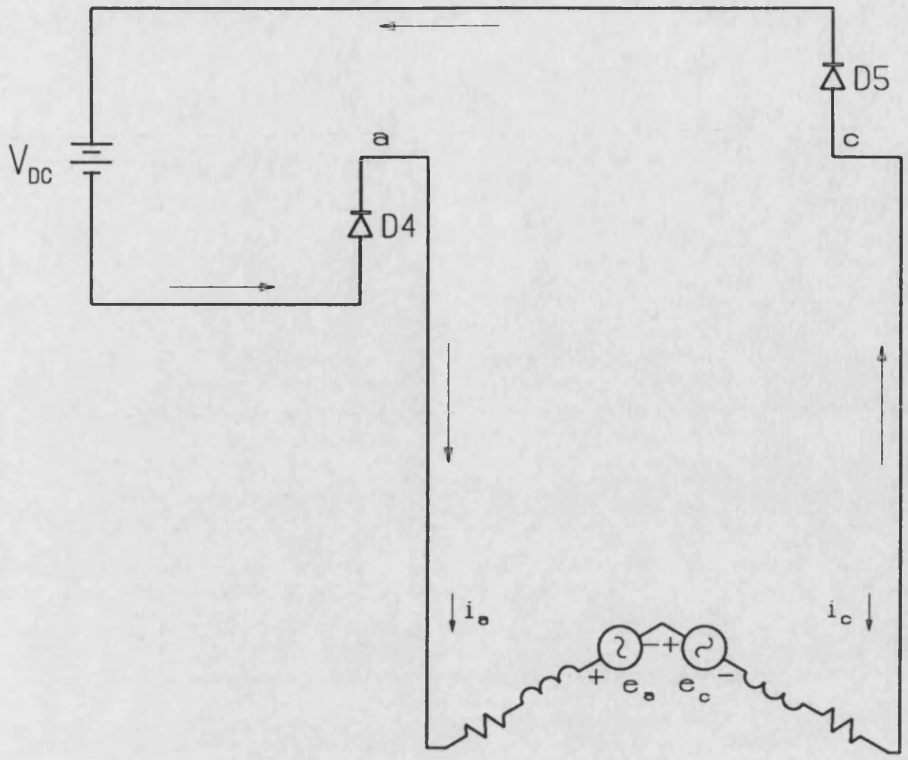

(b) $t_1 < t < t_2$

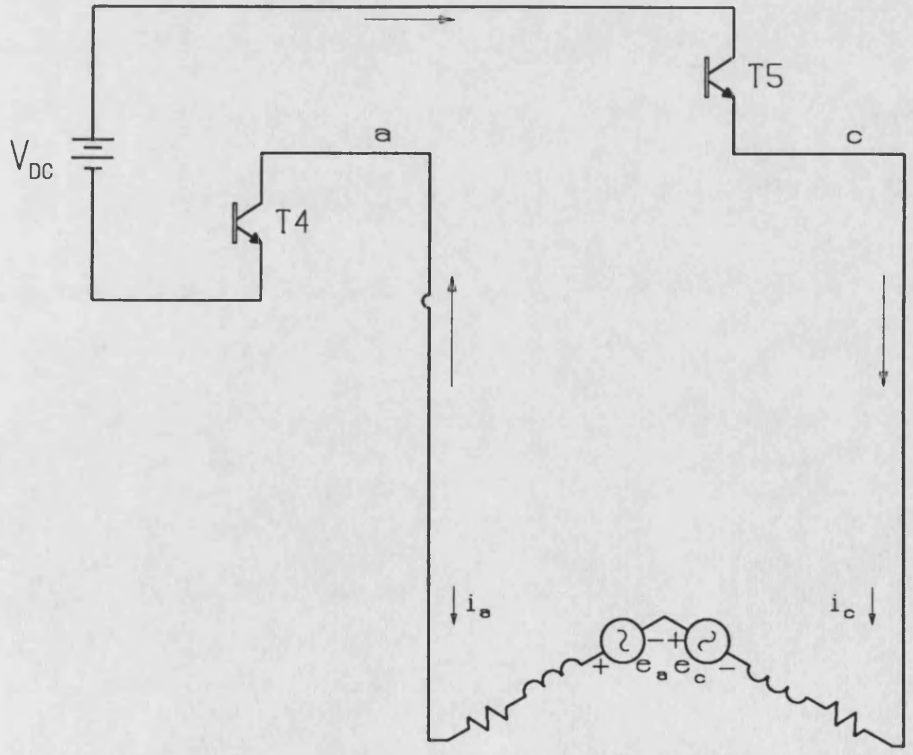

(c) $t_2 < t < t_3$

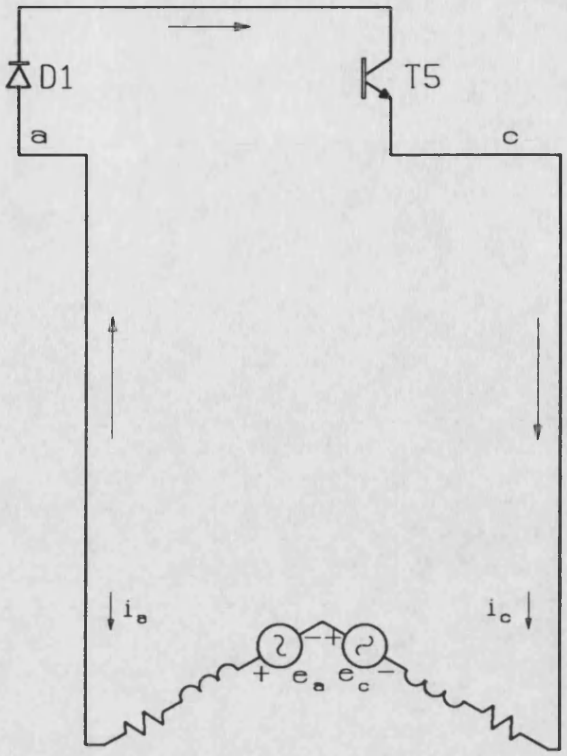

(d) $t_3 < t < t_4$

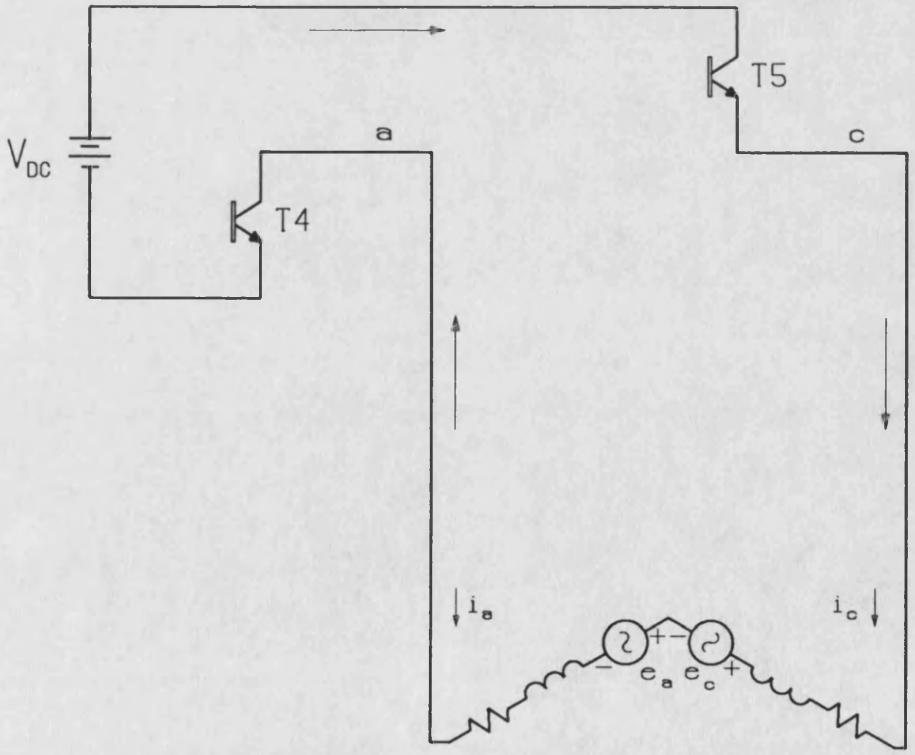

(e) $t_4 < t$

before chopping, I_{max}, bottom transistors of the inverter are disabled due to the normal current chopping function of the driver. This cuts off the supply voltage from the circuit and the new circuit becomes as shown in Figure 4.7(d). Here the current is driven only by the phase emfs, through D1 and T5, which are in turn due to the moving pole system, and this current also produces the decelerating left-hand directed force. During the first part of this period, $t_3<t<t_4$, the current increases at a slower *di/dt* rate compared to the previous period due to the absence of the supply voltage in the circuit. For the whole period, the timing voltage of the driver, shown in Figure 4.6, is low and the supply voltage stays cut-off since the dc current level is above I_{max}. This continues until the current magnitude drops down to I_{max} at t_4 when T4 switches on connecting the supply battery into the circuit. The pole system may have now stopped and started moving to the left and the circuit is now as given in Figure 4.7(e). If, however, it has not stopped then until it does the circuit will be as shown on the figure, except that the emf polarities will be the reverse to those shown. From the time the pole system starts accelerating to the left, its velocity and the force acting on it are both negative. That is the direction transients are over and the operation mode is one-way motion mode.

During the interval from t_3 to t_4, it may happen, before the current drops to I_{max} or the pole system stops, that the associated upper diode of the non-conducting phase is forward biased. This is due to the line to line voltage between the switched-off phase and the phase whose associated upper transistor is conducting, becoming positive. As a result, a new loop is formed in this transient mode and all three phases carry currents. The associated upper diode would be D3 and the line to line voltage V_{bc} in the example taken here. The switches and phases involved will depend on the switching interval in which the direction signal change takes place and therefore on the placement of the end sensors.

These circuit and operation modes will be modelled in Chapter 5 in order to simulate the dynamic behaviour of the inverter and the overall system.

4.4 Conclusions

One-way and oscillatory operations of the brushless tubular motor have been explained. It has been shown that oscillatory operation of the system can be achieved using a standard 3-ϕ brushless DC motor driver designed for rotary machine applications. This is done by merely using two additional position sensors to detect the excitation stroke ends and a simple memory device.

Normal and transient operation modes of the system, both electrically and mechanically, have been described using the actual system specifications. During direction transients, which take place between a direction signal change and the excitation reaching the stationary end point in the oscillatory motion, the phase currents vary differently from one-way motion transients. During this period, especially for the time when only phase emfs drive the currents and the excitation is decelerated fast, the current magnitude limiter of the driver chip cannot prevent the phase currents from going beyond the predetermined value. These currents can be excessive in the case of high excitation speeds where phase emfs are high and may be dangerous for the switching devices of the inverter. For the speeds involved, however, these currents are reasonable as will be shown later.

CHAPTER 5
DYNAMIC PERFORMANCE SIMULATION OF THE TUBULAR BRUSHLESS DC MACHINE

5.1 Introduction

This chapter gives the derivation of a numerical model for the dynamic simulation of the tubular permanent magnet motor and its associated power electronics drive circuitry. The governing electrical circuit equations for the system are derived from the classical representation of the three phase synchronous machine model. Parameters for these equations are obtained from finite element methods and they are solved numerically in order to simulate the electrical performance of the system. The mechanical performance of the system is also predicted in conjunction with the system electrical performance to yield a full dynamic simulation of the overall system.

Permanent magnet machines can be of two different types. In the first of these, the permanent magnet synchronous motor (PMSM), the phase of the armature current is not tied to the rotor position so that the phase angle between the mmf wave produced by the armature and the excitation mmf (load angle) varies with load. The PMSM is very similar to the conventional wound rotor synchronous motor and has sinusoidally varying back emfs and therefore requires sinusoidal stator currents to produce a constant torque (force). In the second type, the brushless dc motor (BDCM), the armature current pattern is phase locked to the dc poles just as in a dc machine by using position sensors. The BDCM has a quasi square armature current pattern and in order to produce a constant torque (force) it requires trapezoidal back emfs **[5.1]**.

Since the introduction of permanent magnets for electrical machines excitation, considerable attention has been given to their performance modelling. The classical *d-q* axis model (Park's transform) can safely be applied to a machine with sinusoidally varying excitation and armature mmfs both of which smoothly rotate in a reference frame. For machines which involve nonsinusoidal mmfs the *d-q* axis model is not the best approach. Instead, a technique based on phase variables offers many advantages **[5.1]**.

Most of the earlier papers used the *d-q* axis technique for machines with both sinusoidal and rectangular phase currents and simulated the steady-state electrical performance of permanent magnet machines **[5.2-5.6]**. The first papers on the modelling of brushless DC motors with a digital approach for calculating the mechanical performance of the system, as well as the electrical, appeared in the literature in the early 80's **[5.7, 5.8]**. This technique, based on the *abc* frame with no transformation involved, combined the machine and the power electronics drive circuitry with either current or voltage source inverter and modelled the switching nature of the system in the time domain. This digital simulation method proved useful for the dynamic modelling of the permanent magnet machines and has been used by other authors for steady-state and transient calculations **[5.9, 5.10]**. Both *d-q* axis and *abc* frame techniques have been adapted by other authors for the simulation of PMSM and BDCM's for models of conventional geometry and control **[5.11-5.15]**, for a microprocessor based PMSM drive **[5.16]** and a BDCM system taking into account rotor dumping effects **[5.17]**.

All of these studies, however, simulated the rotary permanent magnet machine and there is an absence of published work on the performance simulation of linear versions. Yamamoto analysed the starting characteristics of a permanent magnet flat-type linear motor using equivalent magnetic circuits and analytical expressions for one-way motion **[5.18]**. This device, however, acts as a pulse motor. Yoshida

simulated the performance of a flat-type long armature linear synchronous motor analytically, using per-phase equivalent circuits **[5.19]**. However, the simulation is based on a preset duty-cycle and does not include the phase variables and dynamic performance of the system.

This thesis presents what is to the best of the author's knowledge the first numerical simulation of the dynamic performance of a permanent magnet linear machine which can predict both electrical and mechanical performances of a drive system **[5.20]**.

5.2 Machine Model and the Derivation of Machine Equations and Equation of Motion

A decoupled *abc* model of a star connected, floating neutral three phase permanent magnet machine, with balanced phase impedances, is derived in this section from a coupled three phase classical machine model. The decoupling procedure makes the assumption that the self and mutual phase inductances are equal. Although this applies to the self inductances of the tubular brushless dc machine, the mutual inductance of one phase is smaller than the other two. However, as will be shown later, this procedure leads to a simplified model which considerably reduces the computer costs of the simulation and gives satisfactory results.

The coupled abc model of the machine is given in Figure 5.1. This model can mathematically be expressed in terms of phase variables as

$$\begin{bmatrix} V_a \\ V_b \\ V_c \end{bmatrix} = \begin{bmatrix} R_a & 0 & 0 \\ 0 & R_b & 0 \\ 0 & 0 & R_c \end{bmatrix} \begin{bmatrix} i_a \\ i_b \\ i_c \end{bmatrix} + \frac{d}{dt} \left\{ \begin{bmatrix} L_a & M_{ab} & M_{ca} \\ M_{ab} & L_b & M_{bc} \\ M_{ca} & M_{bc} & L_c \end{bmatrix} \begin{bmatrix} i_a \\ i_b \\ i_c \end{bmatrix} \right\} + \frac{d}{dx} \begin{bmatrix} \lambda_a \\ \lambda_b \\ \lambda_c \end{bmatrix} \cdot v \qquad \ldots(5.1)$$

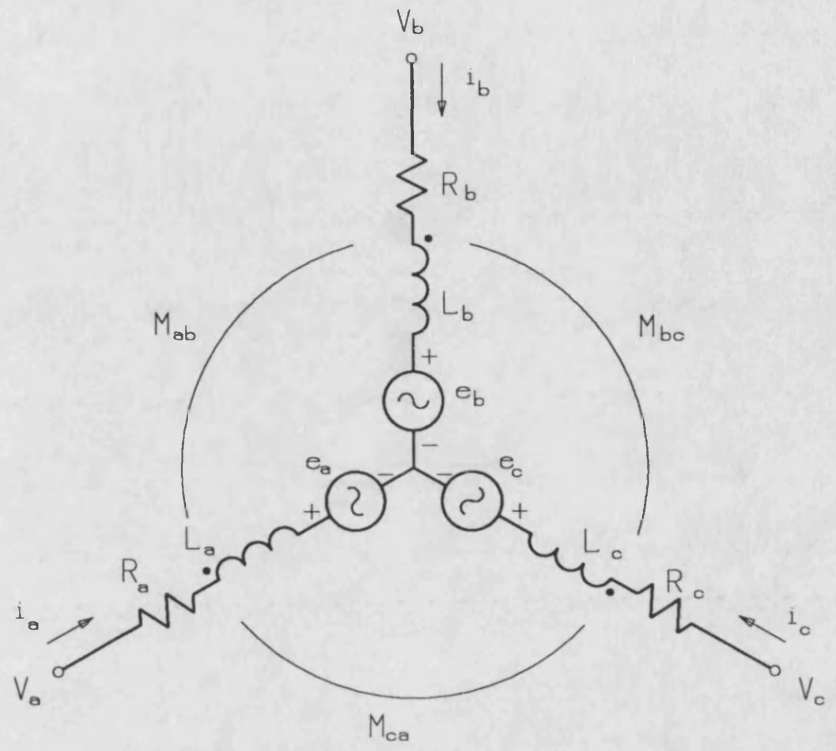

Figure 5.1 The Coupled Machine Model

where R_a, R_b, R_c are the phase resistances

L_a, L_b, L_c are the phase self inductances

M_{ab}, M_{bc}, M_{ca} are the phase mutual inductances

$\lambda_a, \lambda_b, \lambda_c$ are the phase flux linkages

x is the excitation displacement

$v = dx/dt$ is the instantaneous excitation velocity

This model assumes zero eddy current and hysteresis losses (core losses). The assumption is valid due to the usage of laminations in the armature and the low frequencies involved.

The last vector on the right side of the equation has the product of two differentials and therefore introduces non-linearity in the equation. It is also the only parameter which varies with respect to excitation position and thus time. The elements of this vector represent the back emfs induced in the armature phases due to the motion of the permanent magnets and are indicated on the figure as e_a, e_b and e_c.

Equation 5.1 can be simplified by a decoupling procedure [5.8]. The first part of this procedure makes the following assumptions:

- Armature phase resistances are equal: This is true since all three phases have equal numbers of series coils.

$$R_a = R_b = R_c = R \qquad \ldots(5.2)$$

- Armature phase self and mutual inductances are equal: This assumption is valid for the self inductances but an approximation for the mutual inductances. As can be seen from Chapter 3, phase self inductances are very nearly equal. For the mutual inductances, however, two phases are equal and the third one is smaller than the other two. For the simplified model this

procedure leads to, it is assumed here that the mutual inductance between phases a and b have the value of the other two mutual inductances. This approximation is an acceptable one considering the ease with which the simplified model can be implemented on the computer. Thus

$$L_a = L_b = L_c = L \qquad \ldots(5.3a)$$

$$M_{ab} = M_{bc} = M_{ca} = M \qquad \ldots(5.3b)$$

- Inductances do not change with excitation position and hence time: This is because the relative permeability of the permanent magnet material is very close to unity and hence the magnetic air-gap is constant, as explained in Chapter 3.

These assumptions lead to the following equation for the system.

$$\begin{bmatrix} V_a \\ V_b \\ V_c \end{bmatrix} = \begin{bmatrix} R & 0 & 0 \\ 0 & R & 0 \\ 0 & 0 & R \end{bmatrix} \begin{bmatrix} i_a \\ i_b \\ i_c \end{bmatrix} + \begin{bmatrix} L & M & M \\ M & L & M \\ M & M & L \end{bmatrix} \frac{d}{dt} \begin{bmatrix} i_a \\ i_b \\ i_c \end{bmatrix} + \frac{d}{dx} \begin{bmatrix} \lambda_a \\ \lambda_b \\ \lambda_c \end{bmatrix} \cdot v \qquad \ldots(5.4)$$

This equation can further be modified with the following, which is the second part of the decoupling process;

For a star connected winding Kirchhoff's current law gives

$$i_a + i_b + i_c = 0 \qquad \ldots(5.5)$$

The first derivative of this with respect to time yields

$$\frac{di_a}{dt} + \frac{di_b}{dt} + \frac{di_c}{dt} = 0 \qquad \ldots(5.6)$$

The second (inductance) term at the right hand side of Eqn. 5.4 can be written as

$$\begin{bmatrix} L\frac{di_a}{dt}+M\frac{di_b}{dt}+M\frac{di_c}{dt} \\ M\frac{di_a}{dt}+L\frac{di_b}{dt}+M\frac{di_c}{dt} \\ M\frac{di_a}{dt}+M\frac{di_b}{dt}+L\frac{di_c}{dt} \end{bmatrix}$$

With the help of Eqn. 5.6, this term can further take the form

$$\begin{bmatrix} (L-M)\frac{di_a}{dt} \\ (L-M)\frac{di_b}{dt} \\ (L-M)\frac{di_c}{dt} \end{bmatrix}$$

and incorporating this into Eqn. 5.4 yields

$$\begin{bmatrix} V_a \\ V_b \\ V_c \end{bmatrix} = \begin{bmatrix} R & 0 & 0 \\ 0 & R & 0 \\ 0 & 0 & R \end{bmatrix} \begin{bmatrix} i_a \\ i_b \\ i_c \end{bmatrix} + \begin{bmatrix} (L-M) & 0 & 0 \\ 0 & (L-M) & 0 \\ 0 & 0 & (L-M) \end{bmatrix} \frac{d}{dt} \begin{bmatrix} i_a \\ i_b \\ i_c \end{bmatrix} + \frac{d}{dx} \begin{bmatrix} \lambda_a \\ \lambda_b \\ \lambda_c \end{bmatrix} \cdot v \quad \ldots(5.7)$$

which is the decoupled machine model equation. The schematic representation of this is shown in Figure 5.2.

Once the phase currents and voltages are known, the machine power flow can easily be calculated. The instantaneous power components can be computed, neglecting the core losses, by multiplying both sides of Eqn. 5.7 by the transverse of the phase current vector. This is shown below in general matrix form

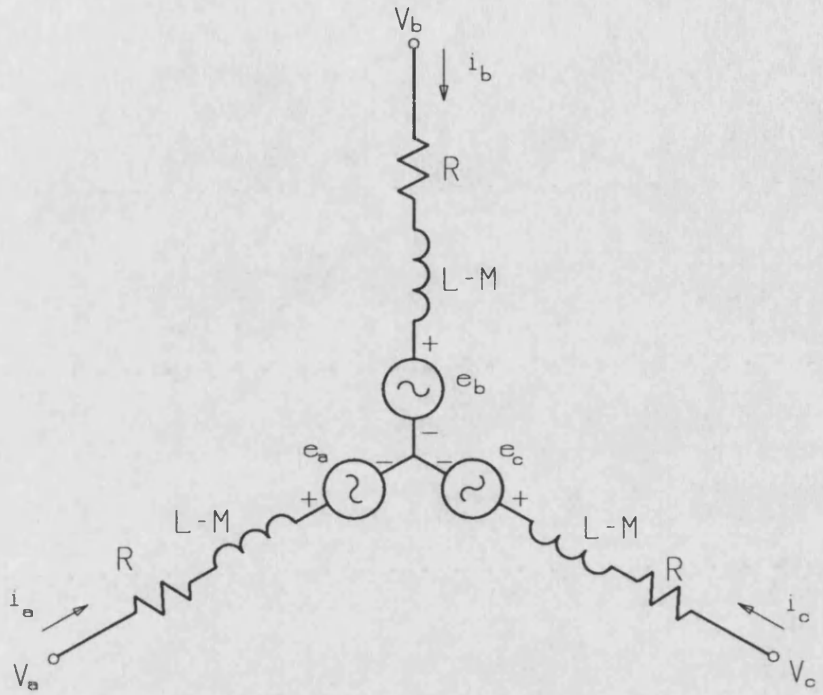

Figure 5.2 The Decoupled Machine Model

$$[i]^T[V] = [i]^T[R][i] + [i]^T[L-M]\frac{d}{dt}[i] + [i]^T\frac{d}{dx}[\lambda]\cdot v \qquad \ldots(5.8)$$

where the term on the left hand side of the equation and the three terms on the right hand side correspond to the following components respectively:

1. The instantaneous terminal power.
2. The instantaneous armature ohmic losses.
3. The instantaneous reactive power stored in the armature winding inductances.
4. The instantaneous electromagnetic power which represents the electromechanical energy conversion.

The instantaneous electromagnetic force can be calculated by

$$F_{em} = [i_a \quad i_b \quad i_c]\begin{bmatrix} e_a \\ e_b \\ e_c \end{bmatrix}\cdot\frac{1}{v} = [i_a \quad i_b \quad i_c]\frac{d}{dx}\begin{bmatrix} \lambda_a \\ \lambda_b \\ \lambda_c \end{bmatrix} \qquad \ldots(5.9)$$

which is the force exerted on the excitation by the armature currents, i.e. motor action.

In order to model the dynamics of the moving parts, a mechanical equation is required which relates acceleration to the total force acting on the excitation. This total force may be found by adding together the end-effect force (F_{end}) described in Chapter 3 and the electromagnetic force (F_{em}). The end-effect force, unlike the tooth cogging force, exists in the machine and has to be taken into account in the modelling process. The tooth cogging force has been eliminated by skew and therefore can be ignored. Hence, the mechanical equation becomes

$$F_{em} + F_{end} = m\frac{dv}{dt} \qquad \ldots(5.10)$$

where m is the mass of the moving parts.

These equations which relate the system electrical quantities to the mechanical quantities can be used to simulate both the transient and steady state performance of the tubular permanent magnet motor.

5.3 Modelling of the Machine Power Supply System

The second part of the drive system, the three phase inverter with its control electronics, is modelled in this section.

The abc phase variable model of the machine which was explained in the previous section can be solved when phase voltages and emfs are known. As mentioned earlier, phase emfs can be calculated using phase flux linkages and the excitation speed. Phase voltages (driver outputs), on the other hand, are switched continuously in order to produce the rectangular phase currents for the machine. It is therefore necessary to model the inverter system for the overall system simulation.

The schematic model in which the inverter model is associated with the decoupled machine model is given in Figure 5.3. In this model the voltage, V_{DC}, of the supply battery is represented by two voltage sources with a value $V_{DC}/2$ in order to establish a point with zero potential to which voltages in the circuit can be referred. As can be seen on the diagram, the voltages of the points a, b and c, can be $V_{DC}/2$, $-V_{DC}/2$ and 0. The resistor, R_s , is the sense resistor used to control the current magnitude. R_{ext}, on the other hand, is the resistance of the wire which connects the

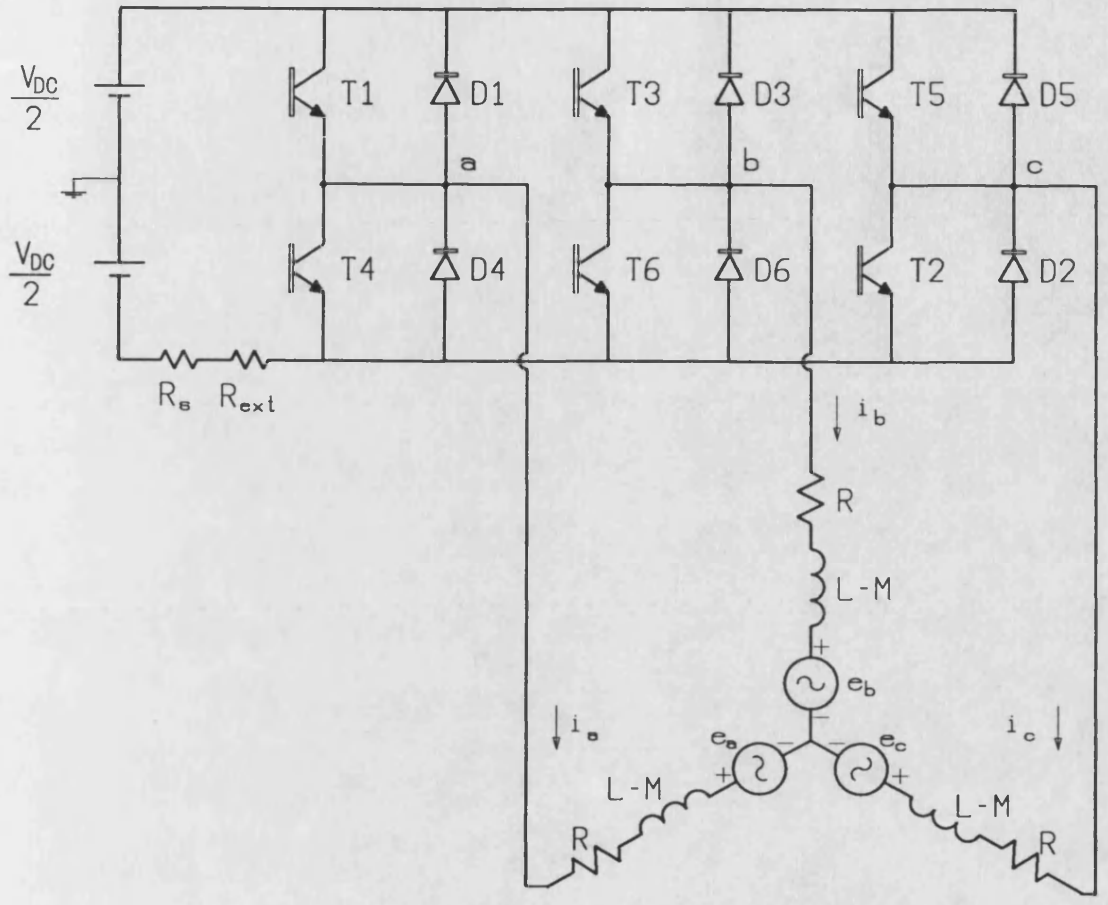

Figure 5.3 Inverter-Machine Model

battery to the inverter. Both these resistors are in the circuit when the voltage source supplies current to the phases. Phase emfs, e_a , e_b and e_c , are calculated using the Fourier series representation of the phase flux linkages as explained in Chapter 3.

The following assumptions are made in this model:

- Transistors and diodes are assumed to be ideal switches with no switching losses.

- The supply battery is represented by an ideal voltage source, its potential being equal to the open circuit voltage.

- Hall effect sensors are assumed to have no hysteresis.

5.3.1 Modelling of the Logic Signal Decoder

It was shown in Chapter 4 that the different switching intervals required for the inverter in order to achieve the brushless DC motor action were determined using a logic decoder. With two transistors conducting at a time (120 ° conduction), 6 intervals cover the whole operation cycle. These intervals are 60 ° in length and are given in Table 5.1.

The inverter switching modelling simulates the actual hardware. That is the switching interval of the inverter is decided by the excitation position signals (H1, H2 and H3) which are determined by the excitation position with respect to the armature and the direction signal. This is in turn decided by the excitation position and the direction of excitation motion. These signals are defined as logic variables and the switching intervals 1 to 6 are calculated using the logic equations

Table 5.1

Operation of the Inverter-Machine System

DS	H1	H2	H3	Top ON TR.	Bottom ON TR.	V_a $(V_{DC})/2$	V_b $(V_{DC})/2$	V_c $(V_{DC})/2$	Switching Interval
1	1	0	1	1	6	+	-	0	1
1	1	0	0	1	2	+	0	-	2
1	1	1	0	3	2	0	+	-	3
1	0	1	0	3	4	-	+	0	4
1	0	1	1	5	4	-	0	+	5
1	0	0	1	5	6	0	-	+	6
0	1	0	1	3	4	-	+	0	4
0	1	0	0	5	4	-	0	+	5
0	1	1	0	5	6	0	-	+	6
0	0	1	0	1	6	+	-	0	1
0	0	1	1	1	2	+	0	-	2
0	0	0	1	3	2	0	+	-	3

$$SI1 = DS \cdot H1 \cdot \overline{H2} \cdot H3 + \overline{DS} \cdot \overline{H1} \cdot H2 \cdot \overline{H3}$$

$$SI2 = DS \cdot H1 \cdot \overline{H2} \cdot \overline{H3} + \overline{DS} \cdot \overline{H1} \cdot H2 \cdot H3$$

$$SI3 = DS \cdot H1 \cdot H2 \cdot \overline{H3} + \overline{DS} \cdot \overline{H1} \cdot \overline{H2} \cdot H3$$

$$SI4 = DS \cdot \overline{H1} \cdot H2 \cdot \overline{H3} + \overline{DS} \cdot H1 \cdot \overline{H2} \cdot H3$$

$$SI5 = DS \cdot \overline{H1} \cdot H2 \cdot H3 + \overline{DS} \cdot H1 \cdot \overline{H2} \cdot \overline{H3}$$

$$SI6 = DS \cdot \overline{H1} \cdot \overline{H2} \cdot H3 + \overline{DS} \cdot H1 \cdot H2 \cdot \overline{H3} \qquad \ldots(5.11)$$

5.3.2 Circuit Models; One-way Motion

The switching nature of the inverter results in changing circuit configurations both steady-state and transient. These circuit configurations, as will be shown, can be divided into groups or "modes" each of which can be represented by a circuit model. These circuit modes simulate the working conditions of the inverter-machine model of Figure 5.3 and constitute sub-sets of it. The technique used to determine the circuit mode is based on the switching interval information. That is, the transistors which conduct and hence the directions of phase voltages and currents are determined using the switching intervals of Table 5.1.

Each switching interval corresponds to the same circuit topology but with different phases involved. This means that the voltages and emf directions are the same in corresponding phases in each interval. It can be observed from Table 1 that there is one switching interval and thus one circuit configuration for two excitation positions. These positions are for opposite direction of excitation motion (or direction signal). However, since they occur 180 ° apart (reversed Hall signals, hence opposite excitation poles), the phase emfs for both directional cases have the same polarity.

The transients that occur when the switching interval changes can be dealt with in the same way as above this time considering which transistor is to switch on and which transistor to switch off. The transient currents through the diodes can also be decided.

As an example, two circuit configurations which correspond to switching intervals 1 and 2 are drawn in Figure 5.4. It may be seen from the circuit diagrams that voltage and emf polarities, parameters and current directions, with the exception of the values of the phase emfs, are the same. This leads to a common circuit model given in Fig. 5.5 which can be used for all switching intervals. This model is called the "one-way operation one-loop model" and represents the inverter-machine model with no phase current commutation present. The model includes two phases of the armature winding and therefore is a derivative of the complete decoupled model of Section 5.2. It may be noticed that the DC supply voltage of the model is designated as $V_{(ch)}$ instead of V_{DC}. This is done in order to incorporate the current magnitude controller of the driver chip into the modelling process. As will be explained later, this controller disconnects the supply battery, along with R_s and R_{ext}, from the circuit in order to keep the current within a specified level. Due to this "chopping" action, the voltage $V_{(ch)}$ in the model is current dependent and is equal to either V_{DC} or zero. The same applies for $R_{s(ch)}$ and $R_{ext(ch)}$.

In order to apply the model, the first step is to appropriately adapt the present phase/supply connections to the model using the switching interval information. This is done by using the matrix given in Table 5.2 in tabular form. The rows of this matrix correspond to switching intervals and columns to phases. It serves as a means to transform the present circuit configuration into the one-loop model in order that the model can be created independently and solved. It may be noticed that the same matrix can conveniently be used to obtain the phase emf polarities for the model. This can be explained by comparing the emf polarities of the examples given in

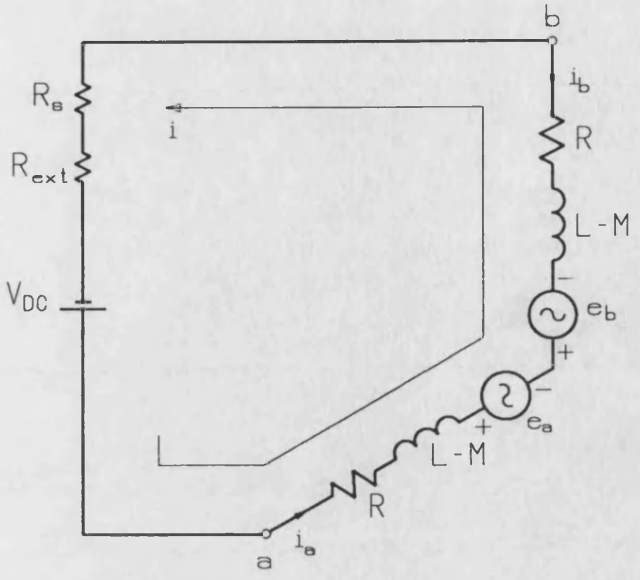

(a) Switching Interval 1

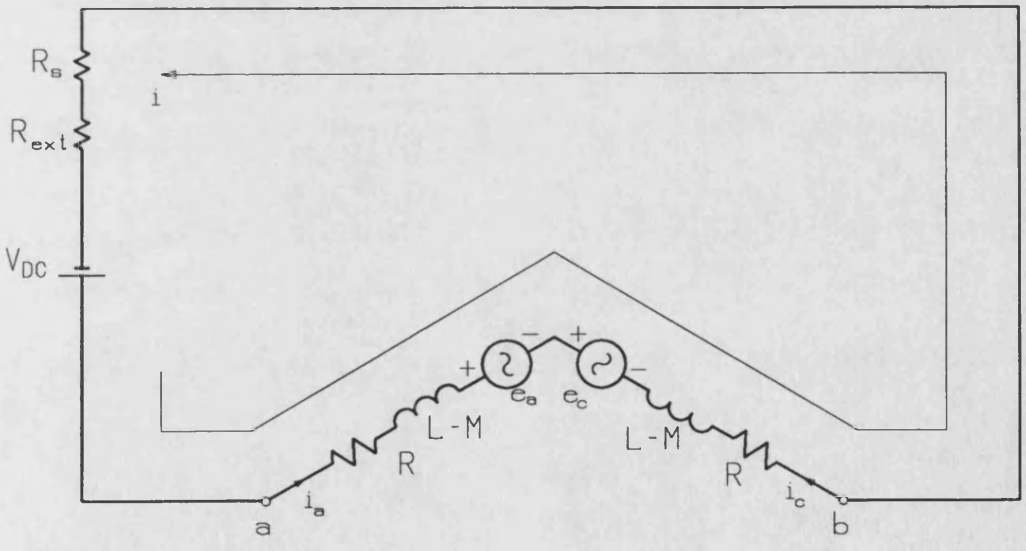

(b) Switching Interval 2

Figure 5.4 Circuit Configurations in One-Way Operation One-Loop Mode

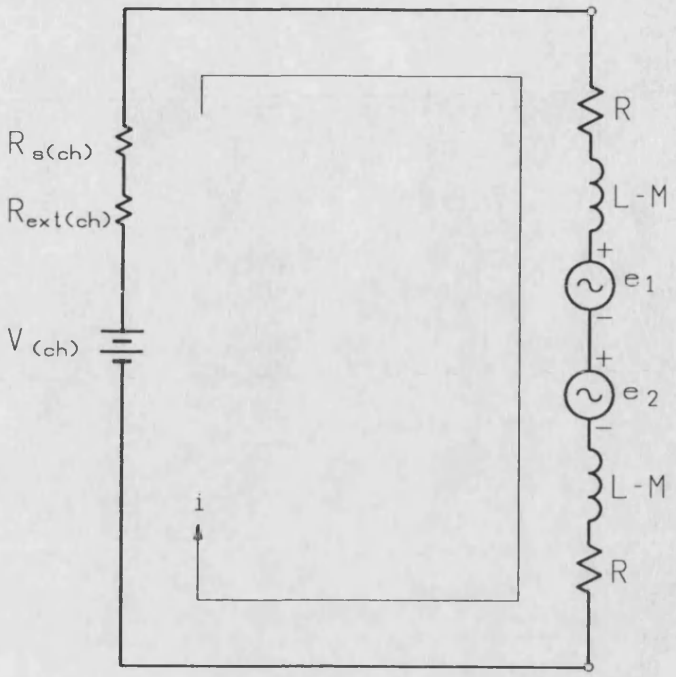

Figure 5.5 One-Way Operation One-Loop Circuit Model

Table 5.2

Transformation Matrix Used for One-Loop Model

	a	*b*	*c*
1	1	-1	0
2	1	0	-1
3	0	1	-1
4	-1	1	0
5	-1	0	1
6	0	-1	1

Figure 5.4 with the positive emf polarities of the machine given in Figure 5.3. In each row of the matrix in Table 5.2 the positive entry is for e_1 of the one-loop model and the negative entry for e_2. Thus, for switching interval 1; $e_1 = e_a$ and $e_2 = -e_b$ and for switching interval 2; $e_1 = e_a$ and $e_2 = -e_c$.

The model is then solved for the loop current using

$$V_{(ch)} = \{2R + R_{s(ch)} + R_{ext(ch)}\} \cdot i + 2(L - M)\frac{di}{dt} + (e_1 + e_2) \qquad \ldots(5.12)$$

where subscript *(ch)* suggests that the parameter is subject to the chopping action. That is, depending on the value of *i*, *(ch)* subscripted values may have either their associated value or zero.

This current may then be used to calculate the phase currents. This is again done by the same matrix of Table 5.2, this time, however, using the transpose of the matrix. This can be shown using the same examples above. For the switching interval 1:

$$\begin{bmatrix} i_a \\ i_b \\ i_c \end{bmatrix} = i \cdot \begin{bmatrix} 1 \\ -1 \\ 0 \end{bmatrix} = \begin{bmatrix} i \\ -i \\ 0 \end{bmatrix}$$

and for 2:

$$\begin{bmatrix} i_a \\ i_b \\ i_c \end{bmatrix} = i \cdot \begin{bmatrix} 1 \\ 0 \\ -1 \end{bmatrix} = \begin{bmatrix} i \\ 0 \\ -i \end{bmatrix}$$

which can be seen on the circuit diagrams of Figure 5.4.

The above considerations are for the case when there is no phase current commutation. As explained in Chapter 4, during the current commutation, one transistor switches off disconnecting its associated phase from the supply and another switches on. The inductive current of the phase whose transistor has switched off flows through a freewheeling diode until its associated energy is dissipated in the phase resistors and becomes zero. At the same time, the current of the phase whose associated transistor has switched on increases. During this period, therefore, all three phases carry currents and the circuits have two loops. This period has also been incorporated into the modelling process.

As in the case of switching intervals, the commutation from one interval to another is the same for all cases in terms of circuit parameters and polarities thus leading to a common circuit model which can represent all the cases involving different phases. This may be explained by the help of Figures 5.6 and 5.7. Figure 5.6 shows the circuits for commutation from intervals 1 to 2 and from 3 to 4 for positive direction (when the excitation moves from left to right). For the loop with the voltage source which has been established by the on-going transistor, for each of these commutation cases, the circuit is the same, that is it has the same voltage and emf polarities and current directions. This also applies to the other loop with decaying current and therefore by appropriately assigning the correct phases, a model can be set up and applied to all possible commutation cases.

For negative direction the above consideration is also valid and the circuits drawn in Figure 5.7(a) and (b) which give the commutation conditions going from 3 to 2 and from 5 to 4 respectively are also similar. However, when Figure 5.6(a) is compared with Figure 5.7(a), it may be observed that the newly established switching interval, 2, results in the same circuit for the ON loop (with i_{on}) in both direction cases, but the OFF loops (with i_{off}), with decaying phase currents, are different. The same

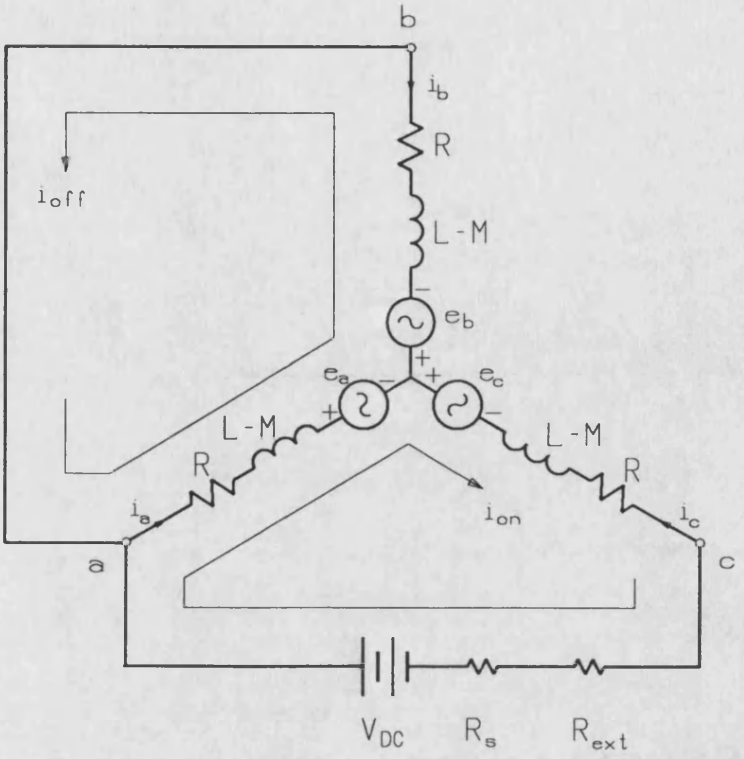

(a)

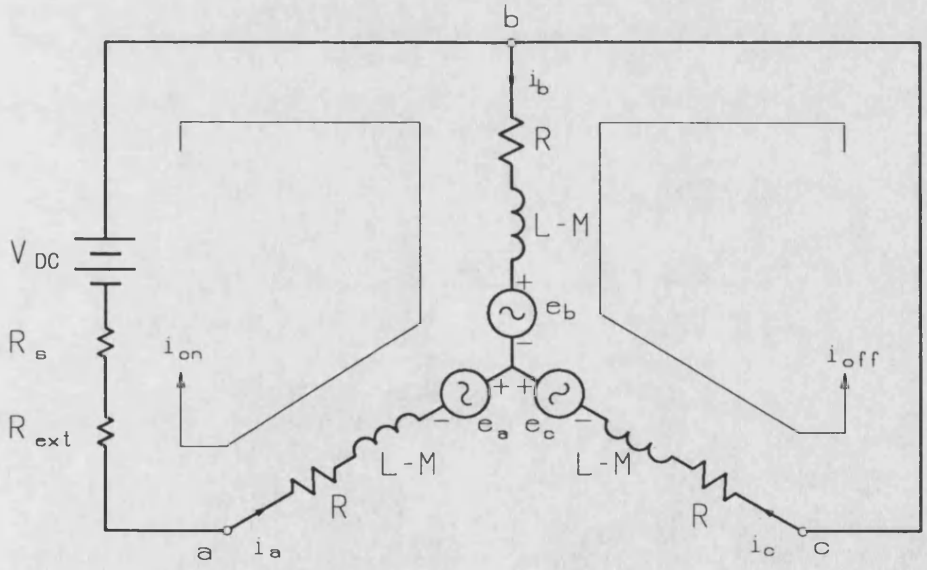

(b)

Figure 5.6 Circuit Configurations in One-Way Operation Two-Loop Mode, Positive Speed (DS=0)
(a) 1→2 Commutation
(b) 3→4 Commutation

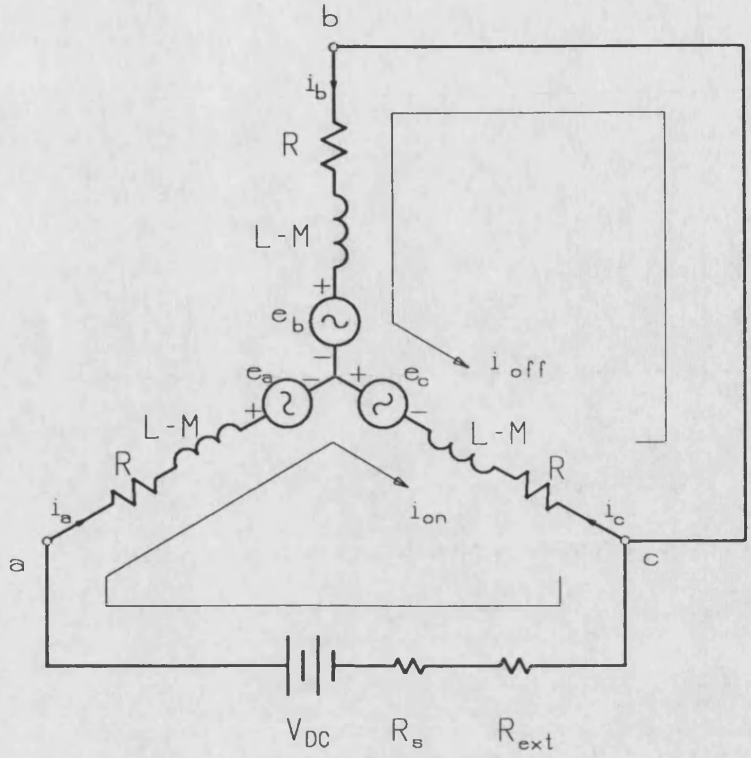

(a)

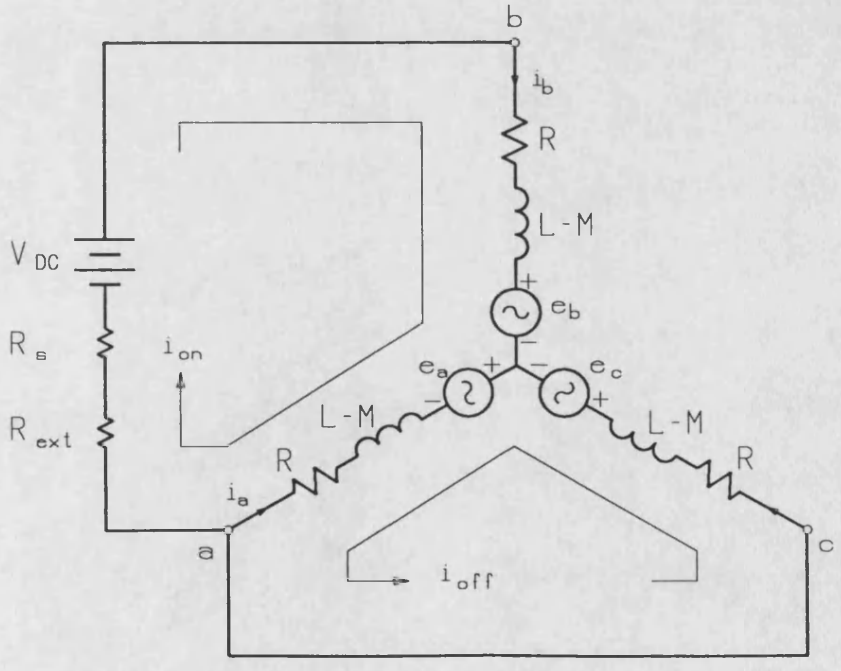

(b)

Figure 5.7 Circuit Configurations in One-Way Operation Two-loop Mode, Negative Speed (DS=1)
(a) 3→2 Commutation
(b) 5→4 Commutation

argument applies to the comparison between Figures 5.6(b) and 5.7(b). Thus, although the same circuit model can be used for both positive and negative directions, the transformation from the current circuit configuration to the model is different.

Figure 5.8 illustrates the model for this operation mode, namely the "one-way operation two-loop model". It may be noticed that unlike the one-loop model, this model has line to line emfs. The transformation is carried out using two matrices, each of which is for one direction of excitation motion. These matrices are given in Tables 5.3 and 5.4 in tabular form. Rows of the matrices correspond to commutation occurrences between switching intervals and columns to phase connections.

In order that the circuit construction of the model is complete, line to line emfs of the model, E_{on} and E_{off} have to be obtained using the phase emfs. These are calculated independently from the switching interval with the polarities shown in Figure 5.3. This can also be achieved using the same matrices and may be illustrated by the examples taken in the model derivation above. Using the positive direction matrix of Table 5.3 for the emfs of the two-loop model, one can write $E_{on}=-e_{ca}=-e_c+e_a$ and $E_{off}=e_{ab}=e_a-e_b$ for the 1-2 commutation. For the negative direction commutation of 3-2, it can be written that $E_{on}=-e_{ca}=-e_c+e_a$ and $E_{off}=e_{bc}=e_b-e_c$. These can be verified by the emf polarities of Figures 5.6(a) and 5.7(a).

This model is then solved by mesh current network technique for the loop currents i_{on} and i_{off} using

$$\begin{bmatrix} V_{(ch)} \\ 0 \end{bmatrix} = R \cdot \begin{bmatrix} 2 & 1 \\ 1 & 2 \end{bmatrix} \begin{bmatrix} i_{on} \\ i_{off} \end{bmatrix} + \{R_{s(ch)} + R_{ext(ch)}\} \cdot \begin{bmatrix} 1 & 0 \\ 0 & 0 \end{bmatrix} \begin{bmatrix} i_{on} \\ i_{off} \end{bmatrix}$$

$$+(L-M) \cdot \begin{bmatrix} 2 & 1 \\ 1 & 2 \end{bmatrix} \frac{d}{dt} \begin{bmatrix} i_{on} \\ i_{off} \end{bmatrix} + \begin{bmatrix} E_{on} \\ E_{off} \end{bmatrix} \qquad \ldots(5.13)$$

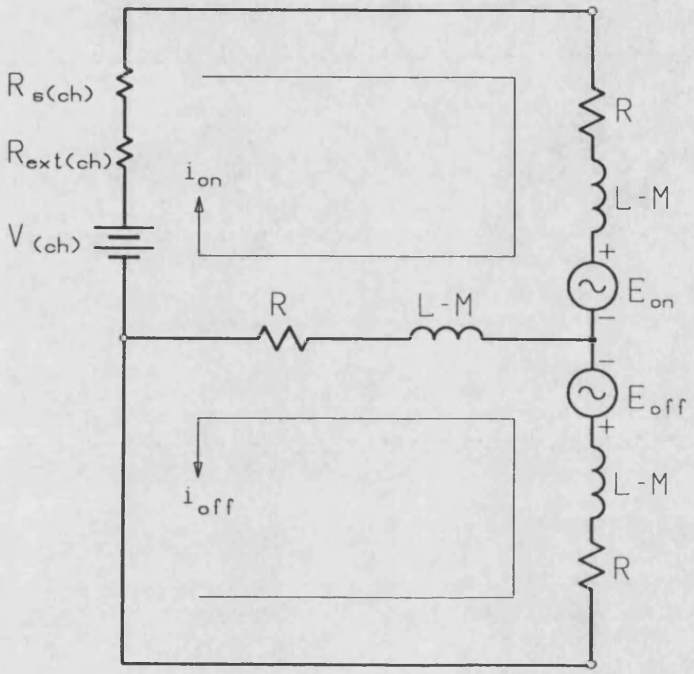

Figure 5.8 One-Way Operation Two-Loop Circuit Model

Table 5.3

Transformation Matrix Used for Two-Loop Model

Positive Speed (DS=0)

	a-b	*b-c*	*c-a*
1→2	1(off)	0	-1(on)
2→3	0	1(on)	-1(off)
3→4	-1(on)	1(off)	0
4→5	-1(off)	0	1(on)
5→6	0	-1(on)	1(off)
6→1	1(on)	-1(off)	0

Table 5.4

Transformation Matrix Used for Two-Loop Model

Negative Speed (DS=1)

	a-b	*b-c*	*c-a*
1→6	1(off)	-1(on)	0
2→1	1(on)	0	-1(off)
3→2	0	1(off)	-1(on)
4→3	-1(off)	1(on)	0
5→4	-1(on)	0	1(off)
6→5	0	-1(off)	1(on)

where *(ch)* specifies that the parameter is subject to the chopping action and is therefore either zero or has its associated value.

Phase currents are then calculated using these two mesh currents and the back-transformation matrices given in Tables 5.5 and 5.6 for positive and negative excitation directions respectively. This is done in a similar fashion to that of one-loop model given above.

The circuit mode is determined by constantly checking the excitation position signals. If there is no change in H1, H2 or H3, then it is one-loop, if one of them changes, then there is a change in the switching interval and the two-loop mode is chosen and the present circuit conditions are represented by the appropriate model. The two-loop model is used until i_{off} drops to zero and the one-loop model takes over thereafter.

Current magnitude control (chopping) is modelled in the same way as the hardware operates: the magnitude of the DC link current is constantly checked and if it exceeds the predetermined value, then the supply voltage $V_{(ch)}$ and $R_{a(ch)}$ and $R_{ext(ch)}$ resistors are zero for a period (t_{off}). At the end of this period the DC link is reconnected and the above variables are in the models with their actual values. This is, of course, done for the one-loop model and on-loop of the two-loop model.

5.3.3 Circuit Models; Oscillatory Motion

The models described above can be used for both directions of excitation motion. However, as mentioned in Chapter 4, when the excitation reaches one "end-stop", it must be decelerated and accelerated in the other direction in order to achieve the oscillatory action. This, as explained earlier, is achieved by employing two extra Hall effect end-sensors which can detect a travel-end and, using this, change the direction signal (DS) accordingly. Reversed direction signal requires reversed

Table 5.5

Back-Transformation Matrix Used for the Calculation of Phase Currents

From Two-Loop Model, Positive Speed (DS=0)

	i_a	i_b	i_c
1→2	$(i_{off}+i_{on})$	$-i_{off}$	$-i_{on}$
2→3	i_{off}	i_{on}	$-(i_{off}+i_{on})$
3→4	$-i_{on}$	$(i_{off}+i_{on})$	$-i_{off}$
4→5	$-(i_{off}+i_{on})$	i_{off}	i_{on}
5→6	$-i_{off}$	$-i_{on}$	$(i_{off}+i_{on})$
6→1	i_{on}	$-(i_{off}+i_{on})$	i_{off}

Table 5.6

Back-Transformation Matrix Used for the Calculation of Phase Currents

From Two-Loop Model, Negative Speed (DS=1)

	i_a	i_b	i_c
1→6	i_{off}	$-(i_{off}+i_{on})$	i_{on}
2→1	$(i_{off}+i_{on})$	$-i_{on}$	$-i_{off}$
3→2	i_{on}	i_{off}	$-(i_{off}+i_{on})$
4→3	$-i_{off}$	$(i_{off}+i_{on})$	$-i_{on}$
5→4	$-(i_{off}+i_{on})$	i_{on}	i_{off}
6→5	$-i_{on}$	$-i_{off}$	$(i_{off}+i_{on})$

phase voltages and thus currents for the same excitation position. The reversed phase currents, in turn, exert reversed electromagnetic forces on the moving excitation, thus forcing it first to stop and then accelerate it in the reverse direction. The period from the time direction signal changes until the excitation is stopped completely, "direction transients", is also incorporated into the simulation process in order that a complete modelling of the system can be realised.

Practical aspects of the oscillatory operation were examined in Chapter 4. In this section the operation modes will be outlined, for modelling purposes, with the help of Figures 5.9 and 5.10. Figure 5.9 shows direction signal, force and velocity directions and Figure 5.10 switching intervals with ideal Hall-effect sensor positioning and simplified emf waveforms for both directions of speed throughout the machine operation cycle. With direction signal 0, the phase sequence is abc and the excitation is accelerated to the right (positive increasing position) by the positive force. As the excitation approaches the right-hand-end, direction signal becomes 1. Depending on the positions that the left and right end sensors, ESleft and ESright, are placed the switching interval changes by ±3 for the same excitation position interval, imposing reversed supply voltage [Figure 5.10]. Except for a very short period during which they are being forced to zero, phase currents reverse and so does the electromagnetic force. This short period is indicated in Figure 5.9, being exaggerated for clarity. Therefore, for most of the interval when "direction transients" flow, the electromagnetic force direction is reversed to that of the excitation direction, thus decelerating the excitation [Figure 5.9]. This transient interval lasts until the excitation velocity is zero, when it starts accelerating to the left.

The one-way circuit models of the previous section are used for the normal (one-way) operation mode periods where direction signal is 0 and the excitation velocity is positive or direction signal is 1 and the excitation velocity is negative [Figure 5.9]. For the "direction transients" interval, there are two sub-intervals that

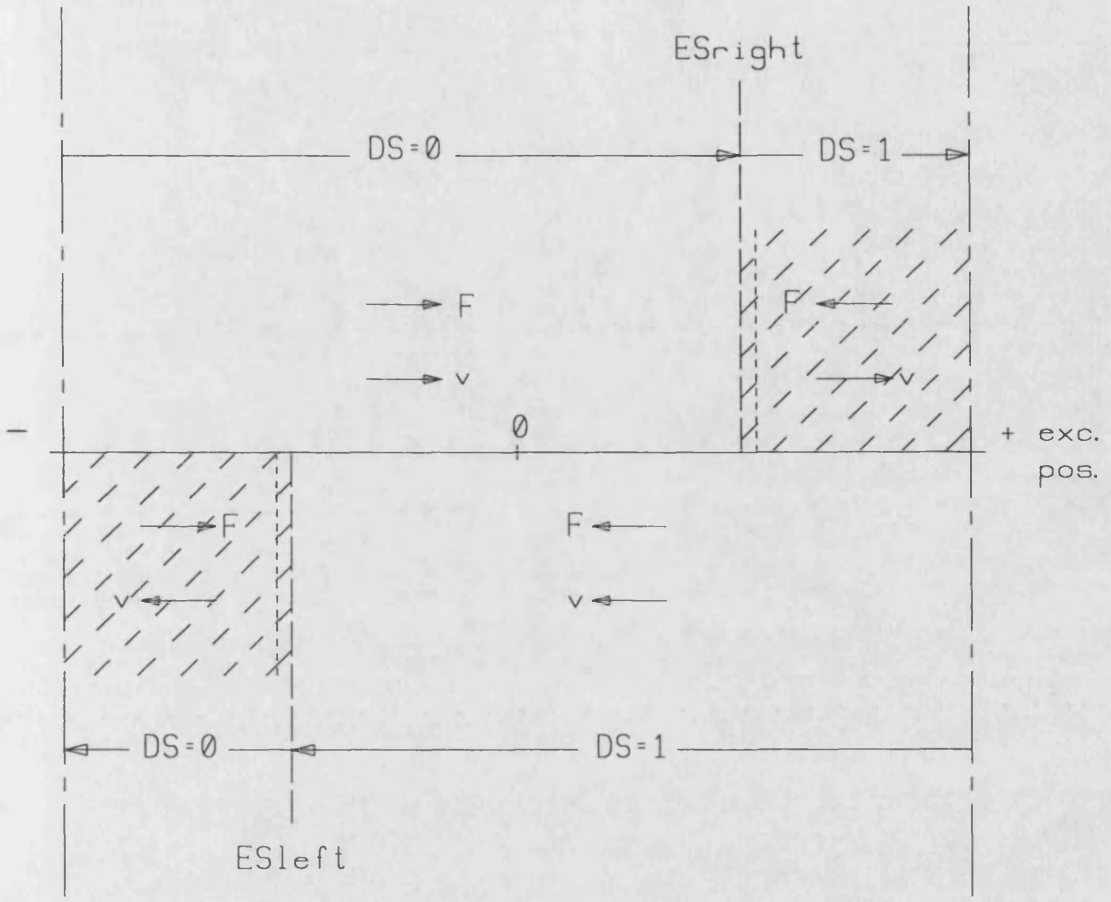

one-way operation

direction transients

F force exerted on excitation

v excitation velocity

Figure 5.9 Operation Modes for Oscillatory Operation Showing Excitation Force, Velocity and Position

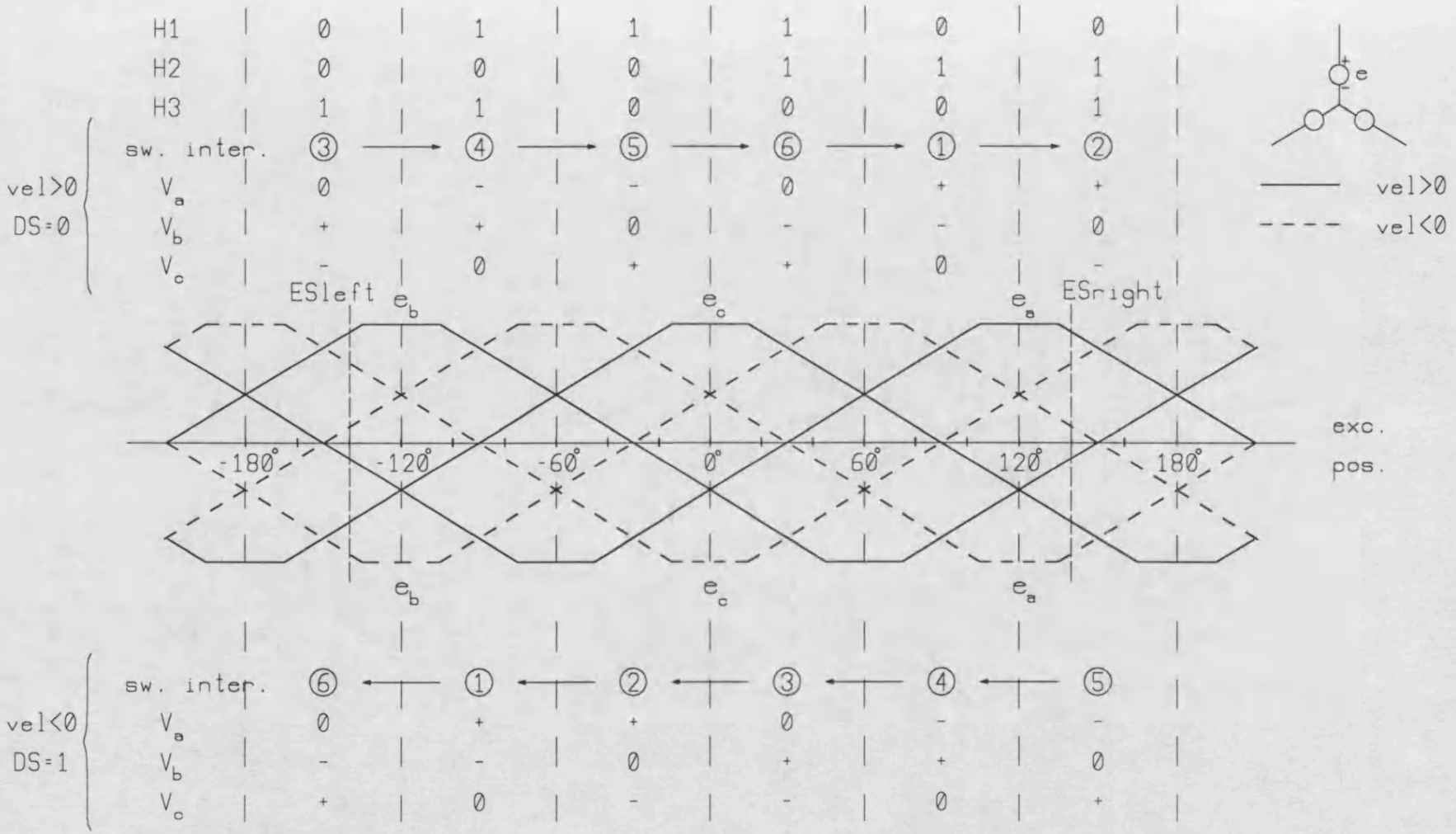

Figure 5.10 Switching Intervals with Ideal Excitation Position Signals and Simplified Phase Emfs for Both Directions of Motion

should be considered. The first of these starts with the change of direction signal and has a one-loop circuit configuration. The second sub-interval starts when the associated upper diode of the phase, which is off according to the switching interval information, becomes forward biased and thus establishes a two-loop circuit. The "direction transients" interval was explained in Section 4.3.2 of Chapter 4 for the first sub-interval and the different circuit configurations set up by the inverter were drawn. In this section, a one-loop circuit model for the first sub-interval will be given and the second sub-interval will be explained and the circuit model for it will be derived.

The right-hand-end "direction transients" interval which was used in Chapter 4 will again be used here as an example. Suppose that ESright is placed at the 140 ° location. Until the excitation reaches this position, the switching interval is 2 and the circuit configuration is as given in Figure 4.7(a). When the excitation reaches this position and direction signal becomes 1, the switching interval of the inverter becomes 5 and this requires reversed phase voltages [Figure 5.10]. From this moment onwards the circuit can be modelled by a one-loop circuit model similar to the one described above for one-way motion, except that the supply voltage is reversed. This "direction transients one-loop model" is given in Figure 5.11. Since the excitation still moves to the right the phase emfs have the same polarities and they support the supply voltage [Figure 4.7(c)], which can also be seen on the model diagram of Figure 5.11. Therefore, the current reverses fast and when it reaches the predetermined limit for the DC value the DC link is cut-off from the circuit and the reversed current is driven by emfs only as redrawn in Figure 5.12(a). This cut-off period, unlike in the one-way operation mode, is indefinite and continues until the current drops to the predetermined value. This is also included in the circuit model.

The adaptation of the present circuit to the model is performed as in the one-way operation model using matrices. It may be observed that this model has the same

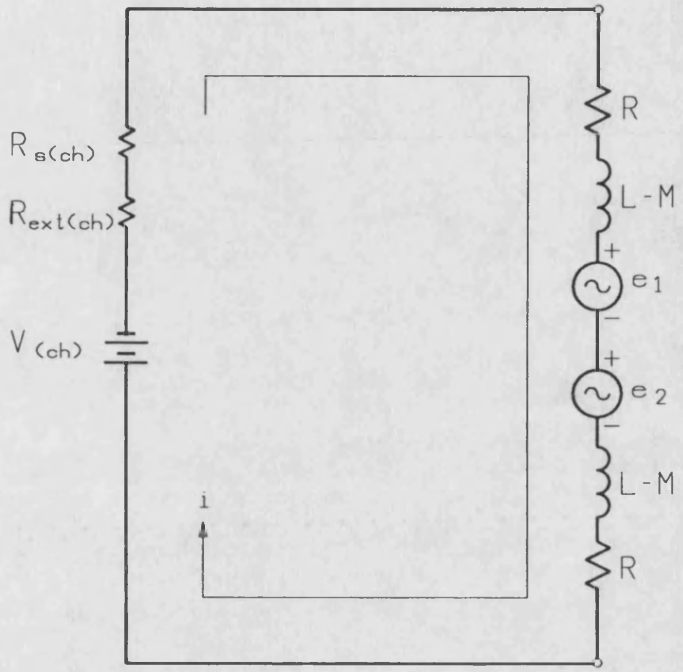

Figure 5.11 Direction Transients One-Loop Circuit Model

mesh current direction as in the other one-loop model. This is in order to keep the solution technique consistent and so that Eqn. 5.12 can be used again with only a reversed supply voltage:

$$-V_{(ch)} = \{2R + R_{s(ch)} + R_{ext(ch)}\} \cdot i + 2(L - M)\frac{di}{dt} + (e_1 + e_2) \qquad \ldots(5.14)$$

For much of this period, $V_{(ch)}$, $R_{s(ch)}$ and $R_{ext(ch)}$, are zero because of the turned off bottom transistors, i.e. current magnitude control, and the currents freewheel through a diode and an upper transistor.

The excitation, although being decelerated, continues to move to the right and, when it reaches the position where the total line to line voltage between the off-phase and the + phase, whose associated top transistor is on (b and c respectively for this case as the new switching interval is 5), including the inductive and resistive voltages and emfs (V_{bc} here), becomes positive, thus forward biasing diode D3. With this diode conducting, all three phases have currents and the circuit becomes a two-loop one, as shown in Figure 5.12(b). The equivalent circuit model for this mode is a variation of the one-way motion two-loop model and is given in Figure 5.13. Transformation to this, ''direction transients two-loop model'' is not systematic and depends on the emf polarities and values and therefore on the excitation position and the interval in which the direction signal change takes place. Instead the transformation was achieved taking the right and left-hand-end transients separately.

The model is solved for the mesh currents using

$$\begin{bmatrix} 0 \\ 0 \end{bmatrix} = R \cdot \begin{bmatrix} 2 & 1 \\ 1 & 2 \end{bmatrix} \begin{bmatrix} i_1 \\ i_2 \end{bmatrix} + (L - M) \cdot \begin{bmatrix} 2 & 1 \\ 1 & 2 \end{bmatrix} \frac{d}{dt} \begin{bmatrix} i_1 \\ i_2 \end{bmatrix} + \begin{bmatrix} E_1 \\ E_2 \end{bmatrix} \qquad \ldots(5.15)$$

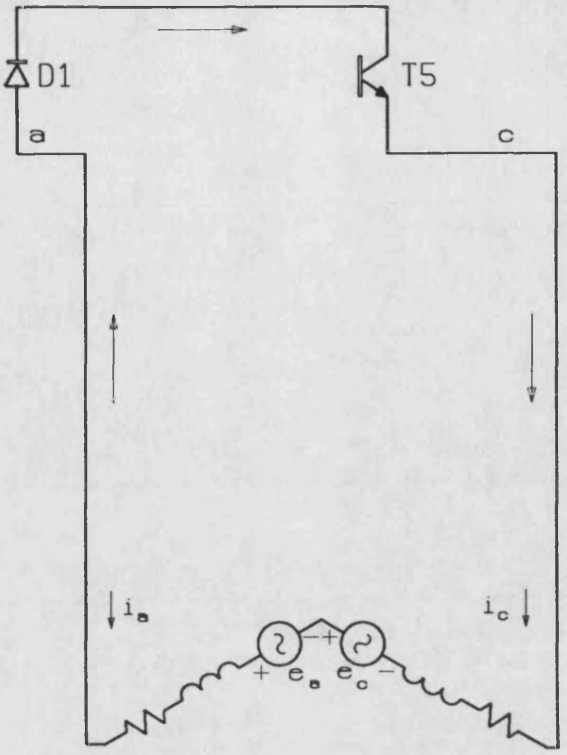

(a)

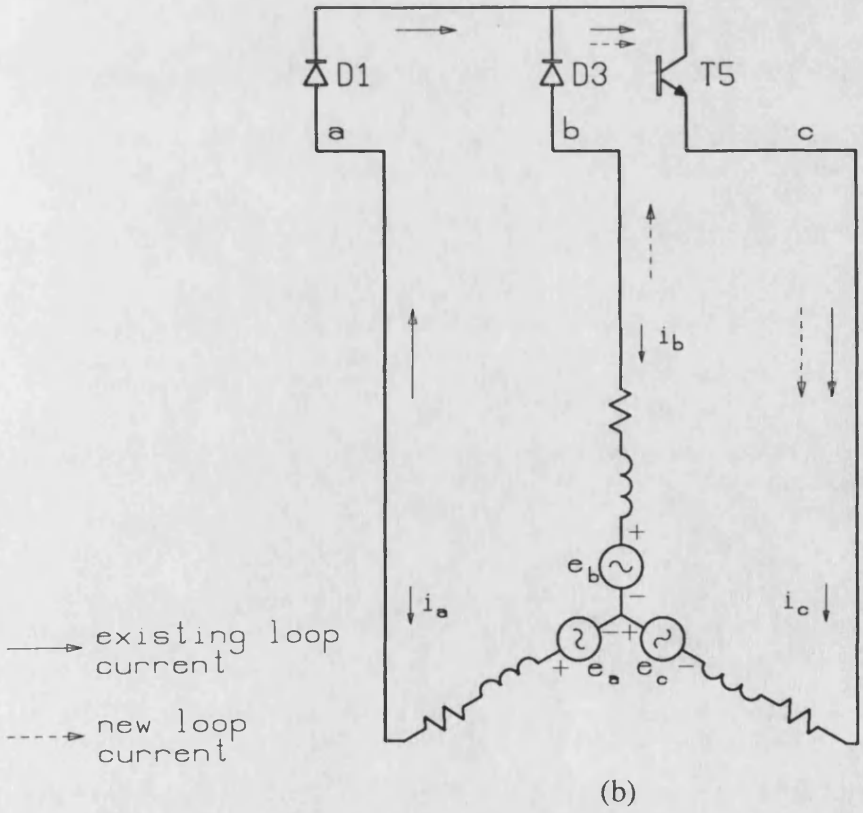

(b)

Figure 5.12 Circuits Formed in the Right-Hand-End Direction Transients Interval
(a) One-Loop Circuit
(b) Two-Loop Circuit

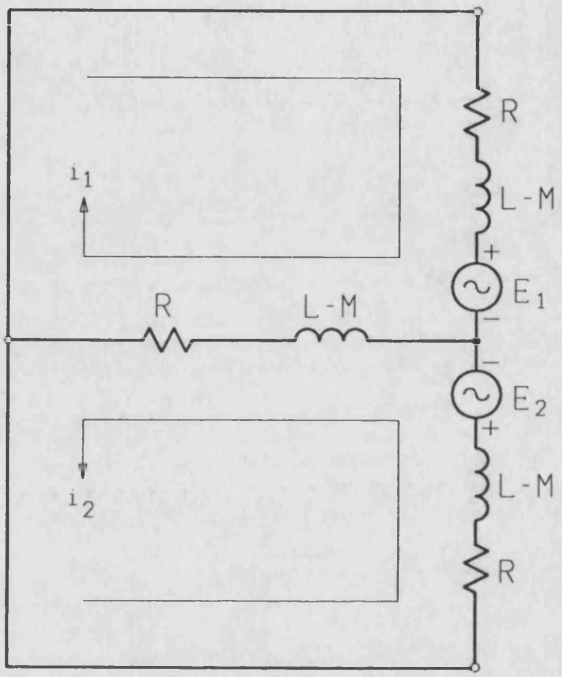

Figure 5.13 Direction Transients Two-Loop Circuit Model

Phase currents and voltages are again calculated using the same transformation matrices taking each excitation direction separately. Notice that this model and its associated equation also use line to line emfs.

This mode requires constant checking of the related phase-to-phase total voltages during the first one-loop section of the interval. It lasts until the end of "direction transients". That is, when the excitation stops and the phase currents are low enough for the bottom transistors to switch on again by which time the off-phase current drops to zero.

5.4 Solution of the System Equations

The numerical method used in the solution of the system equations is based on a "step-by-step" technique **[5.21-5.23]**. This method of solution involves start values of electrical and mechanical variables for a finite time-step-interval and, assuming linear variation, calculates the variables at the end of each time interval. The mathematical representation of the method can be illustrated by using the general matrix form of Eqn. 5.8, which represents the decoupled machine model as below:

$$[V] = [R][i] + [L - M]\frac{d}{dt}[i] + [e] \qquad \ldots(5.16)$$

and rewriting this in the discrete-time form as:

$$\frac{[V]' + [V]''}{2} = [R]\left\{\frac{[i]' + [i]''}{2}\right\} + [L - M]\left\{\frac{[i]'' - [i]'}{\delta t}\right\} + \frac{[e]' + [e]''}{2} \qquad \ldots(5.17)$$

where primes $'$ and $''$ indicate the variables at the beginning and end of the time-step interval, δt, respectively. In this equation, functions are averaged over the time interval and the time derivative of functions is expressed in finite difference form.

The principle of this numerical technique is based on the initial collection of the parameters for the first time-step interval. Taking zero step-start values, the above equation is solved for the step-end current matrix, $[i]''$ using:

$$[i]'' = \frac{\{[V]' + [V]''\} - \{[e]' + [e]''\} - [i]'\{[R] - 2[L - M]/\delta t\}}{[R] + 2[L - M]/\delta t} \qquad \ldots(5.18)$$

For the next time-step interval, step-end values of the previous interval are considered as step-start values and recalculating the variable parameter, $[e]''$, the above equation is solved again. This operation is carried out for the duration under consideration.

A close examination of the above equation will reveal that the step-end emf matrix, $[e]''$, is required when the phase currents are to be calculated at the end of a time interval. The value of phase emfs, on the other hand, depends on the new excitation position and velocity which are in turn determined by the total force acting on the excitation at the end of the interval. This force, however, is a function of the phase currents. All the system variables are, therefore, interrelated and an iterative process is required. One solution to this can be realised by having an initial guess for one of the variables within each time-step interval and, updating the guess with an appropriate process, finding the solution when a convergence is reached.

The way this is done can be explained by writing the discrete-time equivalents of the other equations derived above in previous sections. The phase back emf vector at the end of the interval can be calculated by

$$[e]'' = \left[\frac{d\lambda}{dx}\right]'' \cdot v'' \qquad \ldots(5.19)$$

where the space derivative matrix of the flux linkage is not written in discrete-time form taking λ and x as separate functions, but the derivative itself is used as a function. This is because the flux linkage and thus its space derivative are expressed by a Fourier series. Therefore, the derivative can be evaluated at any excitation position, x, independently from time and thus the current time-step interval.

In order to evaluate this equation, however, both step-end position and excitation velocity need to be known. This is where an iterative guess has to be made. This must be for a variable which will reveal step-end values for both position and velocity. This variable may therefore be acceleration, $a^{"}$, velocity, $v^{"}$, or excitation position, $x^{"}$. Equation 5.19 can then be evaluated for step-end emf vector, $[e]^{"}$. With this known, Eqn. 5.18 can now be used to calculate the step-end current vector, $[i]^{"}$, for the time-step.

The electromagnetic thrust force equation can be written in discrete-time form, for the step-end, using Eqn. 5.9 as

$$F_{em}^{"} = \frac{\{[i]^T\}^{"} \cdot [e]^{"}}{v^{"}} \qquad \ldots(5.20)$$

from which it can be calculated. Here, $[i]^T$ is the transpose of the current matrix and is a row vector. This equation is also independent of time and can be used in the same form for step-start values.

The mechanical equation representing the mechanics of the moving parts can be written for the step end values as

$$F_{em}^{"} + F_{end}^{"} = m \cdot a^{"}$$

and step-end acceleration can be calculated using

$$a'' = \frac{F''_{em} + F''_{end}}{m} \qquad \ldots(5.21)$$

Here, magnetic end-effect force, F_{end}, is a function of position only and is therefore independent of the time-stepped approach.

With the acceleration obtained, $a=dv/dt$ can be used to relate it to the velocity by writing this equation in discrete-time form as

$$\frac{a' + a''}{2} = \frac{v'' - v'}{\delta t}$$

where step-start and end values of acceleration are averaged over the interval. The step-end velocity can then be evaluated using

$$v'' = v' + \left\{\frac{a' + a''}{2}\right\} \cdot \delta t \qquad \ldots(5.22)$$

The excitation position at the end of the interval can now be calculated from the following equation which is written from the equation $v=dx/dt$

$$\frac{v' + v''}{2} = \frac{x'' - x'}{\delta t}$$

thus

$$x'' = x' + \left\{\frac{v' + v''}{2}\right\} \cdot \delta t \qquad \ldots(5.23)$$

Step-end value of the variable that was guessed at the beginning of the time-step interval can now be evaluated using the corresponding one of the above three

equations 5.21, 5.22 and 5.23. This calculated value is then checked against the guessed value. If they agree within a specified tolerance, then the last calculated set of step-end values are taken as the true solution for the step and the variables are integrated forward in time. Otherwise, the first guess is exchanged with the last value of the guessed variable and the same time-step interval is reiterated.

In the above equations, step-start values need not be calculated since they are known from the previous step.

5.4.1 Discrete-Time Equivalents of the Equations of Circuit Models

Equation 5.17 describes the general *3*-ϕ machine model. In this section, derivatives of this general equation which represent the four circuit models, will be expressed in discrete-time form.

a) One-way operation, one-loop model

Equation 5.12 can be rewritten as:

$$\frac{V'_{(ch)}+V''_{(ch)}}{2}=\{2R+R_{s(ch)}+R_{ext(ch)}\}\left\{\frac{i'+i''}{2}\right\}+2(L-M)\left\{\frac{i''-i'}{\delta t}\right\}+\left\{\frac{e'_1+e''_1}{2}+\frac{e'_2+e''_2}{2}\right\}$$

and step-end loop current can be calculated using

$$i''=\frac{\{V'_{(ch)}+V''_{(ch)}\}-\{(e'_1+e''_1)+(e'_2+e''_2)\}-2i'\{R-2(L-M)/\delta t\}}{2\{R+2(L-M)/\delta t\}} \qquad \ldots(5.24)$$

b) One-way operation, two-loop model

Equation 5.13 can be rewritten in general matrix form as below:

$$[V] = [R][i] + [R_{s(ch)} + R_{ext(ch)}][i] + [L - M]\frac{d}{dt}[i] + [E]$$

where

$$[V] = \begin{bmatrix} V_{(ch)} \\ 0 \end{bmatrix} \qquad [R] = R \cdot \begin{bmatrix} 2 & 1 \\ 1 & 2 \end{bmatrix} \qquad [i] = \begin{bmatrix} i_{on} \\ i_{off} \end{bmatrix}$$

$$[R_{s(ch)} + R_{ext(ch)}] = (R_{s(ch)} + R_{ext(ch)}) \cdot \begin{bmatrix} 1 & 0 \\ 0 & 0 \end{bmatrix}$$

$$[L - M] = (L - M) \cdot \begin{bmatrix} 2 & 1 \\ 1 & 2 \end{bmatrix} \qquad \text{and} \qquad [E] = \begin{bmatrix} E_{on} \\ E_{off} \end{bmatrix}$$

In this equation E_{on} and E_{off} are line to line emfs and subscript *(ch)* indicates that the parameter is subject to chopping. In discrete-time form this equation can be written as:

$$\frac{[V]' + [V]''}{2} = [R]\left\{\frac{[i]' + [i]''}{2}\right\} + [R_{s(ch)} + R_{ext(ch)}]\left\{\frac{[i]' + [i]''}{2}\right\} + [L - M]\left\{\frac{[i]'' - [i]'}{\delta t}\right\} + \frac{[E]' + [E]''}{2}$$

and step-end current matrix for the loop currents can then be found using

$$[i]'' = \frac{\{[V]' + [V]''\} - \{[E]' + [E]''\} - \{[R] + [R_{s(ch)} + R_{ext(ch)}] - 2[L - M]/\delta t\}[i]'}{[R] + [R_{s(ch)} + R_{ext(ch)}] + 2[L - M]/\delta t} \quad \ldots(5.25)$$

c) Direction transients, one-loop model

Using Eqn. 5.14 the corresponding expression becomes

$$-\left\{\frac{V'_{(ch)}+V''_{(ch)}}{2}\right\}=\{2R+R_{s(ch)}+R_{ext(ch)}\}\left\{\frac{i'+i''}{2}\right\}$$

$$+2(L-M)\left\{\frac{i''-i'}{\delta t}\right\}+\left\{\frac{e'_1+e''_1}{2}+\frac{e'_2+e''_2}{2}\right\}$$

The equation for the step-end loop current is then

$$i''=\frac{-\{V'_{(ch)}+V''_{(ch)}\}-\{(e'_1+e''_1)+(e'_2+e''_2)\}-2i'\{R-2(L-M)/\delta t\}}{2\{R+2(L-M)/\delta t\}} \qquad \ldots(5.26)$$

d) Direction transients, two-loop model

Equation 5.15 which represents this model can also be converted into discrete-time form by first rewriting it in the general matrix form as below:

$$0=[R][i]+[L-M]\frac{d}{dt}[i]+[E]$$

where matrices $[i]$ and $[E]$ are

$$[i]=\begin{bmatrix} i_1 \\ i_2 \end{bmatrix} \quad , \quad [E]=\begin{bmatrix} E_1 \\ E_2 \end{bmatrix}$$

and the other matrices are the same as those for the one-way operation case and E_1 and E_2 are line to line emfs. This equation can first be transferred into the discrete-time format and step-end loop currents can be computed as follows:

$$0=[R]\left\{\frac{[i]'+[i]''}{2}\right\}+[L-M]\left\{\frac{[i]''-[i]'}{\delta t}\right\}+\frac{[E]'+[E]''}{2}$$

and from this

$$[i]'' = \frac{-\{[E]' + [E]''\} - \{[R] - 2[L - M]/\delta t\}[i]'}{[R] + 2[L - M]/\delta t} \qquad \ldots(5.27)$$

5.5 Dynamic Simulation of the Drive System for Oscillatory Operation

The previous sections explained, in detail, the modelling equations which can be adapted for both steady-state and transient simulation. This section concentrates on the application of the modelling technique for oscillatory motion including both steady-state and transient modes of operation and also excitation start-up from zero speed.

A flow chart of the simulation algorithm is given in Figure 5.14. The simulation run starts from zero excitation position which corresponds to the line of symmetry. The system equations are used so that when the excitation moves to the right from the line of symmetry the displacement is positive and increases as given in Chapter 3 and Appendix D. Excitation velocity is also positive by the effect of the positive force acting on the excitation. Phase emfs are calculated by taking the space derivative for all harmonics of the Fourier series of phase flux linkages and multiplying this derivative series by the instantaneous excitation velocity as explained in Chapter 3. The procedure involved in this algorithm is explained below:

(i) The first three blocks of the flow chart perform the preliminary initialization before entering the time-stepping loop. The input data are the system parameters such as phase and other resistances, inductances, battery voltage, excitation position signals, H1, H2 and H3 and left and right-hand-end sensor positions, ESleft and ESright and time-step length. Also included in the input data are phase flux linkages with end-effects and end-effect force. These are

entered at 10 ° intervals. Phase flux linkages are then interpolated and Fourier series is calculated by calling a subroutine. Next a further initialization is done for the first time-step interval and step-start values are set to zero.

(ii) Upon entering the time-stepping loop step the variables are updated and equations are integrated forward in time.

(iii) The required estimate is then made for the step-end velocity and the velocity estimate loop is entered. The excitation position is calculated using Eqn. 5.23. With known excitation velocity and position, now phase emfs can be calculated by calling a subroutine which uses the calculated Fourier series of the flux linkage.

(iv) The inverter switching interval is then determined using excitation position and direction signals. Next the circuit mode is chosen and the corresponding model is solved for phase variables.

(v) Eqn. 5.20 is then executed to calculate the instantaneous electromagnetic force. End-effect force is also calculated here by calling a subroutine which uses Lagrangian interpolation in order to find the function value for the excitation position.

(vi) Excitation Acceleration and velocity are then calculated by Eqns. 5.21 and 5.22 respectively. Next, the calculated velocity is compared with the estimated velocity. If these values agree within 0.01 % then the velocity value is accepted as the correct value. If, however, they do not, the velocity estimate is set equal to the calculated velocity and the velocity estimate loop is reiterated, steps (iii) to (vi) are repeated until the step-end velocity converges.

(vii) Next a check is done for the steady-state conditions. This is necessary since it takes a few oscillations for the excitation to stabilize. If the steady-state conditions are satisfied, an initiation is executed for the data storage. The moment when this check is done was chosen to be the time when the direction signal changes from 0 to 1 while the excitation is at the right-hand-end of its travel. Step variables are stored into arrays.

(viii) The time iteration is repeated and the equations are integrated forward in time. This is done for the storage period as specified.

(ix) Next variables are printed into files.

The direction signal (DS) determination algorithm block is given in Fig. 5.15. This block determines the logical value of direction signal using the step-end values of excitation position and velocity. Its function can be understood with the help of Fig. 5.9. If the excitation velocity is positive and if its position is further than the right end-sensor (ESright), direction signal is 1, otherwise 0. If, however, the excitation velocity is negative and the excitation has passed (ESleft), direction signal is 0, otherwise 1. The excitation position signals H1, H2 and H3 are only functions of excitation position and together with direction signal are used to determine the inverter switching interval using the logical equations described in Section 5.3.1.

A flow chart of the circuit solution block where the circuit mode is defined and the corresponding model is solved for the current phase connection is shown in Fig. 5.16. This algorithm can also be explained with Fig. 5.9. The first partition of the circuit modes is affected by determining whether it is "one-way operation" or "direction transients" mode. This is decided by direction signal and the excitation velocity. In the one-way operation mode the decision of the circuit mode is first made by the control of a switching interval change. If there is "NO" change then a second check is performed on the off-phase current since there may have been a change in

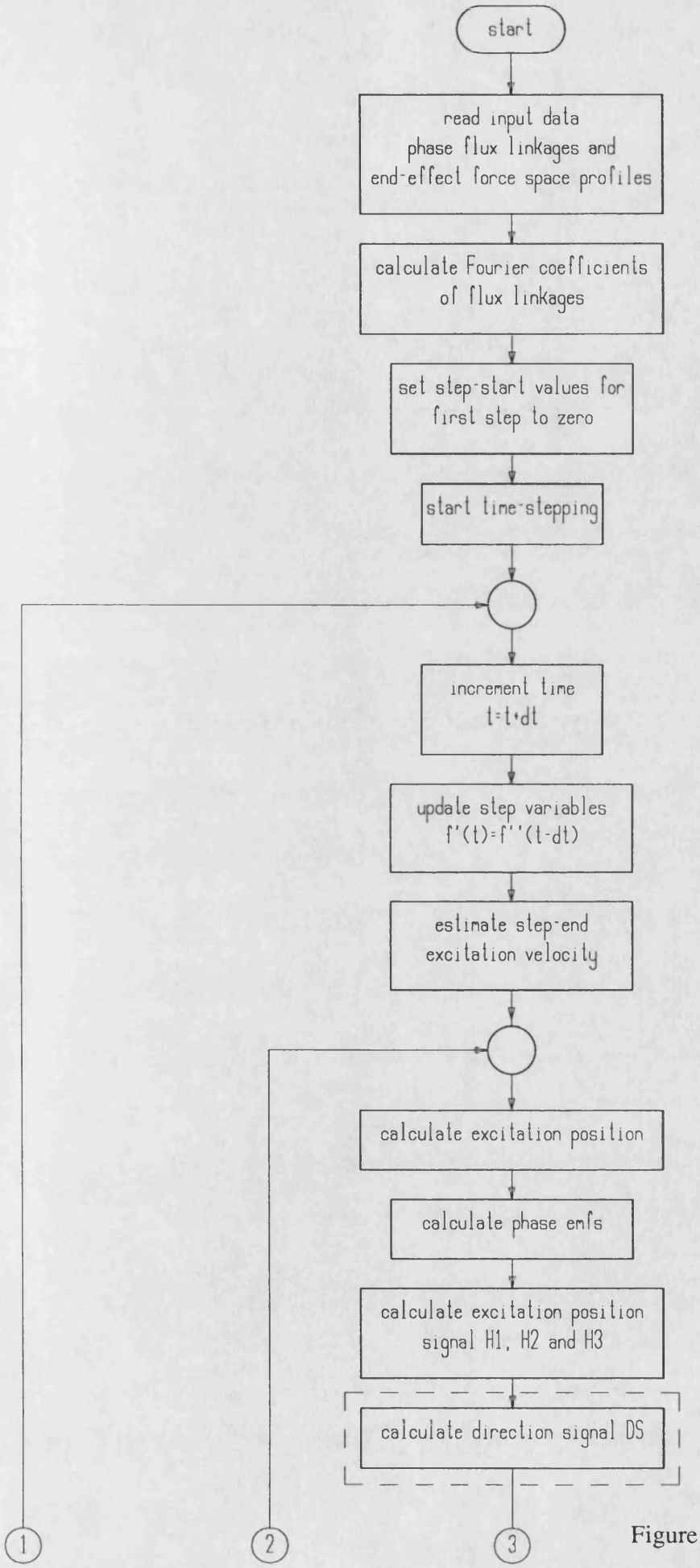

Figure 5.14 Flow Chart of the Simulation Program

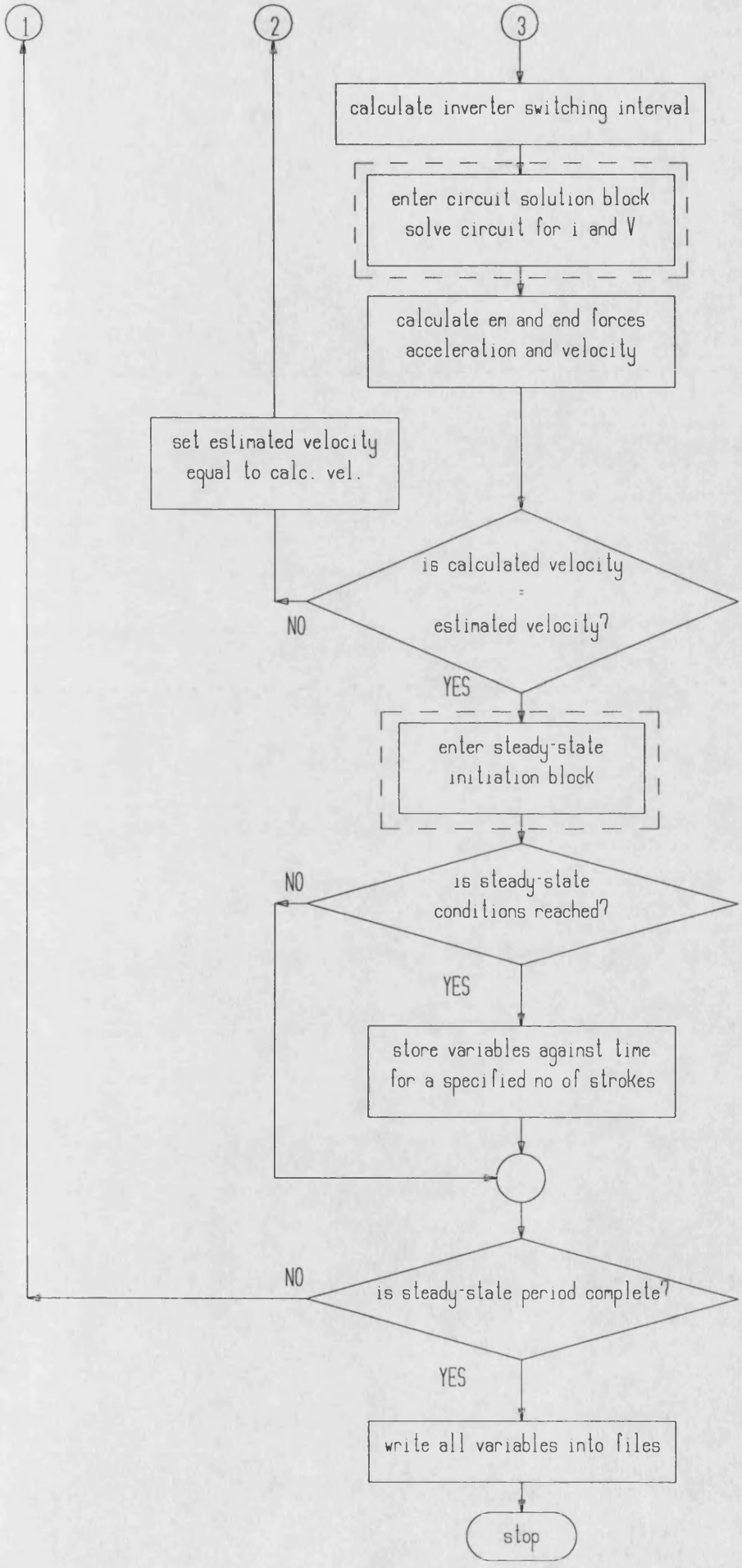
1
2
3
calculate inverter switching interval
enter circuit solution block
solve circuit for i and V
calculate em and end forces
acceleration and velocity
set estimated velocity
equal to calc. vel.
is calculated velocity
=
estimated velocity?
NO
YES
enter steady-state
initiation block
NO
is steady-state
conditions reached?
YES
store variables against time
for a specified no of strokes
NO
is steady-state period complete?
YES
write all variables into files
stop

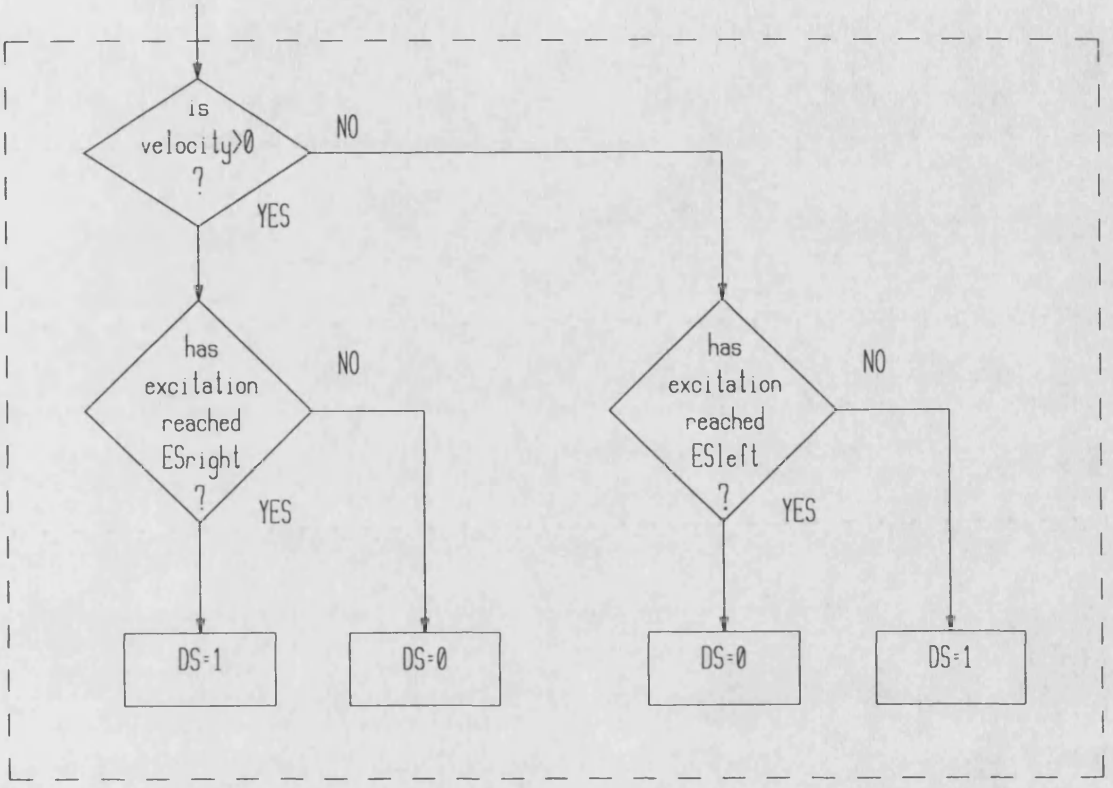

Figure 5.15 Flow Chart of the Direction Signal Determination Block

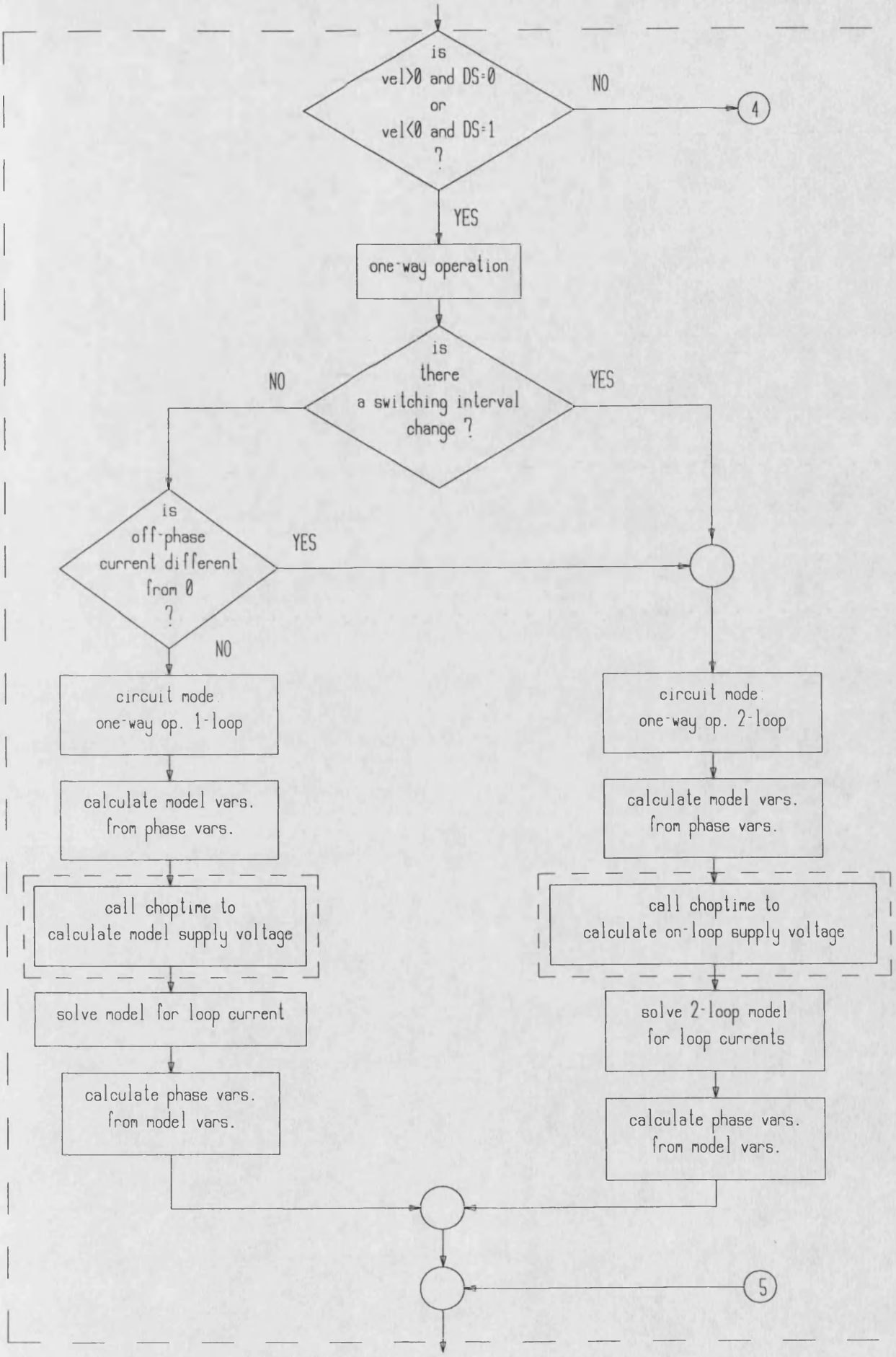

Figure 5.16 Flow Chart of the Circuit Mode Determination and Model Solution Block

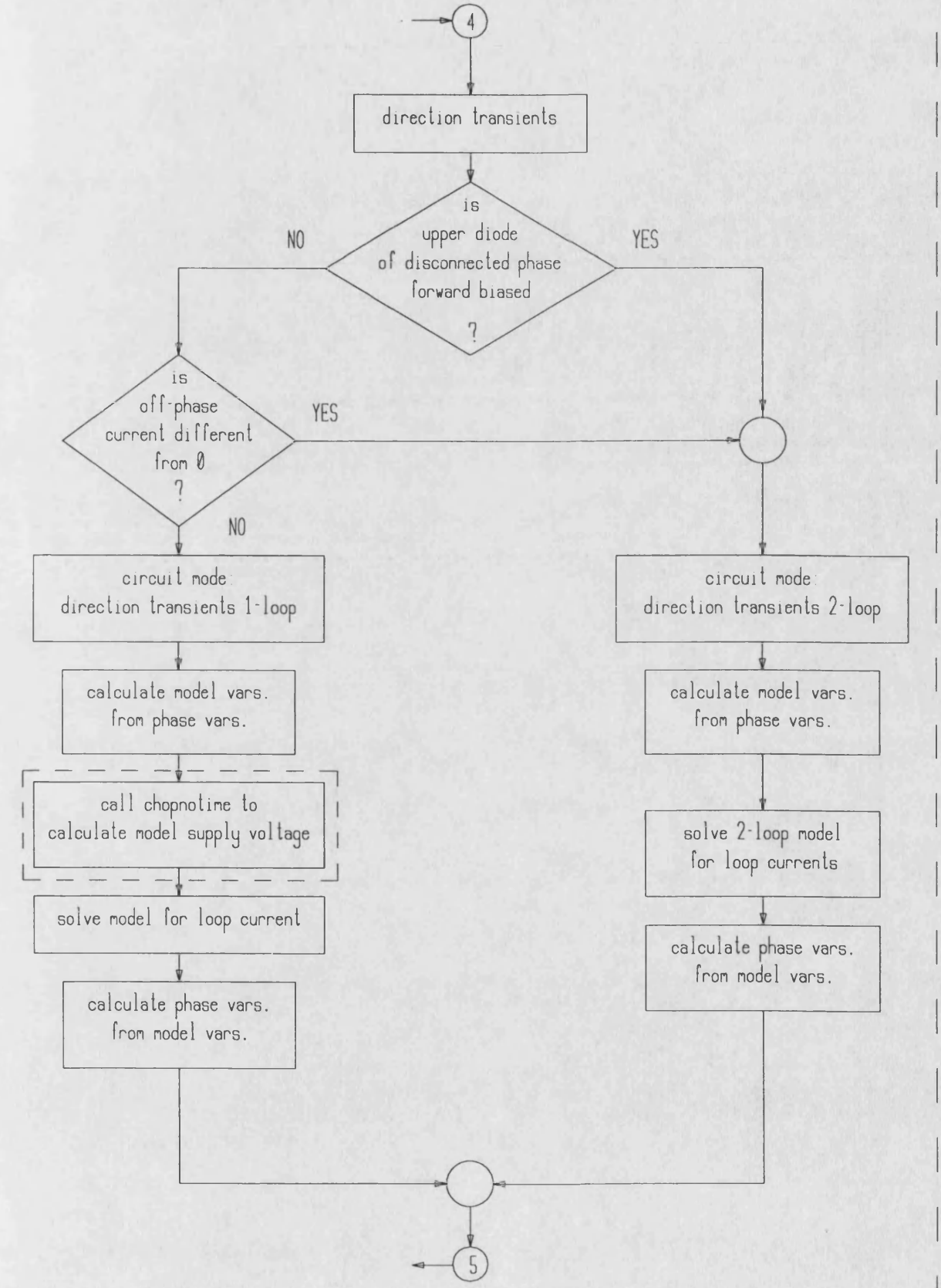
4
direction transients
is upper diode of disconnected phase forward biased ?
NO
YES
is off-phase current different from 0 ?
YES
NO
circuit mode direction transients 1-loop
calculate model vars. from phase vars.
call chopnotime to calculate model supply voltage
solve model for loop current
calculate phase vars. from model vars.
circuit mode direction transients 2-loop
calculate model vars. from phase vars.
solve 2-loop model for loop currents
calculate phase vars. from model vars.
5

a previous step and thus a third phase current may still be circulating through the diodes. If this is also a "NO" then it is a one-loop circuit. If one of the checks gives "YES", it is a two-loop circuit.

In the case of "direction transients" the circuit mode is chosen in a similar fashion, although this time a check is first made for the line to line voltage between + and 0 phases, which are defined by the switching interval. This, of course, uses the step-start currents and voltages for the calculations. If again both checks give "NO" it is a one-loop circuit, if a "YES" is encountered then it is a two-loop circuit.

In all four circuit modes the corresponding model is first constructed for the step-start values using phase variables. The model is then solved locally for the step-end loop currents using the related equation of Section 5.4.1. Step-end variable values of the model are then used to reconstruct the three-phase machine model for the step-end conditions. The two two-loop models are solved by a common subroutine. This performs matrix manipulation and, using mesh current methods, solves the circuit for mesh (loop) currents.

Supply voltage and the variables indicated with *(ch)* subscript on the three of the four models are determined by two subroutines simulating the current magnitude controller function of the driver. These subroutines primarily specify the status of the model supply voltage which in turn determines the other chopping-dependent variables. The first of these subroutines, "choptime", simulates the normal operation of the driver chopper and is called by one-way operation models. The second, "chopnotime", is for the "direction transients" and called by the one-loop model only.

Flowcharts of these two sub-programmes are illustrated in Figs. 5.17(a) and (b). Choptime sets the supply voltage to zero for a specified turn-off time (t_{off}) once the

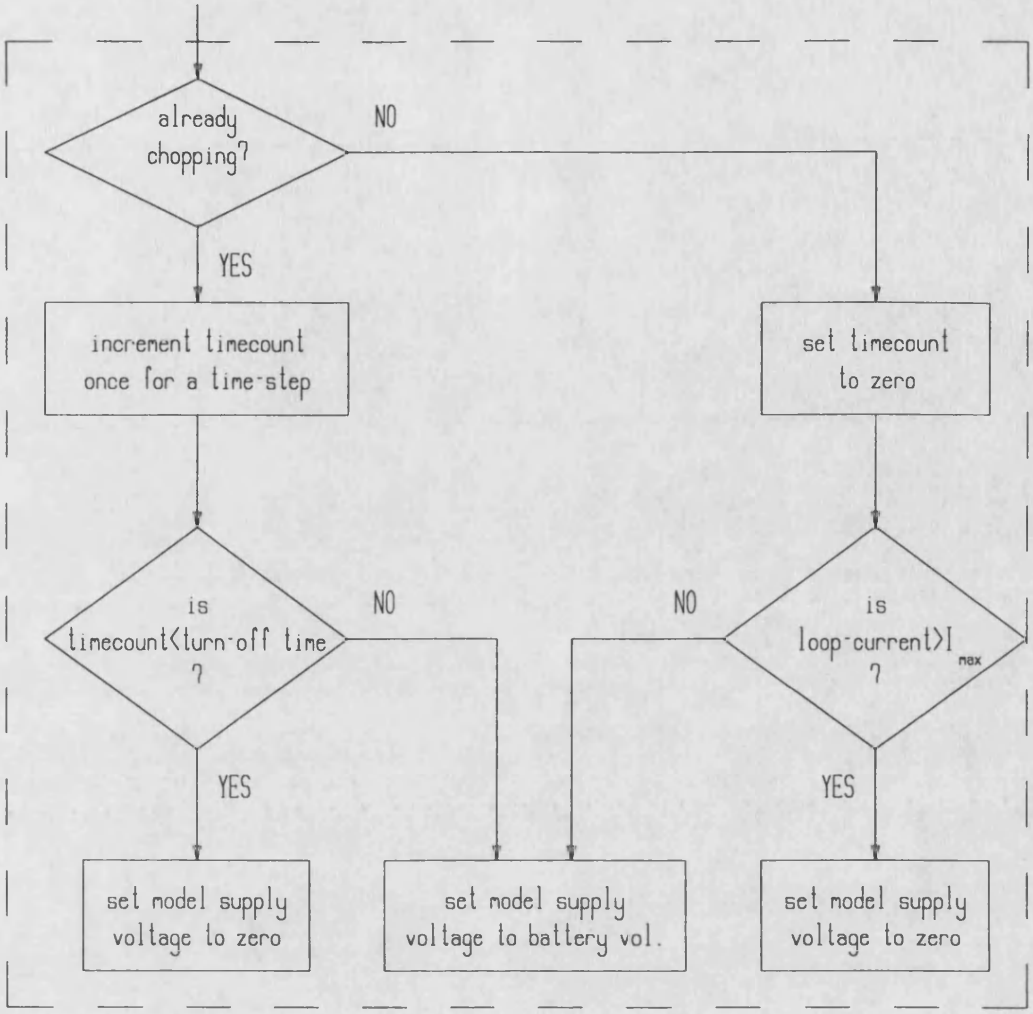

(a) Subroutine Choptime

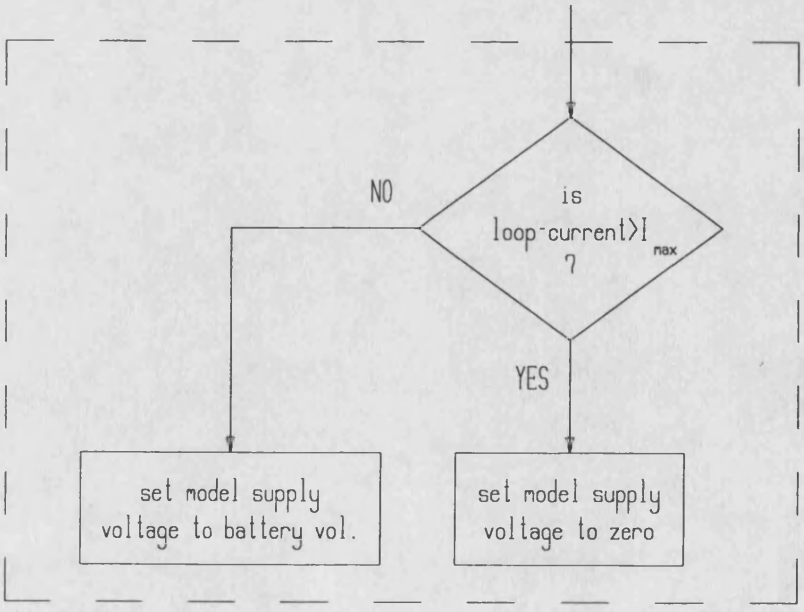

(b) Subroutine Chopnotime

Figure 5.17 Flow Charts of the Chopper Algorithms Used

current exceeds the maximum allowable DC current level, I_{max}. The value of this current is determined by the sense resistor using

$$I_{max} = 0.5/R_s$$

an equation defined by the driver hardware [please see Appendix F]. Subroutine chopnotime, on the other hand, works according to the current level and chops the voltage as long as the current is above I_{max}.

Another block in the simulation program checks and initiates the steady-state conditions. This is given in Fig. 5.18. The block is executed when a change in direction signal is encountered. If the excitation is approaching the right-hand-end of its travel (left to right stroke) then it is the moment when direction signal changes from 0 to 1 which takes place once every period of excitation oscillation. The third control in the block involves checking the steady-state conditions and upon entering the following section the instant in time and the stroke are accepted as the start of the steady-state period.

In the simulation program calculated values were used for end-effect force, phase flux linkages and phase self and mutual inductances. However, measured values were used for the other parameters. These are phase, R_s and R_{ext} resistances, battery voltage, mass of the moving parts and displacement values which define the excitation position and direction signals. These parameters are given in Table 5.7 where n_h is the maximum number of harmonics used in the Fourier series representation of the flux linkage and ESleft and ESright are left and right end-sensors which determine the direction signal. Fig. 5.19 gives the experimental excitation position signals used in the program.

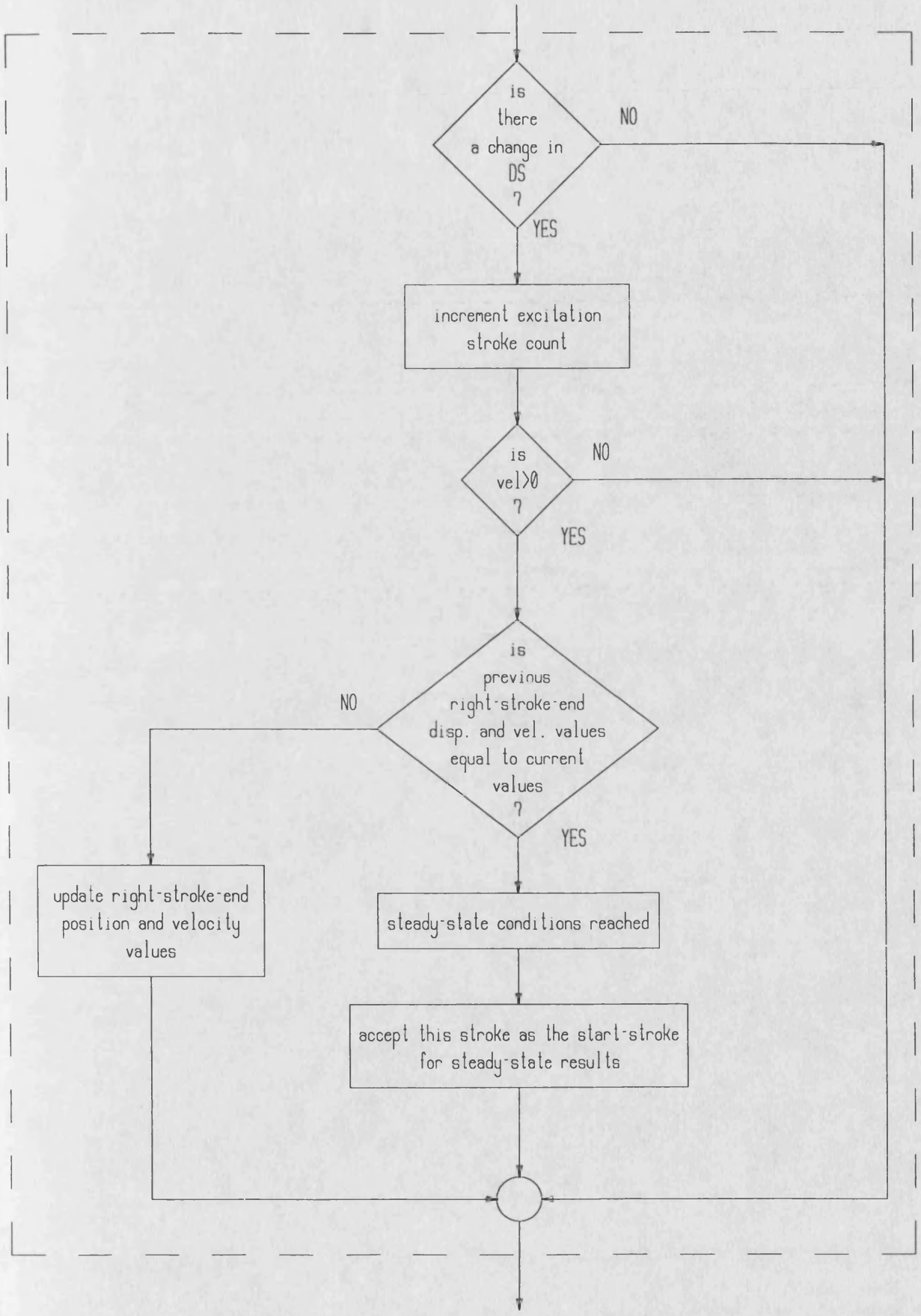

Figure 5.18 Flow Chart of the Steady-State Initiation Block

Table 5.7

Parameter Values Used in the Simulation Run

Parameter	Value
R	1.6 Ohm
L	0.0360 H
M	-0.0095 H
R_s	1.0 Ohm
R_{ext}	0.0 Ohm
V_{DC}	12.7 V
m	7.662 kg
n_h	25
ESleft position	-107.1°
ESright position	104.5°

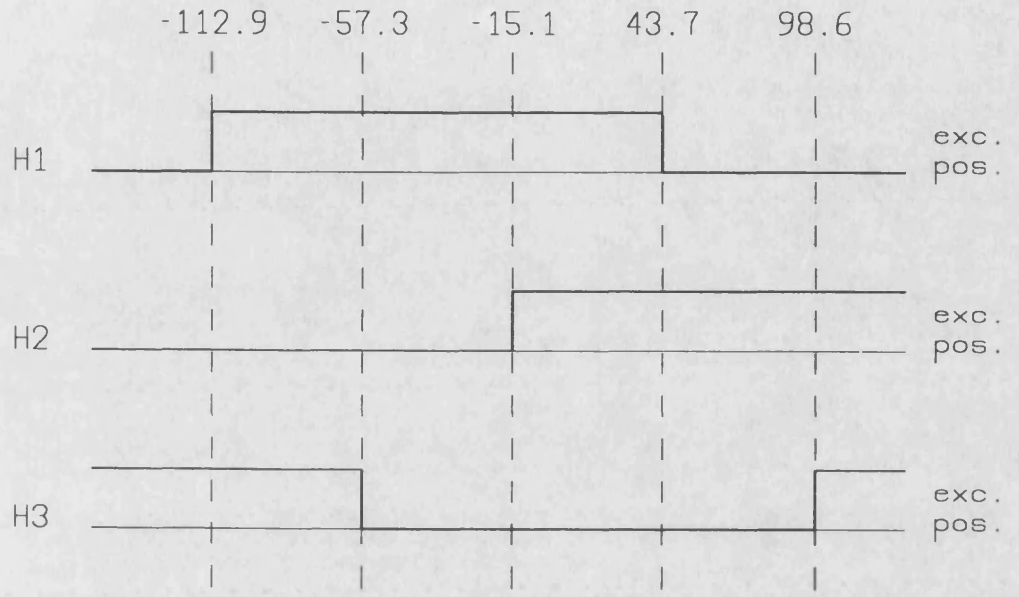

Figure 5.19 Measured Excitation Position Signals Used in the Simulation Program

5.6 Experimental Verification of the System Simulation

The prototype brushless dc tubular motor was tested using oscillatory operation in order that a comparison could be made with the simulation results. Mechanical measurements were performed by measuring the total force acting on the excitation. This was arranged by means of a strain-gauge load-cell which was placed between the ground and armature with the armature isolated from the ground and floating using a linear bearing [Figure 5.20]. This force, measured using a digital oscilloscope, was then transferred to a microcomputer and from this to a mainframe computer. Experimental excitation velocity was then obtained by numerically integrating the excitation acceleration which was obtained by dividing the total measured force to the mass of moving parts for a complete period (excitation oscillation) and using

$$\int_0^T v\,dt = 0$$

This is valid for oscillatory operation and states that the total displacement for a cycle is zero.

The position of the excitation was then calculated by further integrating the velocity profile in time also for a complete cycle. In order to obtain the actual experimental position profile a reference point whose displacement value is known is needed which corresponds to the integration constant in mathematical terms.

All mechanical and electrical measurements were recorded using a digital oscilloscope. These waveforms were then transferred to the computer and plotted using the same graphics software as the simulation results.

The simulation program was written in *Fortran 77* for *Multics* and *Unix* operating systems. Simulation started from the line of symmetry where $x = 0$ and the

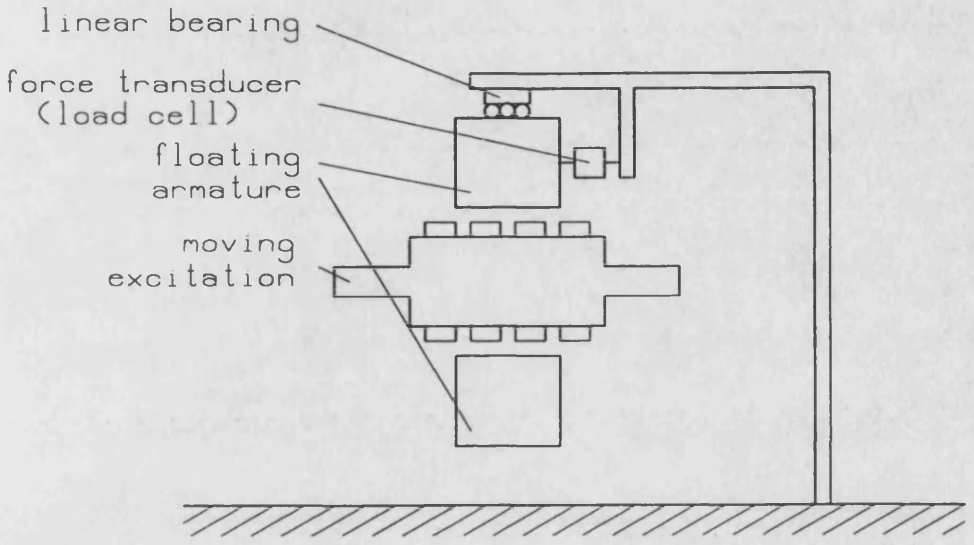

Figure 5.20 Experimental Set-Up Used for Mechanical Measurements

excitation first moved to the right because of the force in that direction. It was found that the results were independent of the time-step length for 0.1-0.5 msec range. Steady-state conditions were reached after 10 oscillations using 0.5 msec time-step length. The results were stored and plotted for two excitation oscillations i.e. four strokes.

Figures 5.21, 5.22 and 5.23 show the simulated and experimental phase currents for the oscillatory motion. The maximum dc current level was chosen to be 0.5 A for this run by appropriately choosing the sense resistor. It can be observed that the general agreement between predicted and experimental results is good for the normal operation where chopping action takes place. During "direction transients", however, where currents are high, the agreement is not so good. This is partly because of the relatively high voltage drops across switches and simplifications made in the analysis. However, the overall correlation is good.

Figure 5.24 shows simulation results for the logical variables, i.e. excitation position signals H1, H2 and H3 and direction signal. Figure 5.25 also gives the experimental results for these variables. These signals, as was explained earlier, define the status of the inverter switches being on or off. The correlation is good except for H1. The reason for this is that the excitation moves further in the simulation results at this excitation position where the excitation is at the left-hand-end region and H1 changes according to Fig. 5.19. The length of the excitation oscillation period can be clearly seen on direction signal plots. The simulated period is 703 msec and the experimental one is 732 msec.

Phase to neutral voltages of phases a, b and c are given in Figs. 5.26, 5.27 and 5.28 respectively. These voltages inherently have spikes due to the switching action. The overall agreement is good and shows that the simulation program can be used to calculate phase voltages as well as other variables. It may be observed that during

periods when the simulated voltage is zero, the experimental value, although near, is not. This is due to the assumption made in the analysis that phase inductances are equal and balanced. The difference, however, is a small one.

The predictions for the mechanical performance of the system are compared with the experimental results on Figures 5.29, 5.30 and 5.31. Figure 5.29 illustrates the total force acting on the excitation including the magnetic end-effect force with predicted and experimental results plotted on the same graph. Figure 5.30 compares the results for the instantaneous excitation velocity and Figure 5.31 for excitation position. It will be observed that the simulation results are reasonably accurate given the severe transients involved in the oscillatory operation and the assumptions made in the analysis.

It may be noticed that when the direction signal changes the phase currents reverse fast and increase to about three times the maximum dc current value allowed for the normal (one-way) operation. The actual value of these current peaks is determined by the phase emfs which are in turn proportional to the instantaneous excitation speed. The current control of the driver chip cannot stop these currents and if they exceed the maximum current value the driver is designed for, they may damage the driver switches. During this period ("direction transients") the excitation is decelerated by the reversed electromagnetic force (reversed motor action).

The simulation program can be useful to obtain results that may not be measured practically. Figures 5.32(a), (b) and (c) give the phase to neutral back emfs. Figure 5.33 shows the electromagnetic force exerted on the excitation by the armature phase currents i.e. motor action. The decelerating force during "direction transients" can easily be seen and is about 4 times the average force produced during the normal operation mode. A comparison between total force of Figure 5.29 and the

electromagnetic force of Figure 5.33 shows the impact of the end-effect force on the total force acting on the excitation. Figure 5.34 illustrates the logical values of the operation modes of the drive system. Figure 5.34(a) gives the periods when "direction transients" are on, i.e. from direction signal change till the excitation is stopped. Figure 5.34(b) gives the periods when all three phases have currents, i.e. two-loop mode, in both normal operation and the "direction transients".

It was shown in Chapter 3 that the steady-state thrust force as calculated by finite element analysis varies nearly sinusoidally with the force angle, i.e. the angle between the excitation and the armature mmfs. Figure 3.11 of Chapter 3 shows this force and the average force for 60 ° - 120 ° force angle interval, which is the interval the machine is designed for, is about 26 N at 1 A phase currents and thus 13 N at 0.5 A. A constructive comparison can be made when this average force value is compared with the normal operation average value of the electromagnetic force obtained from the simulation program [Figure 5.33]. This average value for the normal operation (one-way) mode is also around 13 N for the same phase currents of 0.5 A.

The simulation program was also used to compute the instantaneous power flow inside the machine. Figures 5.35, 5.36 and 5.37 give the terminal power, i.e. the power obtained from the battery, armature ohmic losses and machine electromagnetic power, which is the power the moving excitation uses, respectively. A close inspection of the terminal power graph of Fig. 5.35 will reveal that, during "direction transients" [Figure 5.34(a)], the battery does not supply energy to the system. The energy during these instants is consumed in the armature phases and the copper losses increase considerably, as can be seen on Figure 5.36. The energy is supplied by the kinetic energy of the excitation and the machine works as a generator. This can be observed from Figure 5.37 where the power component responsible for the input to the excitation is negative during "direction transients".

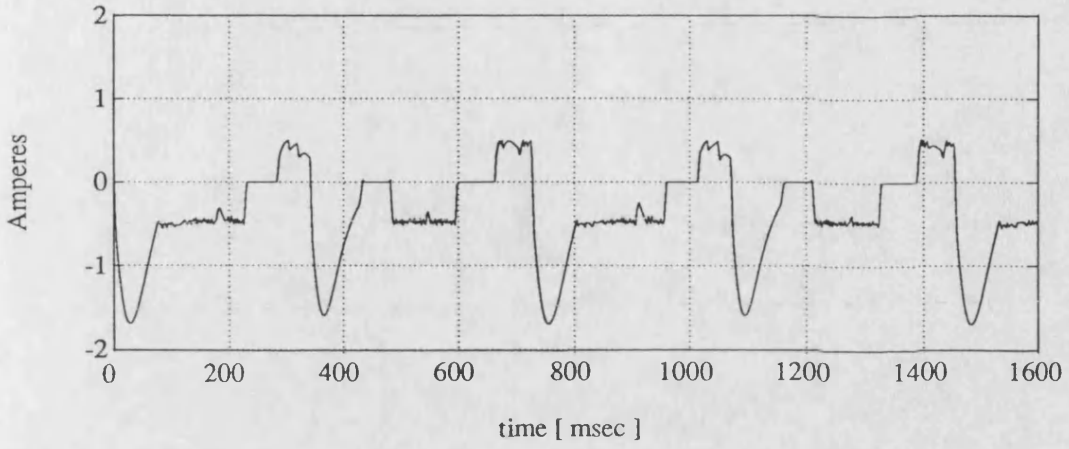

(a)

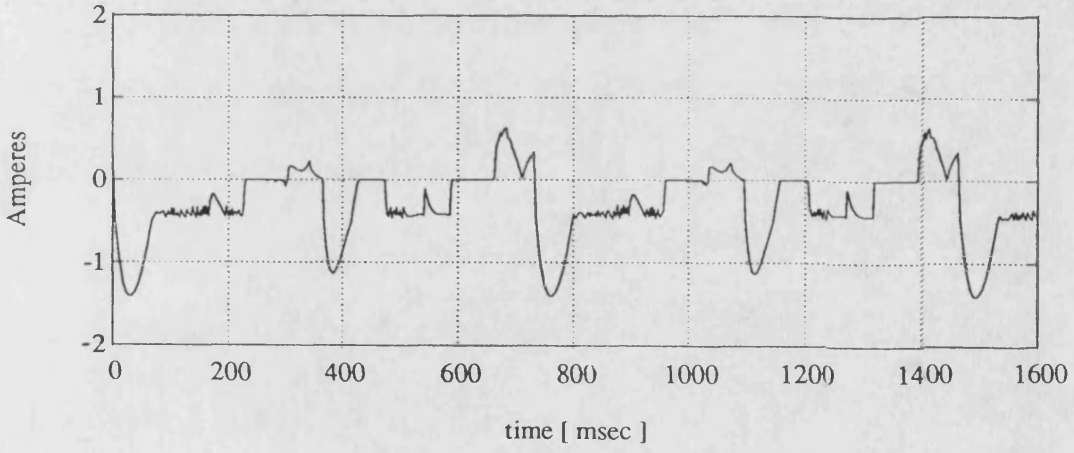

(b)

Figure 5.21 Phase a Current
(a) Simulation
(b) Experiment

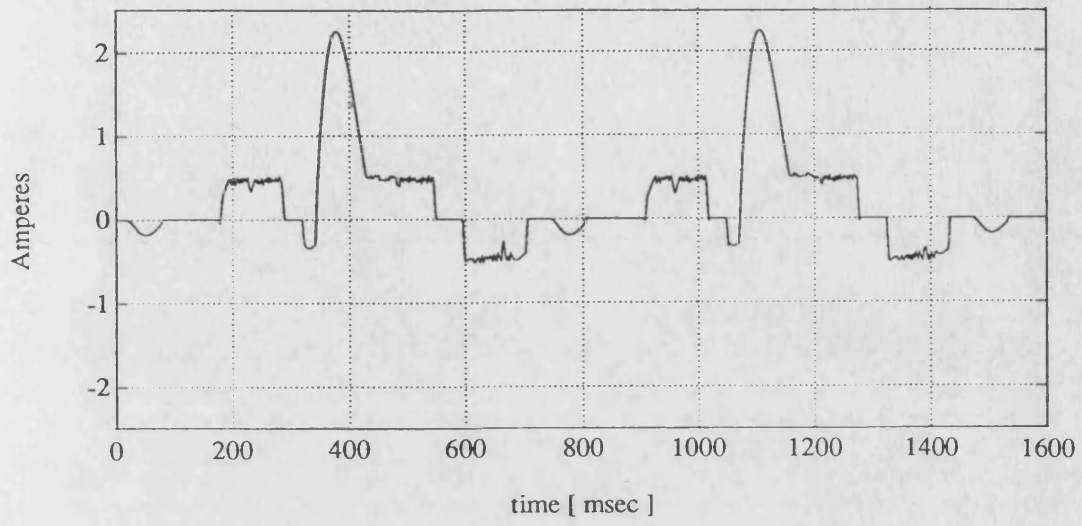

(a)

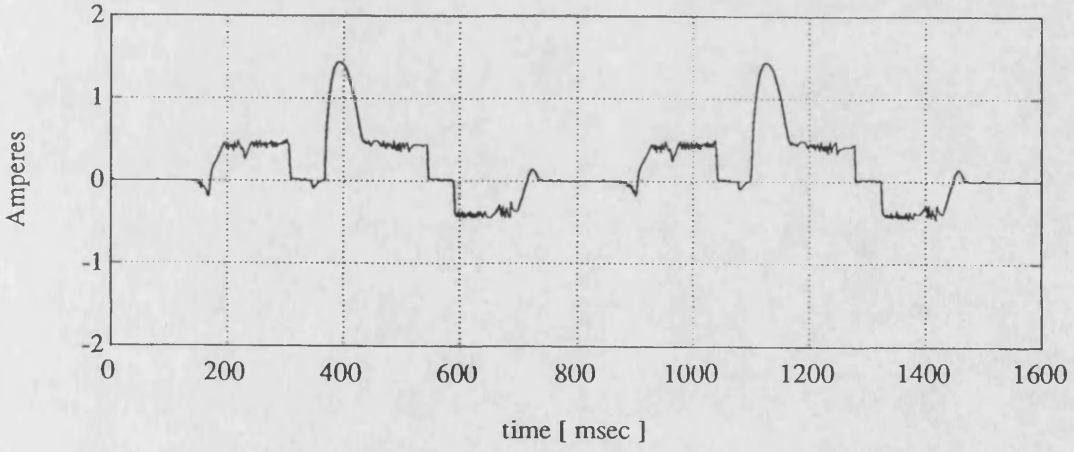

(b)

Figure 5.22 Phase b Current
(a) Simulation
(b) Experiment

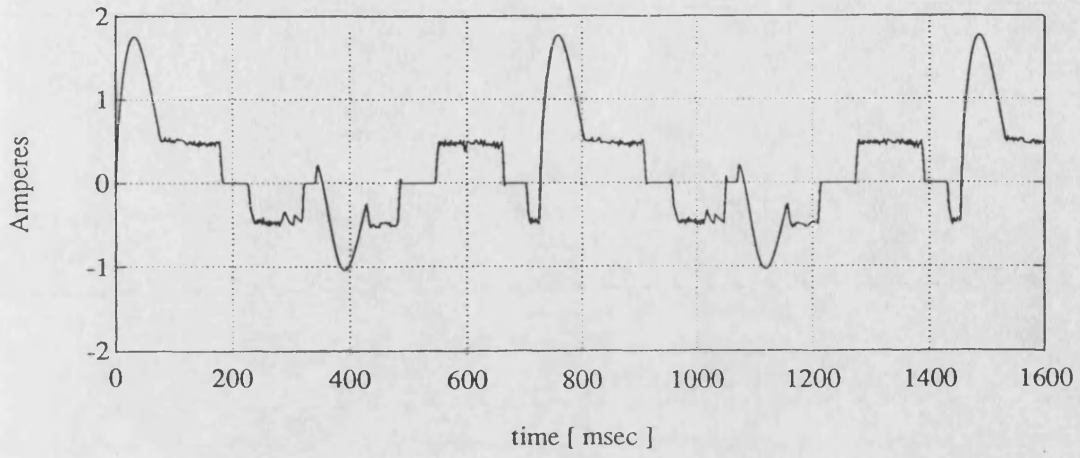

(a)

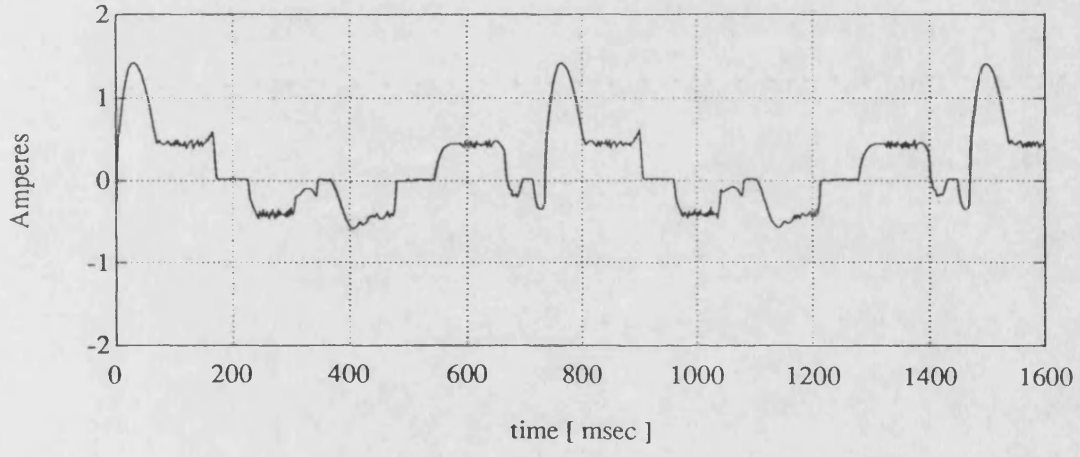

(b)

Figure 5.23 Phase c Current
(a) Simulation
(b) Experiment

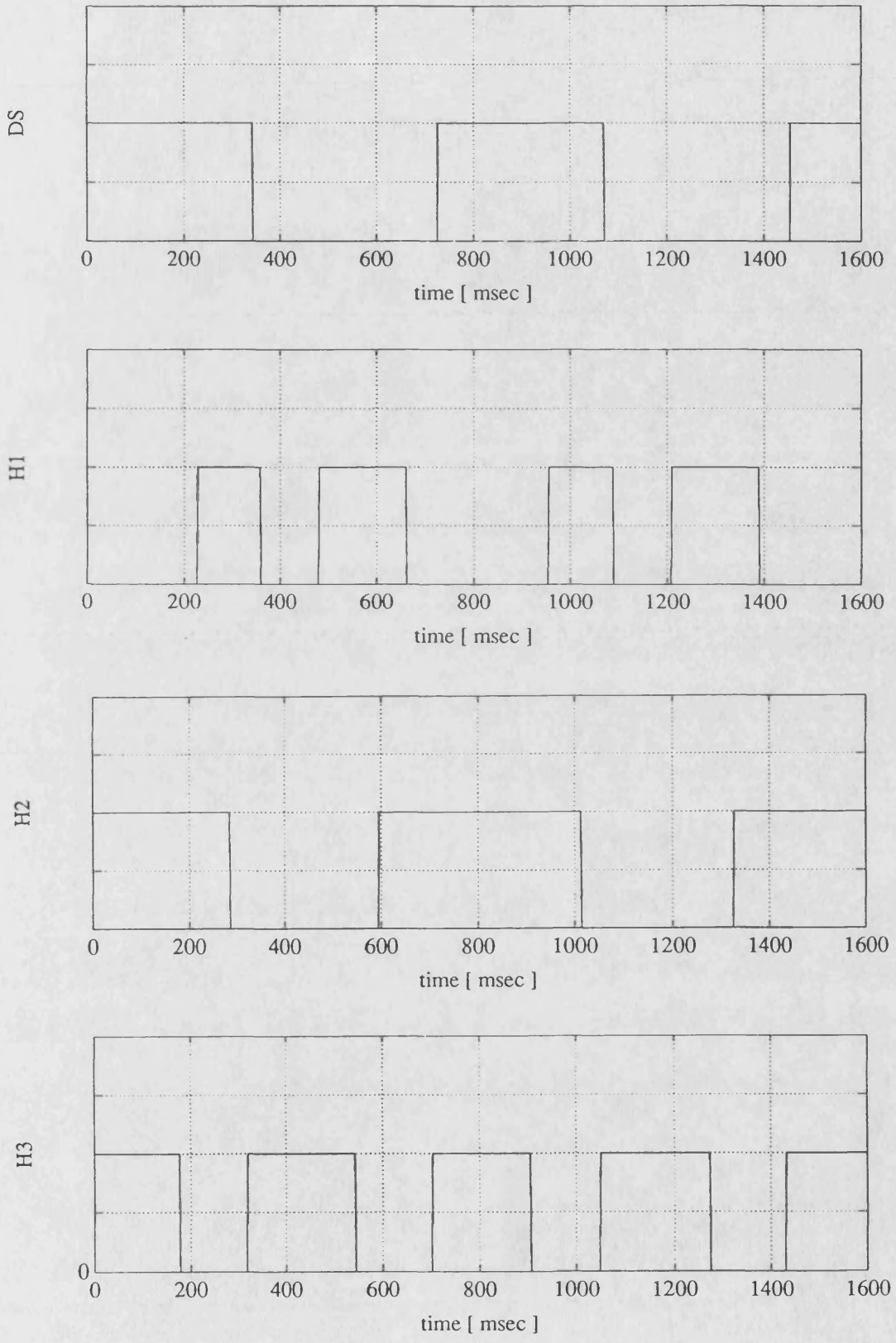

Figure 5.24 Simulated Direction and Excitation Position Signals

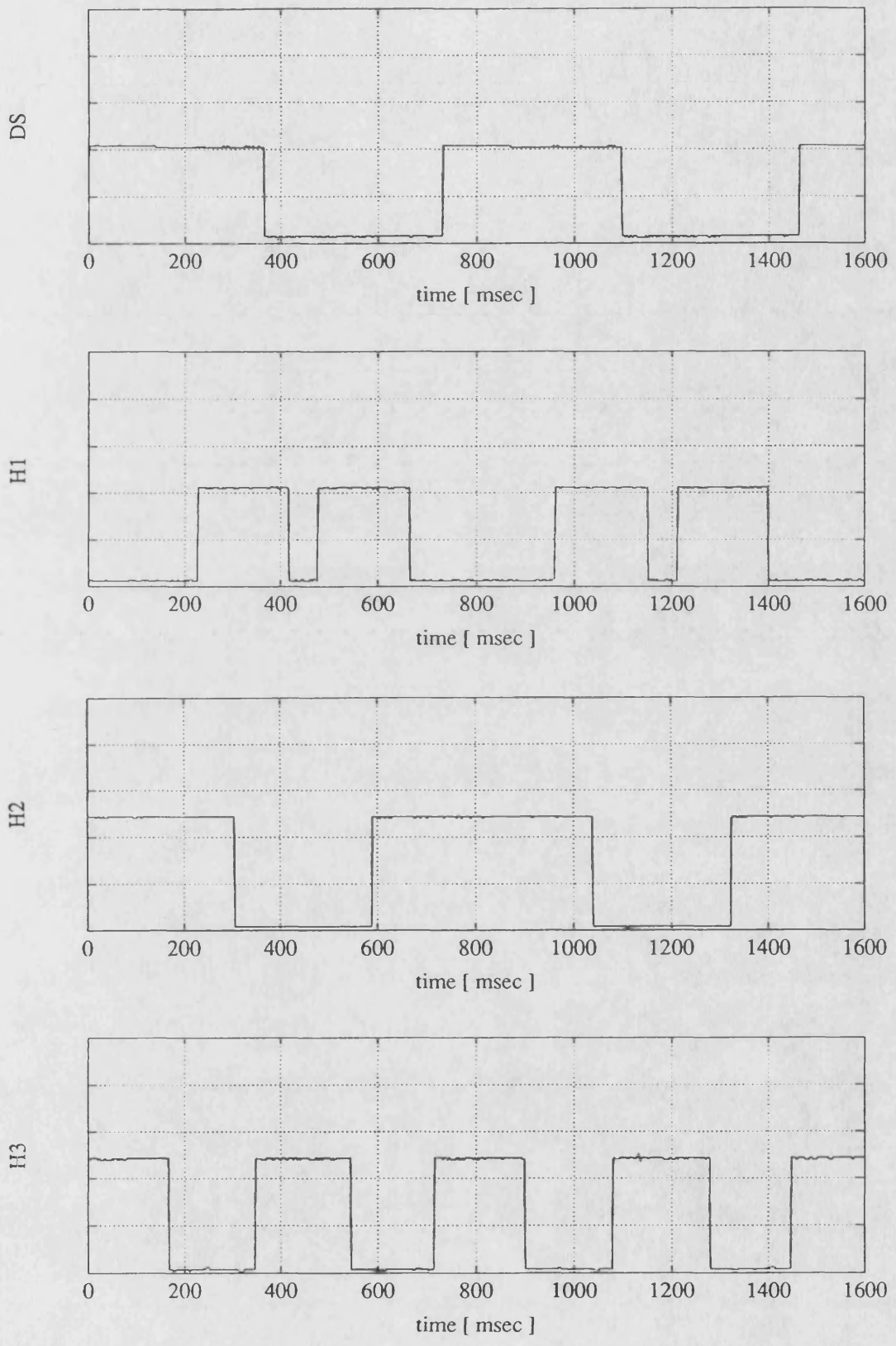

Figure 5.25 Experimental Direction and Excitation Position Signals

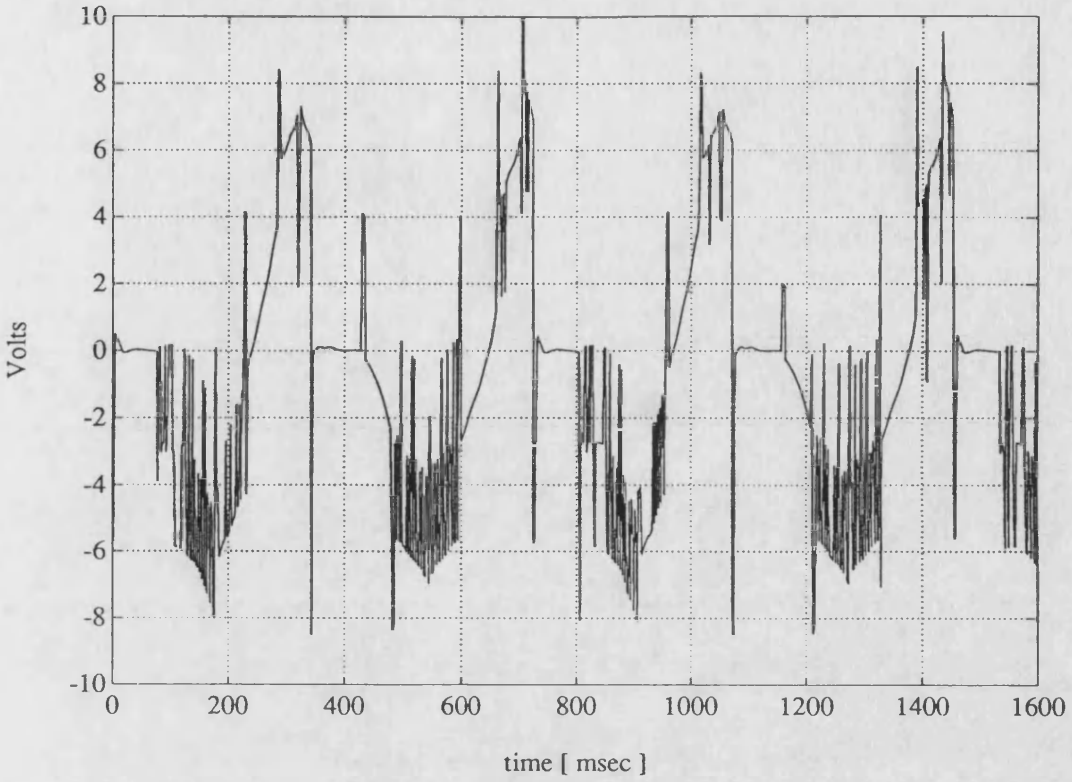

(a)

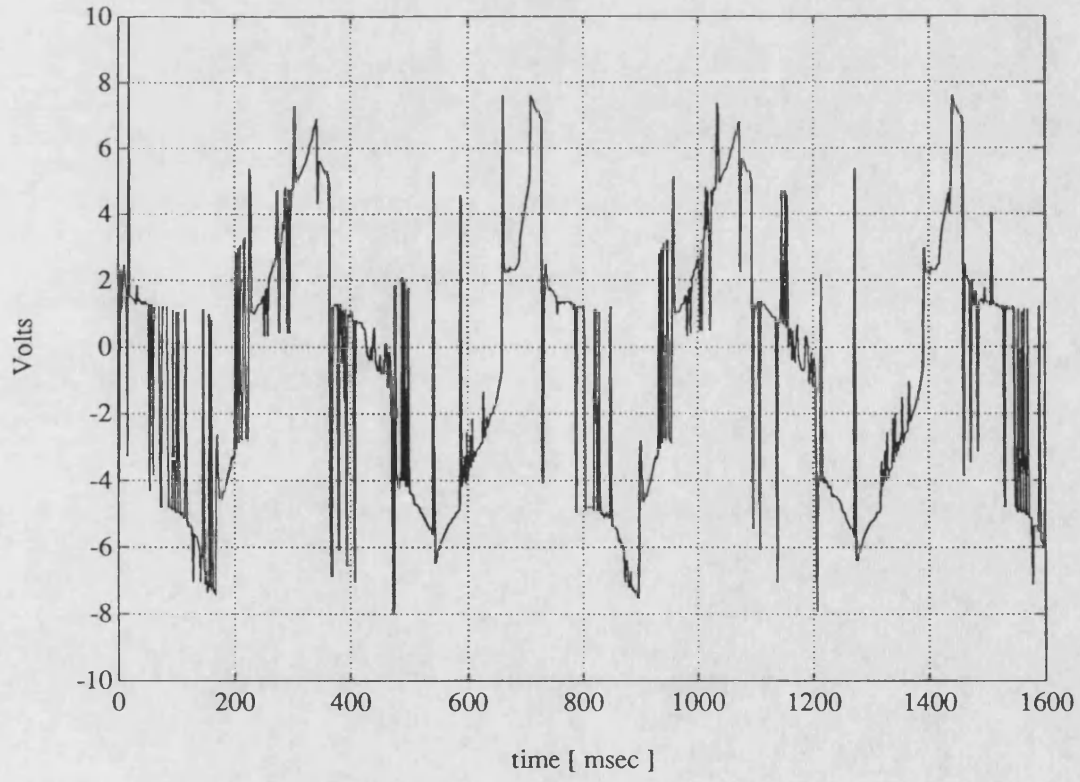

(b)

Figure 5.26 Phase a Phase to Neutral Voltage
(a) Simulation
(b) Experiment

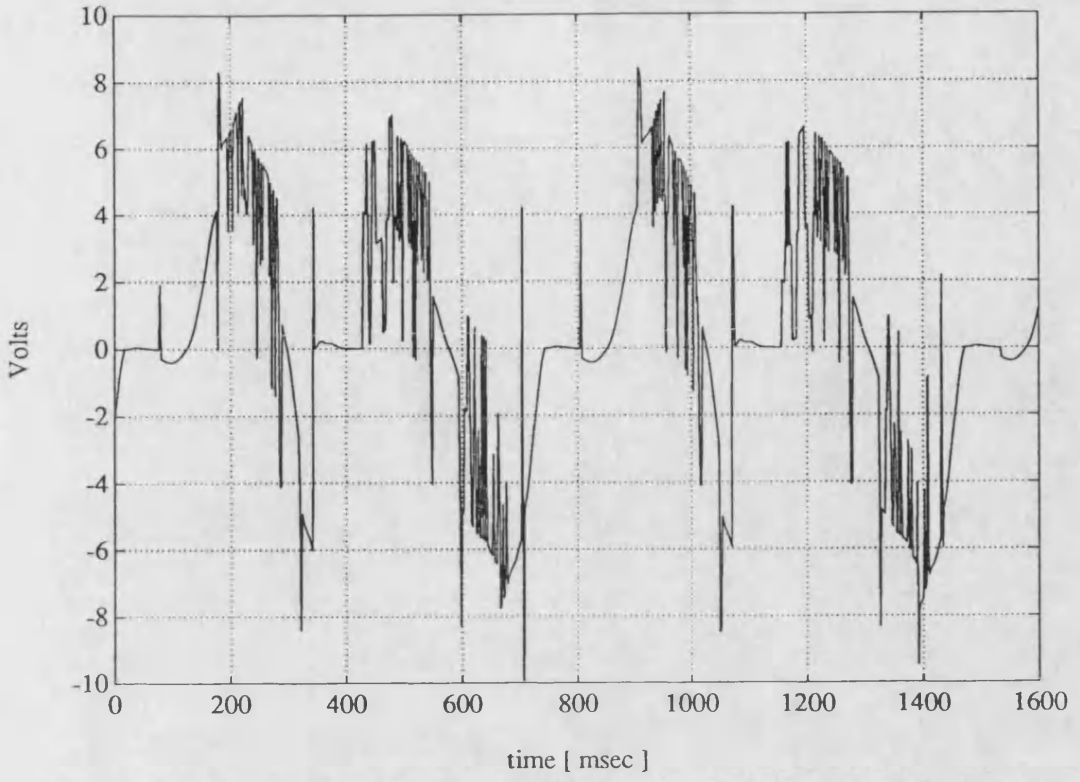

(a)

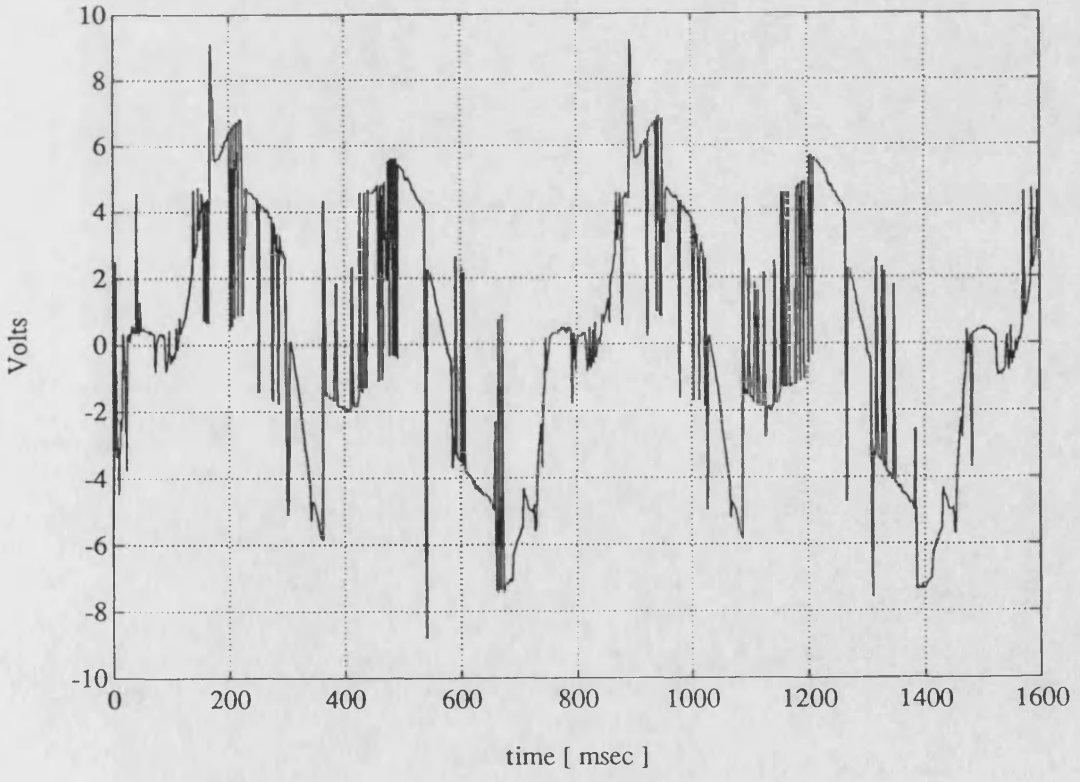

(b)

Figure 5.27 Phase b Phase to Neutral Voltage
(a) Simulation
(b) Experiment

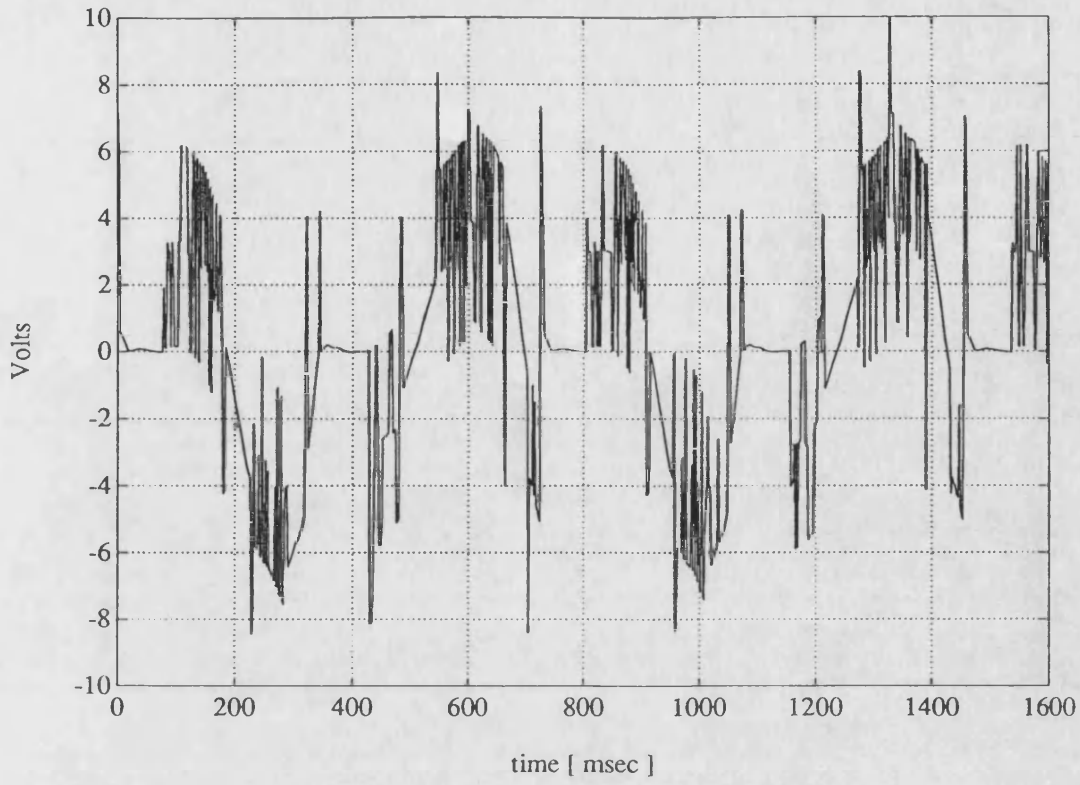

(a)

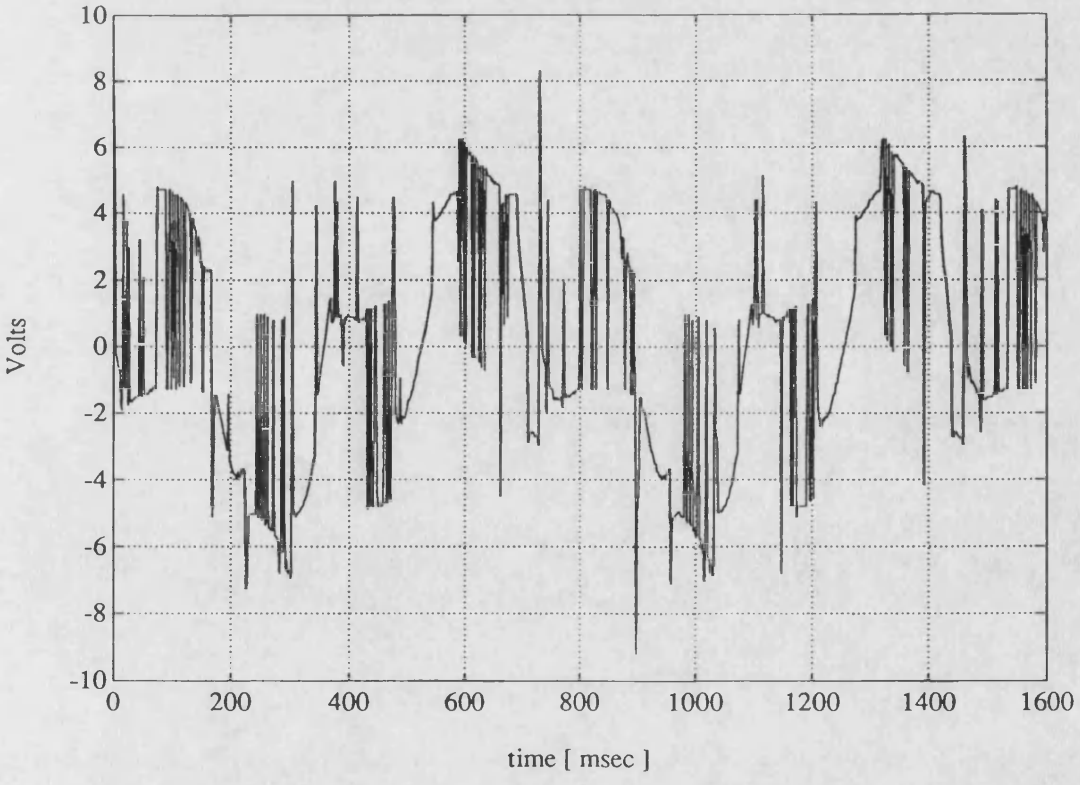

(b)

Figure 5.28 Phase c Phase to Neutral Voltage
(a) Simulation
(b) Experiment

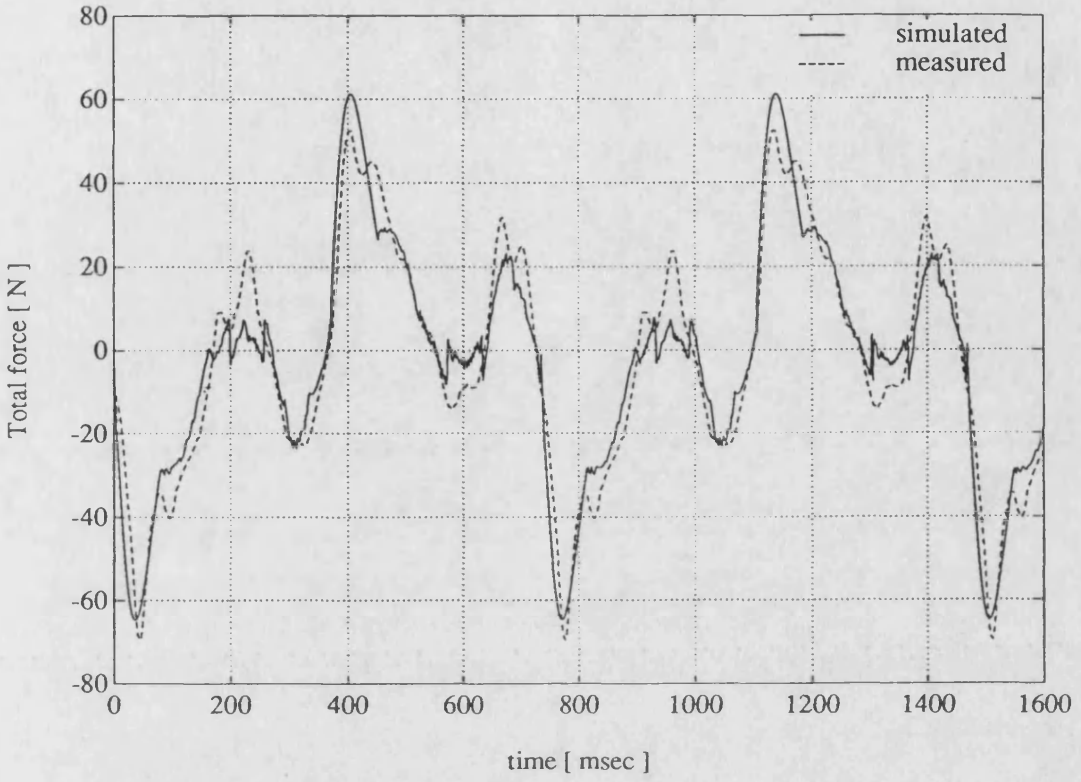

Figure 5.29 Simulated and Measured Total Force Acting on the Excitation

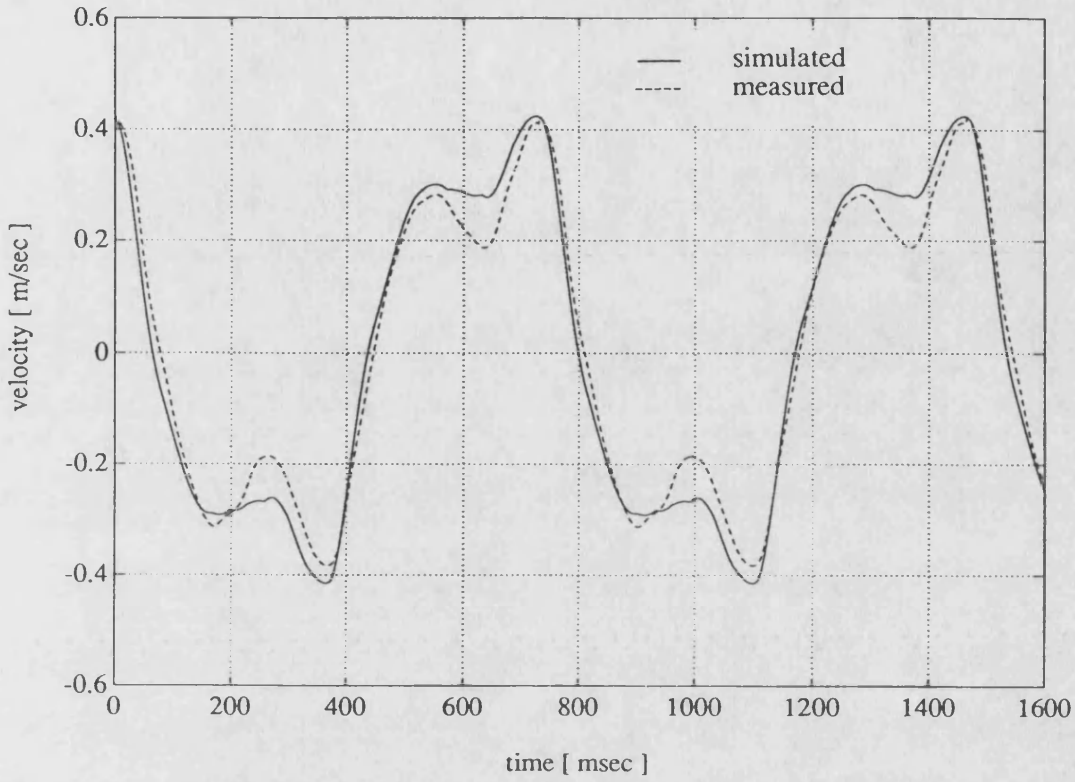

Figure 5.30 Simulated and Measured Excitation Velocity

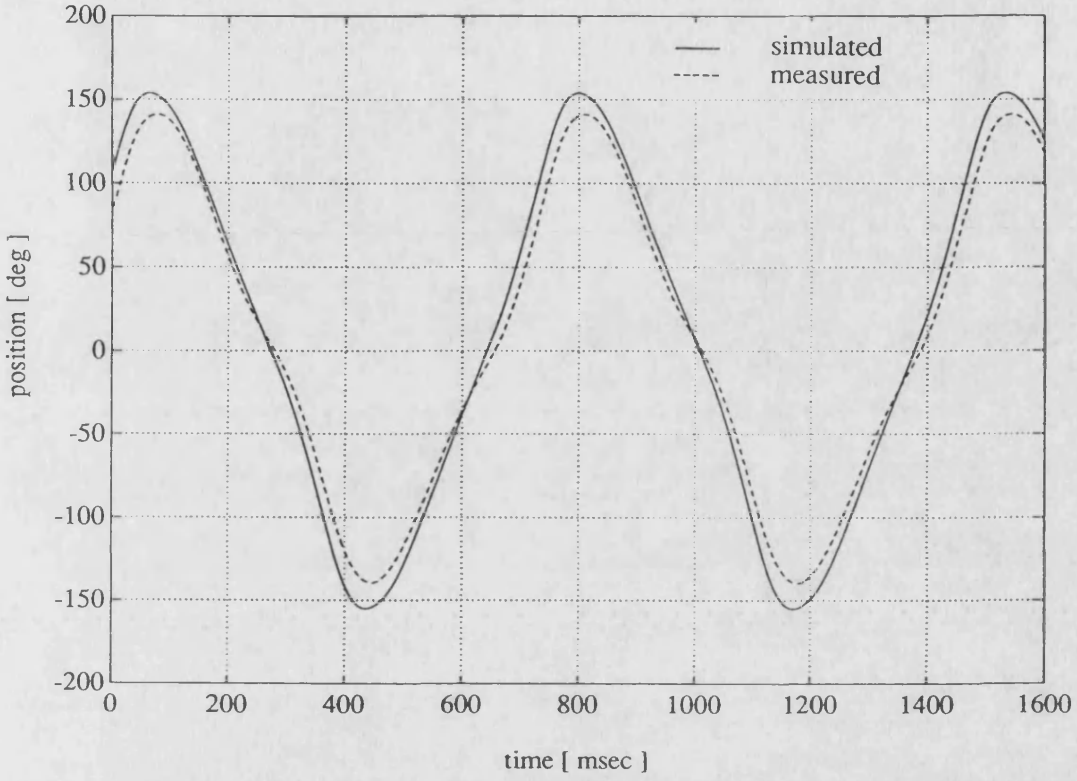

Figure 5.31 Simulated and Measured Excitation Position

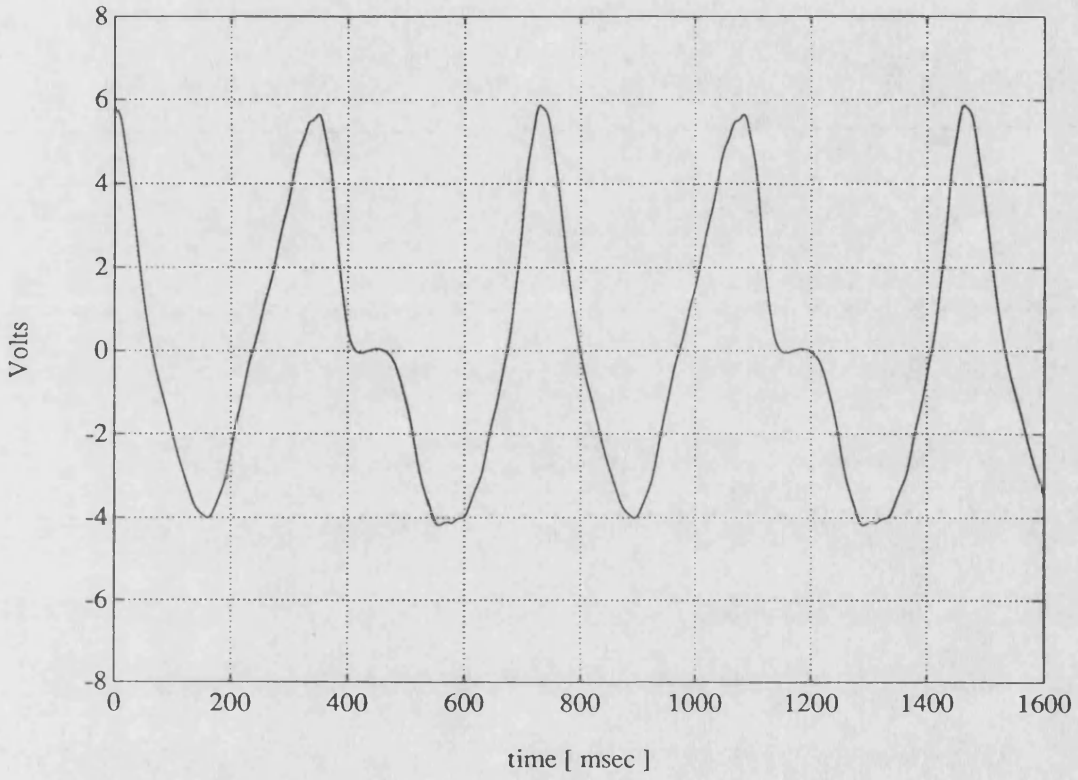

(a)

Figure 5.32 Simulated Phase to Neutral Emfs
(a) Phase a
(b) Phase b
(c) Phase c

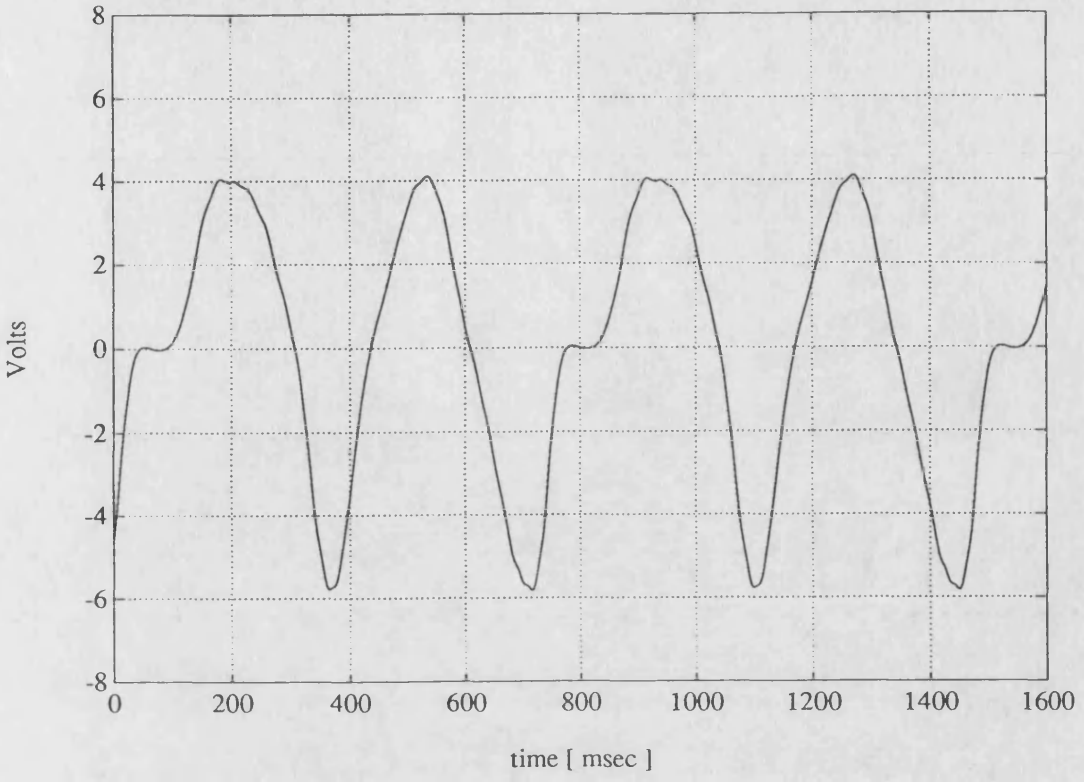
Volts
8
6
4
2
0
-2
-4
-6
-8
0
200
400
600
800
1000
1200
1400
1600
time [msec]

(b)

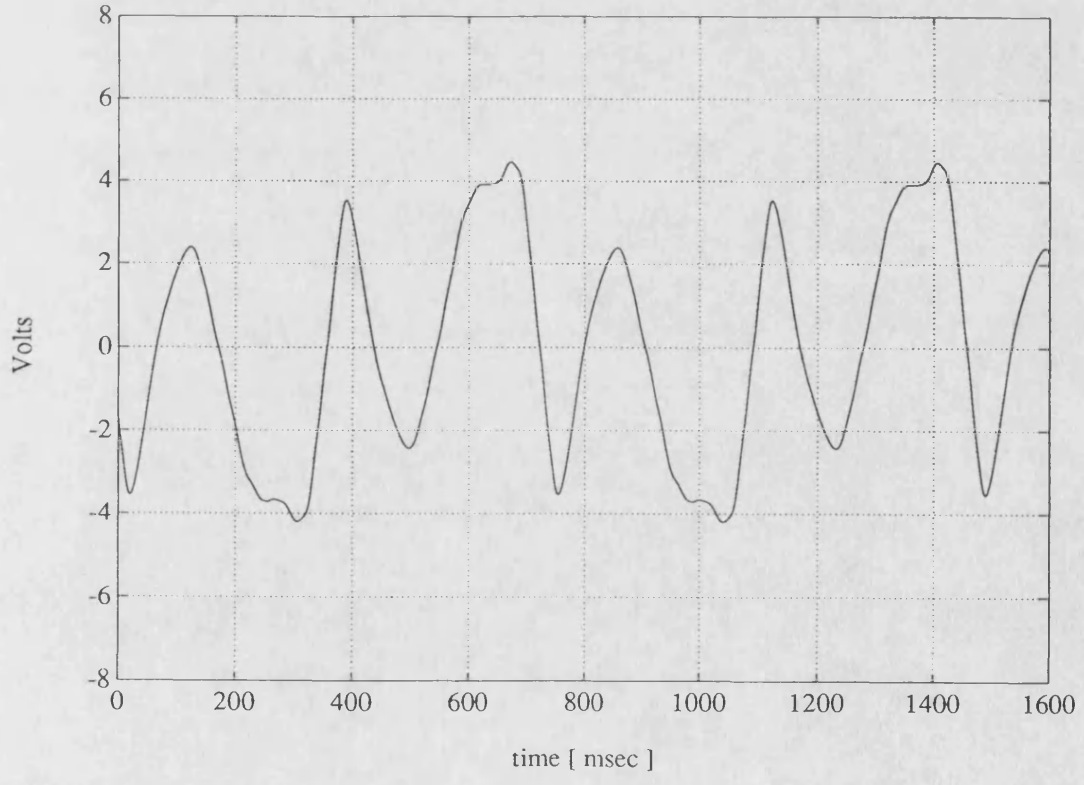
Volts
8
6
4
2
0
-2
-4
-6
-8
0
200
400
600
800
1000
1200
1400
1600
time [msec]

(c)

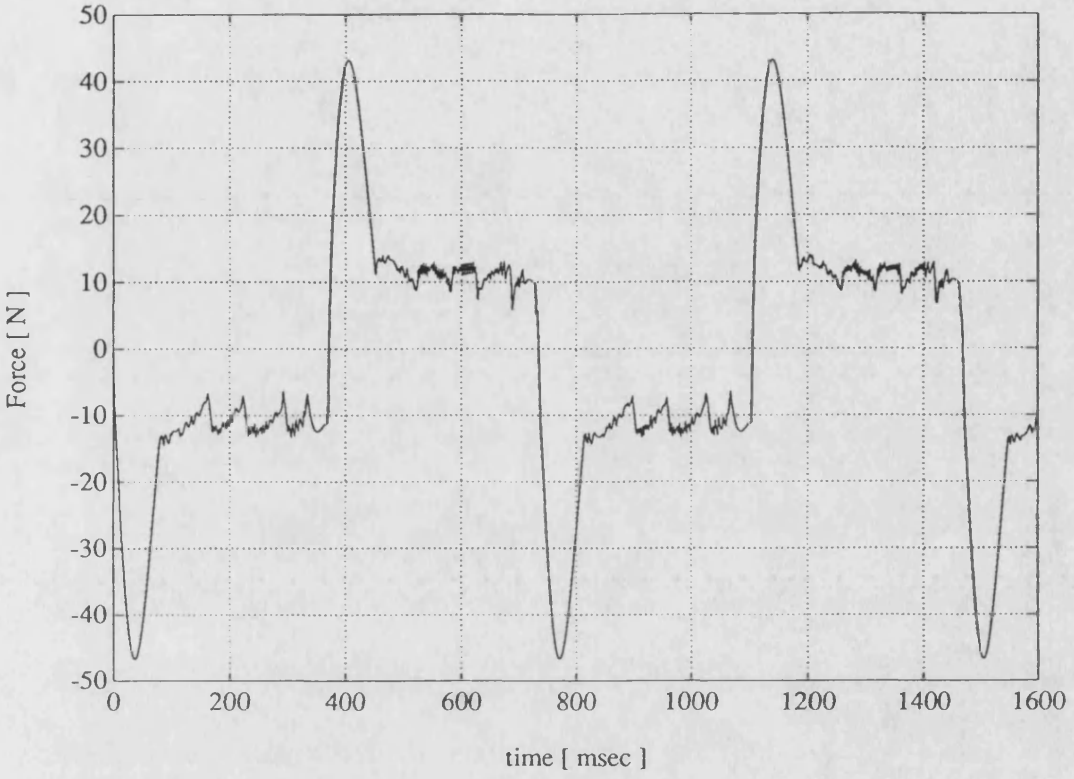

Figure 5.33 Simulated Machine Electromagnetic Force

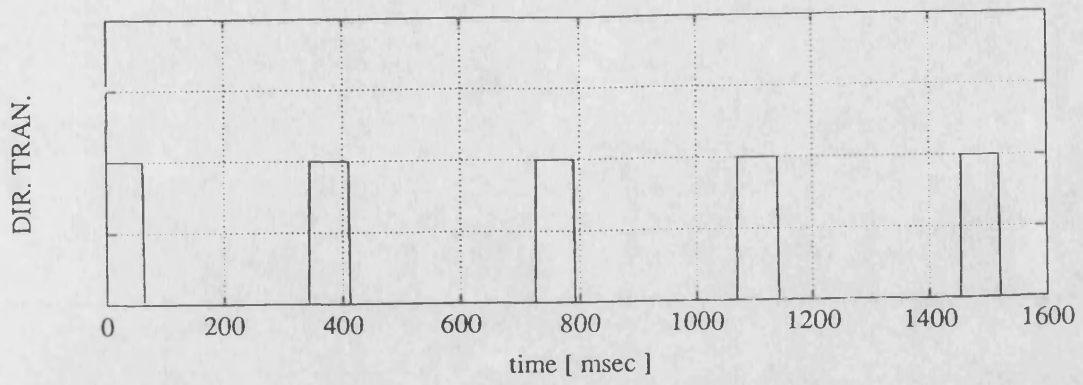

(a)

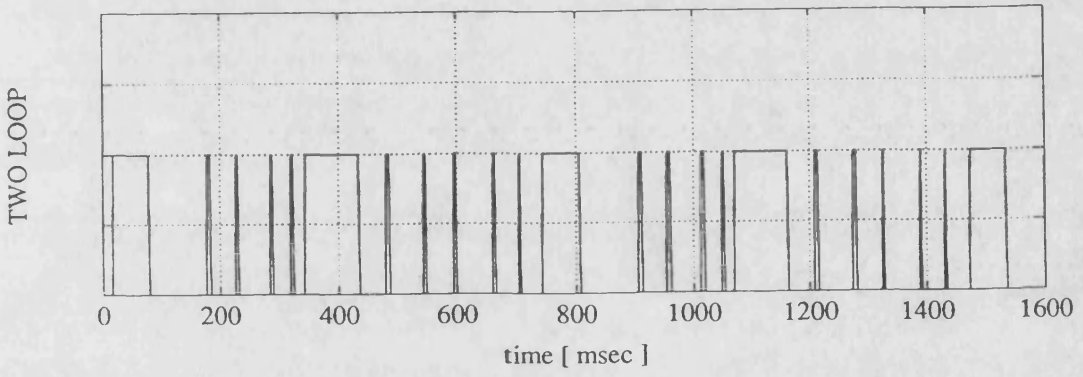

(b)

Figure 5.34 Simulated Plots of the Oscillatory Operation Showing the Intervals of
(a) Direction Transients
(b) Two-Loop Mode

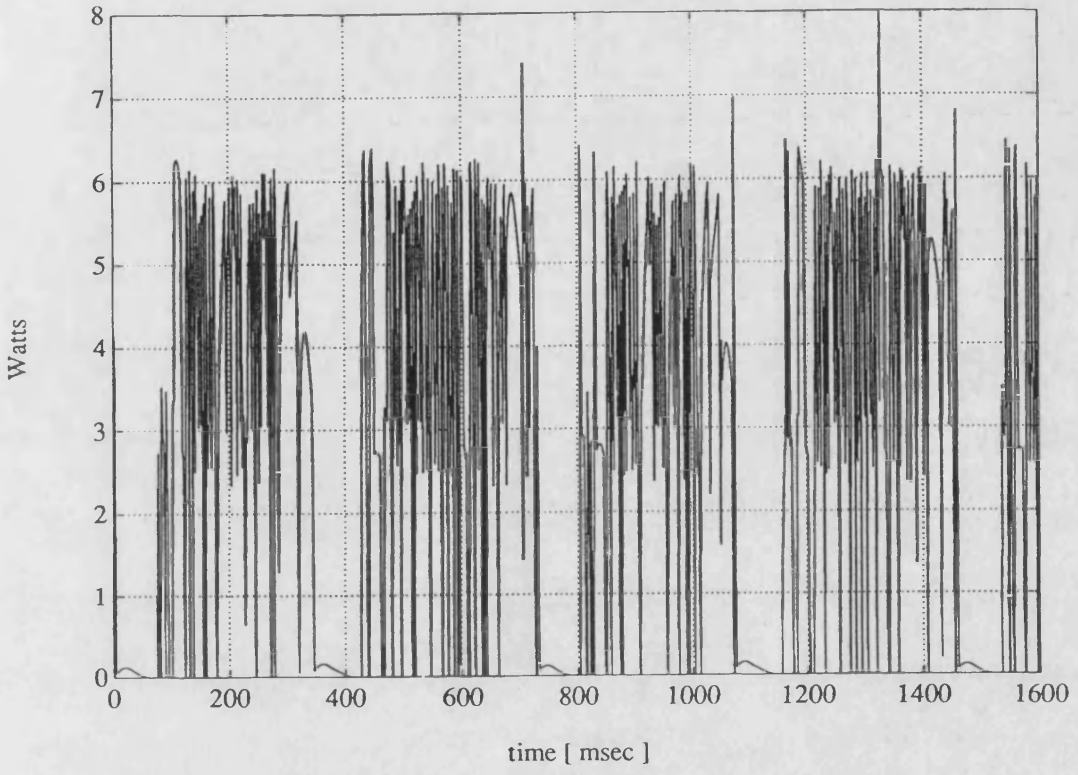

Figure 5.35 Simulated Machine Terminal Power

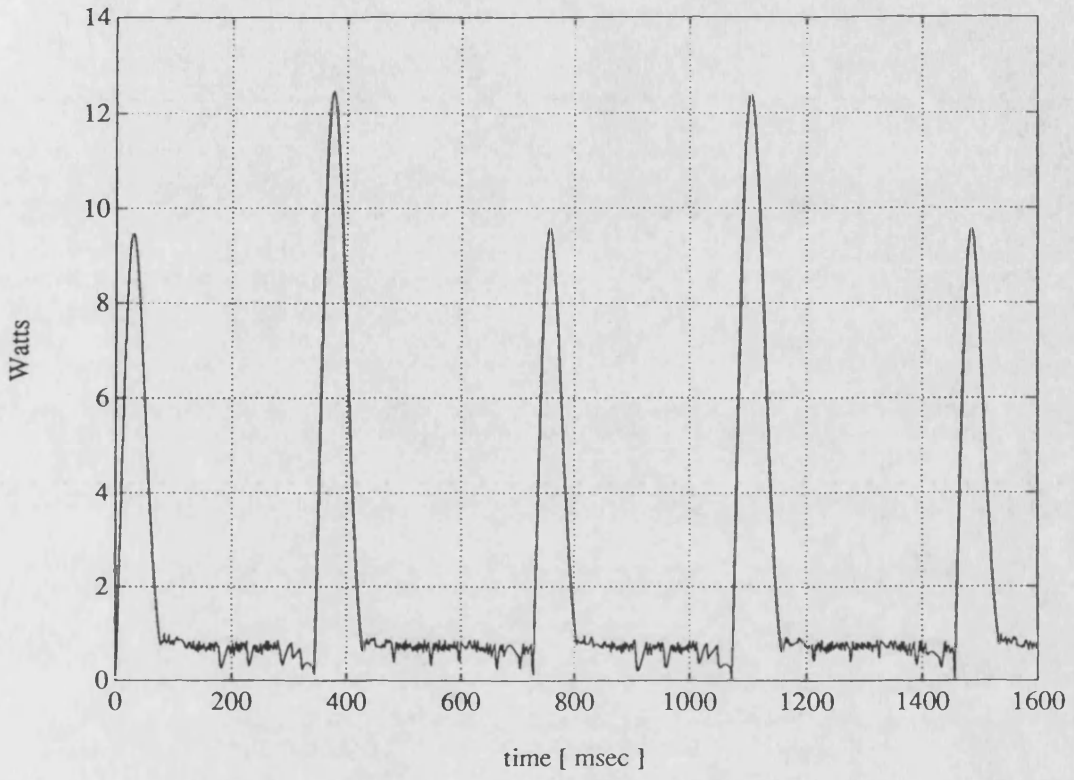

Figure 5.36 Simulated Machine Armature Ohmic Losses

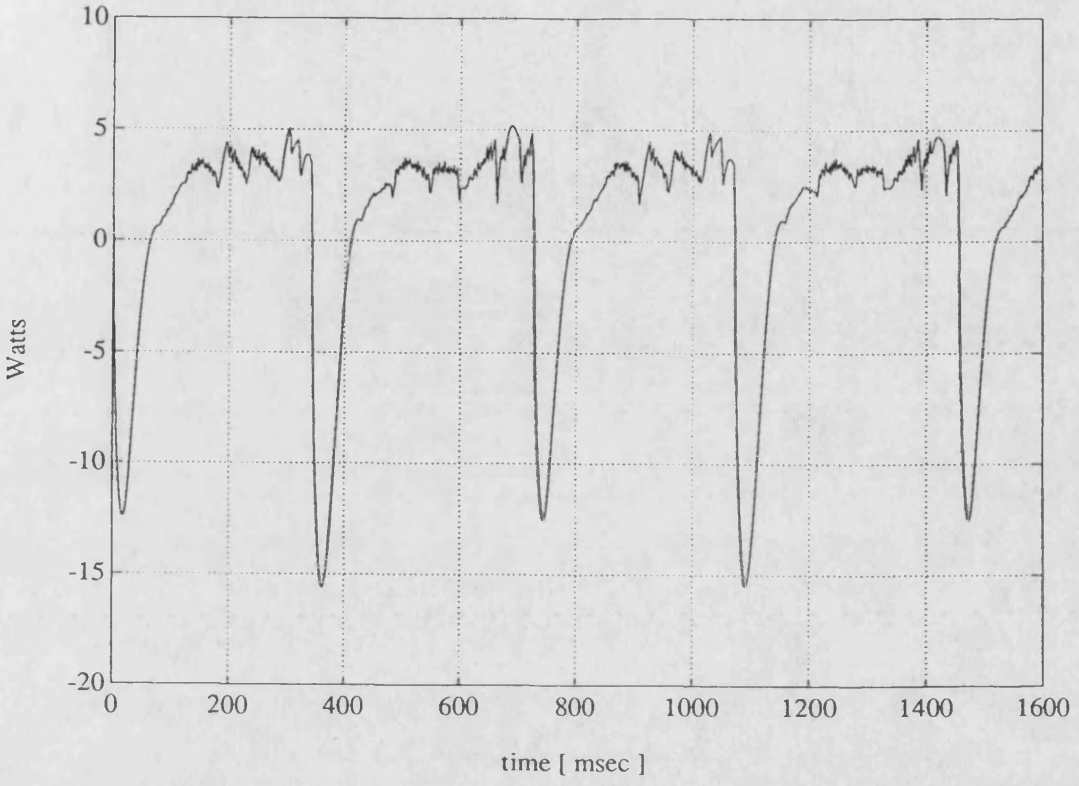

Figure 5.37 Simulated Machine Electromagnetic Power

5.7 Conclusions

A simulation technique based on a decoupled abc phase variable model has been presented. The technique assumes that the three phase inductances are equal. This, although not true for the mutual inductances, leads to a simple machine model which reduces the software development and computer run times considerably.

A numerical tool is essential because of the nonsinusoidally varying parameters involved and the switching nature of the associated drive system. The results obtained from the simulation program were verified by the experimental results. The general agreement between these two sets of results is good. It was shown that the program can be used to obtain additional results which experimentally are not easily accessible.

The technique was used to simulate the machine performance for the oscillatory motion where both mechanical and electrical transients are present. This proves that the modelling method is capable of simulating the performance of the machine for any operation mode.

The dynamic performance simulation is the last stage of a computer aided design process which involves the design, parameter calculation and performance prediction of the brushless tubular permanent magnet machine.

CHAPTER 6

DESIGN OPTIMIZATION OF THE TUBULAR BRUSHLESS DC MACHINE

6.1 Introduction

The previous chapters presented a process by which the overall performance of the tubular brushless dc machine can be predicted and then compared this prediction with the test data obtained from a prototype machine. The comparison revealed a good agreement between the simulated and the test results which confirms the validity of the modelling approach. This modelling process is a useful tool in design optimization since it can save on development costs and speed up the design process.

However, before the relatively expensive simulations are performed a simpler process must be used to estimate the size of machine required for the proposed duty. This analytical approach is presented in this chapter.

6.2 Derivation of the Equations Used in the Optimization Procedure

The following machine specifications are predetermined in the design procedure:

- Neodymium-Iron-Boron (NdFeB) type magnet material is to be used.
- Excitation back iron is to be a solid bar rather than a tube.
- Saturation effects due to armature reaction are ignored.
- Armature has four blocks.
- Current density is taken to be 5 A/mm^2.
- The driver for the machine is Unitrode 3620 with a maximum current limit of 3 A and input voltage 8 - 40 V.

Figure 6.1 gives the machine with geometrical dimensions. Also shown on Figure 6.1(a) are two flux paths of the permanent magnet field. Path 1 is the path when half of the magnet flux passes through the armature back iron and the excitation core. This is the case that would always take place in the case of an infinitely long machine and is the minimum flux that exists in the armature and excitation back iron paths of the actual machine geometry. Path 2, on the other hand, is the path which represents the case when all magnet flux passes through the armature and excitation back iron regions and is the maximum flux that can exist. This is particularly the case for the middle section of the machine and the maximum flux is lower for the outer parts, as shown in Chapter 3. The peak value of the sinusoidal working flux in these regions and thus the coils flux linkages vary between these minimum and maximum values according to the location of the excitation poles with respect to the armature. Path 2 with the upper limit will be used in the analysis.

The geometry of the excitation core can be related to the pole-pitch by using the continuity of the flux which states that the excitation core flux is equal to the air-gap flux neglecting the leakage flux. Thus taking path 2:

$$B_c \frac{\pi}{4} d_1^2 = \beta t_p (d_1 + 2l_m + 2g) \pi B_g \qquad \ldots(6.1)$$

where B_c is the excitation core flux density

d_1 is the core diameter

t_p is the pole-pitch

β is the ratio of the magnet width to pole-pitch

l_m is the magnet length

g is the air-gap length

B_g is the air-gap flux density

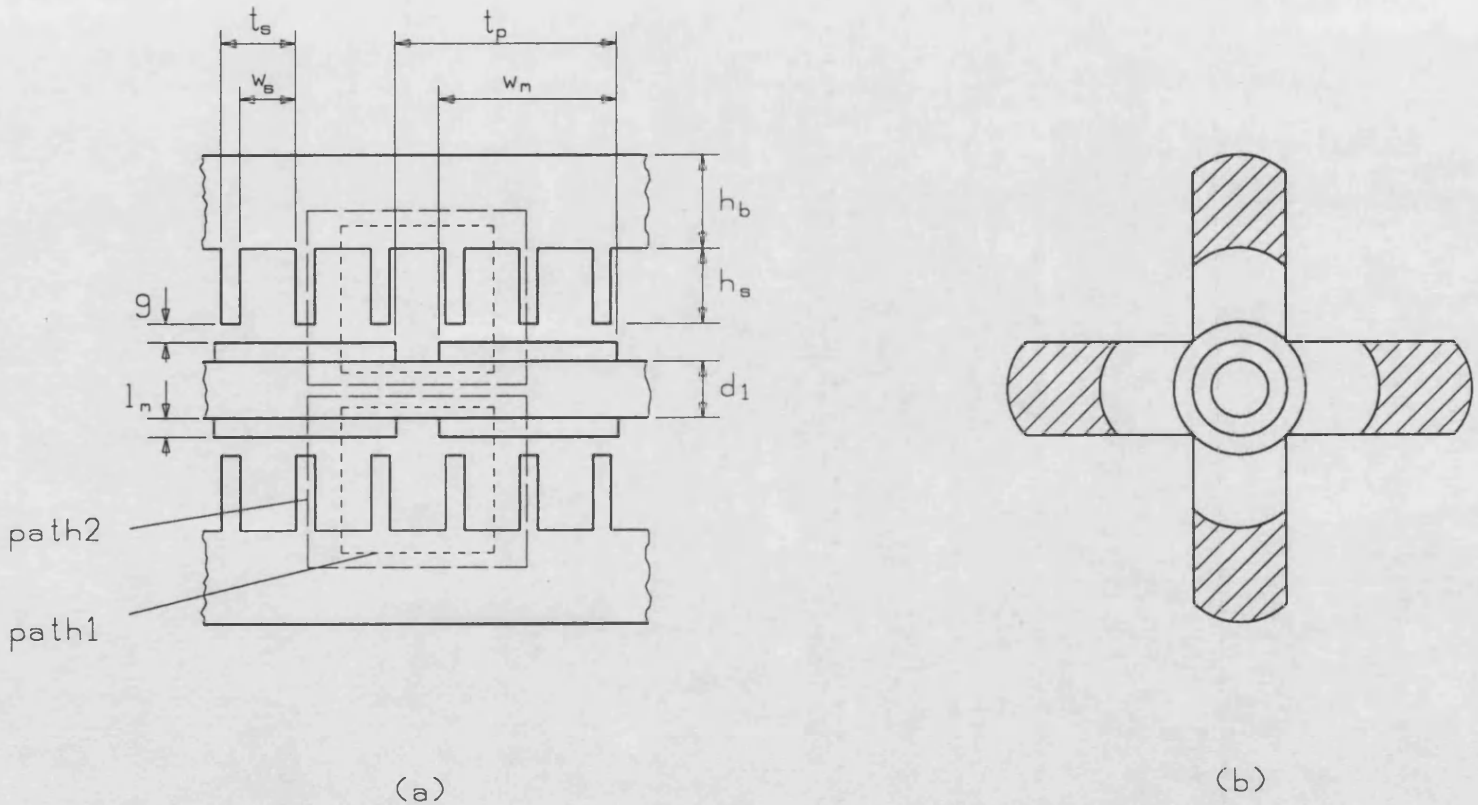

Figure 6.1 Tubular Machine Geometry

Magnet length can be expressed in terms of air-gap flux density assuming that the permeability of the magnet material is equal to that of free space and neglecting leakage flux and fringing, i.e. taking

$$B_m = B_g$$

as below

$$l_m = \frac{g_{eff} B_m}{H_m \mu_0} \qquad \ldots(6.2)$$

where g_{eff} is the effective air-gap length

H_m is the working point magnetising force of the magnet

μ_0 is the permeability of free space.

Effective air-gap length can be calculated using Carter's coefficient **[6.1]**:

$$g_{eff} = g\left\{\frac{5g + (1-\alpha)t_s}{5g + (1-\alpha)t_s - (1-\alpha)^2 t_s}\right\} \qquad \ldots(6.3)$$

where t_s is the slot-pitch and

$$\alpha = \frac{t_t}{t_s} \qquad \ldots(6.4)$$

where t_t is the tooth-width

The amount of flux entering a tooth is equal to the magnet pole flux (right-hand side of Eqn. 6.1) divided by the number of teeth (or slots) in a pole hence

$$\phi_t = \beta \frac{t_p}{N_s}(d_1 + 2l_m + 2g)\pi B_g \qquad \ldots(6.5)$$

where ϕ_t is the tooth flux

N_s is the number of slots (or teeth) per pole

which can be expressed as

$$N_s = \frac{t_p}{t_s} \qquad \ldots(6.6)$$

The radial cross sectional area of a tooth for the whole circumference can be calculated by

$$A_t = \alpha \frac{t_p}{N_s}(d_1 + 2l_m + 2g)\pi \qquad \ldots(6.7)$$

The tooth flux density can then be found using Equations 6.5 and 6.7, thus

$$B_t = \frac{\beta}{\alpha} B_g \qquad \ldots(6.8)$$

Taking again that all the magnet flux passes through armature backing iron, i.e. path 2 on Figure 6.1(a), the total cross-sectional area of armature backing iron for four blocks must be equal to the radial cross sectional area of a tooth for the whole circumference multiplied by the number of tooth (or slots) per pole , N_s, yielding

$$A_{arm} = \alpha t_p (d_1 + 2l_m + 2g)\pi \qquad \ldots(6.9)$$

where A_{arm} is the total cross-sectional back-iron area of the four-block armature.

Since the armature flux is equally shared between four blocks, that is a quarter of the flux passes through a quarter of the available cross section area shown hatched in Figure 6.1(b), the back iron height of the armature blocks can be calculated by

$$h_b = \frac{A_{arm}}{(d_1 + 2l_m + 2g)\pi} = \alpha t_p \qquad \ldots(6.10)$$

which assumes a rectangular cross-section area for simplicity instead of the hatched areas on the Figure.

Slot width, on the other hand, can be expressed in terms of pole-pitch as

$$w_s = (1-\alpha)\frac{t_p}{N_s} \qquad \ldots(6.11)$$

Cross sectional area of the armature winding wire can be calculated taking the maximum phase current the Unitrode chip can provide and the current density as given above, i.e.

$$A_w = \frac{I_{ph}}{J_s} = \frac{3}{5} = 0.6mm^2$$

where A_w is the wire cross sectional area

I_{ph} is the phase current

J_s is the net slot current density.

The net slot area, on the other hand, can be found by subtracting the wall insulation thickness from the gross slot-area, as indicated in Figure 6.2, as below, following Veinott **[6.2]**.

$$A_{slot-net} = h_s w_s - [2(h_s - t_{ins}) + w_s]t_{ins} \qquad \ldots(6.12)$$

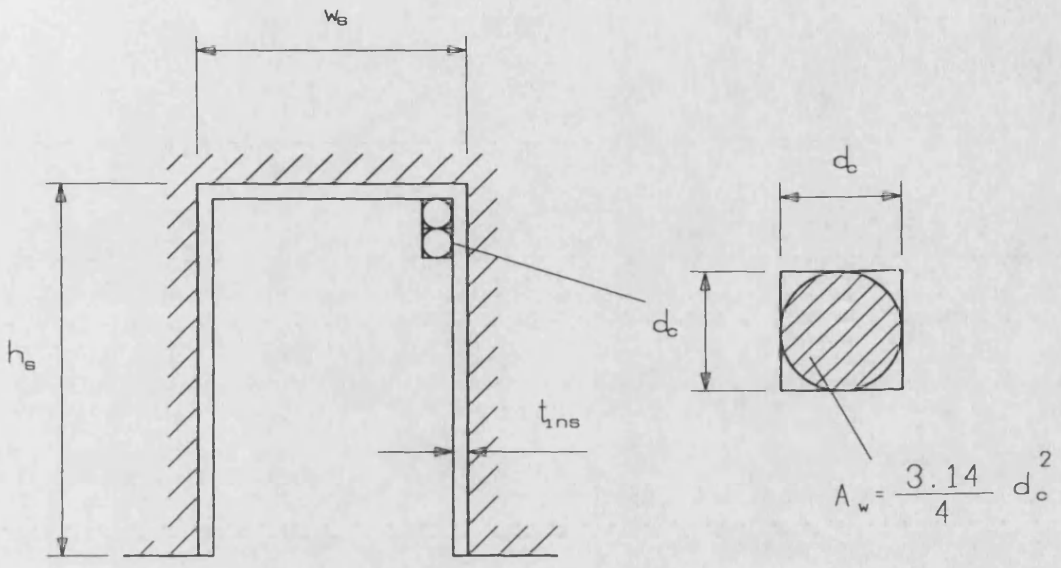

Figure 6.2 Slot Details and Calculation of the Net Wire Area

where h_s is the slot-depth (height)

t_{ins} is the slot wall-insulation thickness

From this the net copper area can be calculated as drawn in detail on Fig. 6.2

$$A_{Cu} = \frac{\pi}{4}\{h_s w_s - [2(h_s - t_{ins}) + w_s]t_{ins}\} \qquad ...(6.13)$$

The number of turns in a coil can then be calculated by dividing the net copper area by the wire cross sectional area, hence

$$N_c = \frac{A_{Cu}}{A_w} = \frac{A_{Cu}}{0.6} \qquad ...(6.14)$$

The slot current can also be calculated using

$$I_s = A_{Cu} \cdot J_s$$

The standstill force per armature pole can now be expressed as below:

$$F_{pp} = B_g(d_1 + 2l_m + 2g)\pi \cdot 2I_s \qquad ...(6.15)$$

which assumes that two slot currents per pole will be contributing to the force production which is the case with the chip at hand.

The outer diameter of the machine is

$$d_{out} = d_1 + 2(l_m + g + h_s + h_b) \qquad ...(6.16)$$

Consequently, the machine volume per pole assuming a whole outer tube for simplicity is

$$Vol_{pp} = \pi\left(\frac{d_{out}}{2}\right)^2 t_p \qquad \ldots(6.17)$$

Finally, the force per unit of machine volume can be calculated by

$$F_{per-Vol} = \frac{F_{pp}}{Vol_{pp}} \qquad \ldots(6.18)$$

which can be maximised in the optimization procedure.

6.3 An Optimum Design Algorithm

The optimum design for a specific machine dimension can be obtained in terms of the other machine dimensions based on the maximum force per volume of the machine.

The following values are taken in the optimization process:

- Number of armature slots (or teeth) per pole [N_s] is 3
- Magnet working flux density [B_m] is 0.5 T
- Corresponding magnetising force [H_m] is 450 kA/m
- Peak air-gap flux density [B_g] is 0.5 T
- Iron saturation flux density [B_t, B_c] is 1.5 T
- Air-gap length [g] is 0.5 mm
- β is taken to be 0.8
- Slot wall insulation thickness [t_{ins}] is 0.5 mm.

A computer program whose flow chart is given in Figure 6.3 was written. In this program, all specifications mentioned previously are entered as input data. A pole-pitch value is then chosen. Following this α, t_s, w_s are calculated using Eqns. 6.8,

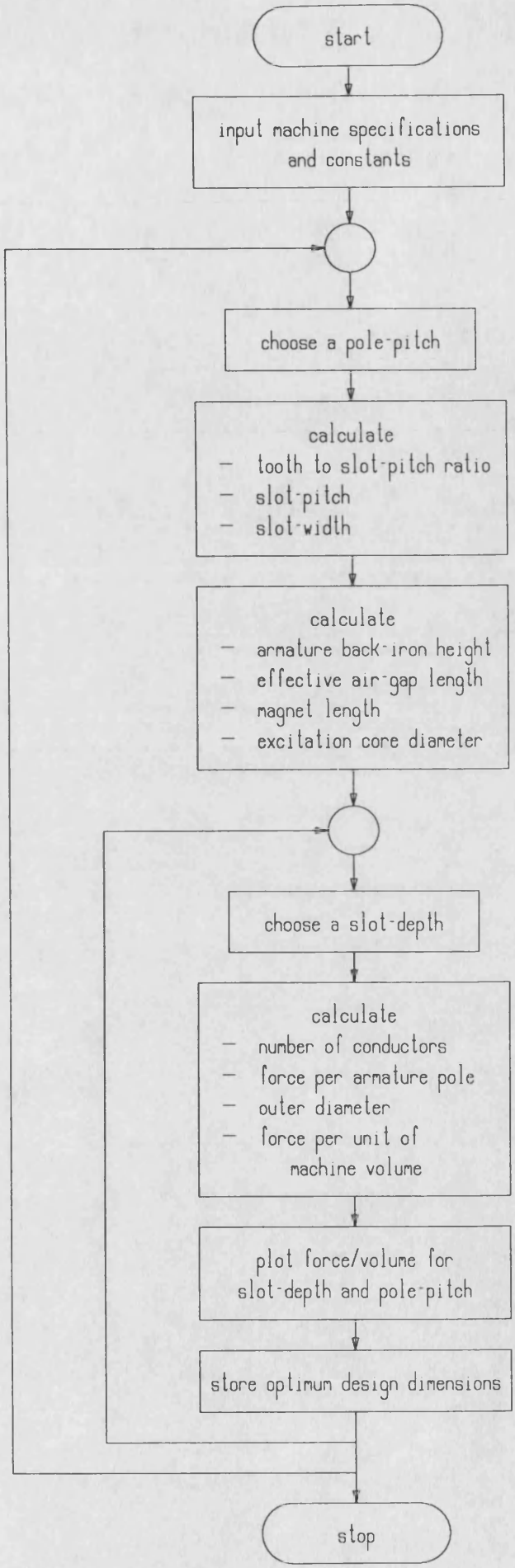

Figure 6.3 Flow Chart of the Design Optimization Program

6.6 and 6.11 respectively. Using these h_b, g_{eff}, l_m and d_1 are then computed using Eqns. 6.10, 6.3, 6.2 and 6.1 respectively. N_c, I_s, F_{pp}, d_{out}, V_{pp} and $F_{per\text{-}Vol}$ are calculated using their respective equations above. The results are then stored and plotted against slot-depth and given in Figure 6.4. It will be observed from the graph that, except for small pole-pitches, the maximum force occurs at reasonable slot-depth values and that the peak flattens as the pole-pitch increases.

The program also stores dimensions of an optimum design for a particular pole-pitch or outer diameter and can easily be adjusted for any other.

6.4 Including the Power Conditioner Chip in the Design Procedure

Upon obtaining the optimum design based on force per volume for a particular dimension of the machine, the design procedure can be extended to cover the chip input voltage and machine output requirements. This enables the designer to obtain a design, for example, with a required output force, and decide the number of armature poles and choose another design, if necessary, to achieve this. The Unitrode 3620 chip will again be considered here. However, another driver can easily be adopted.

The armature phase resistance can be calculated using the dimensions of an optimum design obtained above. For a machine with one slot per pole and phase, the phase resistance for an armature pole-pair is equal to the coil resistance multiplied by 2 (two coils per pole-pair), i.e.

$$R_{ph} = 2\left\{\rho\frac{N_c}{A_w}\cdot(d_1 + 2l_m + 2g + h_s)\pi\right\}p \qquad \ldots(6.19)$$

where R_{ph} is the phase resistance per pole-pair

ρ is the resistivity of copper

p is the number of pole-pairs

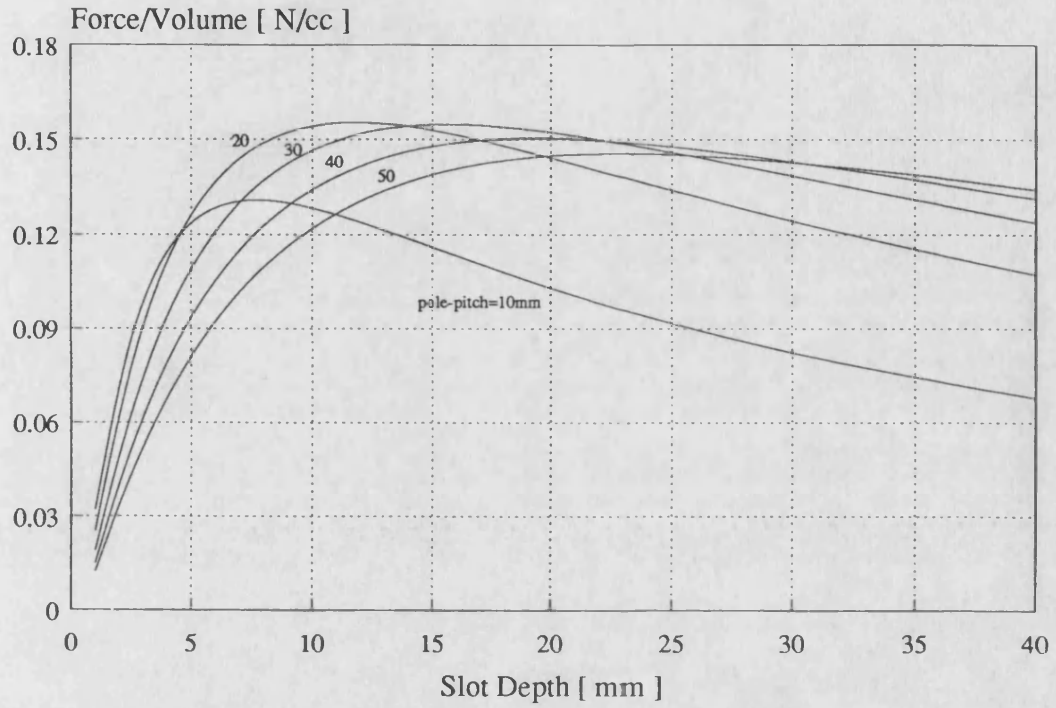

Figure 6.4 Graphs of Machine Force per Volume for Different Pole-Pitches

and the term in brackets is the mean diameter of a coil turn. Phase voltage drop due to the phase resistance for a pole-pair of armature is therefore

$$V_{res} = I_{ph} \cdot R_{ph} = 3 \cdot R_{ph} \qquad \ldots(6.20)$$

It was given in Chapter 3 that the phase flux linkages and thus induced emfs vary sinusoidally with respect to the excitation position. The peak value of phase flux linkage waveform can be computed by multiplying the coil linkage per turn by the number of turns in a coil and two to express the quantity on a per pole-pair basis thus

$$\lambda_{peak} = 2N_c\{\beta t_p(d_1 + 2l_m + 2g)\pi B_g\}p \qquad \ldots(6.21)$$

which is the peak value of the fundamental component of the phase flux linkage per pole-pair, i.e.

$$\lambda = \lambda_{peak} \sin\left(x\frac{\pi}{t_p}\right) \qquad \ldots(6.22)$$

where x is the excitation displacement.

The space derivative of this sine-wave multiplied by the maximum required excitation speed will yield the maximum peak emf value of an armature phase, hence

$$e_{peak(max)} = v_{max}\left\{\lambda_{peak}\frac{\pi}{t_p}\right\} \qquad \ldots(6.23)$$

The total maximum required input voltage per phase and pole-pair can then be calculated by adding together the two voltages and multiplying this by two since two phases are supplied by the input supply at a time, thus

$$V_{pp} = 2\{V_{res} + e_{peak(max)}\} \qquad \ldots(6.24)$$

Notice that line-to-line total emf will be less than twice the phase emf value since the two waveforms are separated by 120 ° phase difference. However, this is done for simplicity.

This voltage can be checked against the maximum voltage that can be applied to the driver input (8 - 40 V for Unitrode 3620). The number of pole-pairs can then be calculated to suit the force requirements or a different design may be chosen and the design procedure can be iterated accordingly.

An example can be given to verify the analysis. The optimum design for 30 mm pole-pitch, which was obtained in the previous section occurs at about 16 mm slot-depth value as can be seen from Figure 6.4. The machine dimensions and design parameters are given in Table 6.1. A two-pole machine constructed to these specifications can sustain 27.3 N force at a maximum speed of 1m/s.

6.5 Conclusions

A design optimization procedure has been presented. This procedure can be used to design a tubular brushless dc machine for a required machine dimension and/or specification and is easy to implement, particularly because of the presence of linearity that exists in the machine.

Table 6.1

An Optimum Design Data Set

Core Diameter	:	10.3 mm
Pole-Pitch	:	30 mm
Slot-Width	:	7.3 mm
Slot-Height	:	16 mm
Armature Back-Iron Height	:	8 mm
Magnet-Length	:	1 mm
Magnet-Width	:	24 mm
Air-Gap Length	:	0.5 mm
Effective Air-Gap Length	:	1.1 mm
Outer Diameter	:	61 mm
Wire Cross Section Area	:	0.6 mm^2
Number of Turns in a Coil	:	128
Slot Current	:	386 A
Force per Pole-Pair	:	27.3 N
Force per Volume	:	0.155 N/cc
Phase Resistance per Pole-Pair	:	0.67 ohm
Peak Phase Flux Linkage per Pole-Pair	:	0.127 Wb
Maximum Excitation Speed	:	1 m/s
Peak Phase Back Emf per Pole-Pair	:	13.34 V
Required Driver Input Voltage per Pole-Pair	:	30.7 V

CHAPTER 7

RECOMMENDATIONS AND CONCLUSIONS

The design, construction and complete computer modelling of a new class of power electronics fed three phase, permanent magnet brushless dc tubular machine has been presented. The simulation results have been verified against test results performed on a prototype machine. The computer modelling process involves two stages. The first utilizes finite element methods to calculate the static forces and the machine parameters. These parameters are used in the second stage to simulate the dynamic performance of the overall drive system by applying an abc phase variable machine model.

Chapter 2 investigates the formation of the brushless tubular machine geometry. The practical aspects of the design and construction lead to a fairly simple model facilitating the assembly. Magnet skewing was applied to the prototype machine to eliminate the unwanted tooth cogging forces instead of the more familiar slot skew. This step-skew proved to be a good alternative to the other technique for its ease of implementation and versatility.

Finite element modelling of the machine is presented in Chapter 3 by which the standstill forces and machine parameters were calculated. 2D representation was found to be sufficient provided the step skew was modelled by adding together space phase shifted versions of the reference segment calculations. Calculations were verified by comparing the results from different techniques and measurements.

Two unwanted forces exist in permanent magnet tubular machines at zero armature currents. These are due to tooth cogging and finite armature length effects.

It was shown that the tooth cogging effect can be modelled by 2D finite element methods and eliminated by a quasi one-slot skew on the excitation. It was found that this force can also be eliminated by a skew of two or four slots.

The effect of magnet skewing on the parameters and forces was also investigated. Its effect on standstill forces, particularly on magnetic cogging forces mentioned above, was studied in detail in the search for a minimum total magnetic cogging force. Although there are indications from the 2D analysis that a two-slot skew would be better, a 3D finite element analysis will be necessary to investigate the results that this skew may bring. Therefore for the present time it can be said that a skew of one slot is recommended since it completely eliminates the tooth-cogging force and reduces the end-effect force.

Using a complete shell as the armature rather than the actual four-block structure, because of the 2D FE used, had no effect over the modelling process for the conditions investigated. However, if a high field permanent magnet material and/or high current loadings are used, this may give rise to an error due to higher saturation levels in the experimental model. This may also cause more leakage flux due to the air regions between the armature blocks of the experimental model. In this case it would be necessary to use 3D finite element methods. It may also be worth calculating the end-effect force and the impact of end effects on the machine parameters for a short-secondary machine.

Chapter 4 gives the theory of operation of classical brushless dc machines and goes further to explain the linear brushless machine operation. A standard rotary machine driver is used to produce the required variable frequency phase currents and the oscillatory operation necessary for linear machines. The open loop drive scheme

is used in this study. For a machine with a longer stroke, a closed loop speed control system may be exploited in order to keep the maximum excitation velocity within specified values and to achieve constant speed.

A driver that can produce higher currents for the machine phases may be desirable when the machine is to drive a load. This however should be considered with the maximum current that the magnet material used can withstand without being demagnetised. Regenerative braking capabilities will also be useful, especially when the excitation is being decelerated at the end of its travel. Hall effect sensor positioning may also be improved in order to obtain the highest possible force from the machine. For a long excitation machine they can be placed outside the armature, thus enabling one to easily control their placement.

The demagnetising effect of the armature reaction was studied in detail. Because of the "jumping" nature of the armature field, different magnetic circuits are formed between armature and excitation. All these possible circuits were analysed. The maximum allowable armature phase current level for the magnets used was specified by the case with the most pronounced demagnetising effect. A magnet material with a higher coercive force will improve this limitation and thus make a better machine.

The armature reaction effect on the excitation field, which is a more familiar concept in dc machines, was also studied and found to cause no saturation effect in the machine iron parts. This is mainly because of the large effective air-gap in the machine due to the near unity permeability of the magnet material. However, in configurations involving smaller air-gaps for the armature field, such as an armature field orientation which does not go through magnets, this would not be valid and a further analysis may be necessary.

Chapter 5 presents a computer aided analysis technique to simulate the dynamic performance of the machine and power conditioner. Based on the abc reference frame, this method uses the calculated parameters obtained in Chapter 3. System equations which describe both the machine and the inverter supply are solved by a step by step numerical method, to find the dynamic performance of the system in an oscillatory mode. It is shown that a complete modelling of these machines can be achieved.

The simulation uses a decoupled machine model which assumes equal phase self and mutual inductances. This is not readily possible for linear machines in general and therefore a coupled model may be used. However, this must be considered carefully as it would greatly increase the software development and computer run times. Also an inverter model using a lumped parameter network in which all transistors and diodes are present, including the phase variables may be used.

An optimization procedure based on analytical formulae is given in Chapter 6. This linear approach is satisfactory and was confirmed using the prototype machine design.

APPENDIX A

SPECIFICATIONS OF FERROXDURE 330

FERROXDURE 330

anisotropic ceramic material

GENERAL

This specification relates to tests carried out on test pieces made from each batch of material taken from normal production. The test piece has dimensions of approximately ϕ 35 x 12 mm.

Magnets manufactured from this material conform generally to this specification but, owing to the method of manufacture and to the variation in size and shape, some limits cannot always be realized, or indeed checked by measurement on the magnet. However, a minimum-flux test or similar test described in each magnet specification, can be used as a basis for performance guarantees.

COMPOSITION

Ferroxdure 330 is a strontium ferrite, the main constituent being $SrFe_{12}O_{19}$.

MAGNETIC AND ELECTRICAL PROPERTIES OF THE TEST PIECE

Temperature of the test piece is 25 ± 2 °C unless otherwise specified.

		typ.	min.		typ.	min.	
Remanence	B_r	370	360	mT	3700	3600	Gs
Coercivity	H_{cB}	240	225	kA/m	3000	2800	Oe
Polarization coercivity	H_{cJ}	245	230	kA/m	3100	2900	Oe
Maximum BH product	$(BH)_{max}$	25,5	24,0	kJ/m³	3,2	3,0	MGsOe
Magnetic flux density corresponding to $(BH)_{max}$	B_d	180		mT	1800		Gs
Magnetic field strength corresponding to $(BH)_{max}$	H_d	145		kA/m	1800		Oe
Recoil permeability	μ_{rec}	1,1			1,1		
Remperature coefficient of B_r (−40 to + 200 °C)		−0,2		%/K	−0,2		%/°C
Temperature coefficient of H_{cJ} (−40 to + 200 °C)		≈ 0,95		kA/m/°C	≈ 12		Oe/°C
Saturation field strength	H_{sat}		875	kA/m		11 000	Oe
Resistivity	ρ	10^4		Ωm	10^6		Ωcm
Curie point		450		°C	450		°C

PHYSICAL PROPERTIES

Density	typ.	4,65 x 10^3 kg/m³	(4,65 g/cm³)
Coefficient of linear expansion (20 to 300 °C)	⊥ MA 8 and	// MA 13	· 10^{-6}/K
Hardness (Moh's scale)	typ.	6,5	

DIRECTION OF MAGNETIZATION

Ferroxdure 330 is an anisotropic material, and has therefore a preferred direction of magnetization (Magnetic Axis), which must be shown on the magnet drawing.

QUALITY AND FINISH

The material allows magnets to be produced having a good, clean finish and appearance according to the appropriate visual limit samples.

TYPICAL DEMAGNETIZATION CURVE (25 °C)

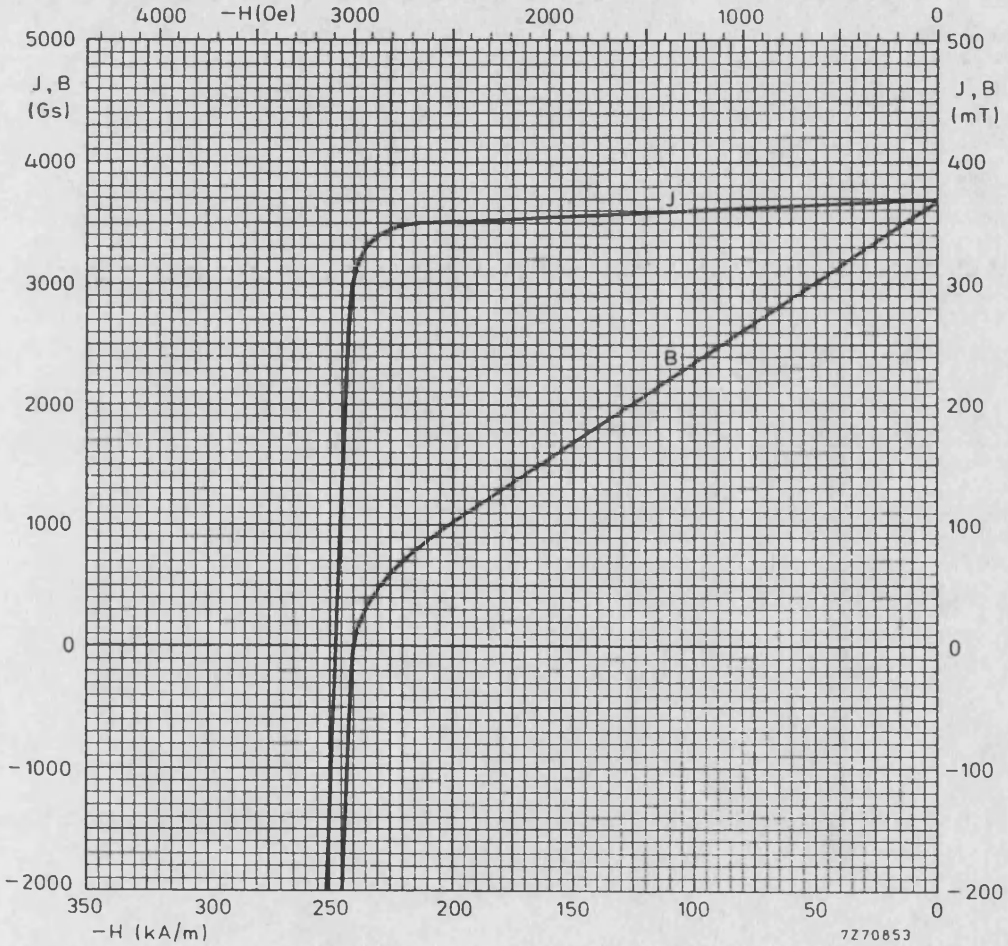

Figure A1

APPENDIX B

MAGNETISATION OF THE EXCITATION PERMANENT MAGNET POLES

The magnetiser used for the magnets are given in Figure B1. The poles are shaped in the form of an arc to suit the 120° span permanent magnet segments. The two coils each with 10 turns are connected in series. The amount of mmf required to fully saturate the magnets [given in App. A] was obtained by supplying the magnetiser from a bank of car batteries. The current level was controlled by a circuit breaker connected in series with the batteries.

The current that needed to saturate the magnets can be calculated neglecting the iron mmf drops:

$$2H_{pm(sat)} \cdot l_m = 2NI$$

where $H_{pm(sat)}$ is the saturation magnetising force of the permanent magnet [875 kA/m]

l_m is the magnet length [7.37 mm]

N is the number of turns in a coil [10]

The required current can then be calculated using above equation:

$$I = 645 \text{ A}$$

The applied current was increased by about 20 % in order to encounter the leakage and iron saturation effects.

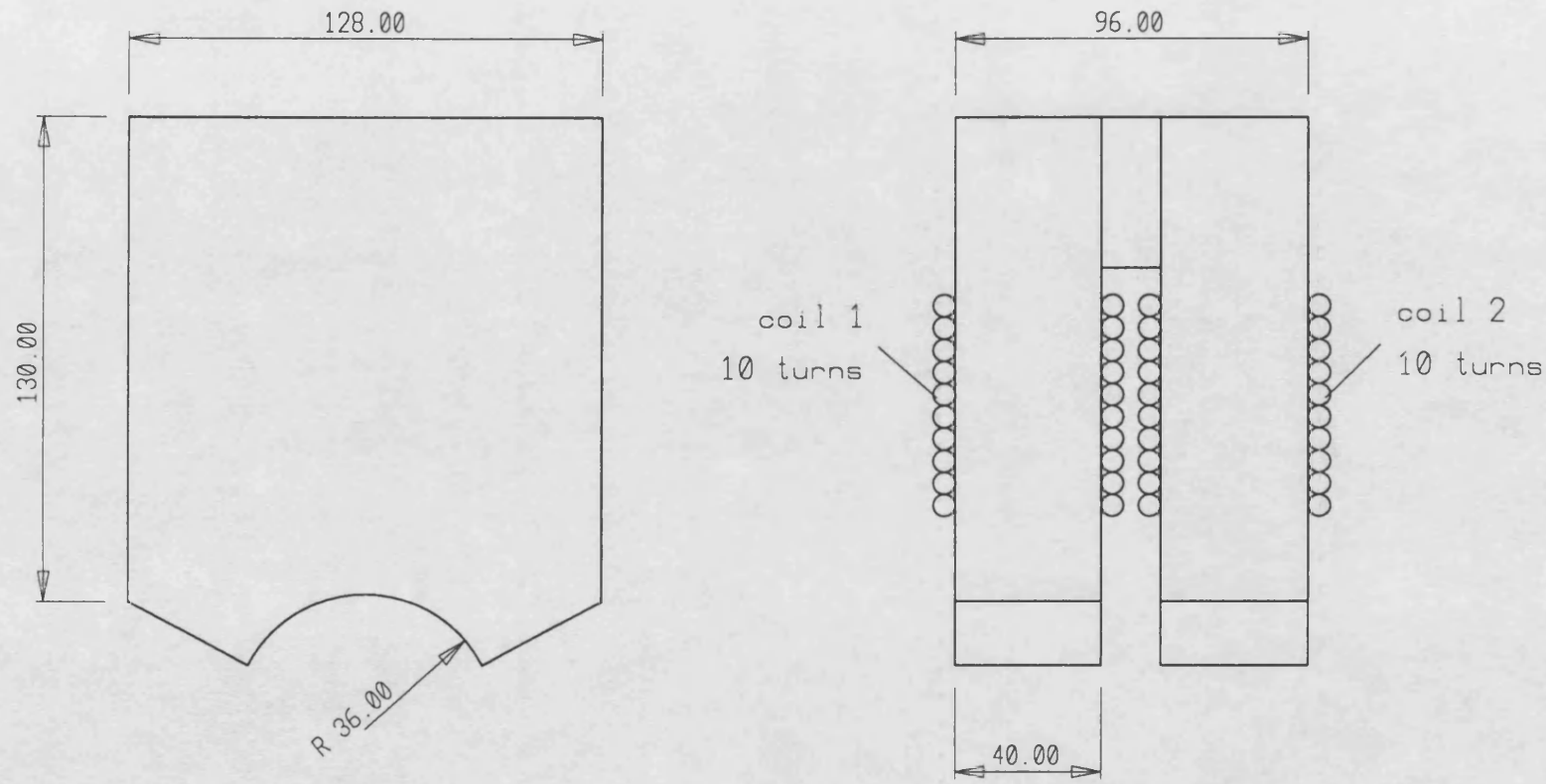

Figure B1 The Magnetiser Used to Magnetise the Excitation Poles

APPENDIX C

B-H CURVE OF THE IRON MATERIAL USED IN FINITE ELEMENT MODELLING

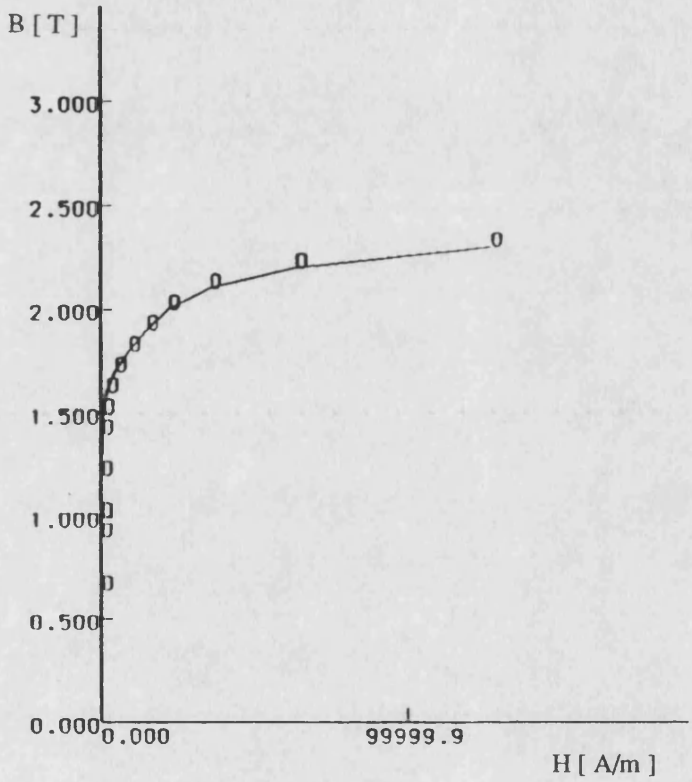

Figure C1

APPENDIX D

POSITIVE FORCE AND POSITION DIRECTION CONVENTIONS USED AND THE TIME-INSTANT TAKEN IN STANDSTILL FORCE CALCULATIONS AND MEASUREMENS

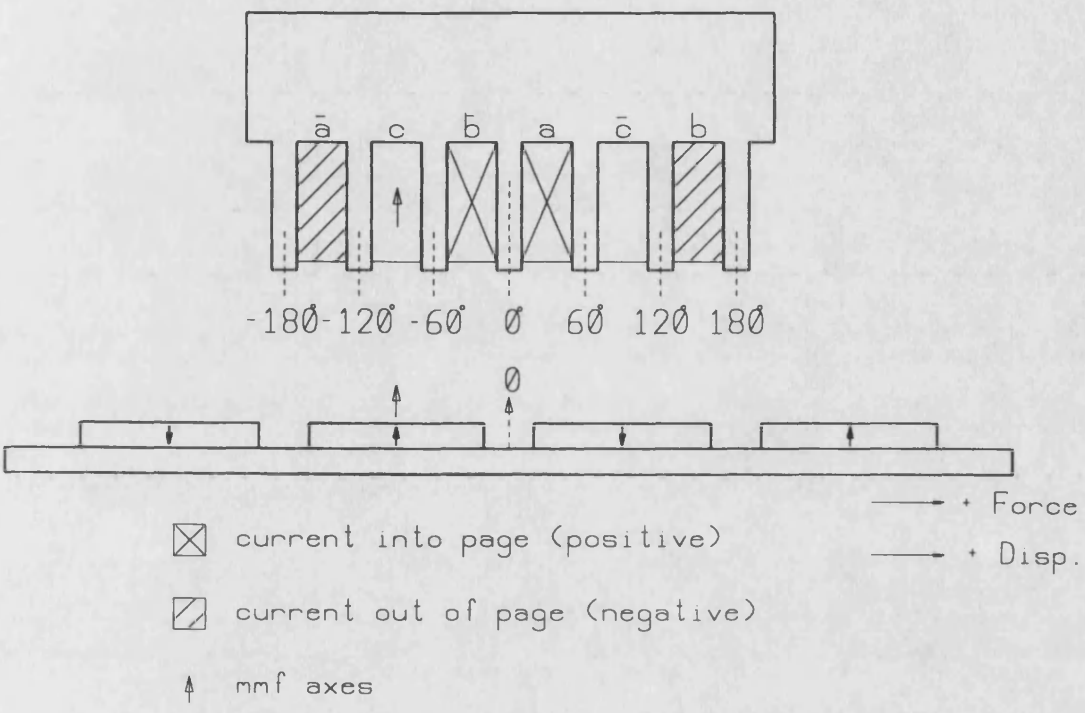

(a) Armature current and mmf distribution

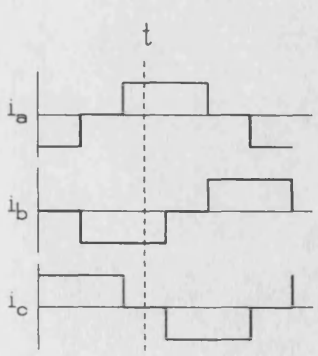

(b) Time instant taken

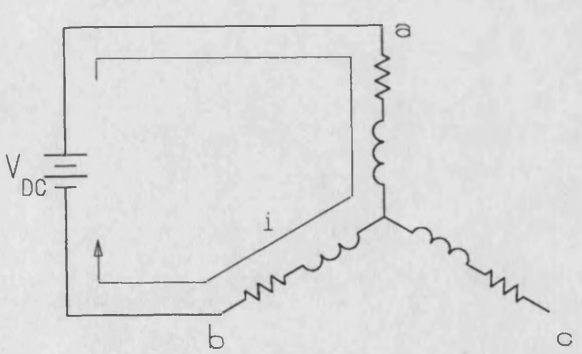

(c) Corresponding circuit used

Figure D1

APPENDIX E

DEMAGNETISATION EFFECT OF THE ARMATURE REACTION

Permanent magnet poles on the excitation are subject to a demagnetising force due to the existence of the air regions. For long air-gap lengths the working point of magnet moves down on the demagnetisation curve. In a typical machine the air-gap is small and the magnets work on the upper side of the curve.

However, armature currents also have a demagnetising effect on the magnets. This effect may take the working point down beyond the knee of the demagnetisation curve and cause permanent changes in the permanent magnet magnetisation. When this happens the new recoil line that is created will be another line below the demagnetisation curve and thus the magnet will supply less excitation flux. It may also take the working point to the third quadrant where the magnet polarity will be reversed. Care, therefore, should be taken in order to prevent the magnet point being driven beyond the knee on the magnet BH curve.

Figure E1 shows all possible magnetic circuits formed by the moving excitation covering 0° - 180° range of the force angle δ. It can be observed that demagnetisation and/or remagnetisation occur either on one pole or two. Cases ii, iii and iv are only possible during the machine operation. The other cases are included since they are formed during the steady-state force measurements. However, cases i, ii and iii will be dealt with here as demagnetisation occurs in their magnetic configurations only.

A first order estimate will be made in this analysis. It will be assumed that mmf drops in the iron are negligible and that the magnet and air-gap magnetising forces are constant over their respective distances along the flux path taken. These paths are taken where the field is strongest.

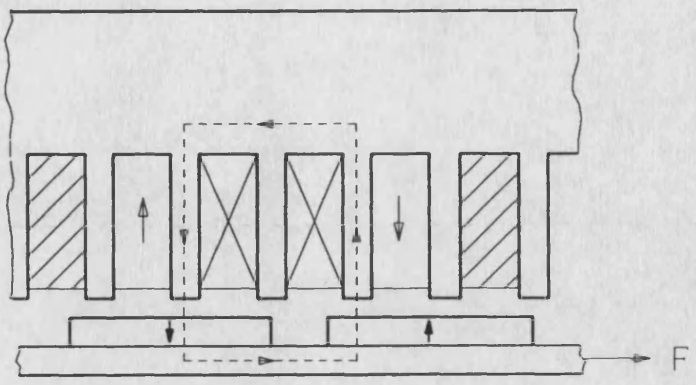

(a) Case i; 180°>δ>140°

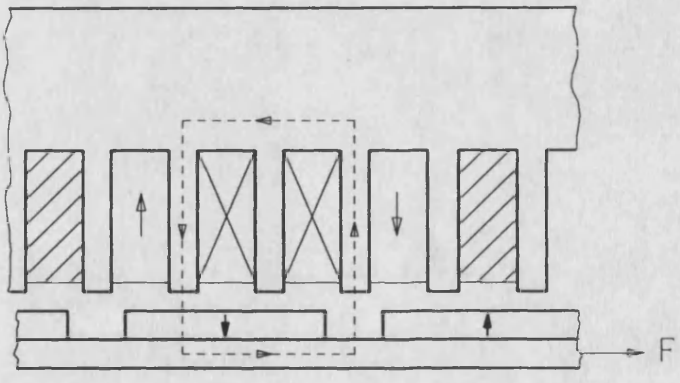

(b) Case ii; 140°>δ>100°

Figure E1 Magnetic Circuits Formed by the Moving Excitation

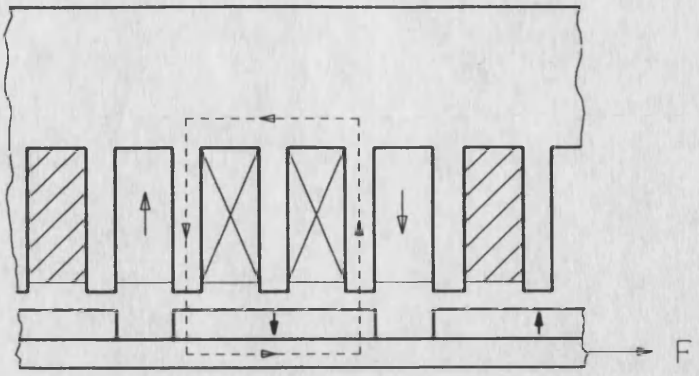

(c) Case iii; 100°>δ>80°

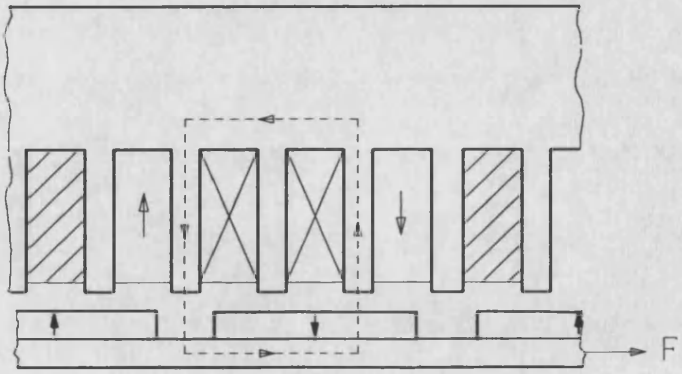

(d) Case iv; 80°>δ>40°

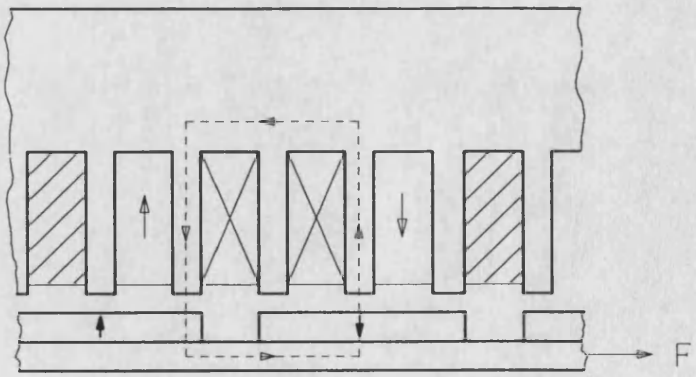

(e) Case v; 40°>δ>0°

a) Case i: (180° > δ > 140°)

Circuital law around the path of Figure E1(a) yields

$$2H_m l_m + 2H_g l_g = -2N_c I \qquad \ldots(E1)$$

where N_c is the number of turns in a coil

I is the coil (phase) current

l is length

and subscripts m and g stands for magnet and gap respectively. Taking

$$H_g = \frac{B_g}{\mu_0} \qquad \ldots(E2)$$

and assuming

$$B_g = B_m \qquad \ldots(E3)$$

along the path, Eqn. E1 becomes

$$B_m = -\frac{N_c I \mu_0}{l_g} - \frac{H_m l_m \mu_0}{l_g} \qquad \ldots(E4)$$

This equation describes the working line applicable to the demagnetisation curve of the magnet. The intercept of this line on the H-axis is

$$-\frac{N_c I}{l_m}$$

and its slope with respect to the H-axis is given by

$$-\frac{l_m \mu_0}{l_g}$$

The intercept point of the line is determined by the coil current and its slope only by the dimensions. A family of curves were drawn on Figure E2 taking

l_m = 7.37 mm

l_g = 1.5 mm

N_c = 150

which are the actual values of the prototype machine. It will be observed that a coil current above *9 A* will take the working point beyond the knee and thus demagnetise the respective magnets.

This calculation can be carried out more directly by combining Eqn. E4 with the equation which represents the linear part of the demagnetisation curve as given below

$$B_m = 1.1\mu_0 H_m + B_r \qquad \ldots(E5)$$

where B_r is the remanence of the magnet yielding

$$H_m = -\frac{N_c I}{l_m + 1.1 l_g} - \frac{B_r}{\mu_0} \cdot \frac{l_g}{l_m + 1.1 l_g} \qquad \ldots(E6)$$

which gives the total demagnetisation force acting on the magnets. Notice the first term on the right-hand side of the equation represents the demagnetising force of the armature field and the second that of the air-gap.

Along with the above constant values taking

$B_r = 0.37$ T gives

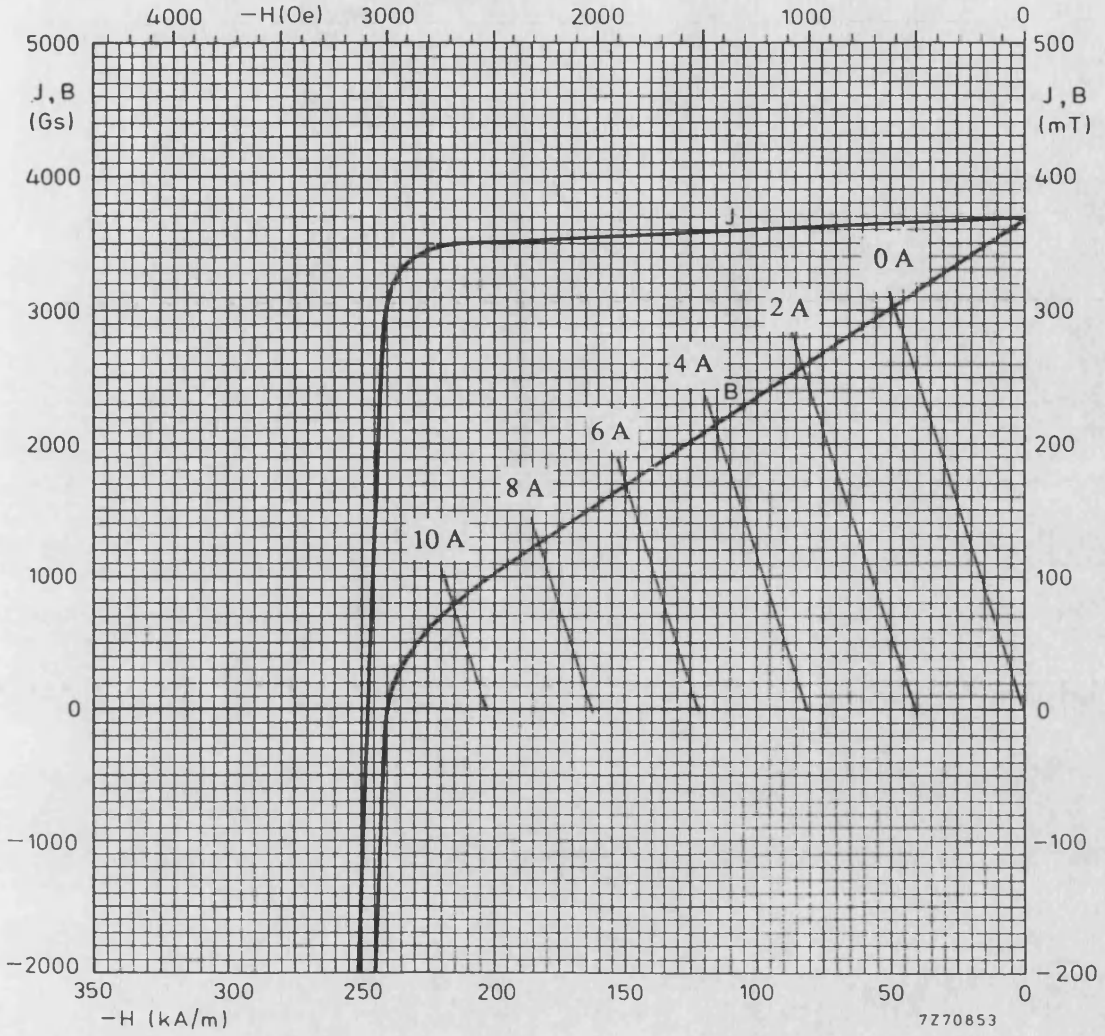

Figure E2 Working Lines of the Permanent Magnets at Different Armature Currents for Case i

H_m = - 16629.7I - 48963.9 A/m

which can be used to calculate the current value that corresponds to the maximum allowable H value on the demagnetisation curve. This H value is -210 kA/m [please see Fig. E2] and thus the maximum phase current that can be applied is

I_{max} = 9.7 A

This equation type will now be applied to the other two configurations.

b) Case ii: (140° > δ > 100°)

Assuming that the magnetising force in all air regions along the path of Figure E1(b) is the same Ampere's law applied to the path gives

$$H_m l_m + H_g(2l_g + l_m) = -2N_c I \qquad \ldots(E7)$$

Using Eqns. E2, E3 and E5 the above equation yields the following:

$$H_m = -\frac{2N_c I}{l_m + 1.1(2l_g + l_m)} - \frac{B_r}{\mu_0} \cdot \frac{2l_g + l_m}{l_m + 1.1(2l_g + l_m)} \qquad \ldots(E8)$$

This equation can be evaluated putting the values of the constants given above, hence

H_m = -15977I - 162608.9 A/m

The maximum value of the phase current corresponding to the maximum demagnetising force value of -210 kA/m can then be found

I_{max} = 2.97 A

A phase current above this value will partially demagnetise the parts of the magnet that face the armature teeth which carry most of the armature flux. This is the most extreme case due to having one magnet pole present in the path.

c) Case iii: (100° > δ > 80°)

As the path shown on Figure E1(c) for this case is for the armature field and not for the permanent magnet field the two fields will be calculated separately and will then be combined. Taking the armature field first around the path of Figure E3(a) Ampere's law gives

$$2H_{g(a)}(l_m + l_g) = -2N_c I \qquad \ldots(E9)$$

Here, the air-gap magnetising forces illustrated on the figure and the subscript *(a)* stands for armature. Note that this equation assumes that the permeability of the magnet material is equal to that of air. Magnetising force in the air-gap due to the armature currents can then be found using

$$H_{g(a)} = -\frac{N_c I}{l_m + l_g} \qquad \ldots(E10)$$

Taking the magnet field now the circuital law applied to either of the paths shown in Figure E3(b) gives

$$2H_m l_m + 2H_g l_g = 0 \qquad \ldots(E11)$$

for the H directions shown on the figure. Combining this equation with Eqns. E2, E3 and E5 as done for the previous cases also yields

$$H_m = -\frac{B_r}{\mu_0} \cdot \frac{l_g}{l_m + 1.1 l_g} \qquad \ldots(E12)$$

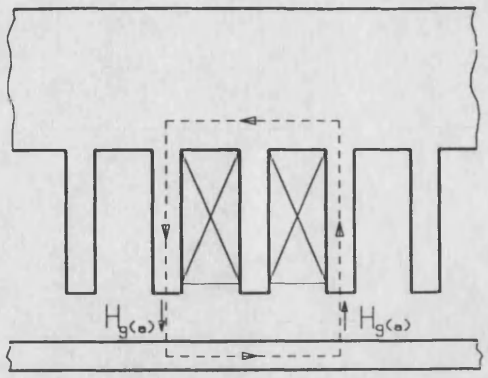

(a)

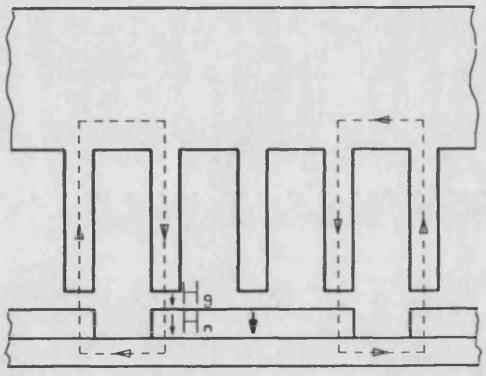

(b)

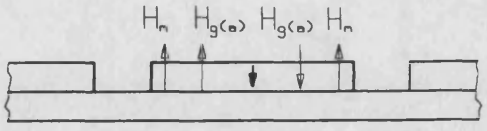

(c)

Figure E3 Fields Calculated for Case iii
(a) Armature Field
(b) Excitation Field
(c) Resultant Magnetising Forces (H Shown in Positive Values)

which represents the demagnetising force from the air-gap.

The above two forces are drawn in Figure E3(c) with their directions arranged so that they all have positive values. It can be observed that the left-hand side of the pole is subject to a demagnetising force and the right-hand side to a remagnetising force from the armature reaction. The maximum current can be found by combining Eqns. E10 and E12 to calculate the total demagnetising force acting on the left-hand side of the pole as below

$$H_{m(left)} = -\frac{N_c I}{l_m + l_g} - \frac{B_r}{\mu_0} \cdot \frac{l_g}{l_m + 1.1 l_g} \qquad \ldots(E13)$$

which when evaluated for the constants and dimensions becomes

$$H_{m(left)} = -16911I - 48964 \text{ A/m}$$

and the maximum allowable phase current can again be calculated using the maximum allowable H value:

$$I_{max} = 9.52 \text{ A}$$

which is almost equal to case i.

Case ii should therefore define the limit to the phase current that can safely be applied to the machine phases without affecting the magnets permanently. This is about 3 A for the prototype machine. The normal running current that the driver chip can provide is also 3 A.

APPENDIX F

DATA SHEETS FOR UNITRODE UC3620

LINEAR INTEGRATED CIRCUITS

Switchmode Driver For 3-ϕ Brushless DC Motors

FEATURES

- 2A Continuous, 3A Peak Output Current
- 8V to 40V Operation
- Internal High Gain Amplifier for Servo Applications
- TTL Compatible Hall Inputs
- Mask Programmable Decode Logic
- Pulse-by-Pulse Current Limiting
- Internal Thermal Shutdown Protection
- Under-Voltage Lockout
- 15 Lead, 25W Multiwatt® Package

DESCRIPTION

The UC3620 is a brushless DC motor driver capable of decoding and driving all 3 windings of a 3-phase brushless DC motor. In addition, an on-board current comparator, oscillator, and high gain Op-Amp provide all necessary circuitry for implementing a high performance, chopped mode servo amplifier. Full protection, including thermal shutdown, pulse-by-pulse current limiting, and under-voltage lockout aid in the simple implementation of reliable designs. Both conducted and radiated EMI have been greatly reduced by limiting the output dv/dt to 150V/μs for any load condition.

The UC3620 offers standard 60 mechanical degree, four-pole, hall decoding per Table 1. Other decoding options are available via mask programming at the factory.

ABSOLUTE MAXIMUM RATINGS (Note 1)

Supply Voltage, V_{CC} 40V
Output Current, Source or Sink
  Non-Repetitive (t = 100μsec), I_O 3A
  Repetitive (80% on - 20% off; t_{ON} = 10ms) 2.5A
  DC Operation 2A
Analog Inputs ..... -0.3 to +V_{CC}
Logic Inputs ..... -0.3 to +V_{CC}
Total Power Dissipation (at T_{CASE} = 75°C) 25W
Storage and Junction Temperature ..... -40°C to +150°C

Note: 1. All voltages are with respect to ground, pin 8. Currents are positive into, negative out of the specified terminal.

THERMAL DATA

Thermal Resistance Junction-Case, θ_{jc} ..... 3°C/W Max
Thermal Resistance Junction-Ambient, θ_{ja} ..... 35°C/W Max

BLOCK DIAGRAM

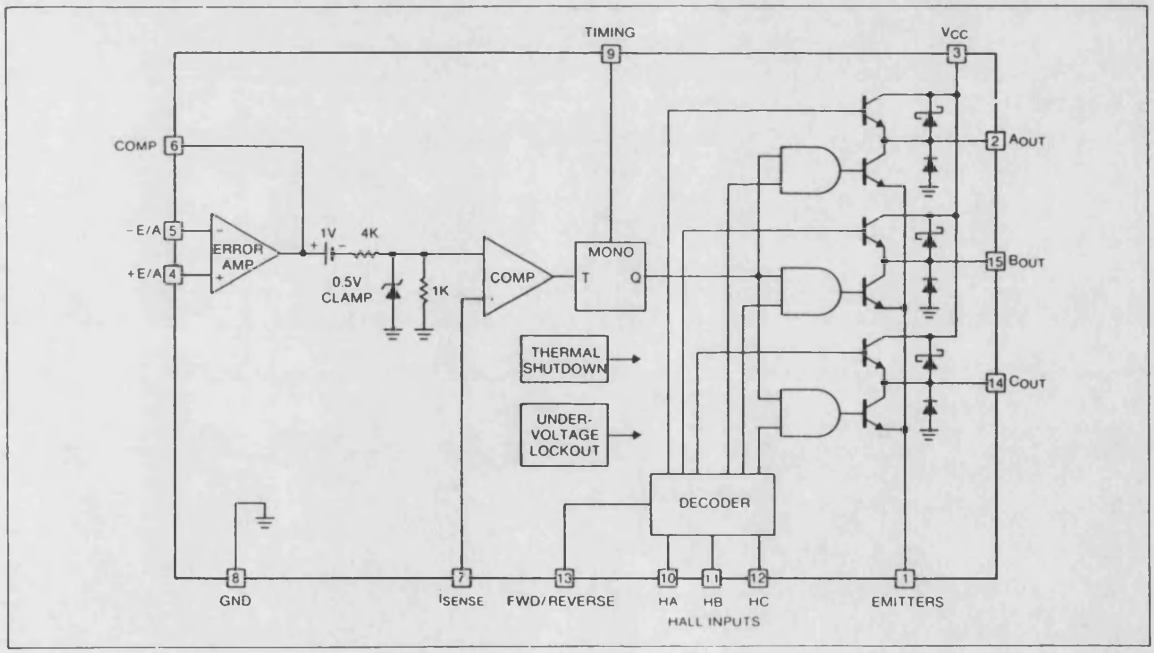

6/85

UNITRODE

MECHANICAL DATA

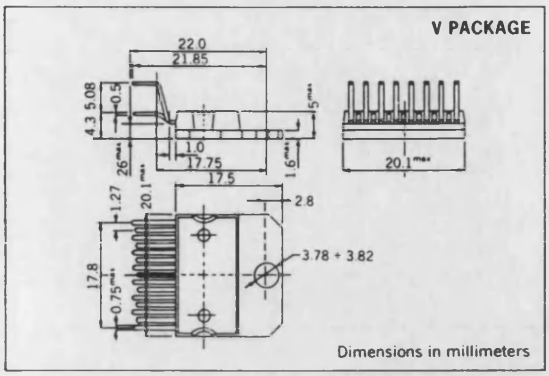

CONNECTION DIAGRAM (TOP VIEW)

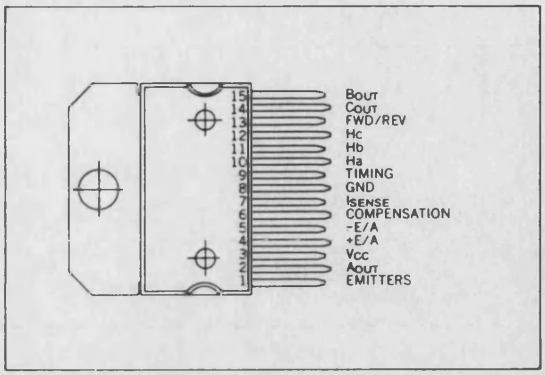

ELECTRICAL CHARACTERISTICS (Unless otherwise stated, these specifications apply for T_A = 0°C to 70°C; $V_{CC(PIN\ 3)}$ = 20V, R_T = 10k, C_T = 2.2nF)

PARAMETER	TEST CONDITIONS	MIN.	TYP.	MAX.	UNIT
Error Amplifier Section					
Input Offset Voltage			1.5	10	mV
Input Bias Current			-.25	-2.0	μA
Input Offset Current			15	250	nA
Common Mode Range	V_{CC} = 8V to 40V	0		V_{IN}-2	V
Open Loop Gain	$\Delta V_{PIN\ 6}$ = 1V to 4V	80	100		dB
Unity Gain Bandwidth	T_j = 25°C, Note 2		0.8		MHz
Output Sink Current	$V_{PIN\ 6}$ = 1V		2		mA
Output Source Current	$V_{PIN\ 6}$ = 4V		8		mA
Current Sense Section					
Input Bias Current			-2.0	-5	μA
Internal Clamp		.425	0.5	.575	V
Divider Gain		.180	0.2	.220	V/V
Internal Offset Voltage		.8	1.0	1.2	V
Timing Section					
Output Off Time		18	20	22	μs
Upper Mono Threshold			5.0		V
Lower Mono Threshold			2.0		V
Decoder Section					
High-Level Input Voltage		2.0			V
Low-Level Input Voltage				0.8	V
High-Level Input Current				10	μA
Low-Level Input Current		-10			μA
Output Section					
Output Leakage Current	V_{CC} = 40V			500	μA
V_F, Schottky Diode	I_o = 2A		1.5	2.0	V
V_F, Substrate Diode	I_o = 2A		2.2	3.0	V
Total Output Voltage Drop	I_o = 2A, Note 3		3.0	3.6	V
Output Rise Time	I_o = 2A		150		ns
Output Fall Time	I_o = 2A		150		ns

Notes: 2. These parameters, although guaranteed over the recommended operating conditions, are not 100% tested in production.
3. The total voltage drop is defined as the sum of both top and bottom side driver.

UNITRODE CORPORATION • 5 FORBES ROAD
LEXINGTON, MA 02173 • TEL. (617) 861-6540
TWX (710) 326-6509 • TELEX 95-1064

PRINTED IN U.S.A.

ELECTRICAL CHARACTERISTICS (Unless otherwise stated, these specifications apply for T_A = 0°C to 70°C; $V_{cc(PIN\ 3)}$ = 20V, R_T = 10k, C_T = 2.2nF)

PARAMETER	TEST CONDITIONS	MIN.	TYP.	MAX.	UNIT
Under-Voltage Lockout					
Start-Up Threshold				8.0	V
Threshold Hysteresis			0.5		V
Thermal Shutdown					
Junction Temperature		150		180	°C
Total Standby Current					
Supply Current				55	mA

TABLE 1

STEP	FWD/ REV	H_a	H_b	H_c		AOUT	BOUT	COUT
1	1	1	0	1		H	L	0
2	1	1	0	0		H	0	L
3	1	1	1	0		0	H	L
4	1	0	1	0		L	H	0
5	1	0	1	1		L	0	H
6	1	0	0	1		0	L	H
1	0	1	0	1		L	H	0
2	0	1	0	0		L	0	H
3	0	1	1	0		0	L	H
4	0	0	1	0		H	L	0
5	0	0	1	1		H	0	L
6	0	0	0	1		0	H	L

H = HIGH OUTPUT
L = LOW OUTPUT
0 = OPEN OUTPUT

CIRCUIT DESCRIPTION

The UC3620 is designed for implementation of a complete 3-Φ brushless DC servo drive using a minimum number of external components. Below is a functional description of each major circuit feature.

DECODER

As shown in Table 1, the decoder employs a 60 mechanical degree hall decode scheme (others available via mask programming) to decode and drive each of three high current totem pole output stages. A forward/reverse signal, pin 13, is used to provide direction. At any point in time, one driver is sourcing, one driver is sinking, and the remaining driver is off or tri-stated. Pulse width modulation is accomplished by turning the sink driver off during the monostable reset time, producing a fixed off-time chop mode. Controlled output rise and fall times help reduce electrical switching noise while maintaining relatively small switching losses.

CURRENT SENSING

Referring to Figure 1, emitter current is sensed across R_s and fed back through a low pass filter to the current sense pin 7. This filter is required to eliminate false triggering of the monostable due to leading edge current spikes. Actual filter values, although somewhat dependent on external loads, will generally be in the 1KΩ and 1000pF range.

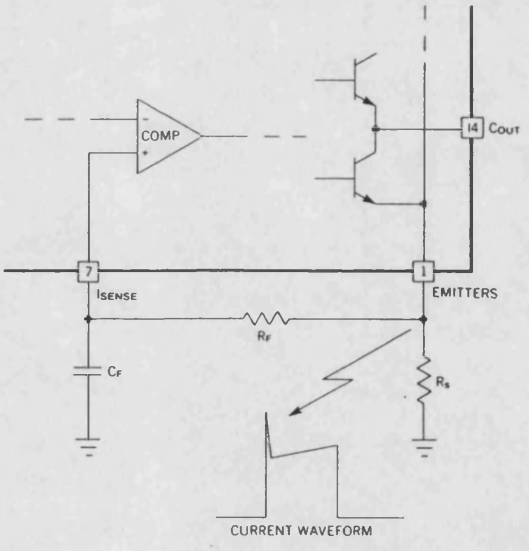

Figure 1. Current Sense Filter

UNITRODE CORPORATION • 5 FORBES ROAD
LEXINGTON, MA 02173 • TEL. (617) 861-6540
TWX (710) 326-6509 • TELEX 95-1064

PRINTED IN U.S.A.

TIMING

An R-C time constant on pin 9 is used by the monostable to generate a fixed off time at the outputs according to the formula:

$T_{OFF} = .916\ R_T C_T$

As the peak current in the emitters approaches the value at the minus (−) input of the on-board comparator, the monostable is triggered, causing the outputs to be turned off. On time is determined by the amount of time required for motor current to increase to the value required to re-trip the monostable. A timing sequence of these events is shown in Figure 2.

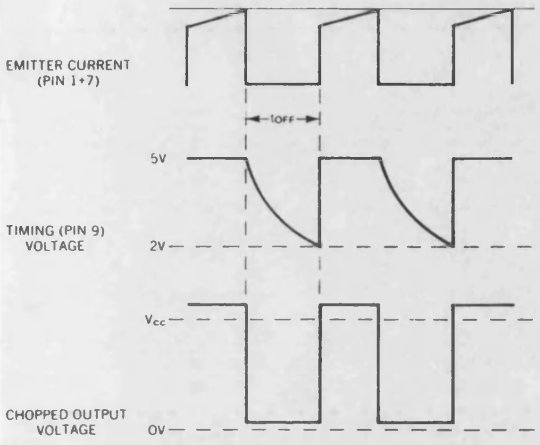

Figure 2. Chopped Mode Timing Diagram

CURRENT LIMIT

Since peak current is being controlled at all times by the internal comparator, a simple voltage clamp at its negative (−) input will limit peak current to a maximum value. A fixed 0.5V internal clamp has been included on the UC3620, and any current spike in the output which generates a sensed voltage greater than 0.5V will immediately shut down the outputs. Actual peak current values may be programmed by selecting the appropriate value of R_s according to the formula:

$$R_s = 0.5/I_{CURRENT\ LIMIT}$$

ERROR AMPLIFIER

A high performance, on-board error amplifier is included to facilitate implementing closed loop motor control. Error voltage generation and loop compensation are easily accomplished by appropriately configuring the gain and feedback of this amplifier. To provide a larger dynamic signal range at the output of the error amplifier, a divide by 5 resistor network is used to reduce the error signal level before applying to the internal comparator. In addition, a one volt offset has been introduced at the output of the error amplifier to guarantee control down to zero current in the output stages. Since this offset is divided by the open loop gain of the feedback loop, it has virtually no effect on closed loop performance.

PROTECTION FUNCTIONS

Protective functions including under-voltage lockout, peak current limiting, and thermal shutdown, provide an extremely rugged device capable of surviving under many types of fault conditions. Under-voltage lockout guarantees the outputs will be off or tri-stated until V_{cc} is sufficient for proper operation of the chip. Current limiting limits the peak current for a stalled or shorted motor, whereas thermal shutdown will tri-state the outputs if a temperature above 150°C is reached.

TYPICAL APPLICATIONS

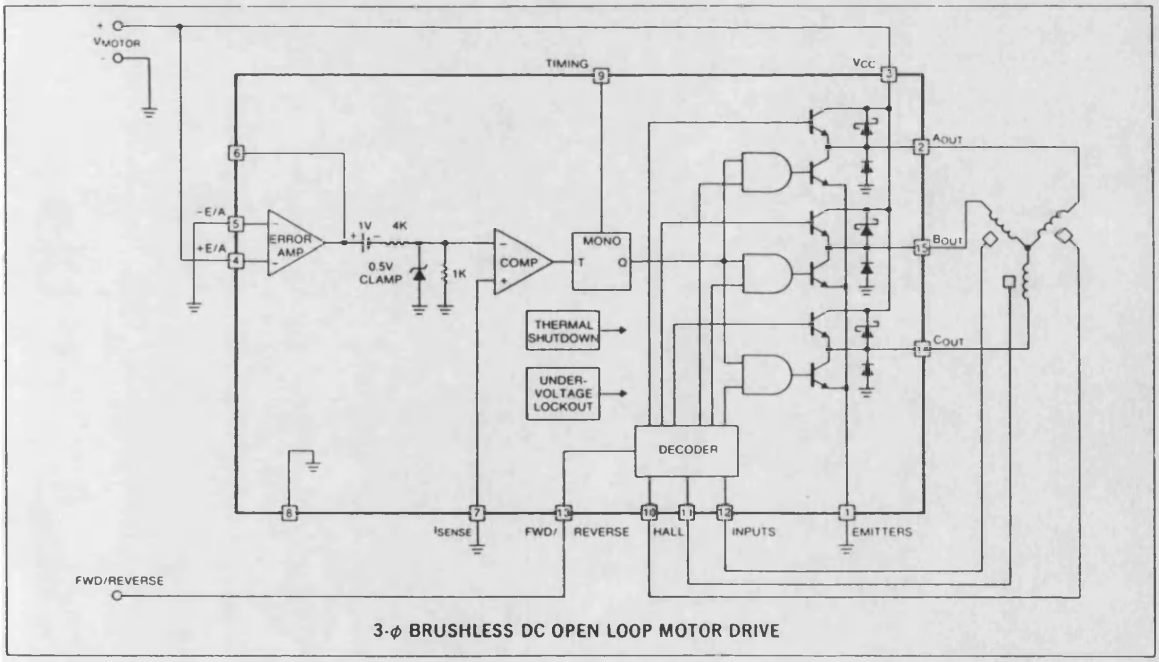

3-ϕ BRUSHLESS DC OPEN LOOP MOTOR DRIVE

UNITRODE CORPORATION • 5 FORBES ROAD
LEXINGTON, MA 02173 • TEL. (617) 861-6540
TWX (710) 326-6509 • TELEX 95-1064

PRINTED IN U.S.A.

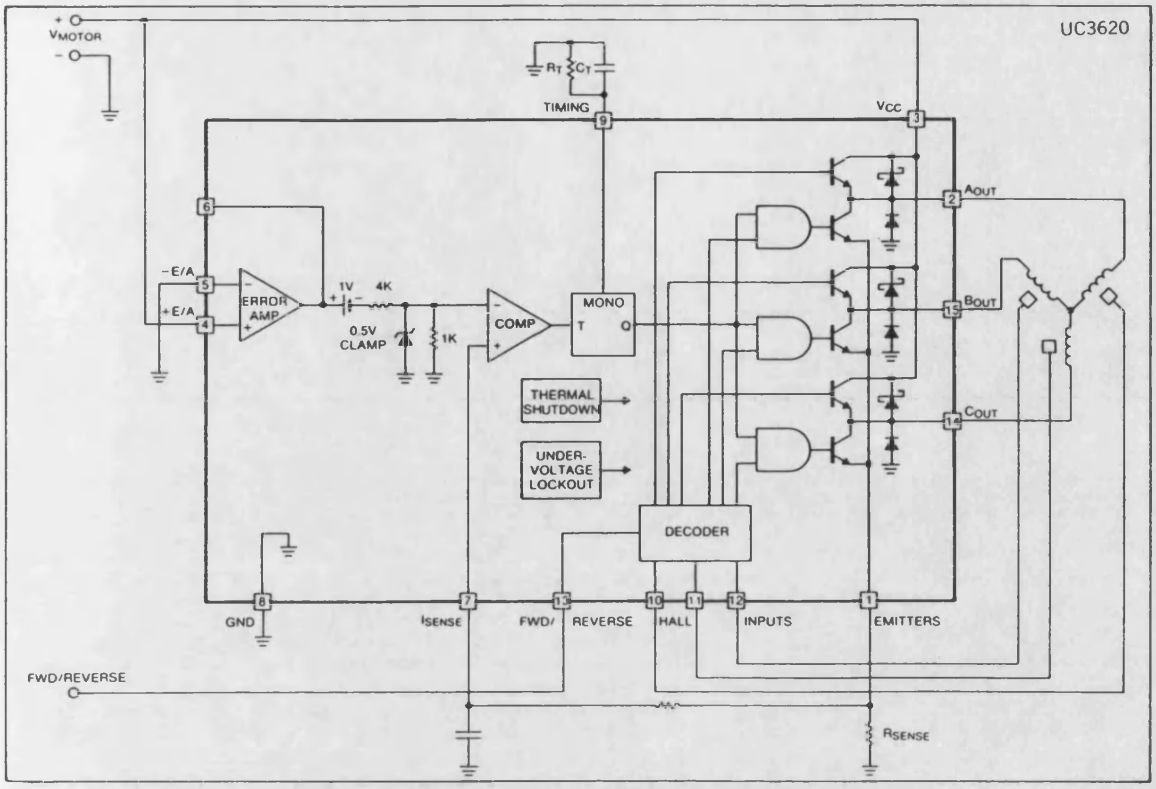

3-ϕ BRUSHLESS DC OPEN LOOP MOTOR DRIVE WITH CURRENT LIMIT

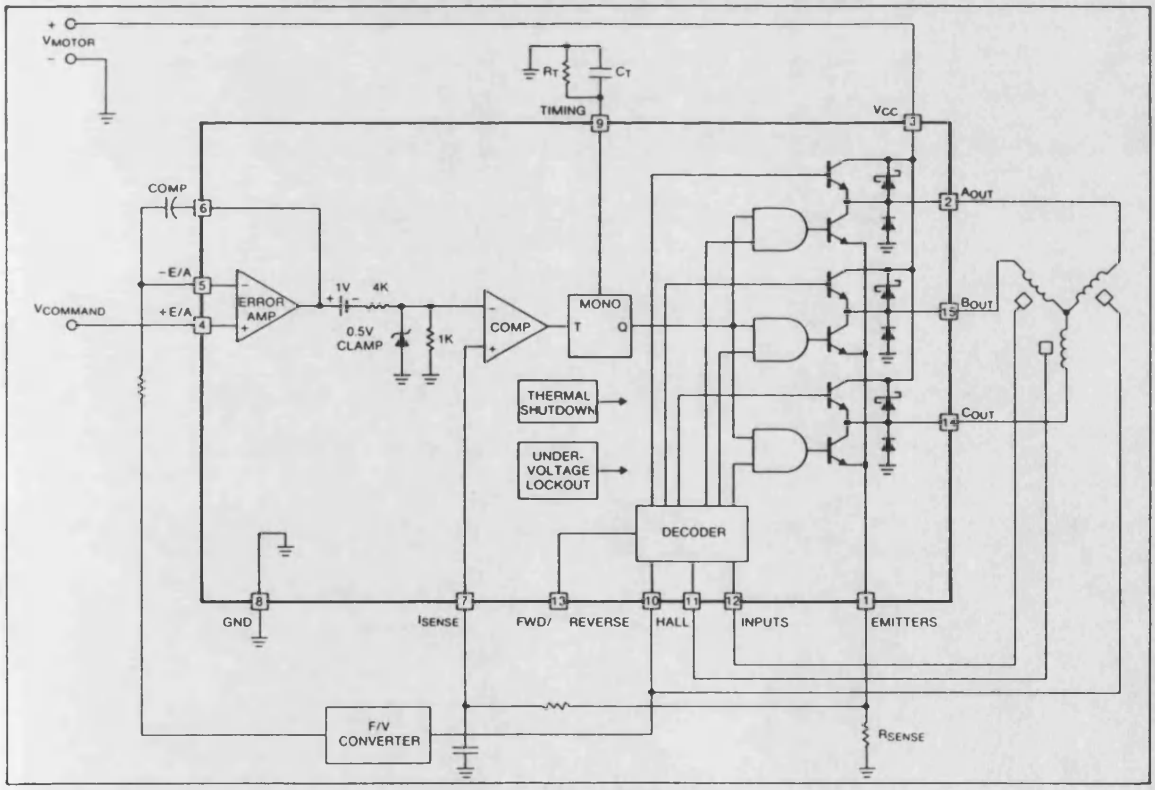

CLOSED LOOP SPEED CONTROL SERVO

UNITRODE CORPORATION • 5 FORBES ROAD
LEXINGTON, MA 02173 • TEL. (617) 861-6540
TWX (710) 326-6509 • TELEX 95-1064

PRINTED IN U.S.A.

APPENDIX G

PUBLICATIONS

Paper Entitled

"Linear Synchronous Tubular Drive System With Permanent Magnet Excitation: Construction and Standstill Forces"

by J. F. Eastham and R. Akmese

Proc. of the 2nd International Conference on Electrical Drives, 20-22 September 1988, Poiana Brasov, Romania, pp. P1-II.

Paper Entitled

"Dynamic Performance of a Brushless DC Tubular Drive System"

by R. Akmese and J. F. Eastham

IEEE Transactions on Magnetics, Vol. MAG-25, pp. 3269-3271, 1989.

Paper Entitled

"Oscillating DC Brushless Linear Motor Supplied by a Power Integrated Circuit"

by J. F. Eastham and R. Akmese

Proceedings of the Fifth Scientific Conference of the Scientific Research Council, 7-11 October 1989, Baghdad-Iraq, Vol. 5, pp. 424-435.

LINEAR SYNCHRONOUS TUBULAR DRIVE SYSTEM WITH PERMANENT MAGNET EXCITATION: Construction and Standstill Forces.

J F Eastham, R Akmese

School of Electrical Engineering

University of Bath

Bath, BA2 7AY, Avon

Abstract. The development of a linear synchronous tubular drive system is described. The standstill forces, including cogging, longitudinal end effect and electromagnetic are investigated. Both 2D finite element and practical results are presented.

INTRODUCTION

Most of the tubular linear machines which have been constructed to date have used the induction principle. However, because of the increase in magnetising current with size the performance of induction machines is limited in small sizes. This limitation can be overcome by using machines which can be alternatively considered as either linear synchronous motors fed from a variable frequency supply or electronically commutated dc machines.

Synchronous machines can be brushless if the excitation is obtained from permanent magnets. Both this feature and the availability of improved permanent magnet materials has given rise to their increased usage in machines. Both rotary and linear types are[1] of interest.

ROTARY BRUSHLESS MACHINES

The usual form of rotary brushless machine is shown in figure 1. This has a permanent magnet rotor and a three phase stationary armature winding. Commonly Hall effect sensors are used to detect rotor position and thus control a 3 phase inverter which in turn supplies the armature winding. Since the coil currents are switched at fixed positions relative to the excitation the electromagnetic effect of a d.c machine is produced.

LINEAR TUBULAR MACHINE CONSRUCTION

Tubular machine geometry can be best explained by subjecting rotary machine geometry to topological changes, following Laithwaite[2] on induction machines. If the rotor and the stator of the machine shown, in Fig 1 is cut along a radial line, AB, and unrolled a flat linear machine is obtained. This is shown in end view in figure 2 and in developed form in figure 3. If this flat linear machine is now rolled up so that lines AB and CD join the tubular form emerges as shown in figure 4. The magnets become radially magnetised cylindrical shells and the armature coils simple circles without end-turns.

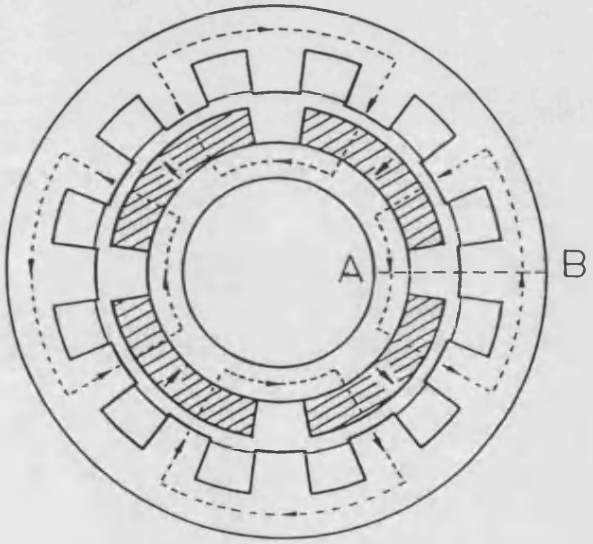

Fig 1. A rotary brushless permanent magnet machine.

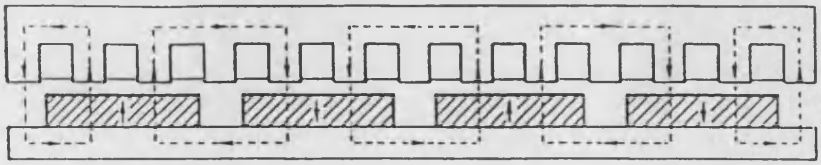

Fig 2. Flat linear permanent magnet machine.

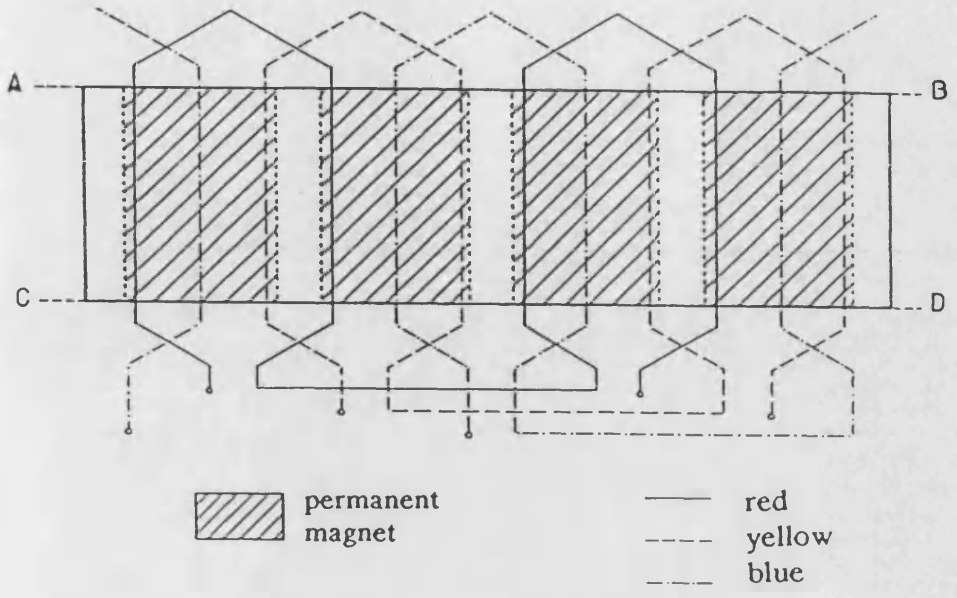

Fig 3. Developed form of flat p.m. machine.

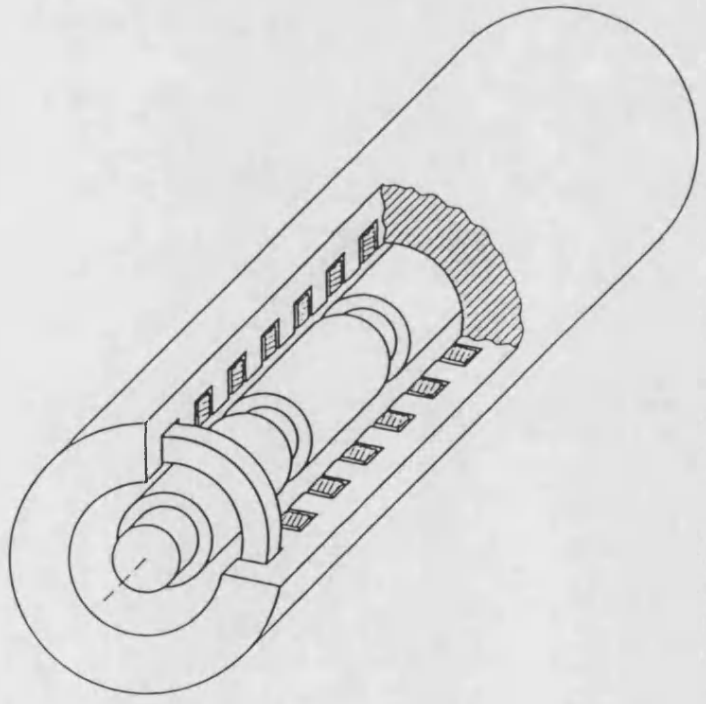

Fig 4. Tubular p.m. motor.

This transformation, however, is not quite enough to construct a practical machine. Two difficulties must be overcome first, a lamination system must be devised that allows for both axial and radial flux paths and secondly a method for armature coil insertion must be conceived. One solution is shown in figure 5. Here the machine is transformed into a four blocked structure each block of which is formed from an axially laminated stack transversely shaped into an arc of a cylinder. The laminations have open slots so that the armature coils can be pre-positioned on a mandrel and the blocks pushed over them.

The machine is modified further in order to eliminate unwanted tooth-cogging forces due to the stator teeth and permanent magnet field. As is shown later, the period of this force is one slot-pitch and it can be eliminated by either a stator slot skew of one slot pitch for the whole circumference or by using a corresponding skew on the permanent magnet rings.

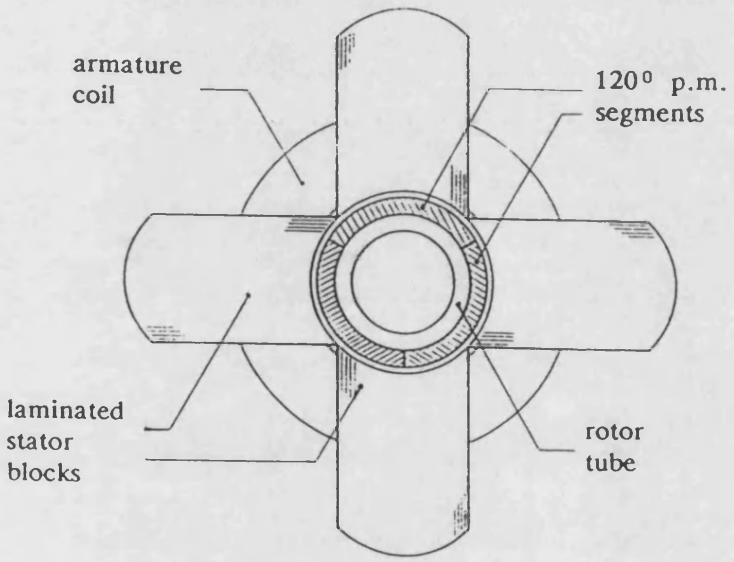

Fig 5. End view of the practical machine.

TUBULAR MACHINE ARMATURE SUPPLY TECHNIQUES.

Essentially the same system is used as in the rotary form of machine. Hall effect sensors are placed on the stator teeth at 120° intervals. These produce the signals shown at H_1, H_2 and H_3 on figure 6 and are combined to turn on the inverter transister switches S1 to S6 as indicated on the figure.

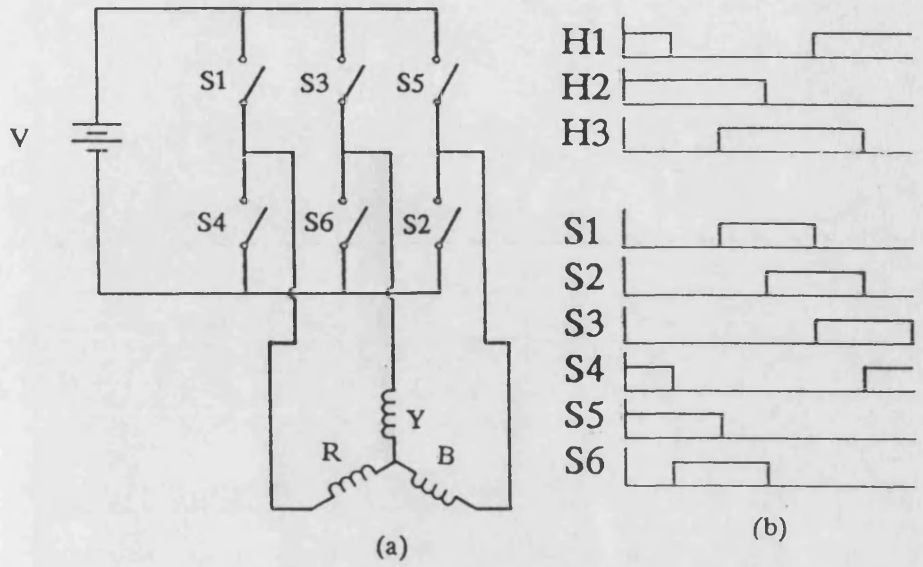

Fig 6. (a) Basic inverter. (b) Hall signals with corresponding switching pulses.

A PRACTICAL MODEL

A short-stator prototype linear tubular motor with two poles on the stator and four poles on the rotor has been constructed. An armature winding with one coil per pole and phase has been used for simplicity. The rotor is step skewed as shown on fig 7 this is a good approximation to the ideal progressive skew. The approximation was made necessary by the lack of skewed magnets rings. Strontium ferrite magnets were used.

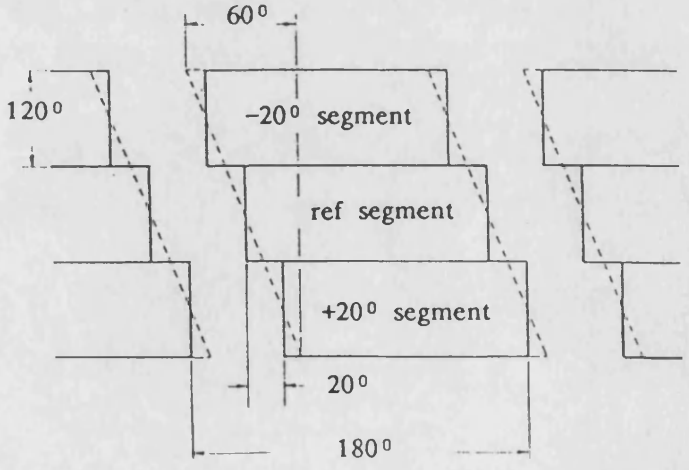

Fig 7. Developed view of p.m. placement.

A smart-power chip, Unitrode 3620, was used as the driver. It includes a three phase inverter with a current amplitude limiter and a Hall effect signal decoder.

FINITE ELEMENT MODELLING

Two axisymmetric finite element (FE) models using a 2D code have been used, the first one shown, in figure 8, has one pole and is used to calculate the tooth cogging force and the electromagnetic force due to stator currents. The other model shown in Fig 9, is a model of the actual machine and is used to calculate the end-effect force due to the finite length of the machine. The rotor cannot be modelled strictly by a 2D method because of the skew. However in each of the models the permanent magnets were first modelled with a simple ring and an approximation to the skewed results obtained by adding together suitably phase shifted versions.

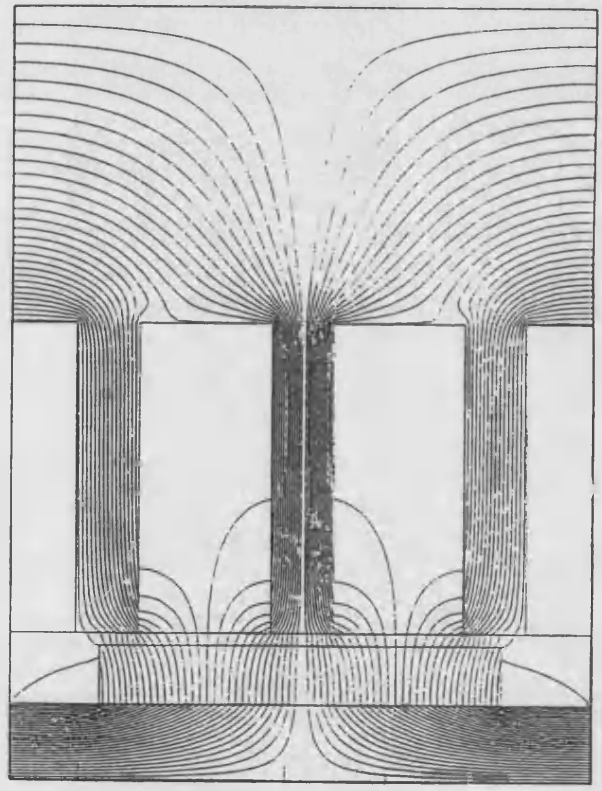

Fig 8. 1-Pole FE Model

STAND-STILL FORCE PRODUCTION

As most applications for actuators involve very low speeds the standstill force performance of the system is of most interest. The results of an investigation is presented below.

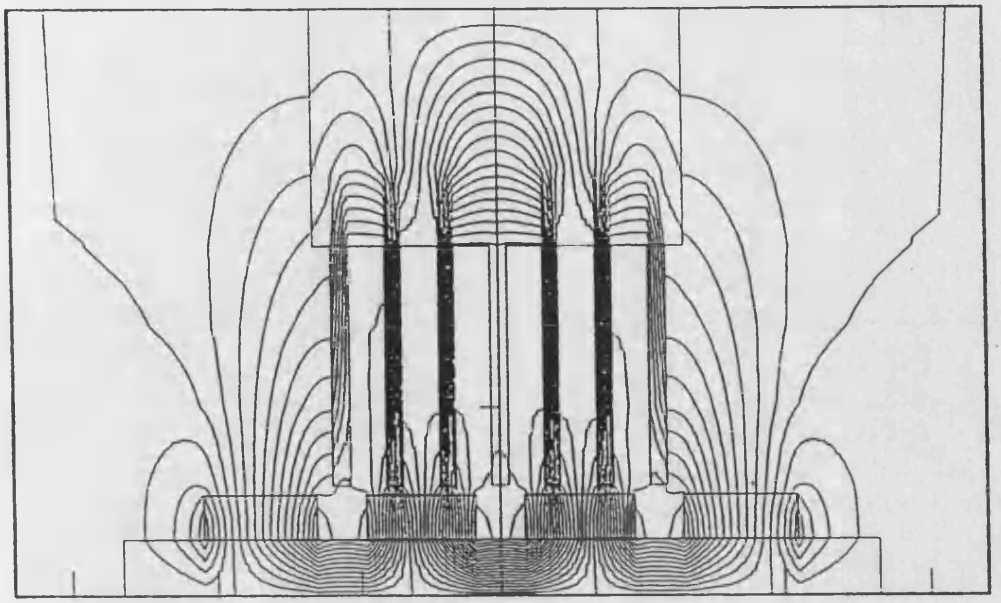

Fig 9. Full FE Model

Tooth cogging forces

The 2D finite element results are shown in figure 10. It will be observed that the space period of the force from the reference segment is 60° or one slot pitch. Hence adding in the forces due to the other segments at ± 20°, a virtual one slot skew, gives a practically zero resultant. This predicted lack of cogging force was confirmed by the practical model.

End effect force

With zero stator current the end effect force shown in figure 11 was measured. This force is due to the finite length of the stator. It can be predicted using the full machine finite element model (figure 9) as indicated. The space period of this force is about 180° or one pole pitch and would require a skew of 3 slot pitches for cancellation.

Electromagnetic Thrust Force

The electromagnetic thrust force was measured with the supply frozen at one particular instant of time (i_r positive, i_y negative, i_b zero) for various displacements of the rotor from the position of symmetry and at a number of armature currents (Figures 12 and 13). It was confirmed that the results could be calculated from the finite element models by combining the results for the electromagnetic force from the one pole model (figure 8) with those from the full machine model (figure 9).

This is of course only possible if saturation effects are not important. However, this is often the case in this form of machine, because of the large effective magnetic gap due to the near unity permeability of permanent magnet material.

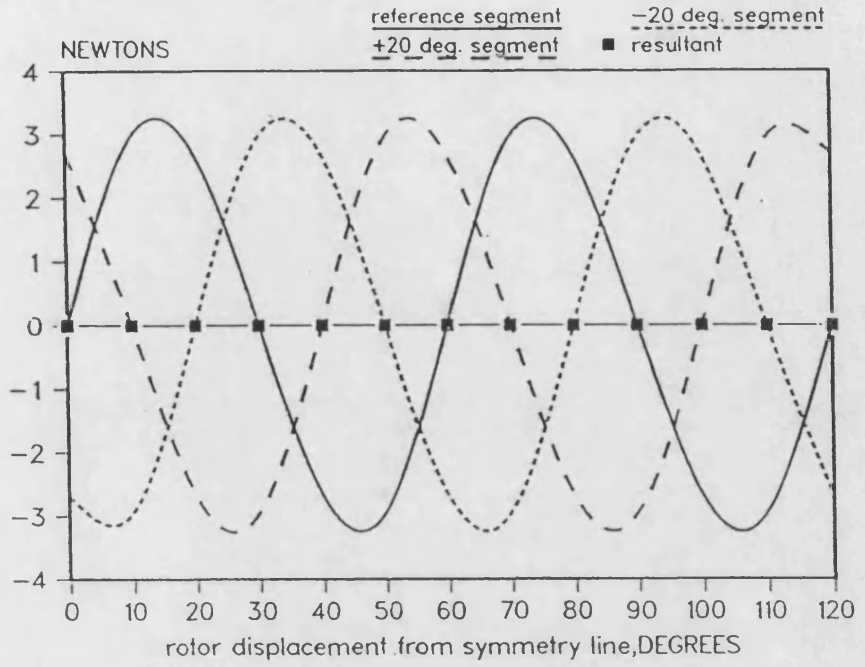

Fig 10. Calculated tooth cogging due to three p.m. segments and resultant force for 20−deg. Skewing.

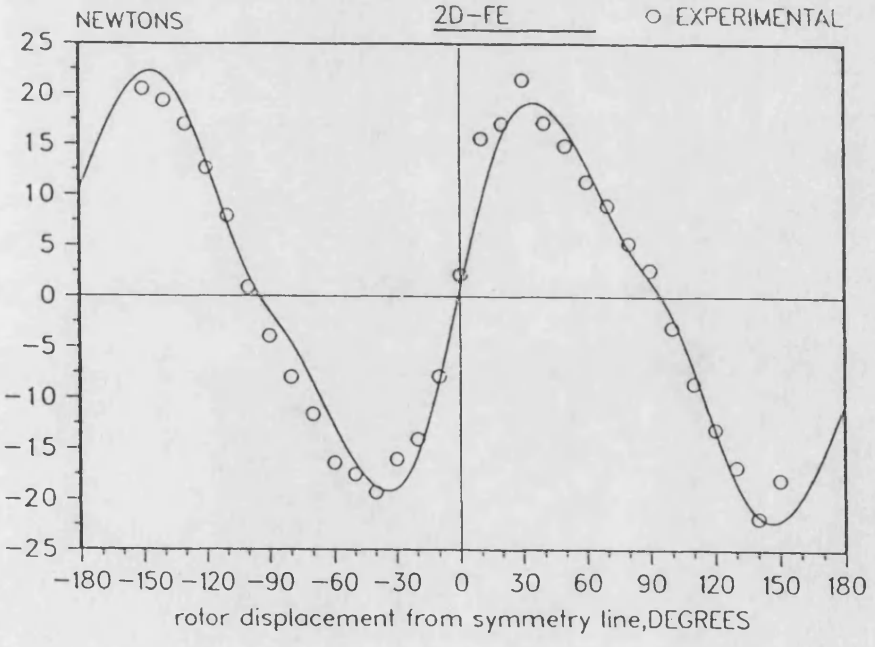

Fig 11. End − effect force.

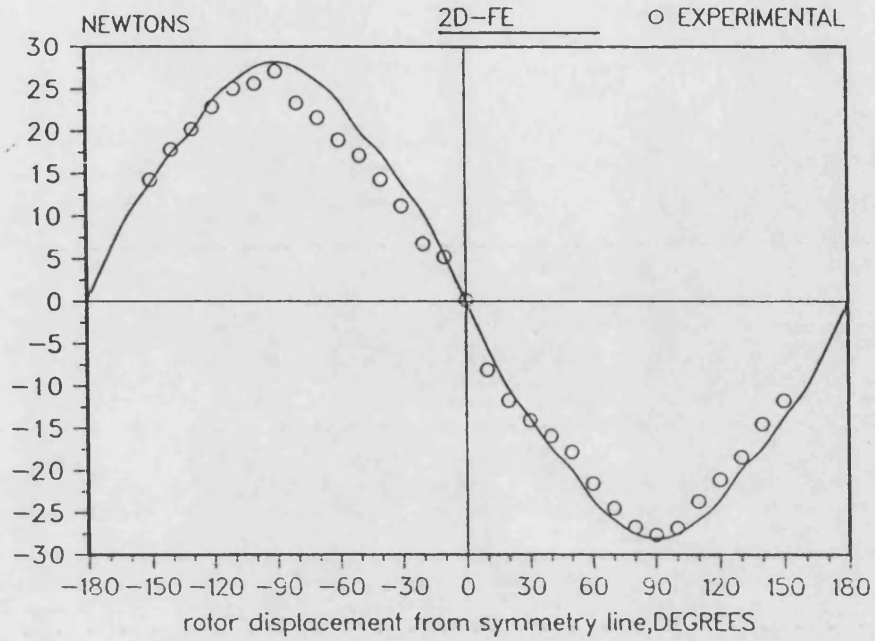

Fig 12. Steady – state thrust force for 1 A DC phase currents

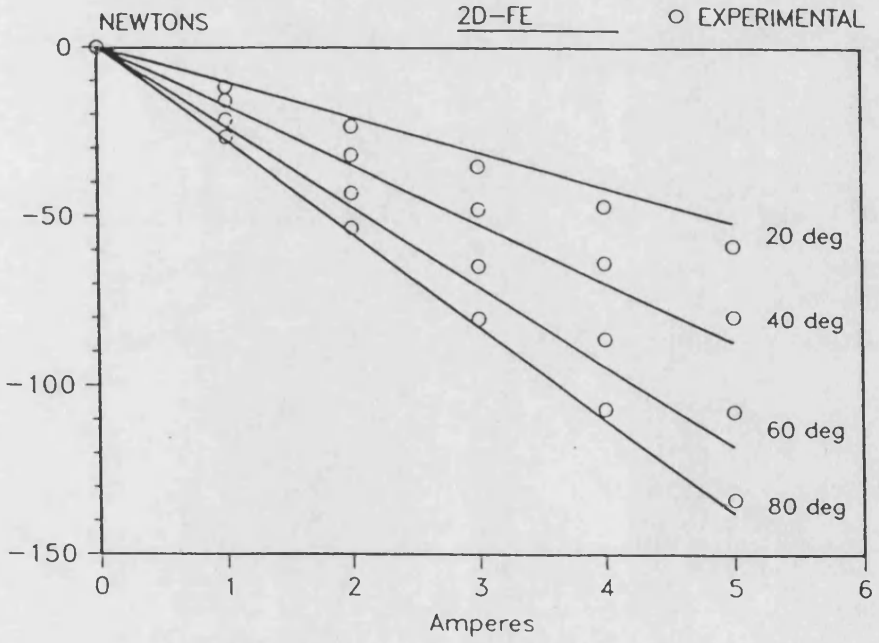

Fig 13. Steady – state thrust force for different DC phase currents

CONCLUSIONS

Two unwanted forces exist in permanent magnet tubular machines at zero armative current. These are due to tooth cogging effects and finite stator length effects. It is shown that the tooth cogging effect can be modelled by 2D finite element methods and eliminated by a quasi one slot skew on the rotor. The end effect force has again been modelled and the results confirmed experimentally but a practical machine with sufficient skew to eliminate the effect remains to be investigated.

It is shown that for the conditions investigated it is possible to superpose the separate calculated forces to produce a composite force that agrees with practice.

REFERENCES

1. Cathey, J. J., Topmiller, D. A., Nasar, S. A. (1986) A Tubular Self-Synchronous Motor for Artifical Heart Pump Drive. IEEE Trans on Biomedical Engineering Vol BME33 No 3.

2. Laithwaite, E. R. (1966) : "Induction Machines for special purposes". Newnes.

DYNAMIC PERFORMANCE OF A BRUSHLESS DC TUBULAR DRIVE SYSTEM

R. Akmese J.F. Eastham
School of Electrical Engineering, University of Bath
Claverton Down, Bath, Avon, BA2 7AY, UK.

Abstract

The paper describes the computer aided analysis of the dynamic performance of a tubular linear machine system with permanent magnet excitation. Finite element techniques are used to find both the machine parameters and the magnetic cogging forces. These forces include not only the conventional tooth cogging force apparent in both linear and rotary machines but also a force unique to permanent magnet linear machines due to the finite length of the stator.

System equations, which describe both the machine and the inverter supply, are solved by a step by step numerical method, to find the dynamic performance of the machine in an oscillatory mode.

The work is verified by experimental results obtained from a practical model.

Introduction

Most of the tubular linear machines which have been constructed to date have used the induction principle. However, because of the increase in magnetising current with size the performance of small induction machines is limited. This is because the magnetising current which gives the excitation, is inversely proportional to (pole-pitch)^2 and hence the force producing rotor current becomes a smaller fraction of the input current as the size of an induction machine is reduced. The limitation can be overcome by using machines with permanent magnet excitation. These must be electronically commutated in the brushless form. A description of one configuration has appeared in the recent literature [1,2]. This has a different magnetic circuit arrangement to the one used for the practical model described in this paper and only the measured performance is described.

Due to both the non-sinusoidal space distribution of the mmfs involved in brushless DC machines and to the non-sinusoidal currents, the classical two-axis theory can give only approximate results. Hence the first papers [3,4] on modelling used a numerical approach to calculate the electrical and mechanical performance of the system. This technique was based on the abc reference frame with no transformation involved. It combined the machine and the power electronic circuitry to model the switching nature of the system in the time domain. This simulation technique was also used by other authors for steady-state and transient calculations [5,6].

All of these studies, however, simulated the rotary permanent magnet machine and there is an absence of published work on the performance of linear versions. Yamamoto analysed the starting characteristics of a flat type permanent magnet pulse driven machine using equivalent magnetic circuits and analytical expressions for one-way motion [7]. Yoshida simulated the performance of a flat-type long stator linear synchronous motor analytically using per phase equivalent circuits [8]. However, the simulation is based on a preset duty-cycle and does not include the phase variables and the dynamic performance of the system.

A Practical System

The Tubular Motor : Construction and Cogging Forces

The practical machine shown in Figure 1 has been constructed. It is a short-stator type with two poles on the stator and four on the rotor [9]. The stator has four laminated blocks and uses open slots. This facilitates construction; the blocks can be assembled over the six circular stator coils which are connected in the conventional sequence. The rotor is step-skewed in order to eliminate unwanted tooth-cogging forces.

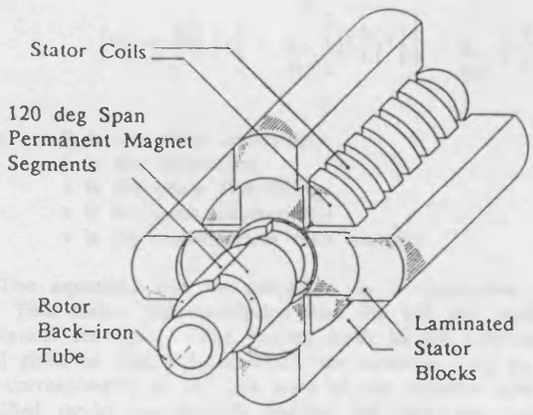

Fig. 1. The practical machine

It will be observed from the figure that three segments each spanning 120^0 are arranged around the periphery to form one pole of the machine. These are radially magnetised. The total effective skew required is one stator slot pitch. Thus, given that the slot spans 60^0, the segments must be displaced by ±20^0 from a central reference segment. It was verified that this system produces zero cogging force by means of both finite-element analysis and practical tests. A 2D finite element model describing one pole of the machine was used to calculate the force from the reference segment. Hence ±20^0 space phase shifted version of this could be added together to yield the total force for the stepped rotor machine. This is, of course, an approximation and it would be better to use a 3D finite element model. However, this would considerably increase the computer time required and the simpler technique gave good results.

Tooth cogging forces are present in both rotary and linear machines. However, linear machines with permanent magnet excitation also have cogging forces due to their finite length. This was modelled using the 2D technique that has just been described, but the finite element model was for the whole structure rather than one pole. Figure 2 illustrates the results and compares them with experiment. It will be observed that the force is roughly sinusoidally distributed and has a wavelength equal to one pole pitch. Skew could again be applied to reduce this force but was not attempted for this machine. Hence end effect force has to be taken into account in the modelling process whereas tooth cogging has been eliminated and can be ignored.

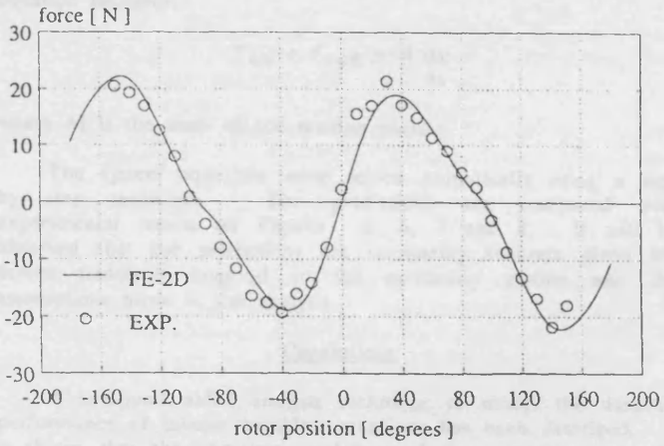

Fig. 2. End-Effect force

Supply System

The machine was supplied by a smart power integrated circuit, the Unitrode 3620. This is a brushless DC motor driver capable of supplying the three phases of the tubular machine. It comprises a Hall signal decoder, a three phase transistor inverter with free-wheeling diodes and a current magnitude limiter. The Hall effect sensors are placed on the stator teeth at 120° intervals (2 slot pitches) to give rotor position signals suitable for the chip decoder. In order to first facilitate transient testing of the system and, secondly, to investigate some potential applications, the machine was set up in an oscillating mode. Extra Hall sensors are required for this to produce 'end-stop' signals.

System Simulation

Machine Parameters

In order to simulate the machine the electrical parameters were calculated. This was achieved by finite element techniques using the 2D whole machine model mentioned above.

The parameters required are the self and mutual inductances of the stator winding and the flux linkage profile of the stator phases due to the permanent magnet field. This latter quantity yields the phase back emfs. These calculated quantities are compared with practical measurements in Table 1 and Figure 3. It will be observed that the agreement is reasonable given the approximations of the 2D finite element used. Table 1 gives only single values for inductances since, in these machines, stator inductance does not change with rotor position. This is because the relative permeability of the permanent magnet material is very close to unity and hence the magnetic gap is constant.

Table 1. Calculated and measured phase inductances (mH)

	Calculated	Measured
L_{AN}	36.01	33.5
L_{BN}	36.01	32.9
L_{CN}	35.87	32.3
M_{AB}	-0.98	-0.4
M_{BC}	-9.55	-10.7
M_{CA}	-9.55	-10.95

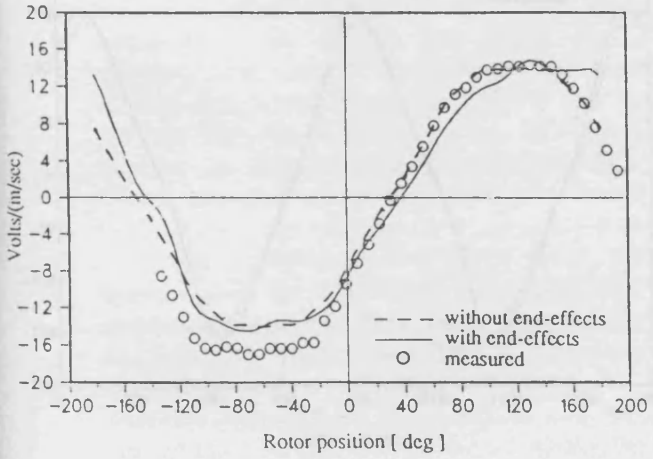

Fig. 3. Phase back emf coefficient

Simulation Technique

The parameters calculated above were used in the system electrical equations. These are shown in the general matrix form below:

$$[V] = [R][i] + \frac{d}{dt}\left[[L][i]\right] + \frac{d}{dx}[\lambda]v$$

where R is the phase resistance
L is the inductance
λ is the phase flux linkage
x is the rotor displacement
v is the instantaneous rotor velocity

The equations can be simplified by a decoupling procedure [4]. This makes the assumption that the self and mutual phase inductances are equal. The process leads to the equivalent circuit model given in Figure 4, in which the terms e_a, e_b, e_c are back emfs corresponding to the last term of the equation above. This simplified model considerably reduces the computer costs of the simulation.

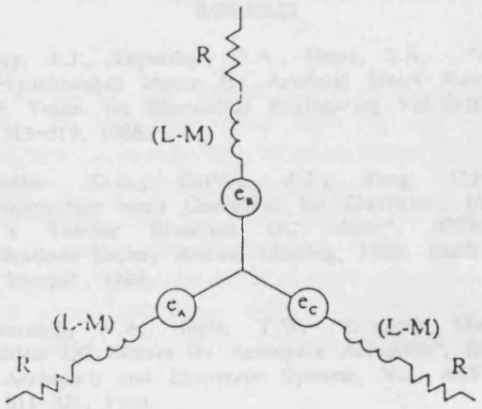

Fig. 4. The decoupled machine model

A mechanical equation is required which relates acceleration to the total force acting on the rotor. This total force may be found by adding the end effect force (F_{end}) mentioned above to the electromagnetic force $F_{em} = [i]\, d/dx\, [\lambda]$ and the mechanical equation becomes:

$$F_{em} + F_{end} = M\frac{dv}{dt}$$

where M is the mass of the moving parts.

The system equations were solved numerically using a step by step technique. The predictions are compared with experimental results on Figures 5, 6, 7 and 8. It will be observed that the predictions are reasonably accurate given the severe transients involved in the oscillatory motion and the assumptions made in the analysis.

Conclusions

A computer aided analysis technique to model the dynamic performance of tubular brushless machines has been described. It is shown that the complete modelling of these machines can be achieved.

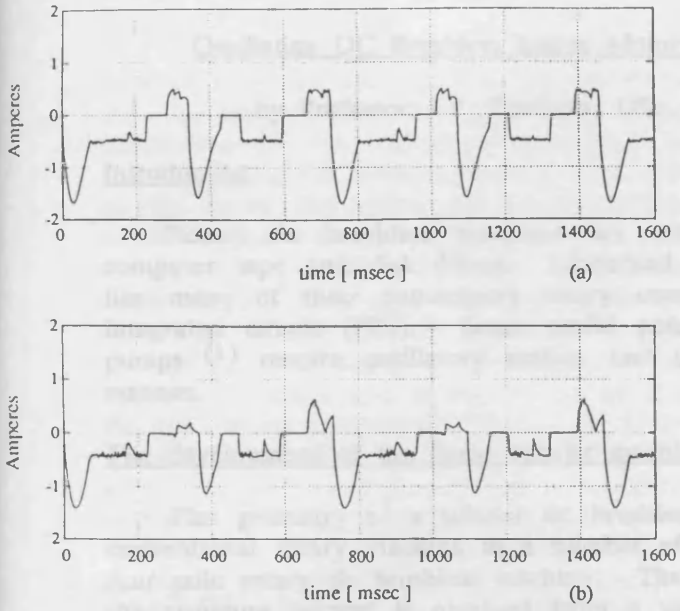

Fig. 5. Phase currents: (a) simulated; (b) measured

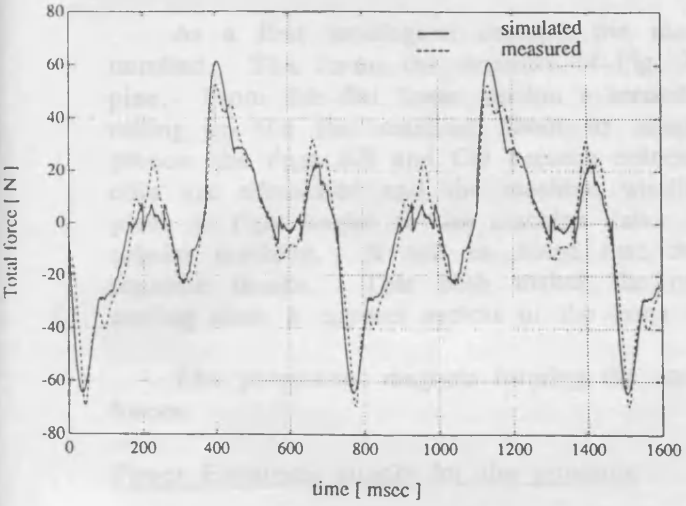

Fig. 6. Total force comparison

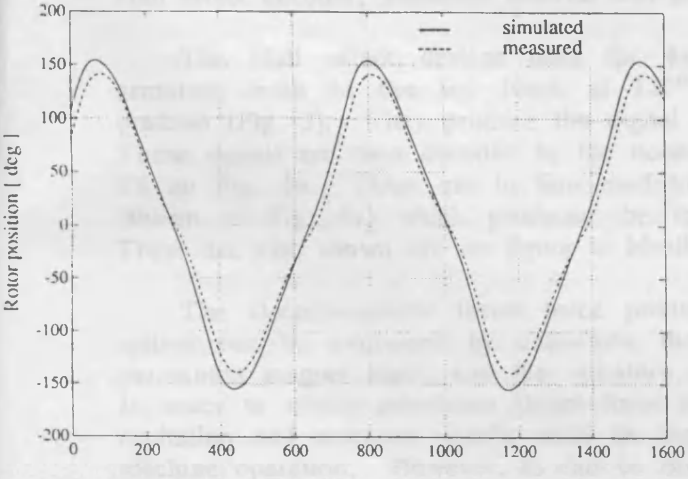

Fig. 7. Rotor position comparison

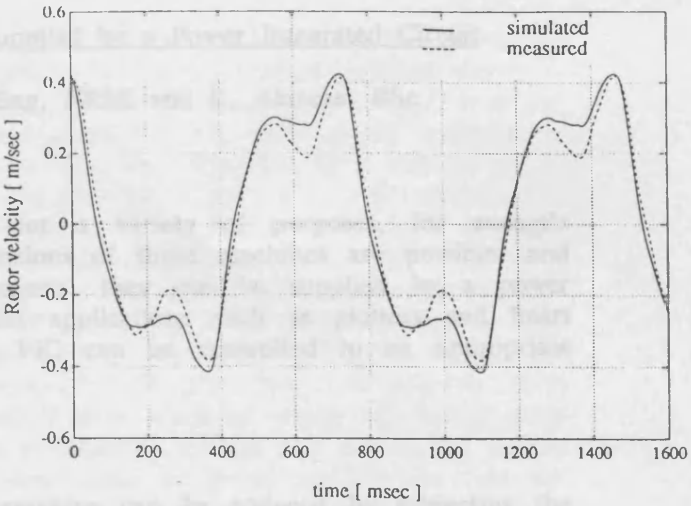

Fig. 8. Rotor velocity comparison

References

[1] Cathey, J.J., Topmiller, D.A., Nasar, S.A. "A Tubular Self-Synchronous Motor for Artificial Heart Pump Drive", IEEE Trans. on Biomedical Engineering Vol.BME33, No.3, pp. 315-319, 1986.

[2] Topmiller, D.A., Cathey, J.J., Yang, C.H. "A Microprocessor-based Controller for Oscillatory Mode Drive of a Tubular Brushless DC Motor", IEEE Industry Applications Society Annual Meeting, 1985, IEEE-IAS-1985, pp. 536-541, 1985.

[3] Demerdash, N.A., Nehl, T.W. "Dynamic Modelling of Brushless DC Motors for Aerospace Actuation", IEEE Trans. on Aerospace and Electronic Systems, Vol. AES-16, No.6, pp. 811-821, 1980.

[4] Nehl, T.W., Fouad, F.A., Demerdash, N.A., Moslowski, E.A. "Dynamic Simulation of Radially Oriented Permanent Magnet-Type Electronically Operated Synchronous Machines with Parameters obtained from Finite Element Solutions", IEEE Trans. on Industry Applications, Vol. IA-18, No.2, pp. 172-182, 1982.

[5] Himei, T., Funabiki, S., Agari, Y., Okada, M. "Analysis of Voltage, Source Inverter-Fed Permanent Magnet Synchronous Motor Taking Account of Converter Performance", IEEE Trans. on Industry Applications, Vol. IA-21, No.1, pp. 279-284, 1985.

[6] Pillay, P., Krishnan, R. "Modelling of Permanent Magnet Motor Drives", IEEE Trans. on Industrial Electronics, Vol. 35, No.4, pp. 537-541, 1988.

[7] Yamamoto, Y. "Analysis of Magnetic Circuit and Starting Characteristics of Flat-Type Linear Pulse Motor with Permanent Magnets", Electrical Engineering in Japan, Vol. 104B, No.5, pp. 102-110, 1984.

[8] Yoshida, K. "Theory and Performance of Long-Stator Linear Synchronous Motors with Samarium Cobalt Permanent-Magnet Excitation", Proceedings of International Conference on Electric Machines, 8-10 September 1986, Munchen, pp. 168-171.

[9] Eastham, J.F., Akmese, R. "Linear Synchronous Tubular Drive System with Permanent Magnet Excitation: Construction and Standstill Forces", 2nd International Conference on Electrical Drives, 20-22 September 1988, Poiana Brasov, Romania, pp. P1-II.

Oscillating DC Brushless Linear Motor Supplied by a Power Integrated Circuit

by Professor J.F. Eastham, DSc, FEng, FRSE and R. Akmese, BSc

Introduction

Rotary dc brushless machines are used for a variety of purposes, for example computer tape and disk drives. Linearised versions of these machines are possible, and like many of their contempory rotary counterparts, they can be supplied by a power integrated circuit (PIC). Some useful potential applications such as plotters and heart pumps [1] require oscillatory motion and the PIC can be controlled in an appropriate manner.

The development of the linear tubular machine

The geometry of a tubular dc brushless machine can be adduced by subjecting the conventional rotary machine to a number of topological changes. Fig. 1 shows a 12 slot four pole rotary dc brushless machine. The excitation is provided by permanent magnets, the armature current is obtained from a variable frequency source which is phase-locked onto the rotor position. The signals for this are obtained from Hall effect field detectors in the machine gap.

As a first topological change, the machine is cut along the radial line A-B and unrolled. This forms the structure of Fig. 2 where Fig. 2a is a side view and Fig. 2b a plan. From this flat linear version a second transformation produces the tubular motor by rolling up the flat machine about its longitudinal axis. It will be noted that in this process the lines AB and CD become coincident which means that the "end-turns" of the coils are eliminated and the machine winding is formed from simple circular coils in a plane at right angles to the machine axis. Fig. 3 shows 3 views of a complete practical tubular machine. It will be noted that the armature iron has been formed from four separate blocks. This both makes the construction easier and improves the machine cooling since it exposes sectors of the armature coils.

The permanent magnets forming the excitation are step skewed to avoid tooth cogging forces.

Power Electronic supply for the armature

The power electronic supply required is an inverter controlled by rotor position detection. A Unitrode smart power integrated circuit is used for this. It comprises a Hall effect decoder, transistor inverter and current limiter [2].

The Hall effect devices used for excitation position sensing are placed on the armature teeth of the top block at 120^{o} intervals and detect the reference segment position (Fig. 3). They produce the digital signals shown as H1, H2 and H3 on Fig. 4b. These signals are then decoded by the decoder to produce the waveforms shown at T1 to T6 on Fig. 4b. These are in turn used to control the transistor switches of the inverter (shown at Fig. 4a) which produces the three phase currents of the armature winding. These are also shown on the figure in idealised form.

The electromagnetic thrust force production of the machine and power conditioning system can be explained by examining the relationship between the distribution of the permanent magnet mmf, and the armature mmf produced by the injected phase currents. In order to obtain maximum thrust force from the machine, the force angle δ, between excitation and armature mmfs, must be kept as close to 90^{o} as possible throughout the machine operation. However, as can be observed from the current waveforms of Fig. 4b, the phase currents stay fixed in space for 60^{o}, which is the switching period length, while the excitation moves. One practical solution to this is to make the switching period take place while the force angle changes between 120^{o} and 60^{o}. This is done by placing the Hall effect sensors with respect to the armature phases in the correct position.

The operation of the basic brushless drive system can be explained by the interaction between armature currents and permanent magnets. For the excitation position shown in Fig. 5a, Hall sensors H1, H2 and H3 will read 1, 0 and 0 respectively from the spacial distribution of the reference permanent magnet mmf. This Hall signal combination corresponds to the switching period 5 as shown in Fig. 4b. The instant is marked as #1 on the figure and makes the inverter switches T4 and T5 switch on for the direction of motion of interest. This produces three phase currents i_a, i_b and i_c with signs −, 0 and + respectively, causing the stator current and mmf distribution shown in Fig. 5a. As a result of excitation and armature mmfs' interaction, the excitation moves in the right direction. These currents stay fixed in time and space while the excitation moves until the end of switching period 5, which is marked as #2(−) on Fig. 4b. The force angle between excitation and armature axes at this instant is 60° (Fig. 5b). At position #2(+) the Hall signal combination changes to 1, 1 and 0 as a result of sensor H2 being under the field of a north pole magnet, giving rise to a switching change and making i_a, i_b and i_c 0, −1 and 1 respectively and to a current distribution as shown on Fig 5c. At this moment, armature mmf suddenly "jumps" 60° forward in space changing the force angle from 60° to 120°. In this new switching interval and fixed armature current and mmf placement, the excitation continues to move on, reducing the force angle from 120° down to 60° where it again becomes 120° due to another switching change. This results in a stator mmf which takes 60° discrete jumps.

The magnitude of the force exerted on the moving rotor is proportional to the product of excitation and armature mmfs and the sine of the angle δ between their axes. Excitation mmf is constant due to the permanent magnet poles and armature mmf is proportional to the magnitude of the current flowing in its winding. Therefore the electromagnetic thrust force is a function of the armature currents and force angle δ.

The current magnitude control is accomplished by sensing the voltage drop across the sense resistor, R_s, and feeding it to the voltage comparator of the chip which compares this voltage with a predetermined reference voltage. The output of this comparator is fed into a monostable multivibrator which controls the on–off states of the bottom transistors of the three inverter legs. When the voltage signal from the sense resistor exceeds the reference voltage, bottom transistors are switched off and the inductive phase currents circulate through the conducting upper transistor and a free–wheeling diode. The off–time of the monostable is determined by appropriately choosing a timing capacitor and a resistor which are connected to the timing input of the chip. Current magnitude can consequently be controlled by the proper selection of R_s.

Direction control for the oscillatory operation

The previous section detailed the basic principles on which the brushless machine operation is based. This involves only unidirectional motion. Reverse direction for the oscillatory operation can be obtained by applying reverse currents, at a rotor position, to those shown in the previous section.

A simplified block diagram of the oscillatory operation of the drive systems is given in Fig. 6. In addition to the driver chip and the tubular motor with Hall sensors for rotor position sensing, it has two additional sensors for travel–end sensing.

Table 1 shows the 60° Hall decoding used for the oscillatory operation of the system.

The digital Forward/Reverse input of the driver chip is used for the direction control by combining it with the other three Hall effect signals to determine the switching position, i.e. the phase current directions of the inverter. The direction signal (DS) was obtained by using two additional Hall effect sensors, end sensors (ES), as a basis of end–stops [Fig. 6]. These sensors, one on the left of the stator and one on the right, are placed on the extensions of the armature frame which holds the four blocks together and are on the line of the reference pm segment travel. They detect the existence of pms in the same way as the other Hall sensors do, reading 0 when their marked side sees a south pole and 1 a north pole or no field. They read the fields of the left and

rightmost segments. Since the leftmost segment is a south pole and the rightmost a north pole, the marked side of ESleft faces the excitation and the unmarked side of ESright. This is done in order to get the same response from the sensors.

The outputs of these sensors are fed into a 1-bit memory latch as shown in Fig. 7 as inputs. This memory uses two TTL NAND logic gates and is made necessary by the need for a memory device which can hold the last reading of the sensor-pair after the excitation has reached an end and reversed. The way the direction control works can be explained by the help of Tables 1 and 2. Suppose that the end-sensors do not see any magnet when the system is switched on (the excitation is in the middle of its travel), then both sensors will be high (1). The Q output of the latch will also be 1. Taking the excitation position to be the same as that in Fig. 5a where one-way motion is explained, position signals H1, H2, H3 will be 1, 0, 0 respectively. According to Table 1, these direction and position signals will give rise to phase currents with the directions +, 0, - for i_a, i_b and i_c respectively. This will move the excitation to the left, that is in the reverse to Fig. 5a. The excitation continues to move in this direction with phase sequence bac in the way explained in the previous section until the left end-sensor detects the left-hand end south pole. At this point it becomes 0, making the latch output 0 as shown in Table 2. This change in the direction signal demands reversed phase currents to those just before the DS change, making the excitation move towards the right. When it moves in this direction, the left end-sensor becomes 1 again as the magnet at the left-hand end of the excitation moves away from the sensor. But the latch output stays the same; thus the excitation carries on in the right-hand direction. This goes on until the right end-sensor detects the right-hand end segment and DS becomes 1 when the excitation is first decelerated by the reversed electromagnetic forces then accelerated in the left-hand direction.

This simple technique, however, should be used with care as, in the case of high excitation speeds, the transient currents which are driven by the phase back emfs can be very high. Since these currents circulate through diodes and phases, they cannot be limited by the chips protection circuitry and can be dangerous for the switching devices.

System Modelling

The machine exhibits two forms of cogging force. The first of these, due to the teeth, has been reduced to zero by the step skew process. The second cogging fence is due to the finite length of the stator and it has been shown [3] that this force is roughly sinusoidal with excitation position and of 1 pole pitch in period. These cogging fences were predicted by a finite element analysis and good agreement was obtained. The FE model was also used to predict the parameters needed to model the system, that is the self and mutual reactances between phases and the induced back emf profiles. These parameters were used in the system equations:

Electrical

$$[V] = [R][i] + \frac{d}{dt}\left[\,[L][i]\,\right] + \frac{d}{dt}[\lambda]v$$

Mechanical

$$F = M\frac{dv}{dt}$$

where

R is the phase resistance
L is the inductance
λ is the phase flux linkage

x is the excitation displacement
v is the instantaneous excitation velocity
F is the total force acting on the excitation
M is the mass of the moving parts.

A step by step method was employed to solve these equations [4] and a sample result for the phase currents is shown in Fig (8).

Conclusions

The operation of an oscillating brushless tubular motor system driven by a power integrated circuit has been described. It is shown that the system can be modelled by a method which combines FE analysis with circuit analysis.

References

(1) Cathey, J.J., Topmiller, D.A., Nasar, S.A., "A Tubular Self-Synchronous Motor for Artificial Heart Pump Drive", IEEE Trans. on Biomedical Engineering, Vol. BME33, No. 3, pp 315-319, 1986.

(2) Claudio de Sa e Silva, "Brushless DC Motors Get a Controller IC that Replaces Complex Circuits", Electronic Design, September 19, pp 149-156, 1985.

(3) Eastham, J.F., Akmese, R., "Linear Synchronous Tubular Drive System with Permanent Magnet Excitation: Construction and Standstill Forces", 2nd International Conference on Electrical Drives, 20-22 September 1988, Poiana Brasov, Romania, pp P1-II.

(4) Akmese, R., Eastham, J.F., "Dynamic Performance of a Brushless DC Tubular Drive System", (Accepted for Publication in September 1989 Issue of IEEE Trans. on Magnetics).

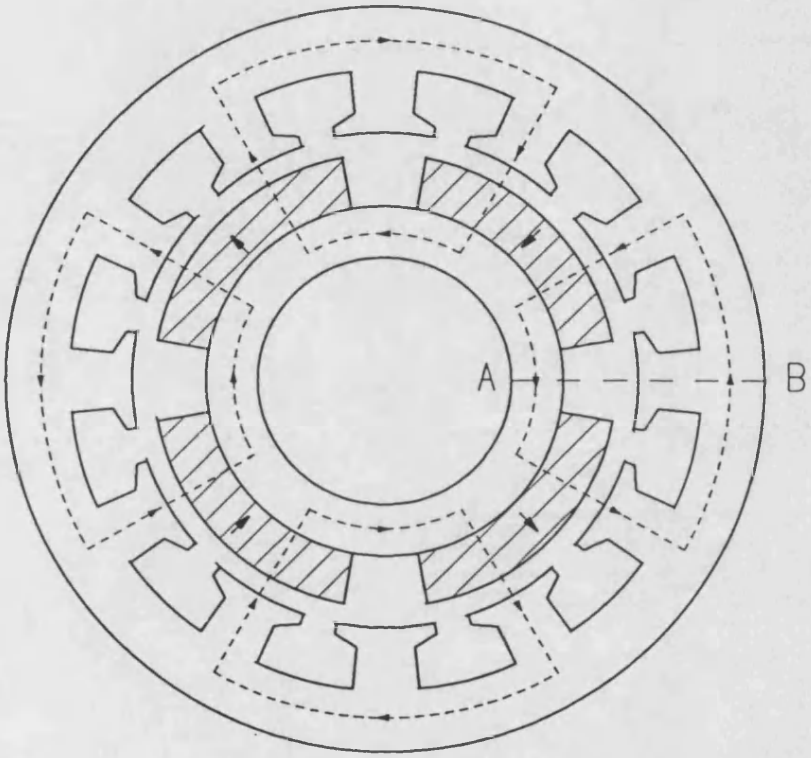

Fig. 1. A rotary dc brushless machine

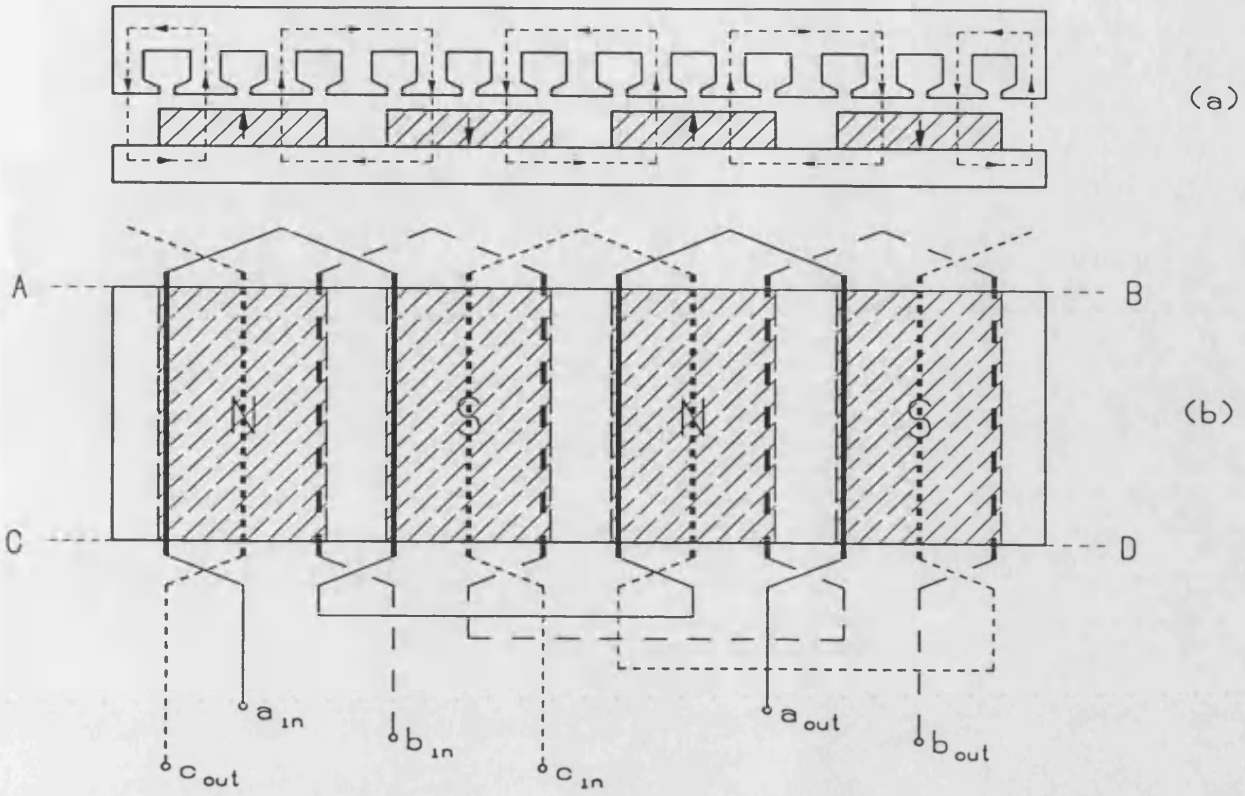

Fig. 2. Flat linear dc brushless machine;
(a) side view
(b) developed form

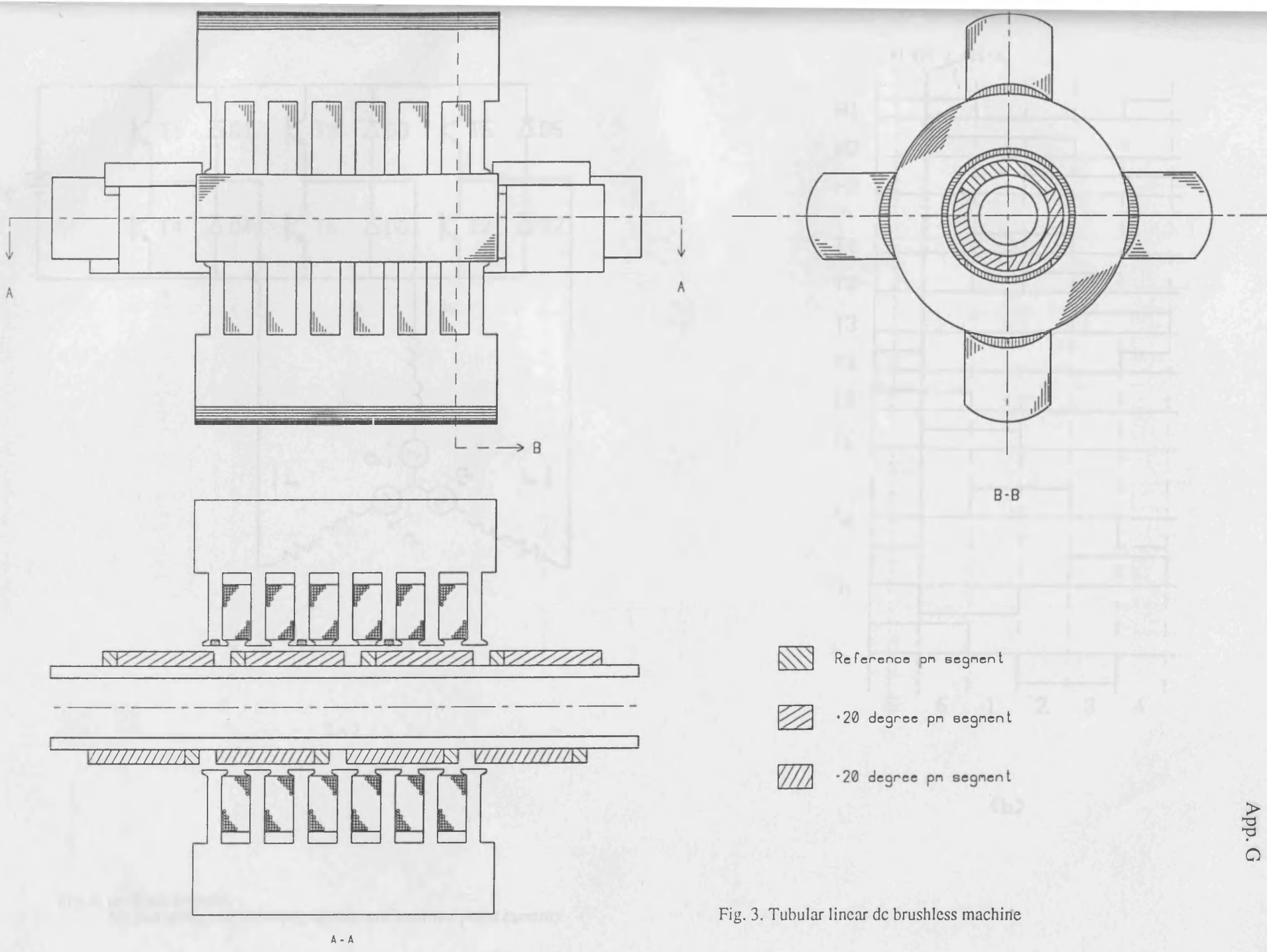

Fig. 3. Tubular linear dc brushless machine

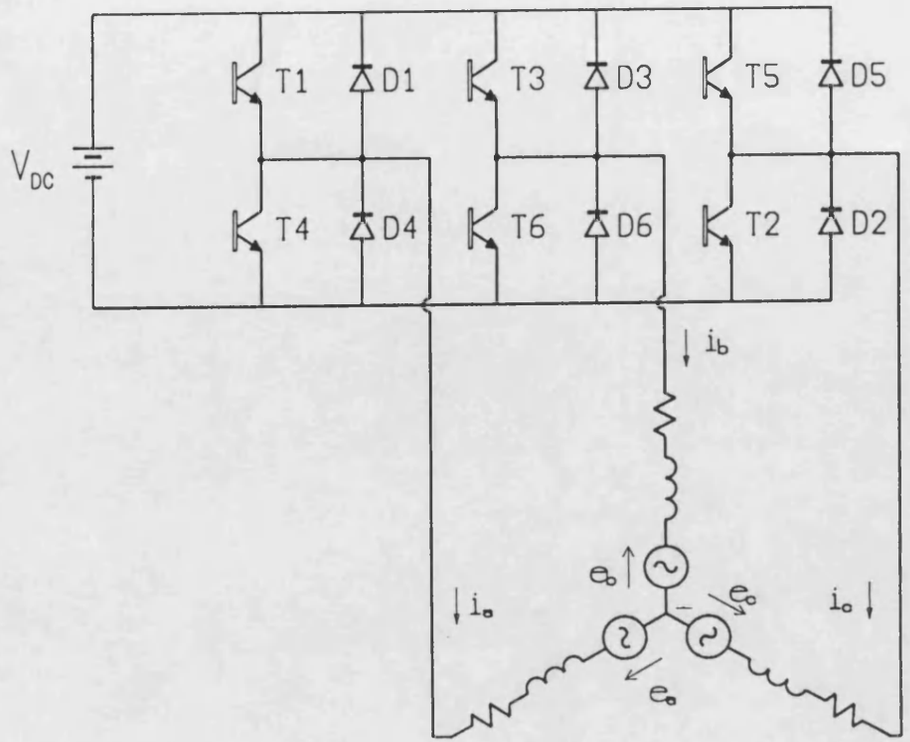

(a)

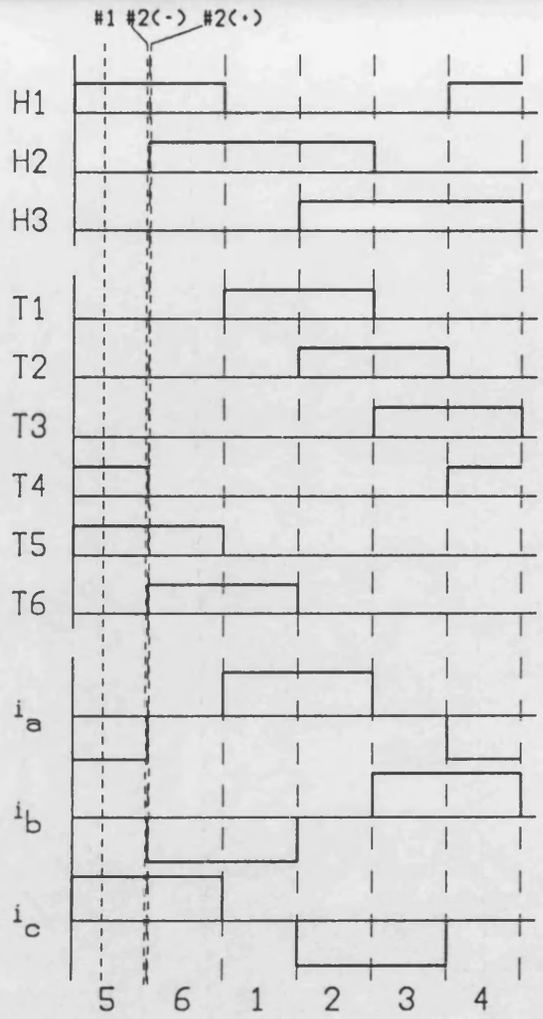

(b)

Fig. 4. (a) Basic inverter
(b) Hall effect and switching signals and idealized phase currents

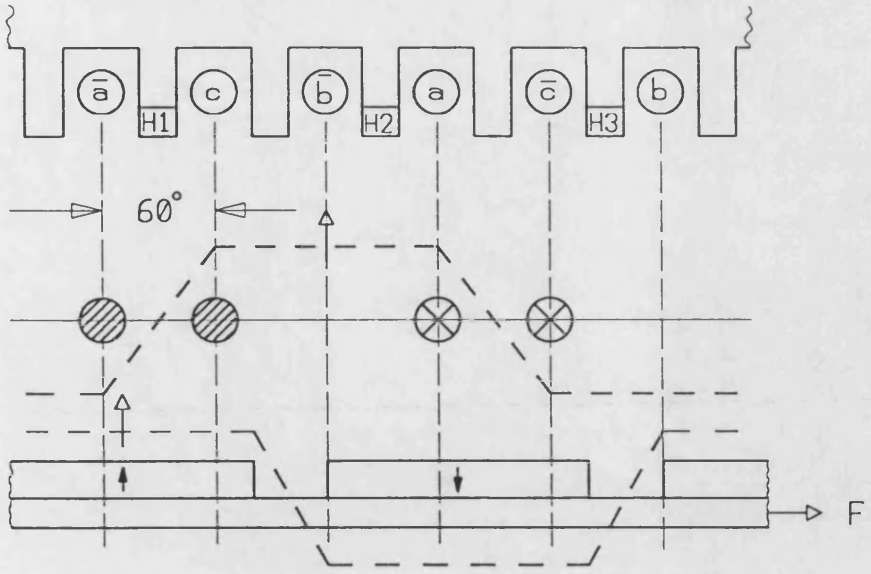

(a) #1; switching interval 5

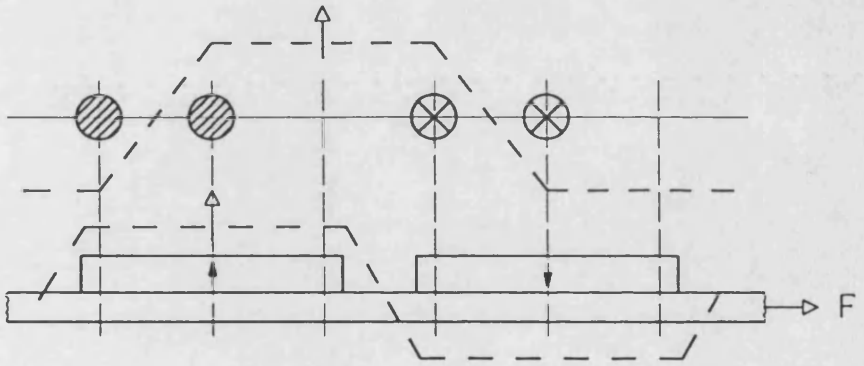

(b) #2(-); end of interval 5

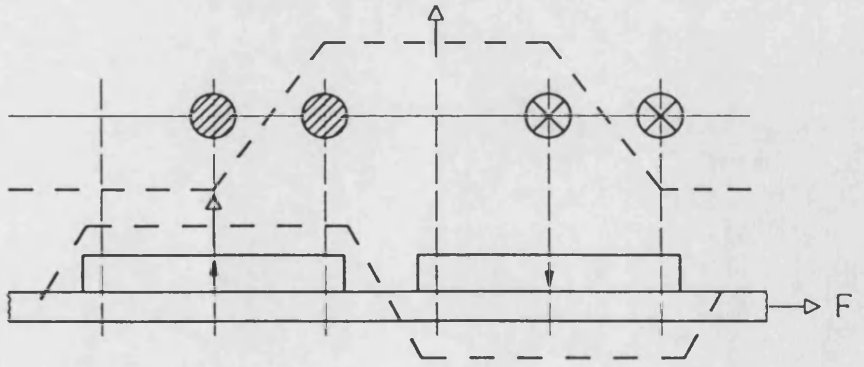

(c) #2(+); start of interval 6

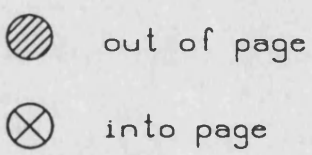

Fig. 5. Force production of the brushless dc machine

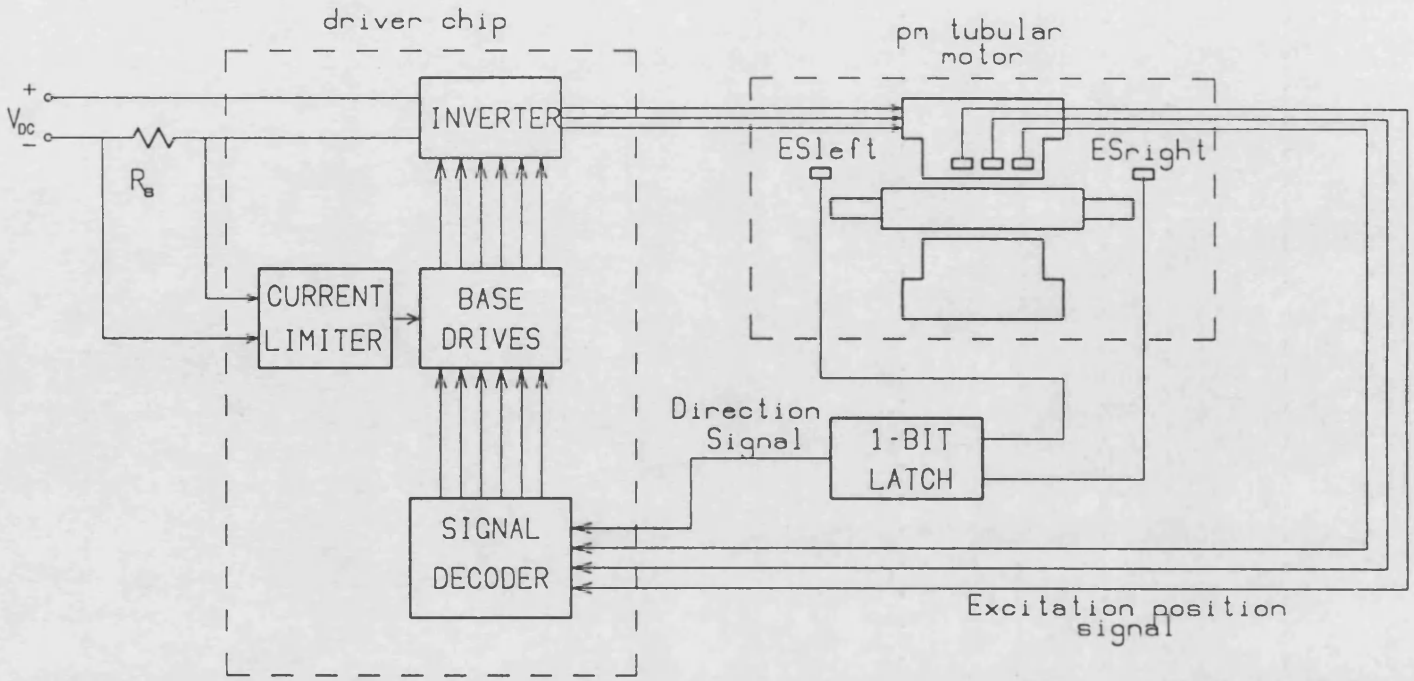

Fig. 6. Block diagram of the oscillating dc brushless machine

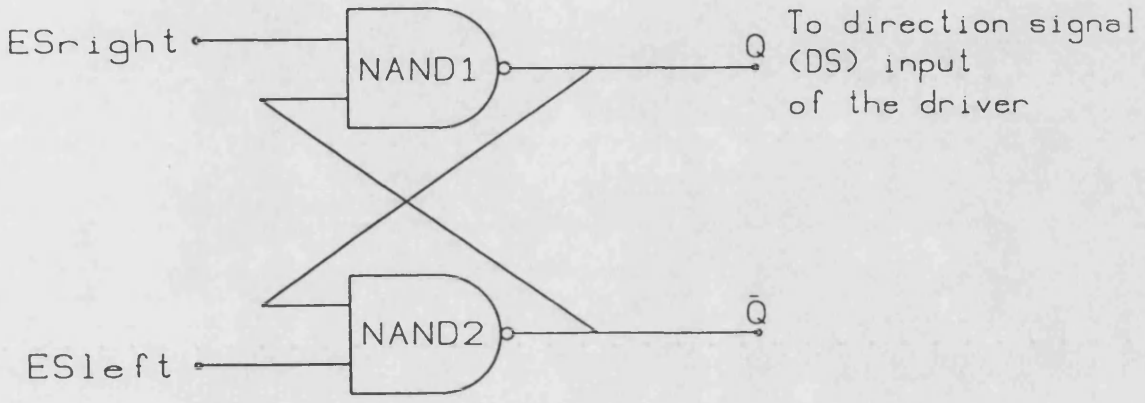

Fig. 7. The direction control latch

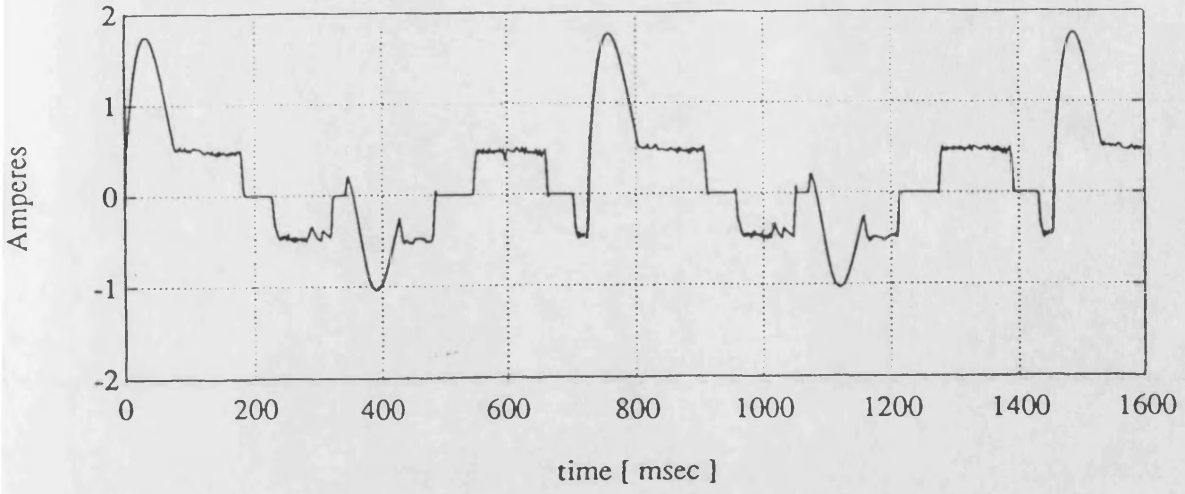

(a)

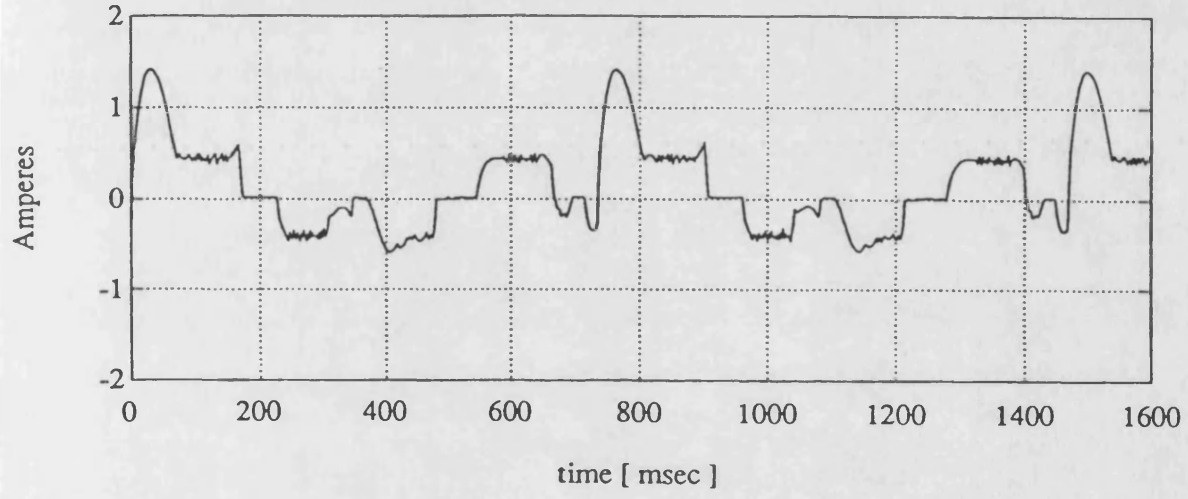

(b)

Fig. 8. Phase currents;
(a) simulated
(b) measured

Table 1. Signal coding used in the oscillatory operation

Direction Signal(DS)	H1	H2	H3	Switching Interval	i_a	i_b	i_c
1	1	0	1	1	+	-	0
1	1	0	0	2	+	0	-
1	1	1	0	3	0	+	-
1	0	1	0	4	-	+	0
1	0	1	1	5	-	0	+
1	0	0	1	6	0	-	+
0	1	0	1	4	-	+	0
0	1	0	0	5	-	0	+
0	1	1	0	6	0	-	+
0	0	1	0	1	+	-	0
0	0	1	1	2	+	0	-
0	0	0	1	3	0	+	-
DS=1; Phase Sequence=bac; Excitation Direction=left DS=0; Phase Sequence=abc; Excitation Direction=right							

Table 2. Operation table of the direction control latch

Excitation Position	ESleft	ESright	Q(DS)	Excitation Direction Command
middle	1	1	1	left
left	0	1	0	right
left	1	1	0	right
right	1	0	1	left
right	1	1	1	left
left	0	1	0	right

REFERENCES

[1.1] Nasar, S. A., Boldea, I., *Linear Electric Motors*, New Jersey: Prentice-Hall, Inc., 1987.

[2.1] Weh, H., Shalaby, M., "Magnetic Levitation with Controlled Permanentic Excitation", *IEEE Trans. on Magnetics*, Vol. MAG-13, No. 5, pp. 1409-1411, 1977.

[2.2] Atherton, D.L., "Maglev using Permanent Magnets", *IEEE Trans. on Magnetics*, Vol. MAG-16, No. 1, pp. 146-148, 1980.

[2.3] Slemon, G.R., Burke, P.E., Terzis, N., "A Linear Synchronous Motor for Urban Transit Using Rare-Earth Magnets", *IEEE Trans. on Magnetics*, Vol. MAG-14, No. 5, pp. 921-923, 1978.

[2.4] Yoshida, K., Weh, H., "A Method of Modelling Permanent Magnets for Analytical Approach to Electrical Machinery", *Archiv für Elektrotechnik*, Vol. 68, pp. 229-239, 1985.

[2.5] Weh, H., May, H., "Achievable Force Densities for Permanent Magnet Excited Machines in New Configurations", *Proc. of International Conference on Electric Machines*, 8-10 September 1986, München, pp. 1107-1111.

[2.6] Deng, Z., Boldea, I., Nasar, S.A., "Forces and Parameters of Permanent Magnet Linear Synchronous Machines", *IEEE Trans. on Magnetics*, Vol. MAG-23, No. 1, pp. 305-309, 1987.

[2.7] Deng, Z., Boldea, I., Nasar, S.A., "Fields in Permanent Magnet Linear Synchronous Machines", *IEEE Trans. on Magnetics*, Vol. MAG-22, No. 2, pp. 107-112, 1986.

[2.8] Yamamoto, Y., Yamada, H., Fukunaga, S., Murashita, J., Hamanaka, Y., Wakiwaka, H., "Artificial Heart Driver Using Flat Type Linear Pulse Motor", *Proc. of International Conference on Electric Machines*, 8-10 September 1986, München, pp. 1187-1190.

[2.9] Ebihara, D., Yoshiura, T., Inoue, M., "Basic Design of a Linear Pulse Motor for Automatic Transfer Machine Systems", *Proc. of International Conference on Electric Machines*, 8-10 September 1986, München, pp. 267-270.

[2.10] Nagasaka, N., "Experimental Results from the Trial Production of PM Type Linear Pulse Motors with Rare-Earth Magnets", *Proc. of International Conference on Electric Machines*, 8-10 September 1986, München, pp. 152-155.

[2.11] Smith, A.C., Appel, A.C., "Determining the Maximum Thrust of a Permanent-Magnet Linear Actuator", 3rd International Conference on Electrical Machines and Drives, 16-18 November 1987, *IEE. Conf. Pub. 282*, pp. 344-347.

[2.12] Koziej, E., Szczypior, J., "A DC Linear Motor with Permanent Magnets", 3rd International Conference on Electrical Machines and Drives, 16-18 November 1987, *IEE. Conf. Pub. 282*, pp. 321-324.

[2.13] Basak, A., Al-Doori, T.H., "Microprocessor Controlled Brushless DC Linear Motor", International Conference on Power Electronics and Variable Speed Drives, London, 1-4 May 1984, *IEE Conf. Pub. 234*, pp. 402-404.

[2.14] Roubicek, O., Pejsek, Z., "Oscillatory Synchronous Linear Motor with Permanent-Magnet Excitation", *IEE Proc.* Vol. 127, Pt. B, No. 1, pp. 8-12, 1980.

[2.15] Olivier, E., Parisy, Ph., Yonnet, J.P., "A Linear Actuator for Robotics", *Proc. of Power Electronics and Applications*, Brussels, Belgium, 16-18 October 1985 (Antwerp, Belgium; Konimklijke Vlaamse Ingenieursvereniging, 85) p3/197-201, Vol. 2.

[2.16] Topmiller, D.A., Cathey, J.J., Yang, C.H., "A Microprocessor-Based Controller for Oscillatory Mode Drive of a Tubular Brushless DC Motor", *IEEE Industry Applications Society Annual Meeting*, 1985, IEEE-IAS-1985, pp. 536-541.

[2.17] Cathey, J.J., Topmiller, D.A., Nasar, S.A., "A Tubular Self-Synchronous Motor for Artificial Heart Pump Drive", *IEEE Trans. on Biomedical Engineering*, Vol. BME-33, No. 3, pp. 315-319, 1986.

[2.18] Laithwaite, E.R., *Induction Machines for Special Purposes*, London: Newnes, 1966, pp. 4-5.

[2.19] Rahman, M.A., Slemon, G.R., "Promising Applications of Neodymium Boron Iron Magnets in Electrical Machines", *IEEE Trans. on Magnetics*, Vol. MAG-21, No. 5, pp. 1712-1716, 1985.

[2.20] *Philips Data Handbook, Components and Materials,* Part 16, *Permanent Magnet Materials*, February 1984.

[3.1] Eastham, J.F., Akmese, R., "Linear Synchronous Tubular Drive System With Permanent Magnet Excitation: Construction and Standstill Forces.", *Proc. of the 2nd International Conference on Electrical Drives*, 20-22 September 1988, Poiana Brasov, Romania, pp. P1-II.

[3.2] Demerdash, N.A., Fouad, F.A., Nehl, T.W., "Determination of Winding Inductances in Ferrite Type Permanent Magnet Machinery by Finite Elements.", *IEEE Transactions on Magnetics*, Vol. MAG-18, No. 6, pp. 1052-1054, 1982.

[3.3] Nasar, S.A., *Electromagnetic Energy Conversion Devices and Systems*, New Jersey: Prentice-Hall, Inc., 1970, pp. 28-31.

[4.1] Claudio de Sa e Silva, "Brushless DC Motors Get a Controller IC That Replaces Complex Circuits", Electronic Design, September 19, pp. 149-156, 1985.

[4.2] Eastham, J.F., Akmese, R., "Oscillating DC Brushless Linear Motor Supplied by a Power Integrated Circuit", Proceedings of the Fifth Scientific Conference of the Scientific Research Council, 7-11 October 1989, Baghdad-Iraq, Vol. 5, pp 424-435.

[4.3] *Magnadur Magnets for DC Motors*, Mullard Ltd, 1970.

[5.1] Pillay, P., Krishnan, R., "Modelling, Simulation and Analysis of a Permanent Magnet Brushless DC Motor Drive", *IEEE Industrial Applications Society Annual Meeting*, 1987, pp. 7-14.

[5.2] Slemon, G.R., Gumaste, A.V., "Steady-State Analysis of a Permanent Magnet Synchronous Motor Drive with Current Source Inverter", *IEEE Trans. on Industry Applications*, Vol. IA-19, No. 2, pp. 190-197, 1983.

[5.3] Davat, B., Hacene, R., Lajoie-Mazenc, M., "Modelling of a Brushless DC Motor with Solid Parts Involving Eddy Currents", *IEEE Trans. on Industry Applications*, Vol. IA-21, No. 1, pp. 202-206, 1985.

[5.4] Rahman, M.A., Quaicoe, J.E., Choudhury, M.A., Slemon, G.R., "Steady-State Performance of Permanent Magnet Synchronous Motors Fed From Delta Modulated Inverters", *IEEE Industrial Applications Society Annual Meeting*, 1984, pp. 1359-1363.

[5.5] Colby, R.S., Lipo, T.A., Novotny, D.W., "A State Space Analysis of LCI Fed Synchronous Motor Drives in the Steady State", *ibid*, pp. 439-444.

[5.6] Krause, P.C., Voyles, R.M., Wasynczuk, O., "Analysis and Simulation of a Brushless DC Servomotor", *Proc. of Motor-Con* 1984, pp. 86-94.

[5.7] Demerdash, N.A., Nehl, T.W., "Dynamic Modelling of Brushless DC Motors for Aerospace Actuation", *IEEE Trans. on Aerospace and Electronic Systems*, Vol. AES-16, No. 6, pp. 811-821, 1980.

[5.8] Nehl, T.W., Fouad, F.A., Demerdash, N.A., Maslowski, E.A., "Dynamic Simulation of Radially Oriented Permanent Magnet-Type Electronically Operated Synchronous Machines with Parameters Obtained from Finite Element Solutions", *IEEE Trans. on Industry Applications*, Vol. IA-18, No. 2, pp. 172-182, 1982.

[5.9] Piriou, F., Razek, A., Perret, R., Le-Huy, H., "Torque Characteristics of Brushless DC Motors with Imposed Current Waveforms", *IEEE Industrial Applications Society Annual Meeting*, 1984, pp. 176-181.

[5.10] Himei, T., Funabiki, S., Agari, Y., Okada, M., "Analysis of Voltage Source Inverter Fed Permanent Magnet Synchronous Motor Taking Account of Converter Performance", *IEEE Trans. on Industry Applications*, Vol. IA-21, No. 1, pp. 279-284, 1985.

[5.11] Consoli, A., Abela, A., "Transient Performance of Permanent Magnet AC Motor Drives", *IEEE Trans. on Industry Applications*, Vol. IA-22, No. 1, pp. 32-41, 1986.

[5.12] Chalmers, B.J., Devgan, S.K., Howe, D., Low, W.F., "Synchronous Performance Prediction for High-Field Permanent Magnet Synchronous Motors", *Proc. of International Conference on Electric Machines*, 8-10 September 1986, München, pp. 1067-1070.

[5.13] Sebastian, T., Slemon, G.R., "Transient Modelling and Performance of Variable Speed Permanent Magnet Motors", *IEEE Industrial Applications Society Annual Meeting*, 1987, pp. 35-39.

[5.14] Spee, R., Wallace, A.K., "Performance Characteristics of Brushless DC Drives", *ibid*, pp. 1-6, 1987.

[5.15] Pillay, P., Krishnan, R., "Modelling of Permanent Magnet Motor Drives", *IEEE Trans. on Industrial Electronics*, Vol. 35, No. 4, pp. 537-541, 1988.

[5.16] Liu, T.H., Young, C.M. Liu, C.H., "Microprocessor-Based Controller Design and Simulation for a Permanent Magnet Synchronous Motor Drive", *ibid*, Vol. 35, No. 4, pp. 516-523, 1988.

[5.17] Hijazi, T.M., Demerdash, N.A., "Computer-Aided Modelling and Experimental Verification of the Performance of Power Conditioner Operated Permanent Magnet Brushless DC Motors Including Rotor Damping Effects", *IEEE Trans. on Energy Conversion*, Vol. 3, No. 3, pp. 714-721, 1988.

[5.18] Yamamoto, Y., "Analysis of Magnetic Circuit and Starting Characteristics of Flat-Type Linear Pulse Motor with Permanent Magnets", *Electrical Engineering in Japan*, Vol. 104B, No. 5, pp. 102-110, 1984.

[5.19] Yoshida, K., "Theory and Performance of Long-Stator Linear Synchronous Motors with Samarium-Cobalt Permanent-Magnet Excitation", *Proc. of International Conference on Electric Machines*, 8-10 September 1986, München, pp. 168-171.

[5.20] Akmese, R., Eastham, J.F., "Dynamic Performance of a Brushless DC Tubular Drive System", *IEEE Trans. on Magnetics,* Vol. MAG-25, pp. 3269-3271, 1989.

[5.21] Arockiasamy, R., "Development and Analysis of Thyristor Controlled Induction Motors", Ph.D Thesis, 1969, Imperial College, University of London.

[5.22] Evans, P.D., "Disc-Geometry Reluctance Motors", Ph.D Thesis, 1977, Imperial College, University of London.

[5.23] Mestha, L.K., "The Principle and Operation of an Induction Stepping Motor", Ph.D Thesis, 1986, University of Bath.

[6.1] Say, M.G., *Alternating Current Machines*, London: Pitman Ltd., 1976.

[6.2] Veinott, C.G., *Theory and Design of Small Induction Motors*, New York: McGraw-Hill Inc., 1959.